

Electrostatic Micro-Tweezers

by

Ayman Alneamy

A thesis
presented to the University of Waterloo
in fulfillment of the
thesis requirement for the degree of
Doctor of Philosophy
in
Systems Design Engineering

Waterloo, Ontario, Canada, 2020

© Ayman Alneamy 2020

Examining Committee Membership

The following served on the Examining Committee for this thesis. The decision of the Examining Committee is by majority vote.

External Examiner: Walter Lacarbonara
Professor, Dept. of Structural and Geotechnical Engineering
Sapienza University of Rome, Italy

Co-supervisor: Eihab Abdel-Rahman
Professor, Dept. of Systems Design Engineering
University of Waterloo, Canada

Co-supervisor: Glenn Heppler
Professor, Dept. of Systems Design Engineering
University of Waterloo, Canada

Internal Member: John Yeow
Professor, Dept. of Systems Design Engineering
University of Waterloo, Canada

Internal-External Member: Mostafa Yavuz
Professor, Dept. of Mechanical Engineering
University of Waterloo, Canada

Internal-External Member: Hector Budman
Professor, Dept. of Chemical Engineering
University of Waterloo, Canada

Author's Declaration

This thesis consists of material all of which I authored or co-authored: see Statement of Contributions included in the thesis. This is a true copy of the thesis, including any required final revisions, as accepted by my examiners.

I understand that my thesis may be made electronically available to the public.

Statement of Contributions

Most of the content of this dissertation has been previously disseminated through a provisional patent, peer-reviewed journal and conference papers. The use of the content from the listed publications in this dissertation has been approved by all co-authors. I am either the first author or co-authored of the following:

- **Provisional Patent**

- **Ayman M Alneamy**, Eihab M Abdel-Rahman, Glenn R Heppler & Mahmoud E Khater. Electrostatic arch micro-tweezers. *U.S. Provisional Patent*. No: 62/895,493. 26 Sep. 2019.

- **Peer-reviewed Journal Papers**

- **Alneamy, A. M.**, Khater, M. E., Abdel-Aziz, A. K., Heppler, G. R., & Abdel-Rahman, E. M. (2020). “Electrostatic arch micro-tweezers.” *International Journal of Non-Linear Mechanics*, 118, 103298.
- **Alneamy, A.**, Khater, M., Al-Ghamdi, M., Abdel-Aziz, A., Heppler, G., & Abdel-Rahman, E. (2020). “Large Oscillation of Electrostatically Actuated Curved Beams.” *Journal of Micromechanics and Microengineering*. (In press: JMM-104691.R1).
- **Alneamy, A.**, Heppler, G., Abdel-Rahman, E., & Khater, M. (2020). “On Design and Analysis of Electrostatic Arch Micro-tweezers.” *Journal of Vibration and Acoustics*. (Under Review: VIB-20-1230).

- **Conference Papers**

- **Ayman Alneamy**, Mahmoud Khater, Ahmed Abdel Aziz, Glenn Heppler & Eihab Abdel-Rahman. Electrostatic Arch Micro-Tweezers. *Euromech 603: Dynamics of Micro and Nano Electromechanical Systems*, Porto, Portugal, September 2018, pp. 88-91.

- **Ayman Alneamy**, Eihab Abdel-Rahman, Glenn Heppler, Ahmed Abdel Aziz & Mahmoud Khater. Chaos in Electrostatically Actuated Arch Beams. *International Nonlinear Dynamics Conference*, Rome, Italy, February 2019, p.312.

- **Ayman M Alneamy**, Eihab M Abdel-Rahman & Glenn R Heppler. Reduced Order Model of Electrostatic Micro-Tweezers. *European Nonlinear Dynamics Conference*, Lyon, France, July 5-10, 2020, pp. 305967.

Abstract

This dissertation presents a novel electrostatic micro-tweezers designed to manipulate particles with diameters in the range of 5–14 μm . The tweezers consist of two grip-arms mounted to an electrostatically actuated initially curved micro-beam. The tweezers offer further control, via electrostatic actuation, to increase the pressure on larger objects and to grasp smaller objects.

It can be operated in two modes. The first is a traditional quasi-static mode where DC voltage commands the tweezers along a trajectory to approach, hold and release micro-objects. It exploits nonlinear phenomena in electrostatic curved beams, namely snap-through, snap-back and static pull-in and the bifurcations underlying them. The second mode uses a harmonic voltage signal to release, probe and/or interact with the objects held by the tweezers in order to perform function such as cells lysis and characterization. It exploits additional electrostatic MEMS phenomena including dynamic pull-in as well as the orbits and attractors realized under harmonic excitation.

Euler-Bernoulli beam theory is utilized to derive the tweezers governing equation of motion taking into account the arm rotary inertia, the electrostatic fringing field and the nonlinear squeeze-film damping. A reduced-order model (ROM) is developed utilizing two, three and five straight beam mode shapes in a Galerkin expansion. The adequacy of the ROM in representing the tweezers response was investigated by comparing its static and modal response to that of a 2D finite element model (FEM).

Simulation results show small differences between the ROM and the FEM static models in the vicinity of snap-through and negligible differences elsewhere. The results also show the ability of the tweezers to manipulate micro-particles and to smoothly compress and hold objects over a voltage range extending from the snap-back voltage (89.01 V) to the pull-in voltage (136.44 V).

Characterization of the curved micro-beam show the feasibility of using it as a platform for the tweezers. Evidence of the static snap-through, primary resonance and the superharmonic resonances of orders two and three are observed. The results also show the co-existence of three stable orbits around one stable equilibrium under excitation waveforms with a voltage less than the snap-back voltage.

Three branches of orbits are identified as a one branch of small orbits within a narrow potential well and two branches of medium-sized and large orbits within a wider potential well. The transition between those branches results in a characteristic of double-peak frequency-response curve. We also report evidence of a bubble structure along the medium-sized branch consisting of a cascade of period-doubling bifurcations and a cascade of reverse period-doubling bifurcations.

Experimental evidence of a chaotic attractor developing within this structure is reported. Odd-periodic windows also appear within the attractor including period-three (P-3), period-five (P-5) and period-six (P-6) windows. The chaotic attractor terminates in a cascade of reverse period-doubling bifurcations as it approaches a P-1 orbit.

Acknowledgments

First of all, I am grateful to Allah Azza wa Jal for empowering me to successfully complete this dissertation which in fact without his help, I would not have the ability and the power to reach this stage in my life.

I would like to take this opportunity to thank all the people who made this dissertation possible and my Ph.D. a wonderful journey. My deepest gratitude goes to my advisors, Prof. Eihab M Abdel-Rahman and Prof. Glenn R Heppler. Their motivations have directed me through different directions either on my personal life or academia. I have been extremely lucky to have supervisors whom care so much about my work and whom respond to my questions and queries so promptly and seriously. It is really hard to describe their personalities and commitments to my development both as a student and a researcher.

They shared with me uncountable knowledge and experiences and always they provided constructive guidance. Their reactions and supports during the summer of 2018 are truly appreciated and will never be forgiven. You have been acting more than supervisors during the last seven years.

I would like to thank members of the examining committee: Prof. Mustafa Yavuz, Prof. John Yeow and Prof. Hector Budman from the University of Waterloo who have taken time to review my dissertation and their constructive comments, which helped me in improving the final version of this work. Special thank goes to Prof. Walter Lacarbonara for acting as the external examiner. His feedbacks were significantly valuable.

I am especially thankful to Dr. Mahmoud Khater who provided detailed comments and suggestions to improve this work. I am extended my thanks and appreciation to my co-authors, Dr. Sangtak Park, Dr. Majed Al-Ghamdi and Dr. Ahmed Abdel-Aziz, for their cooperation and comments through this work.

Many thanks also extend to the classmates Resul Saritas, Alaa Elhady, Mohammed Arabi, Amr Kamel and Charbel Aziz, the colleagues whom I sadly did not have a chance to write papers with, but their helps and feedbacks are highly appreciated. My time at Waterloo was made enjoyable due to the many friends who became a part of my life. Special thank goes to my closest friends Ali Qabur, Tirad Owais and Khaid Alshemari with whom I really enjoyed discussing different aspects of life.

I would also like to thank my best friends in Saudi Arabia Ali Yagup, Ali Qaseem, Asem Mokali, Zailay Mubarak, Ibrahim Qaseem, Ahmed Mokali, Mohammed Qaseem, Ali Mokali, Ahmed Gharama, Maymoun Qaseem, Turkey Muharaq and so many friends whom known how much I love them. I am grateful to my family for encouraging me in all of pursuits and inspiring me to follow my true dreams. I am especially grateful to my parents, Mohammed Alneamy and Liyla Alneamy, whom supported me emotionally and financially and for their endless prayers in all times. Thank you for teaching me that my job in this life was to conduct, to learn new stuff, to teach others and to provide help to those in needs. I always knew that you believed in me and wanted the best for me. A big thank goes to my brothers and sisters for their endless supports.

I would like to thank my lovely wife, Hadel Qaseem. Who without her support, patience, encouragement and understanding during my studies, this Ph.D can't be a real. I am thankful for my daughters, Hetaf and Mehaf, for making us smiling all the time. Finally, this work was financially supported by Jazan University and Saudi Cultural Bureau in Canada. Without their supports, I probably would not have the opportunity to attend the University of Waterloo.

☺Thank you☺

Dedication

To my parents “Mohammed and Liyla” for their prayers.

To my wife “Hadel” for her patient and love.

To my daughters “Hutaf and Mehaf” for their smiles.

To my brothers “Musa and Abdel-Majeed” for their supports.

To my sisters “Sarah, Sohamia, Seham, Samah and Solaf for their encouragement.

with respect and love

Table of Contents

List of Figures	xvi
List of Tables	xxix
Abbreviations	xxxii
List of Symbols	xxxii
1 Introduction	1
1.1 MEMS	1
1.2 Research Motivation	4
1.3 Research Objectives	5
1.4 Organization of the Dissertation	6
2 Literature Review	8
2.1 Initially Curved Micro-beams	8
2.1.1 Static Behavior	10

2.1.2	Dynamic Behavior	11
2.2	Micro-tweezers	14
2.2.1	Electrothermal Micro-tweezers	15
2.2.2	Electrostatic Micro-tweezers	17
2.2.3	Modeling Techniques	20
2.3	Summary	22
3	Tweezers Design and Fabrication	23
3.1	Prototype I	23
3.1.1	Gripping Mechanism	24
3.1.2	Device Parameters	26
3.2	Prototype II	27
3.2.1	Gripping Mechanism	28
3.2.2	Device Parameters	29
3.3	Fabrication Process	29
3.4	Summary	37
4	Tweezers Modeling	38
4.1	Equation of Motion	38
4.1.1	The Potential Energy	42
4.1.2	The Kinetic energy	43
4.1.3	Extended Hamilton Principle	44

4.2	Nondimensional Equation of Motion	51
4.3	Reduced-Order Model (ROM)	52
4.3.1	Static Analysis	55
4.3.2	Variation of the Natural Frequency under Electrostatic Forcing	57
4.3.3	Dynamic Analysis	59
4.4	Summary	60
5	Characterizations of Initially Curved Micro-beams	61
5.1	Static Response	62
5.2	Variation of the Natural Frequency under Electrostatic Forcing	68
5.3	Dynamic Response	73
5.3.1	Linear Case	73
5.3.2	Nonlinear Case	75
5.4	Actuator I	82
5.4.1	Static Response	84
5.4.2	Dynamic Response	86
5.5	Actuator II	94
5.6	Summary	100
6	Characterizations of Micro-Tweezers	102
6.1	Static Operational Mode	102
6.1.1	Platform Deflection	102

6.1.2	Grip Range	106
6.1.3	Dynamic Mode of Operation	108
6.1.4	ROM Validation	112
6.1.5	Variation of the Natural Frequency under Electrostatic Forcing	126
6.2	Summary	127
7	Concluding Remarks	129
7.1	Summary of Contributions	129
7.1.1	Arch Micro-tweezers	129
7.1.2	Initially Curved Beam	131
7.2	Research Limitations	132
7.3	Directions for Future Study	133
7.4	List of Publications	133
	References	137
	APPENDICES	157
	A Masks Design with Integrated Dicing	158
	B Eigenvalues Analysis Including Higher Order Rotary Inertia Terms	162
	C Dynamic Analysis Including Higher Order Rotary Inertia Terms	166

D Supplementary Data	168
D.1 Modal Analysis	168
D.2 ROM Validation	170
D.3 Tweezers Mode Shapes with Flexible Arms	185

List of Figures

1.1	Examples of MEMS devices.	2
2.1	A schematic showing the change in the beam curvature profile as a function of the actuation voltage.	9
2.2	Examples of MEMS initial curved micro-beams based devices.	12
2.3	SEM picture of SU-8 electrothermal micro-tweezers [97].	16
2.4	Linear and rotary interdigitated comb-fingers electrostatic micro-tweezers.	18
3.1	Isometric view of the prototypes I showing an electrostatically actuated initially curved micro-beam carrying two identical and inclined arms.	24
3.2	Tweezers configurations: (a) before and (b) after the snap-through voltage V_S	25
3.3	A schematic showing the tweezers' parameters of prototype I.	26
3.4	Isometric view of the prototype II showing an electrostatically actuated initially curved micro-beam carrying only one inclined movable arm and a stationary arm.	27
3.5	A schematic showing the tweezers' parameters of prototype II.	29

3.6	Metals deposition: (a) a 30 nm thick Cr deposited to serve as an adhesion layer for the metal and (b) A 100 nm thick Au layer sputtered on top of Cr layer.	31
3.7	Photoresist layer: (a) spin-coated to cover the wafer and (b) expose to the UV-light and pattern using Mask 1.	32
3.8	Etching the metallization layers and stripped off the remaining photoresist.	32
3.9	Ph layer spin-coated to cover the wafer.	33
3.10	Ph layer exposed to the UV-light and pattern using Mask 2.	33
3.11	Device layer etching using DRIE.	34
3.12	Unexposed Ph stripped away.	34
3.13	Backside Ph layer exposed to the UV-light and pattern using Mask 3. . . .	35
3.14	Handle layer etching using DRIE and unexposed photoresist stripped away.	35
3.15	Releasing the device layer using wet chemical etcher (HF).	35
3.16	SEM pictures of: (a) the fabricated prototype I before the backside etching step and (b) a close-up on the grip arms.	36
4.1	A schematic of the curved beam carrying two identical arms at points B_1 and B_2	39
4.2	An element of the curved beam showing the location before, marked as \mathbf{P} , and after deformation, marked as \mathbf{P}^*	40
4.3	The nondimensional mode shapes of a straight beam: (a) the first three symmetric modes and (b) the first three anti-symmetric modes.	55
5.1	A schematic of the electrostatic curved beam actuator.	62

5.2	The beam mid-point deflection $w_s(0.5)$ as a function of the RMS voltage obtained from ROMs employing two- (marked with orange lines), three- (marked with magenta lines) and five-symmetric (marked with green lines) modes in the Galerkin expansion without accounting for the electrostatic fringing field. The branches of stable equilibria are marked in solid lines and branches of unstable equilibria are marked in dashed lines.	65
5.3	The beam mid-point deflection $w_s(0.5)$ as a function of the RMS voltage using the five-symmetric modes ROM with parallel-plate model marked with orange lines, Palmer's model marked with magenta lines, Kimbali's model marked with green lines and FEM marked with (●) symbol. The branches of stable equilibria are marked in solid lines and branches of unstable equilibria are marked in dashed lines.	67
5.4	Variation in the first four natural frequencies of the curved beam as a function of the RMS voltage along: the first symmetric in-plane marked with orange line (—), first anti-symmetric in-plane marked with magenta line (—), second symmetric in-plane marked with green line (—) and second anti-symmetric in-plane brown line (—). Zone I represents the first stable equilibrium, corresponding to the beam initial curvature, Zone II represents two stable equilibria at the same RMS voltage and Zone III represents the second stable equilibrium, corresponding to the beam initial counter-curvature.	69

5.5	Variation of the first three natural frequencies as a function of the RMS voltages obtained using the ROM (solid line) and the FEM marked by (●) symbol of: (a) the fundamental natural frequency f_1 corresponding to the first in-plane symmetric mode, (b) the second frequency f_2 corresponding to the first in-plane anti-symmetric mode and (c) the third frequency f_3 corresponding to the second in-plane symmetric mode.	71
5.6	The first four mode shapes $\phi_i(x)$ at $V_{\text{RMS}} = 0$ V of: straight beam mode shapes marked as (solid lines) and actual mode shapes of curved beam obtained by the FEM and marked as (dashed lines).	72
5.7	FRCs of the initially curved beam at $V_{\text{DC}} = V_{\text{AC}} = 2$ V of the beam midpoint: (a) displacement amplitude and (b) RMS velocity. The results obtained analytically using LTI are marked with symbols and shooting method are marked as solid black lines (—) for stable branches of solution.	74
5.8	FRCs of the initially curved beam at $V_{\text{DC}} = V_{\text{AC}} = 40$ V of the beam midpoint: (a) displacement amplitude and (b) RMS velocity. The results obtained analytically using LTI are marked with symbols and shooting method are marked as solid black lines (—) for stable branches of solution and dashed red lines (- -) for unstable branches of solution.	76
5.9	The phase-portraits around the stable equilibrium marked as (●) symbol at voltage waveform $V_{\text{DC}} = V_{\text{AC}} = 40$ V shows superharmonic resonance along the branch of small oscillations of: (a) order-four at $f_{ex} = 9$ kHz, (b) order-three at $f_{ex} = 12$ kHz and (c) order-two at $f_{ex} = 16.5$ kHz and (d) forced resonance with P-1 orbit at $f_{ex} = 30.5$ kHz.	78
5.10	A schematic diagram of the experimental setup.	82

5.11	(a) FFT of the measured mid-point velocity \dot{w} for actuator I under the pulse train $V_{PI} = 18$ V, $f_{ex} = 1$ kHz and duty cycle 0.8 % showing its fundamental frequencies, (b) the first in-plane bending mode and (c) the first out-of-plane bending mode.	83
5.12	The beam mid-point deflection $w_s(0.5)$ of actuator I as a function of RMS voltage calculated from ROMs employing two, three and five symmetric modes. Stable equilibria are marked by solid lines and unstable equilibria are marked by dotted lines.	84
5.13	SEM pictures showing the curved beam configurations: (a) before (initial curvature) and (b) after (counter initially curvature) the snap-through motion.	86
5.14	The measured frequency-response curve of the mid-point RMS velocity for $V_{DC} = V_{AC} = 18$ V shows three stable branches of oscillations: a branch of small orbits correspond to oscillations in a narrow-well and two branches of medium and large orbits corresponding to oscillations in a wider-well. The jump-up through cyclic-fold bifurcation is marked with (●) symbol and the jump-down is marked with (●) symbol.	87
5.15	The simulated frequency-response curve of the mid-point RMS velocity of actuator I for $V_{DC} = V_{AC} = 18$ V shows three branches of stable oscillations marked solid blue lines (—). They are a branch of small orbits corresponding to oscillations in a narrow-well and two branches of medium-sized and large orbits corresponding to oscillations in a wider-well and three branches of unstable oscillations marked dashed red lines (- -).	89

5.16	A bifurcation diagram of the shaded region in the frequency-response curve constructed by stacking one-sided Poincaré sections of the displacement w at positive slope crossings of the axis $\dot{w} = 0$ along: a small orbits branch, superharmonic orbits marked in magenta (—) and P-1 orbits marked in blue (—). A branch of medium-sized orbits is marked in black (—) and a branch of large orbits is marked in green (—).	92
5.17	Phase portraits under the voltage waveform $V_{DC} = V_{AC} = 18$ V corresponding to a single stable equilibrium of $w_s = 2.69$ μm : (a) P-2 at $f_{ex} = 19.03$ kHz, (b) P-4 at $f_{ex} = 18.73$ kHz and (c) P-8 $f_{ex} = 18.53$ kHz.	93
5.18	Phase portraits of three co-existing solution, small in blue (—), medium-sized in black (—) and large in green (—), under the voltage waveform $V_{DC} = V_{AC} = 18$ V, corresponding to a single stable equilibrium of $w_s = 2.69$ μm , and a signal frequency of $f_{ex} = 17.5$ kHz.	94
5.19	FFTs of the measured mid-point velocity (\dot{w}) for actuator II under the voltage waveform $V_{DC} = 30$ V and $V_{AC} = 7.5$ V at four discrete signal frequencies: (a) superharmonic response at $f_{ex} = 13$ kHz and (b) forced response at $f_{ex} = 18$ kHz.	95
5.20	FFTs of the measured mid-point velocity (\dot{w}) for actuator II under the voltage waveform $V_{DC} = 30$ V and $V_{AC} = 7.5$ V at four discrete signal frequencies: (a) resonant response at $f_{ex} = 26$ kHz and (b) resonant response at $f_{ex} = 28.5$ kHz.	96
5.21	FFTs of the measured mid-point velocity (\dot{w}) for actuator II under the signal waveform $V_{DC} = 30$ V and $V_{AC} = 7.5$ V and signal frequency of $f_{ex} = 26.75$ kHz show evidence of a chaotic attractor in: (a) linear scale and (b) dB scale.	97

5.22	<p>FFTs of the measured mid-point velocity (\dot{w}) in dB scale for actuator II under the signal waveform $V_{DC} = 30$ V and $V_{AC} = 7.5$ V shows evidence of a chaotic attractor with odd windows: a period-three (P-3) orbit at $f_{ex} = 26.44$ kHz (a) linear and (b) dB scales, a period-five (P-5) orbit at $f_{ex} = 26.83$ kHz (c) linear and (d) dB scales and a period-six (P-6) orbit at $f_{ex} = 27.19$ kHz (e) linear and (f) dB scales. Evidence of a cascade of reverse period-doubling bifurcations is also shown with (g) linear and (h) dB scales a period-four (P-4) orbit at $f_{ex} = 27.27$ kHz and a period-two (P-2) orbit at $f_{ex} = 27.38$ kHz (i) linear and (j) dB scales.</p>	100
6.1	<p>Variation in the beam mid-point deflection $w_s(0.5)$ as a function of the RMS voltage obtained using: a five-mode ROM accounting for the electrostatic fringing field. The branches of stable solutions are marked as solid green lines (—) and the branches of unstable solutions are marked as dashed green lines (- -). The FEM without arms are marked as (●) symbol and with flexible arms are marked as (◆) symbol.</p>	104
6.2	<p>The tips separation as a function of RMS voltage calculated using the 2D FEM.</p>	106
6.3	<p>A snapshot of the arms configuration (a) before at $V_{RMS} = 95$ V and (b) after at $V_{RMS} = 130$ V the snap-through.</p>	107
6.4	<p>Variation of the first five natural frequencies, 1st SY mode (black), 1st ASY mode (magenta), 2nd SY mode (green), 2nd ASY mode (orange) and 3rd SY mode (blue), of the arch micro-tweezers as the arms length varies from 0 to 250 μm obtained using a 2D FEM.</p>	109

6.5	(a) The first SY, (b) the first ASY, (c) the second SY, (d) the second ASY and (e) the third SY mode shapes of the arch micro-tweezers with arms length of $\ell_a = 250 \mu\text{m}$	110
6.6	A close-up view showing the crossover points between the 1 st ASY, 2 nd SY and 2 nd ASY modes.	111
6.7	Variation of the first five natural frequencies, 1 st SY mode (black), 1 st ASY mode (magenta), 2 nd SY mode (green), 2 nd ASY mode (orange) and 3 rd SY mode (blue), of the arch micro-tweezers as the arms length varies from 0 to 250 μm obtained using a five-mode ROM (solid lines) and a 2D FEM (dotted lines).	113
6.8	The second symmetric mode $\phi_3(x)$ of the tweezers platform (dashed lines) for flexible arms lengths: (a) $\ell_a = 0 \mu\text{m}$, (b) $\ell_a = 50 \mu\text{m}$, (c) $\ell_a = 150 \mu\text{m}$ and (d) $\ell_a = 250 \mu\text{m}$ compared to that of a straight beam (solid lines).	115
6.9	Variation in the locations of the interior nodes marked by (•) of the second symmetric mode $\phi_3(x)$ of the tweezers platform with flexible arms as functions of the arms length. The platform mid-point is marked as a dashed black line (- -). The arms attachment points are marked as dashed blue lines (- -).	116
6.10	The second asymmetric mode $\phi_4(x)$ of the tweezers platform (dashed lines) for flexible arms lengths: (a) $\ell_a = 0 \mu\text{m}$, (b) $\ell_a = 50 \mu\text{m}$, (c) $\ell_a = 150 \mu\text{m}$ and (d) $\ell_a = 250 \mu\text{m}$ compared to that of a straight beam (solid lines).	118

6.11	Variation in the locations of the outer nodes marked with (●) and center node marked with (●) of the second asymmetric mode $\phi_4(x)$ of the tweezers platform with flexible arms as functions of the arms length. The platform mid-point is marked as a dashed black line (- -). The arms attachment points are marked as dashed blue lines (- -).	119
6.12	The third asymmetric mode $\phi_5(x)$ of the tweezers platform (dashed lines) for flexible arms lengths: (a) $\ell_a = 0 \mu\text{m}$, (b) $\ell_a = 50 \mu\text{m}$, (c) $\ell_a = 150 \mu\text{m}$ and (d) $\ell_a = 250 \mu\text{m}$ compared to that of a straight beam (solid lines). . .	120
6.13	Variation in the locations of the outer nodes marked with (●) and interior nodes marked with (●) of the third symmetric mode $\phi_5(x)$ of the tweezers platform with flexible arms as functions of the arms length. The platform mid-point is marked as a dashed black line (- -). The arms attachment points are marked as dashed blue lines (- -).	121
6.14	Variation in the locations of the outer nodes marked by (●), interior nodes marked by (●) and the center node marked by (●) of the third asymmetric mode $\phi_6(x)$ of the tweezers platform with flexible arms as functions of the arms length. The platform mid-point is marked as a dashed black line (- -). The arms attachment points are marked as dashed blue lines (- -).	122
6.15	Variation in the locations of the outer nodes marked by (●, ● and ●) and interior nodes marked by (●) of the fourth symmetric mode $\phi_7(x)$ of the tweezers platform with flexible arms as functions of the arms length. The platform mid-point is marked as a dashed black line (- -). The arms attachment points are marked as dashed blue lines (- -).	123

6.16	Variation in the locations of the outer nodes marked by (● and ●), interior nodes marked by (●) and the center node marked by (●) of the fourth asymmetric mode $\phi_8(x)$ of the tweezers platform with flexible arms as functions of the arms length. The platform mid-point is marked as a dashed black line (- -). The arms attachment points are marked as dashed blue lines (- -).	124
6.17	Variation in the locations of the outer nodes marked by (● and ●), interior nodes marked by (●, ● and ●) of the fifth symmetric mode $\phi_9(x)$ of the tweezers platform with flexible arms as functions of the arms length. The platform mid-point is marked as a dashed black line (- -). The arms attachment points are marked as dashed blue lines (- -).	125
6.18	Variation of the fundamental natural frequency of the tweezers platform as functions of RMS voltage in the absence of arms, ROM results as shown as orange lines (—) and FEM results are shown as (★) symbols, and in the presence of arms ($\ell_a = 250 \mu\text{m}$), ROM results are shown as magenta lines (—) and FEM results are shown as (●) symbols.	127
A.1	Mask1 for the metalization layers.	158
A.2	Mask 2 used to define the device area on the top photoresist layer.	159
A.3	Mask 3 used to define the backside etched area on the bottom photoresist layer.	160
A.4	Wire bonding performed on 68 PGA chip carries for the electrical connection.	161

D.1	Variation of the first five natural frequencies, 1 st SY mode (black), 1 st ASY mode (magenta), 2 nd SY mode (green), 2 nd ASY mode (orange) and 3 rd SY mode (blue), of the arch micro-tweezers with rigid arms as the length varies from 0 to 250 μm obtained using a 2D FEM.	169
D.2	The mode shapes obtained using ROM for a straight beam (dotted lines) and FEM for a curved beam with 250 μm rigid arms (solid lines) and flexible arms (dashed lines): (a) 1 st symmetric (SY) and (b) 1 st anti-symmetric (ASY) modes.	172
D.3	The second symmetric mode $\phi_3(x)$ of the tweezers platform with rigid arms (solid green lines) and with flexible arms (dashed red lines) for arms lengths: (a) $\ell_a = 0 \mu\text{m}$, (b) $\ell_a = 50 \mu\text{m}$, (c) $\ell_a = 150 \mu\text{m}$ and (d) $\ell_a = 250 \mu\text{m}$ compared to that of a straight beam (black dotted lines).	174
D.4	Variation in the locations of the interior nodes marked by (•) of the second symmetric mode $\phi_3(x)$ of the tweezers platform as functions of the arms length: (a) rigid and (b) flexible arms. The platform mid-point is marked as a dashed black line (- -). The arms attachment points are marked as dashed blue lines (- -).	175
D.5	The second asymmetric mode $\phi_4(x)$ of the tweezers platform with rigid arms (solid orange lines) and with flexible arms (dashed red lines) for arms lengths: (a) $\ell_a = 0 \mu\text{m}$, (b) $\ell_a = 50 \mu\text{m}$, (c) $\ell_a = 150 \mu\text{m}$ and (d) $\ell_a = 250 \mu\text{m}$ compared to that of a straight beam (black dotted lines).	177

D.6	Variation in the locations of the outer nodes marked with (●) and center node marked with (●) of the second asymmetric mode $\phi_4(x)$ of the tweezers platform as functions of the arms length: (a) rigid and (b) flexible arms. The platform mid-point is marked as a dashed black line (- -). The arms attachment points are marked as dashed blue lines (- -).	178
D.7	The third symmetric mode $\phi_5(x)$ of the tweezers platform with rigid arms (solid blue lines) and with flexible arms (dashed red lines) for arms lengths: (a) $\ell_a = 0 \mu\text{m}$, (b) $\ell_a = 50 \mu\text{m}$, (c) $\ell_a = 150 \mu\text{m}$ and (d) $\ell_a = 250 \mu\text{m}$ compared to that of a straight beam (black dotted lines).	179
D.8	Variation in the locations of the outer nodes marked with (●) and interior nodes marked with (●) of the third symmetric mode $\phi_5(x)$ of the tweezers platform as functions of the arms length: (a) rigid and (b) flexible arms. The platform mid-point is marked as a dashed black line (- -). The arms attachment points are marked as dashed blue lines (- -).	180
D.9	Variation in the locations of the outer nodes marked by (●), interior nodes marked by (●) and the center node marked by (●) of the third asymmetric mode $\phi_6(x)$ of the tweezers platform as functions of the arms length: (a) rigid and (b) flexible arms. The platform mid-point is marked as a dashed black line (- -). The arms attachment points are marked as dashed blue lines (- -).	181
D.10	Variation in the locations of the outer nodes marked by (●, ● and ●) and interior nodes marked by (●) of the fourth symmetric mode $\phi_7(x)$ of the tweezers platform as functions of the arms length: (a) rigid and (b) flexible arms. The platform mid-point is marked as a dashed black line (- -). The arms attachment points are marked as dashed blue lines (- -).	182

D.11 Variation in the locations of the outer nodes marked by (● and ●), interior nodes marked by (●) and the center node marked by (●) of the fourth asymmetric mode $\phi_8(x)$ of the tweezers platform as functions of the arms length: (a) rigid and (b) flexible arms. The platform mid-point is marked as a dashed black line (- -). The arms attachment points are marked as dashed blue lines (- -). 183

D.12 Variation in the locations of the outer nodes marked by (● and ●), interior nodes marked by (●, ● and ●) of the fifth symmetric mode $\phi_9(x)$ of the tweezers platform as functions of the arms length: (a) rigid and (b) flexible arms. The platform mid-point is marked as a dashed black line (- -). The arms attachment points are marked as dashed blue lines (- -). 184

List of Tables

2.1	Recent works on electrothermal micro-tweezers	17
2.2	Relevant and related works on electrostatic micro-tweezers	19
3.1	Material properties of single crystal Silicon	30
4.1	Scaling orders of the tweezers' parameters	41
5.1	The relative error of the converge analysis at $w_s = -5.63 \mu\text{m}$	64
5.2	Actuators as-designed dimensions in (μm).	81
6.1	Comparison of snap-through and pull-in voltages obtained using the ROM and the 2D FEM.	105
6.2	Comparison of the first five natural frequencies (in kHz) of the micro- tweezers at two arms lengths obtained from a ROM with rigid arms and an FEM with flexible arms.	112
D.1	Comparison of the first five natural frequencies (in kHz) of the micro- tweezers with rigid arms at two arms lengths obtained from a ROM and an FEM.	170

D.2	The mode shapes of the micro-tweezers without and with 50 μm flexible arms obtained using 2D FEM.	185
D.3	The mode shapes of the micro-tweezers with 150 μm and 250 μm flexible arms obtained using 2D FEM.	186

Abbreviations

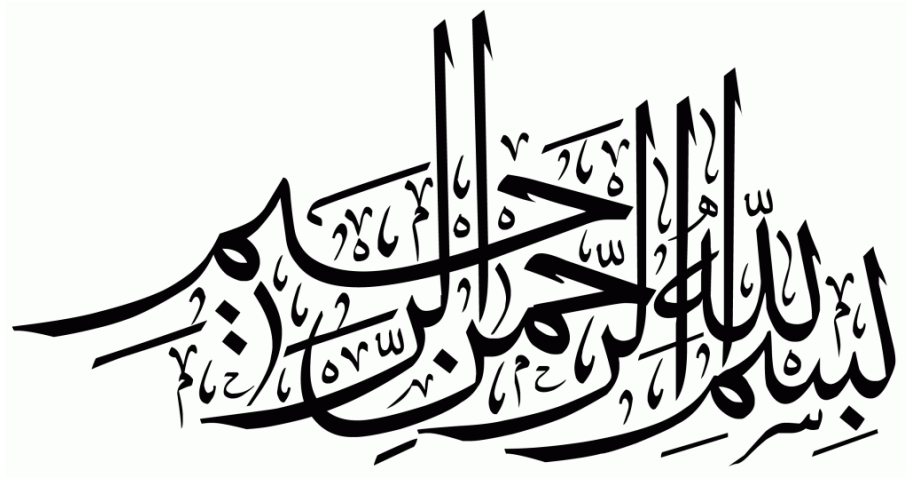
DLP	Digital Light Processor
MDA	Micro-Device-Assembly
MEMS	Micro-ElectroMechanical Systems
PolyMUMPs	PolySilicon Multi-User MEMS Processes
RF	Radio Frequency
SEM	Scanning Electron Microscope
SOIMUMPs	Silicon on Insulator Multi-User MEMS Processes
UW-MEMS	University of Waterloo MEMS Fabrication Process

List of Symbols

A_b	Beam cross-sectional area
δ'_d	Doublet function
ε_{xx}	Axial strain
\mathbf{F}_{es}	Electrostatic force
I_b	Beam second moment of inertia
J_a	Arms moment of inertia
ℓ_1	Distance from the left anchor to the first arm
ℓ_2	Distance from the left anchor to the second arm
Q	Quality factor
V_{RMS}	Root-Mean Square voltage
T_s	Time period
T	Kinetic energy
U	Potential energy
V_{AC}	Signal voltage amplitude
V_{DC}	Bias voltage
V_{B}	Snap-back voltage
V_{P}	Pull-in voltage
V_{S}	Snap-through voltage

α_i	Nondimensional coefficients
β_i	i^{th} roots of characteristic equation
b	Device layer thickness
c_{sf}	Squeeze-film damping coefficient
c_{va}	Damping coefficient in the axial direction
c_{vt}	Damping coefficient in the transverse direction
δ	Differential operator
δ_d	Dirac-Delta function
d	Capacitor gap
f_{ex}	Signal excitation frequency
g_o	Distance between the arms tips
h_a	Arm thickness
h_b	Beam thickness
h_o	Beam mid-point initial rise
h_{sa}	Stationary arm thickness
ℓ_a	Arm length
ℓ_b	Beam length
ℓ_c	Distance between the arms attachment points
ℓ_{sa}	Stationary arm length
m_a	Arm total mass
ω_n	n^{th} natural frequencies
$\phi_i(x)$	i^{th} straight beam mode shape
$q_i(t)$	Dynamic modal coordinates

ℓ_t	Arm tip length
θ	Beam element rotation angle
t	Time in (sec)
u_i	Static modal coordinates
u	Axial displacement
w_d	Dynamic defelection
\mathbf{W}_{nc}	Work done by nonconservative forces
$w_o(x)$	Initial shape of the micro-beam curvature
w_s	Static defelection
w	Transverse displacement
ζ	Coordinate pointing into the curvature



In the name of God, the Most Gracious, the Most Merciful

Chapter 1

Introduction

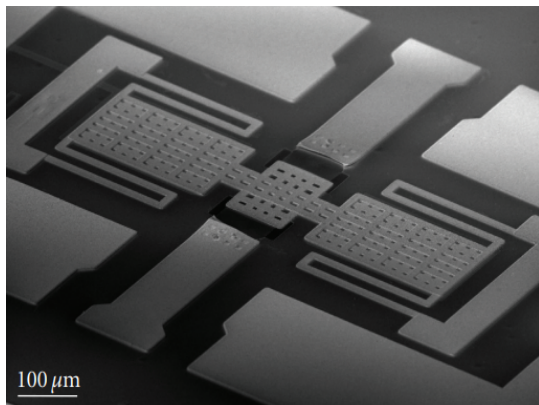
1.1 MEMS

Micro-Electro-Mechanical Systems [MEMS](#) technology is used to create small machines that combine mechanical and electrical components. MEMS fabrication is based on integrated circuit semiconductor fabrication processes, such as bulk micro-machining, surface micro-machining and lithography processes [\[1\]](#). Many commercial processes are available to fabricate MEMS devices such as [PolyMUMPs](#) [\[2\]](#), [SOIMUMPs](#) [\[3\]](#) and [UW-MEMS](#) [\[4\]](#).

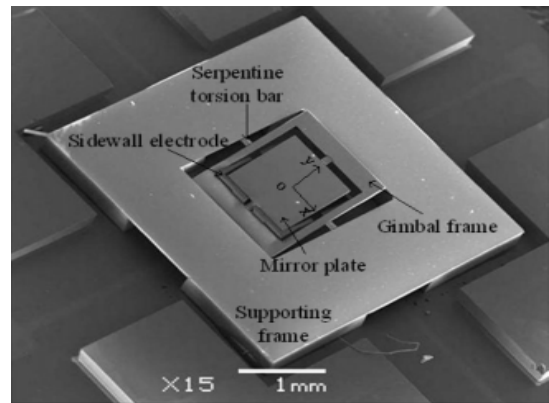
MEMS have the ability to serve either as sensors, to detect physical quantities such as humidity or temperature, and as actuators, to actuate mechanical structures or to manipulate physical quantities such as micro-particles [\[5,6\]](#). Furthermore, they are crucial to the revolution of consumer and industrial technologies due to their advantageous reductions of small size and low cost of production.

MEMS are also able to provide significant improvements in terms of overall performance and sensitivity compared to large devices. Due to the diversity of their application

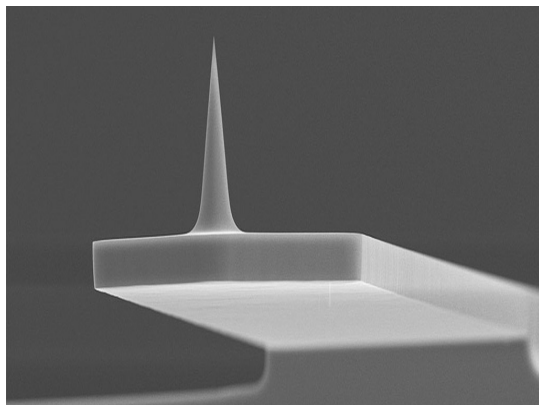
fields, they are prominent in a variety of industries such as MEMS imaging devices, RF communications [7,8], display systems [9] and cells manipulation [10] as shown in Fig. 1.1.



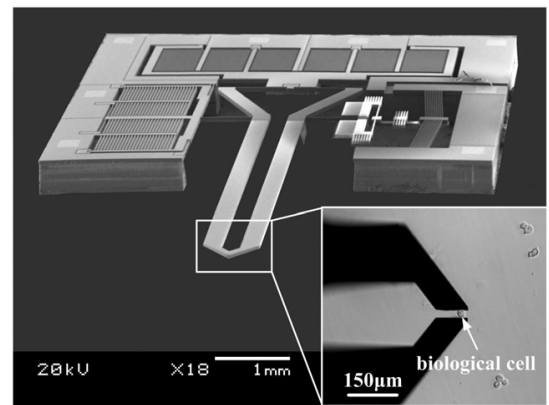
(a) RF MEMS Switch [11]



(b) MEMS Micromirrors [12]



(c) MEMS AFM [13]



(d) MEMS Gripper [14]

Figure 1.1: Examples of MEMS devices.

In fact, there are different methods to excite MEMS devices. These include electrothermal, electromagnetic, piezoelectric and electrostatic [15]. Among these methods, electrostatic actuation has been developed and utilized in a wide variety of applications due to

its many inherent advantages [16].

For example, it offers a good coupling between different energy domains in the micro-scale, requires small current compare to other actuation methods, reduces the overall power consumption, produces a controllable distance and requires a simple fabrication process. The output force of electrostatic actuation is relatively small compare to other actuation methods, but it results in a simple design that involves only two electrodes one of which cannot move, stationary electrode, and another able to move corresponding to the actuation voltage.

Two major configurations of electrostatically actuated micro-structures have been reported, parallel plate capacitor and interdigitated comb-fingers [17]. The electrostatic actuation comes in two forms, attractive force where the two electrodes are carrying opposite charge and repulsive force where the two electrodes are carrying the same charge. However, these actuation methods result in a highly nonlinear phenomena called ‘pull-in’ instability which limits the travel ranges of MEMS devices [18].

Many recent applications require electrostatic micro actuator that combines a large stroke and a low actuation voltage. The counter proportional relationship between the electrostatic force and the square of the capacitive gap and, therefore, the stroke precludes the option of increasing the gap size. Many studies have concentrated on design, modeling and characterization of electrostatic MEMS actuators to improve their performance by increasing the displacement limit at pull-in and decreasing the actuation voltage, respectively.

Literature has examined different methods to obtain large static displacements from electrostatic actuators as well as methods to generate large orbit oscillations. For example, dimples have been combined with other techniques to extend the travel range of electrostatic actuators [19,20]. Several techniques have been also proposed to increase the travel

range, including mechanical magnification [21], repulsive electrostatic actuation [22] and closed-loop control [23–25].

However, these methods require either complicated fabrication processes or complicated actuation and sensing circuits. A passive and simple to implement method to extend the travel range would add value to electrostatic actuation. Examples of additional large stroke actuators include the Digital Light Processor (DLP), MEMS switches, and probes of atomic force microscopes. On the other hand, scanning micromirrors represent oscillatory actuators.

1.2 Research Motivation

A present need exists for the development of Micro-Device-Assembly (MDA) systems. The complexity of micro-particle geometries, their internal micro-structures and varying material properties have led many researchers to developed MEMS devices to precisely locate and manipulate objects such as DNA strands and white and red blood cells. These devices provide a bridge between the macro systems and a tiny world that is only visible under microscopes and with advanced tools.

Automatically handling and manipulating those particles requires consideration of device compatibility, controllability, size, integration with electronics, high resolution, low power consumption and design configuration. In fact, micro-tweezers are the typical end effectors deployed to handle these particles.

The actuation mechanism for micro-tweezers falls into the following categories: electromagnetic, piezoelectric, electrothermal, shape memory alloys (SMAs), optical and electrostatic. Electromagnetic micro-tweezers are larger in size and output force but harder to fabricate [26]. Piezoelectric tweezers have a smaller stroke which restricts their use [27].

By exploiting the macroscopic of phase deformation caused a crystal structure transformation, SMA actuators have been used to actuate micro-tweezers [28]. Electrothermal tweezers are often preferred due to their simplicity of their fabrication. However, they are limited to applications where heat dissipation from the actuator does not damage sensitive targets such as biological cells [29].

Alternatively, electrostatic actuation has been introduced for MEMS tweezers due to many inherent advantages compared to the other actuation techniques. They have been designed with a wide variety of grip mechanisms but only two actuation schemes have been reported: parallel-plate and interdigitated comb-fingers.

The interdigitated comb-fingers come in two configurations: linear and rotary. These types of micro-tweezers are large in size and required complex fabrication processes. On the other hand, only two parallel-plate actuation schemes have been reported to date and we are introduced a third scheme in this dissertation called ‘electrostatic arch micro-tweezers’. It does not required a closed feed-back control and it is much smaller than the existing micro-tweezers in the field.

This design overcomes the drawbacks of existing micro-tweezers, which are a large footprint and a complex fabrication by using the snap-through motion in addition to a simple fabrication process. This will be used as a grip mechanism to grasp and manipulate micro-particles both statically and dynamically.

1.3 Research Objectives

Although the parallel-plate actuators have been implemented in order to build smaller micro-tweezers, there is still a need for further investigations to assess their applicability for such a job. The tweezers' size, grip range and actuation voltage are the most challenging

parameters during the designing phase. In this dissertation, we provide a comprehensive details about the feasibility of using a bistable micro-structure as a platform for the micro-tweezers arms in addition to investigate the static and dynamic modes of the tweezers. In summary, the research objectives are outlined as follow:

- Explain the snap-through behavior in bistable structures.
- Identify the system's parameters that guarantee the existence of snap-through.
- Develop analytical and numerical models for the electrostatic arch micro-tweezers.
- Use the developed models to assess the performance of the platform.
- Investigate the feasibility of building a micro-tweezers on a bistable structure.
- Design and fabricate the micro-tweezers.
- Compare the tweezers' performance to the existing devices in terms of size, grip range and actuation voltage.
- Propose a second generation that has the ability to measure the grip force acting on the objects.

1.4 Organization of the Dissertation

This dissertation is divided into seven chapters. **Chapter 1** gives a brief introduction about MEMS, motivation and objectives of the dissertation. The major contributions of this dissertation are included in Chapters 2 to 7 as explained below:

- **Chapter 2** reviews the literature on the micro-tweezers fundamentals, their principle of operations, design criteria and actuation methods.
- **Chapter 3** presents the implementation of the proposed tweezers' configurations, dimensions, grip and force sensing mechanisms. It also covers the fabrication process and the material properties of the tweezers.
- **Chapter 4** introduces an analytical model of the tweezers based on Euler-Bernoulli beam theory and develops a Reduced-Order model (ROM) for it. The model accounts for the arms inertia, the electrostatic fringing field and the nonlinear squeeze-film damping. Furthermore, a finite element model is built to provide more details about the tweezers' operational range and design space.
- **Chapter 5** presents analytical and experimental investigations for the static and dynamic motions of electrostatically actuated initially curved micro-beams.
- **Chapter 6** addresses the performance of the proposed tweezers and provides a general operational map for it. It also investigates the adequacy of standard Reduced-Order model (ROM) based on straight beam mode shapes as basis functions in representing the tweezers response.
- **Chapter 7** summarizes the contributions and limitations of this work and suggests avenues for future research.

Chapter 2

Literature Review

This chapter reviews of the fundamental concepts required to better understand the work proposed in this dissertation in two parts. The first part focuses on the relevant works and the fundamental features of the initially curved micro-beams and their applications in MEMS. Their modeling techniques, fabrication processes and the limitations of these structures are also summarized. The second part reviews the recent developments in the MEMS micro-tweezers with a detailed comparison in terms of the gripping range, the actuation voltage, the fabrication complexity and the capability to manipulate micro-particles.

2.1 Initially Curved Micro-beams

Electrostatic actuation is most commonly used in MEMS due to inherent advantages of low power consumption and simple fabrication processes. However, the stable travel range of parallel-plate electrostatic actuators is limited by the pull-in instability to one-third of

the capacitive gap [18, 30]. Initially curved fixed-fixed beams ‘arches’ have been proposed as an alternative configuration to increase their travel range [31, 32]. These beams can be configured to exhibit bistability [33–38], co-existence of two stable equilibria, and to move between them depending on the actuation voltage waveform as illustrated in Fig. 2.1.

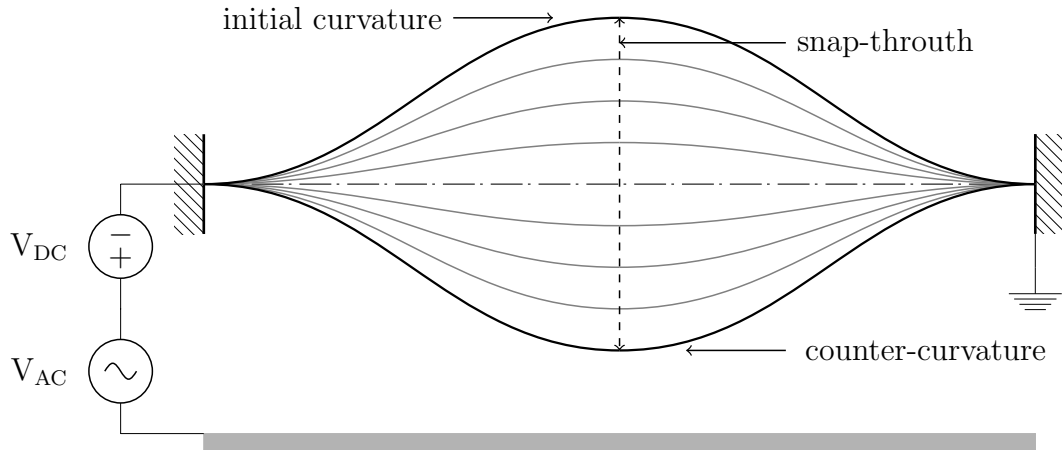


Figure 2.1: A schematic showing the change in the beam curvature profile as a function of the actuation voltage.

Curved beam can be obtained by buckling a straight beam under axial load (pre-stress) or via initial (stress-free) fabrication [39]. The existence of bistability in curved beams is a function of their dimensions and initial rise [40]. Analytical conditions for the existence of bistability in curved beams under electrostatic excitation and axial loads were derived by [41] and [42]. These structures have been used in a variety of applications including macro [43–45] and micro scales, such as switches, sensors, filters, memories and platforms from micro-tweezers [41, 46–50].

The performance of these micro-structures is affected by several design parameters including their initial rise, beam thickness, applied axial load, internal residual stress and excitation force. The designed dimensions and fabrication technique of the initially curved

micro-beams have to be addressed carefully to ensure the existence of the snap-through motion. Alkharabsheh and Younis [51] showed analytically that the stable travel range of an electrostatically actuated MEMS curved beam can be extended by control the axial loads. In the following, we are summarized the static and dynamic behaviors of the initially curved micro-beams under different actuation mechanisms.

2.1.1 Static Behavior

Due to the desirable properties of the initially curved beams, their static behavior were investigated under different excitation mechanisms. Nayfeh and Emam [52] derived analytically an exact solution for the static deflection of bistable beams under axial loads. Qiu *et al.* [53] observed snap-through from one equilibrium to another in manual propping of initially curved beams. The effect of electrostatic forces on the static response and transition between the stable equilibria of initially curved beam has also been investigated analytically and experimentally [41] and [54].

Additionally, Han *et al.* [55] used the Lorentz force to excite a micro-optical switch made of two curved beams to achieve a large stroke. Reducing the switching power consumption in a MEMS switch has been achieved using a pre-shaped buckled beam [56]. Michael and Kwok [57] studied analytically and experimentally the effect of residual stress in the snap-through of a buckled micro-bridge subjected to a thermal load.

Younis and Ouakad [58] used the Galerkin procedure based on the symmetric mode-shapes of both straight and curved beams as basis functions to investigate the static response of initially curved beams under electrostatic excitation. The results showed a close agreement between both approaches. The snap-through motion of a curved beam has been achieved using an electrostatic fringing field [54]. Medina *et al.* [59] studied the bifurca-

tion maps of both symmetric and anti-symmetric buckling of an electrostatically actuated curved micro-beam in the presence or absence of the residual stress.

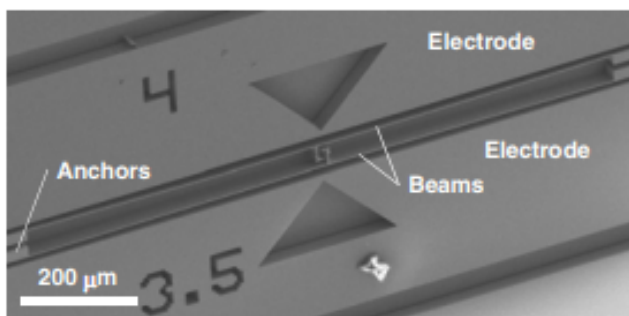
2.1.2 Dynamic Behavior

Many researchers have explored the rich dynamics of the initially curved beams. Ouakad and Younis [60] investigated the dynamic snap-through of electrostatically actuated curved micro-beams near primary resonance. Ruzziconi *et al.* [61] and Ramini *et al.* [62] investigated and demonstrated the co-existence of in-well orbits, around one of the stable equilibria, and cross-well ‘dynamic snap-through’ orbits, spanning both stable equilibria, in primary resonance of the first bending mode.

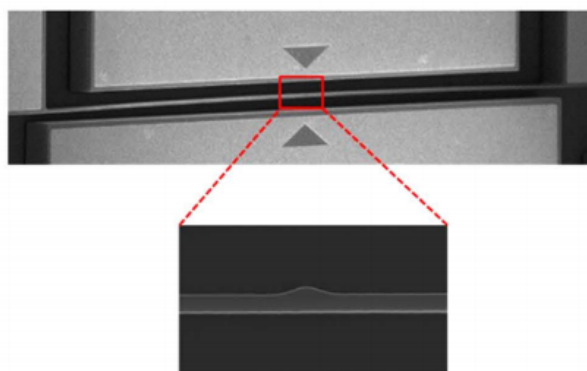
Ramini *et al.* [62] and Hajjaj *et al.* [63,64] found that the response of the first mode was softening while those of higher modes were hardening. Das and Batra [65] studied analytically the dynamic response of un-damped initially curved beam subjected to electrostatic force. They have showed that the beam's response becomes softening before having a snap through motion.

There have been various attempts to utilize bistability and snap-through motions in MEMS applications. Medina *et al.* [66] demonstrated switches that used snap-through to the ON state under electrostatic force and latch onto it under zero voltage. Ouakad and Younis [47], Hajjaj *et al.* [67,68] have used dynamic snap-through to create wide-band MEMS resonators.

Krakovar *et al.* [69] used the dynamic snap-through motion to enhance the sensitivity of a MEMS displacement sensor. Alneamy *et al.* [49,70] used the static snap-through motion as a grip mechanism to build a small and compact electrostatic MEMS tweezers for cells manipulation and characterization.



(a) MEMS Switch [41]



(b) Tunable MEMS Resonator [62]

Figure 2.2: Examples of MEMS initial curved micro-beams based devices.

Despite the extensive increase in MEMS applications such as accelerometer [71], sensors [72], communication and signal processing devices [73], many researchers have turned their attentions to implement a new device configuration or to introduce a new actuation mechanism. In fact, any improvement could lead to significant changes in the device characteristics such as nonlinearity sources. These include mid-plane stretching and nonlinear coupling between electrostatic force and resonator displacement [74] which are playing important role in the system stability.

The dynamic behaviors of MEMS resonators can be designed to ensure stability, how-

ever it could end up into unpredictable region ‘chaos’ caused by several factors including the actuation signal [75,76], design parameters [77] or/and the operational conditions [78]. The chaotic behavior can be obtained either in air ‘in-flight’ mode or in a contact mode [79]. Chaos was observed in the response of DC actuated impact resonators [80] and harmonically excited RF MEMS switches [81] and micro-beams [82]. Similarly, Zhao *et al.* [83] predicted the appearance of chaotic attractors in the response of impact-driven micro actuator [84].

In all of these cases, impact occurred across the surface of the actuator, except for the micro-beam case where impact was limited to the beam tip ‘line contact’. For actuators equipped with dimples impact will occur only over a small proportion of the actuator's surface [20]. Therefore, it is not obvious whether chaos will occur in this case and how prevalent it would be.

Thus, many analytical models have been introduced to locate the chaotic region and, therefore, limit the failure of the system. Among these models, the Melnikov's method is a popular technique in the literature for determination of the system parameters leading to chaos. DeMartini *et al.* [85] derived an expression describing the chaotic region of a MEMS oscillator using Mathieu equation and the Melnikov method was also used to derive the equation of motion.

Similarly, Haghighi and Markazi [86] build a model for chaos prediction and then applied the adaptive fuzzy control algorithm to control the chaotic motion. An algorithm for chaos prediction in MEMS resonators with symmetric double-well potential function has been introduced in [87]. Nayfeh *et al.* [88] numerically evaluated the Melnikov's function in a resonant gas sensor in order predict a critical value for the amplitude of the harmonic electrostatic load. The nonlinear dynamics and chaotic motion of MEMS resonators under random excitation was studied analytically and numerically by Zhang *et al.* [89].

An analytical proof on the existence of chaos in a generalized Duffing-type oscillator has been also presented in [90]. In their study, they expressed a closed formula for the two homoclinic orbits. The previously published works have used the Melnikov method to predict the chaotic motion. This approach is applicable for small excitation amplitudes. Chaos in an electrostatically MEMS initially curved micro-beams has also been reported analytically in [91,92].

Furthermore, chaotic vibrations can be desirable in specific applications such as very sensitive sensors because any change in the control parameter leads to a significant change in the response. For example, Yin and Epureanua [93] measured experimentally a small variation in the mass by detecting the change in the chaotic attractor. Seleim *et al.* [94] studied the dynamic response and the chaotic behavior of a closed-loop MEMS resonator for construction of highly sensitive sensors.

2.2 Micro-tweezers

In the last decade, the developments on actuation of micro-tweezers are accompanied by novel designs and grip techniques. They are operating by applying forces which are provided by their actuators. A variety of prototypes of micro-tweezers with different actuation methods have been developed and introduced as discussed in section 1.2.

Because of their abilities to survive in harsh environment, miniature size and material compatibility, there is an increasing trend of development on MEMS micro-tweezers. These include the domain of microassembly and micromanipulation such as biomedical applications. In the following content, we limit our survey to those excited electrothermally and electrostatically.

2.2.1 Electrothermal Micro-tweezers

Electrothermal actuated micro-tweezers are based on the thermal expansion of the thin metal layer arises due to the Joule effect in the presence of electric current passes through a loop. However, they can not be used to manipulate micro-objects in a fluid. As a result, SU-8 polymer has been used as a structural layer to extend the operation range of electrothermal micro-tweezers in the fluid medium. In fact, they produce a large deformation, strong recovery force and require low driving voltage [95–98]. With these advantages, many electrothermal micro-tweezers have been developed. An example of SU-8 based electrothermal micro-tweezers is shown in Fig. 2.3.

Chronis and Lee [99] designed an electrothermal micro-tweezers using SU-8 as a structural layer and two U-shaped identical actuators made of Au/Cr patterned underneath it. The mismatching in the thermal coefficients between metal layers and SU-8 was used to actuate the tweezers' grip arms and then to manipulate single cells in the fluid. They measured a stroke of 12.5 μm at 2 V.

Another electrothermal micro-tweezers for open and close actions was designed and fabricated to achieved a total stroke of 13 μm at an actuation voltage of 5 V [100]. A novel tweezers design consisting of two hot arms has been fabricated to minimize the heat flow to the tweezers arms as well as to produce a grip stroke of 11 μm at 9 V [101]. Mackay *et al.* [102] fabricated and characterized micro-tweezers based on SU-8 for handling biological samples. Their design was equipped with a tensile force sensor to measure the applied force. Their design showed experimentally a stroke of 80 μm at an actuation voltage of 1.18 V.

Wang *et al.* [103] designed a U-shaped electrothermal micro-tweezers that consist of a combination of thin arms, thick arms, flexures, jaws and anchors to manipulate micro-

particles. The results showed that for an input voltage of 14 V, the jaws deflected 9.1 μm out of a maximum designed stroke of 20 μm . Shivhare *et al.* [104] utilized two in-plane chevron shaped electrothermal actuators with a heat sink to maximize the grip stroke, minimize the voltage requirement and the temperature at the grip arms. They achieved a stroke of 19.2 μm at 1 V.

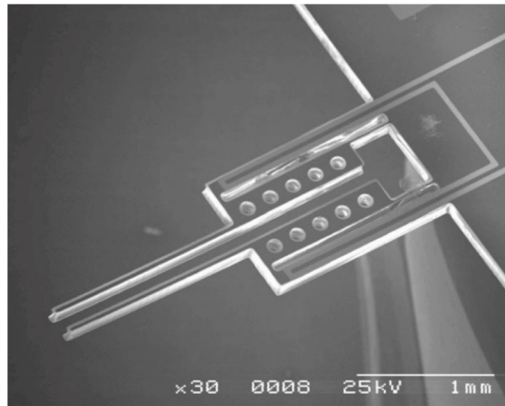


Figure 2.3: SEM picture of SU-8 electrothermal micro-tweezers [97].

Voicu *et al.* [105] introduced a V-shaped electrothermal micro-tweezers, which was fabricated using SU-8, to manipulate particles. The measurements showed an electrical current up to 25 mA required for a tip stroke of 40–42 μm . Considering the target object parameters, micro-tweezers based on a single cell manipulation was designed and fabricated using SU-8 polymer as a structural layer [106]. The design showed a maximum stroke of 50.5 μm at an actuation voltage of 650 mV. As a result, SU-8 was chosen as the structural layer because of its large thermal expansion coefficient than metal layers as well as its capability inside the fluid mediums. Table 2.1 summarizes the recent developments on the electrothermal MEMS tweezers.

In conclusion, electrothermal micro-tweezers are often preferred due to the simplicity

of their fabrication. They also require a small voltage and produce a large grip force. However, they are limited to applications where heat dissipation from the actuator does not damage sensitive targets such as biological cells.

Table 2.1: Recent works on electrothermal micro-tweezers

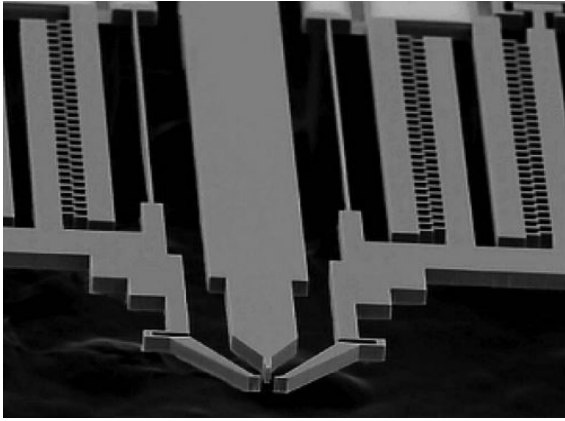
Author	Stroke (μm)	Voltage (V)
Chronis <i>et al.</i> [99]	12.5	2
Volland <i>et al.</i> [100]	50.5	5
Dow <i>et al.</i> [101]	11	9
Mackay <i>et al.</i> [102]	80	1.18
Wang <i>et al.</i> [103]	9.1	14
Shivhare <i>et al.</i> [104]	19.2	1
Somà <i>et al.</i> [106]	50.5	0.65

2.2.2 Electrostatic Micro-tweezers

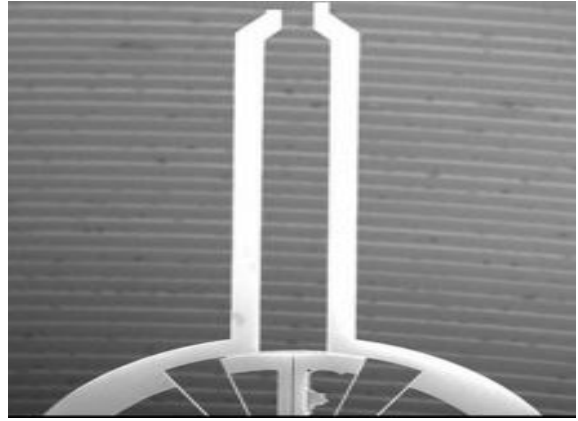
Because of the limitations in the electrothermally actuated micro-tweezers, many researchers have turned their attention to electrostatic actuation due to many inherent advantages compared to the electrothermal actuation [107]. Electrostatic micro-tweezers have been designed with a wide variety of grip mechanisms using only two actuation schemes: parallel-plate and interdigitated comb-fingers. The following content summarizes the recent and related works in the electrostatic MEMS micro-tweezers.

We know that the travel range of electrostatically actuated parallel-plate micro-tweezers is limited by the nonlinear pull-in instability to approximately one-third the capacitive

gap [108]. The tweezers designed by Varona *et al.* [109] and Chang *et al.* [110] presented the only parallel-plate actuation schemes reported to date. Their designs reduce the micro-tweezers size, however, they require more than 45 V to close a gap of 2 μm and 93 V to close a gap of 1.2 μm , respectively.



(a) Linear [111]



(b) Rotary [112]

Figure 2.4: Linear and rotary interdigitated comb-fingers electrostatic micro-tweezers.

Micro-tweezers based on interdigitated comb-finger drives have been more popular with efforts devoted to increase the grip range and reducing the actuation voltage. Many researchers [113–118] utilized flexible beams to convert the linear motion of comb-finger actuators to rotational gripper arms motion. On the other hand, Chen *et al.* [111] used linear comb-fingers, Fig. 2.4(a), to close the grip arms achieving a stroke of 7.5 μm at voltage of 50 V.

Micro-tweezers have also demonstrated the ability to hold objects under a static load, DC voltage, and to release dynamically under AC signal [119]. Other researchers [112, 120] have recently employed rotary comb-fingers, Fig. 2.4(b), to directly actuate the tweezers arms and, therefore, drastically increasing arms without increasing the actuation voltage.

Different interdigitated comb-fingers electrostatic micro-tweezers also reported in [121–123].

Table 2.2 summarizes the recent developments on the electrostatic MEMS tweezers.

Table 2.2: Relevant and related works on electrostatic micro-tweezers

Author	Stroke (μm)	Voltage (V)
Linear comb-fingers		
Volland <i>et al.</i> [113]	20	80
Beyeler <i>et al.</i> [114]	100	150
Chen <i>et al.</i> [115]	25	80
Bazaz <i>et al.</i> [116]	17	50
Hamedi <i>et al.</i> [117]	26	82
Xu [118]	63	72
Chen <i>et al.</i> [111]	7.5	50
Demaghsi <i>et al.</i> [119]	12	55
Rotary comb-fingers		
Chang <i>et al.</i> [112]	94	100
Piriyanont <i>et al.</i> [120]	85	80
Parallel-Plate		
Varona <i>et al.</i> [109]	2	45
Chang <i>et al.</i> [110]	1.2	93
This work	5–14	89–136

2.2.3 Modeling Techniques

Micro-tweezers have traditionally been operated in a quasi-static mode where a slowly-time varying signal drives the grip arms along a trajectory in order to pick or place an object. More recently, a dynamic operational mode was introduced. In this case, they are deployed as test platforms to measure the stiffness of micro objects [124] with the arms oscillating with at a given frequency. This mode poses a challenge to the micro-tweezers design requiring careful analysis of their modal response to guarantee that the arms will maintain their rigidity under dynamic loads.

Design and analysis of micro-tweezers requires robust and high fidelity models where closed form solutions are preferable. However, they are not available for tweezers except for trivial overly simplified cases. To overcome this shortcoming, many studies have used finite-element models (FEMs) to analyze more realistic tweezers at the expense of computational complexity [118, 125].

Reduced-Order Modeling (ROM) has frequently been deployed as an alternative approach to design MEMS-based devices [16, 66, 126] at a reduced computational complexity compared to FEM. This semi-analytical technique discretizes the device equation of motion in terms of a finite number of degrees-of-freedom describing the time-varying amplitudes of basis functions. ROMs based on Galerkin expansion minimize the number of required DOFs by using mode shapes that satisfy the structural boundary conditions [127].

Nayfeh and co-workers [16, 108] developed ROMs for electrostatically actuated straight beam-based MEMS. They found excellent agreement between their predictions of deflection and natural frequency under static loads and those measured experimentally. ROMs that utilize straight beam mode shapes were also found to be adequate to represent the static and dynamic responses of electrostatic initially curved micro-beams [41, 60].

ROMs have also been used to study electrostatically actuated MEMS straight plates [128, 129] as well as initially curved plates [130–132]. To date, no ROM has been developed for MEMS featuring bodies attached within the device structural span. This, however, is important for the analysis of micro-tweezers where the device functionality is a function of the arms motions.

In addition, this is a fundamental problem in macro-scale structural dynamics. The presence of attachments has a significant impact on structure fundamental characteristics, such as its natural frequencies and mode shapes. For example, many studies have shown deviations between the natural frequencies and mode shapes of beams and plates with and without concentrated masses and springs [133–135]. They found that the nodal locations of a cantilever beam change as functions of the location and magnitude of the attached mass [134, 136].

Laura and co-workers [136, 137] also found that the rotary inertia of attached masses can reduce the natural frequencies particularly those of higher modes and where the masses are located close to nodes. Amabili *et al.* [138] observed experimentally that additional modes appear due the placement of a concentrated mass with a large rotary inertia on a rectangular plate.

Similar behaviors have been reported at micro-scale. For example, Alkharabsheh and Younis [139] found that the interior nodes of a straight beam move out towards the supports as their flexibility (nonideality) increases. Hajjaj *et al.* [64] and Alfosail *et al.* [140] found that axial loads lead to modal interactions between the mode shapes of initially curved beams resulting in a crossover phenomenon variety between symmetric and asymmetric modes and veering phenomenon variety between symmetric modes.

The addition of skewed electrostatic fields or other forms of asymmetry along the beam span were also found to result in mode hybridization and veering between symmetric and

asymmetric modes [141, 142]. These changes in the natural frequencies and mode shapes result in complicated dynamics which require careful investigation and a robust model.

2.3 Summary

In summary, most of the electrostatic micro-tweezers used comb-finger drives which guarantee them a larger stroke at the expense of a larger footprint. To date, the use of more compact parallel-plate actuators has been hampered by the small stroke imposed by the pull-in instability. Here, we propose to reduce the footprint of micro-tweezers while increasing their stroke by using parallel-plate curved beams ‘arches’ as a platform for the tweezers’ arms. These actuators can switch from one stable equilibrium to another resulting in a larger stroke. The transition between the two stable equilibria is commonly referred to as snap-through motion.

Chapter 3

Tweezers Design and Fabrication

Previous researchers have focused on using interdigitated comb-figures micro-tweezers which are large in size and complex to fabricate. Here, we present a new compact design that is much smaller and easier to fabricate compared to those presented in the literature, section 2.2. This chapter focuses on the tweezers design, gripping mechanism, force sensing, dimensions and fabrication process. Two arch micro-tweezers prototypes will be presented.

3.1 Prototype I

In prototype I, the arch micro-tweezers consists of two arms inclined towards each other and mounted to an initially curved ‘stress-free’ micro-beam and a sidewall electrode as shown in Fig. 3.1. It exploits the bistable equilibria, resulting from the combination of the snap-through instability and electrostatic actuation, to reduce the separation distance between the two arms allowing them to grasp a large range of micro-objects. The tweezers offer further control beyond the snap-through point, via electrostatic actuation, to increase

pressure on larger objects and to grasp smaller objects.

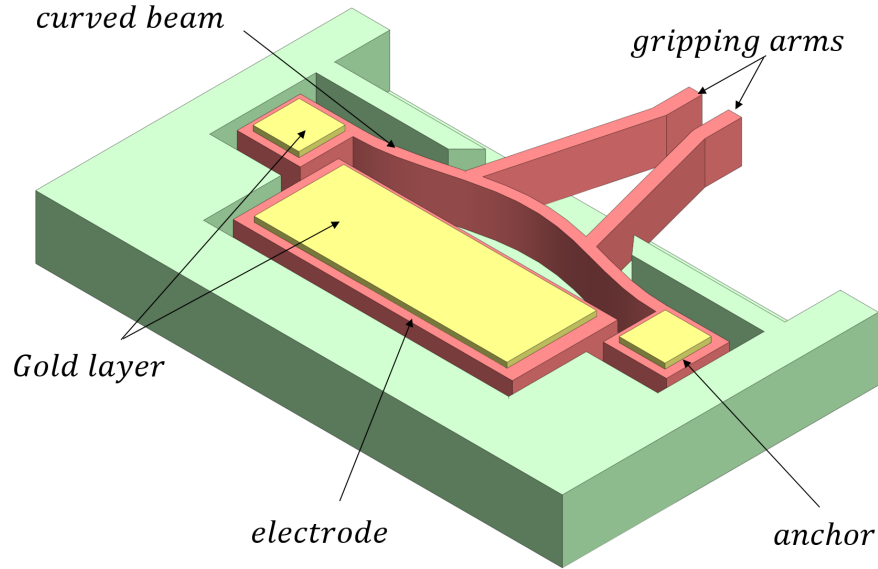


Figure 3.1: Isometric view of the prototypes I showing an electrostatically actuated initially curved micro-beam carrying two identical and inclined arms.

As the electrostatic field strength increases, the beam reduces its curvature, Fig. 2.1, resulting in a reduction of the separation gap between the arm tips. The regulated separation gap and grip force is used to grasp, hold, release or otherwise to manipulate micro-objects placed within the gap.

3.1.1 Gripping Mechanism

This micro-tweezers can manipulate two sets of micro-objects depending on the applied voltage. It can handle coarse (larger) micro-objects under voltages $V(t)$ below a threshold called snap-through voltage V_S corresponding to the initial beam curvature as shown in

Fig. 3.2(a). The actuation voltage $V(t)$ can be a static component, DC voltage, a time-varying component, AC voltage, or a combination of these two components. The tweezers can also grasp finer (smaller) objects when the applied voltage exceeds that threshold snapping the beam to the counter-curvature, Fig. 3.2(b), and reducing the separation distance between the arm tips.

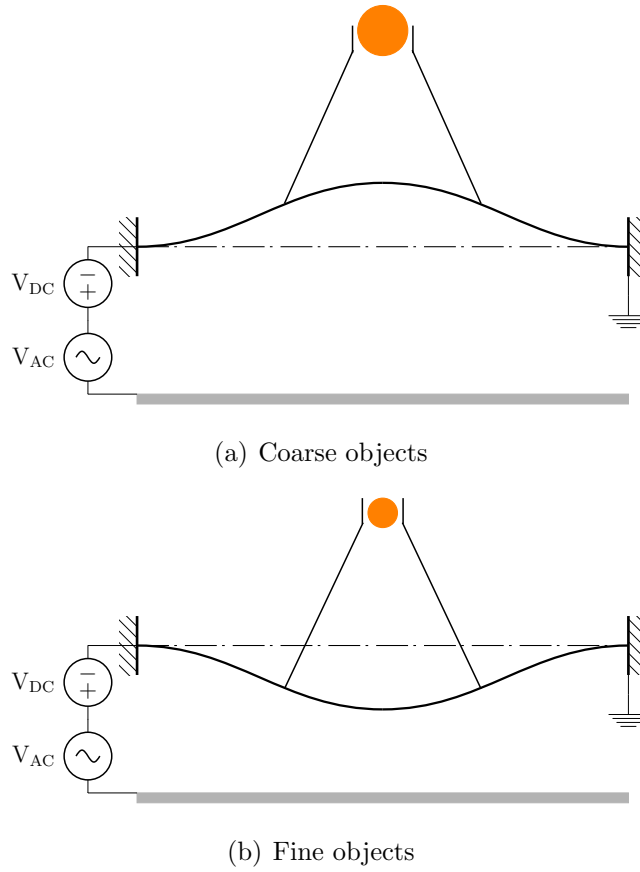


Figure 3.2: Tweezers configurations: (a) before and (b) after the snap-through voltage V_S .

We seek to operate the tweezers in two modes. The first is traditional quasi-static mode where DC voltage V_{DC} commands the tweezers along a trajectory to approach, hold and release micro-objects. It exploits nonlinear phenomena in electrostatic curved beams,

namely snap-through, snap-back and static pull-in and the bifurcations underlying them. The second mode uses a harmonic voltage signal V_{AC} to release, probe and/or interact with the objects held by the tweezers in order to perform function such as cells lysis and characterization. It exploits additional electrostatic MEMS phenomena including dynamic pull-in as well as the orbits and attractors realized under harmonic excitation.

3.1.2 Device Parameters

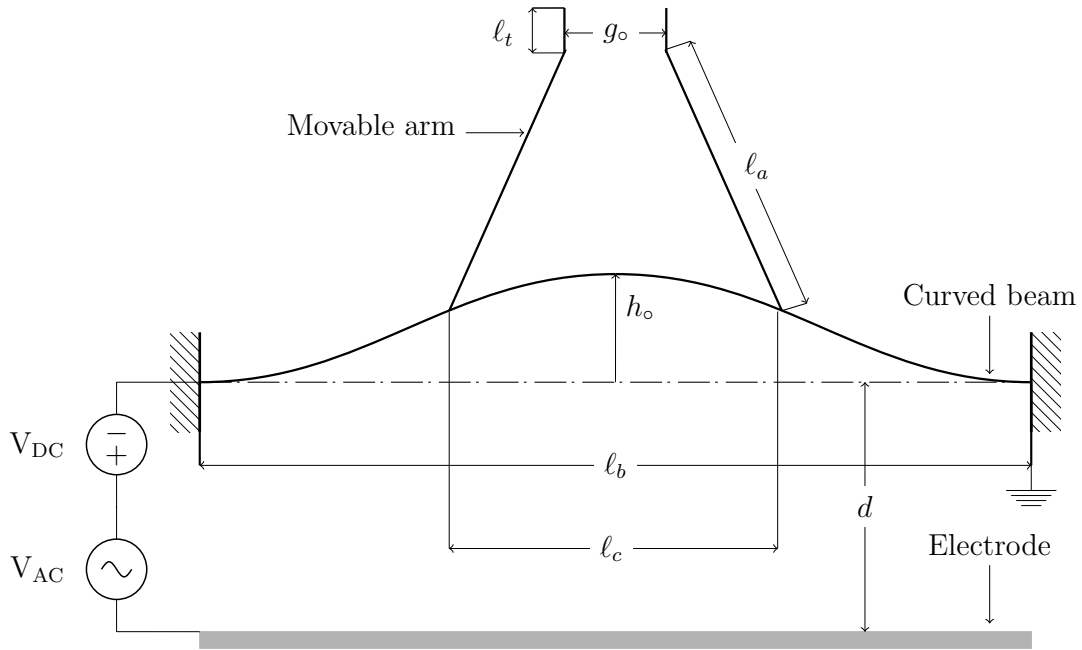


Figure 3.3: A schematic showing the tweezers' parameters of prototype I.

The arch micro-tweezers consists of two identical arms mounted to an initially curved beam and electrostatically actuated via a sidewall electrode as shown in Fig. 3.1. The distance between the end supports l_b is 1000 μm . The beam thickness h_b and initial mid-point rise h_o measured from the reference line are 3 μm and 3.5 μm , respectively. The initial

capacitor gap d measured from the sidewall electrode to the reference line is $11.5 \mu\text{m}$.

The arms length ℓ_a and thickness h_a are $250 \mu\text{m}$ and $4 \mu\text{m}$, respectively, while the tip length ℓ_t is $10 \mu\text{m}$. The distance between the arms attachment points along the reference line ℓ_c is $300 \mu\text{m}$. They are inclined and fabricated at an angle of 55.11° with respect to the cord length. This arrangement results in an initial distance between the arm tips g_o of $14 \mu\text{m}$. The device is made out of a crystal silicon structural layer with a width b of $30 \mu\text{m}$. These parameters are clearly shown in Fig. 3.3.

3.2 Prototype II

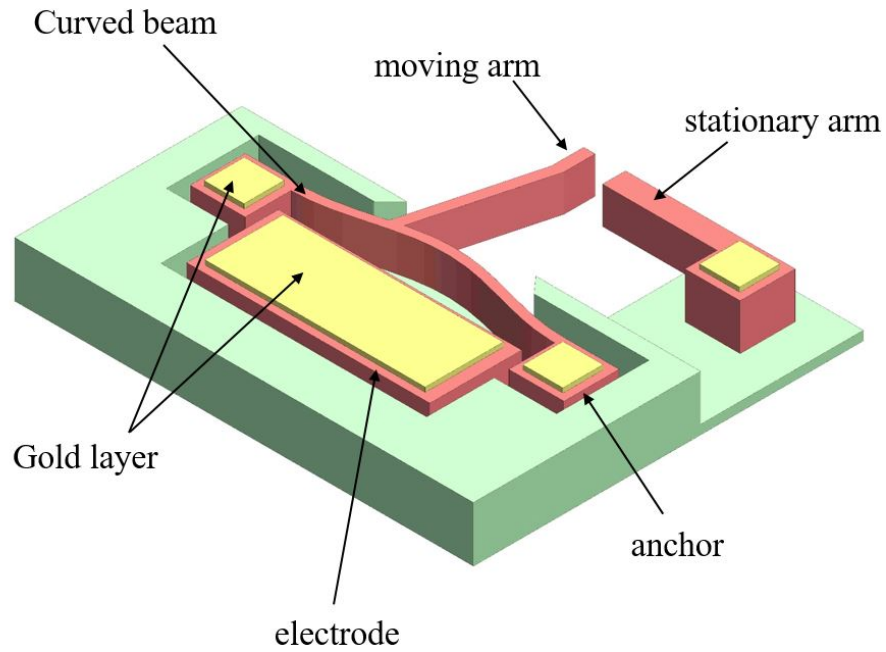


Figure 3.4: Isometric view of the prototype II showing an electrostatically actuated initially curved micro-beam carrying only one inclined movable arm and a stationary arm.

In prototype II, we change the tweezers' arms configuration in order to measure the gripping force acting on the micro-object in addition to the grasp, hold and manipulation processes. Specifically, we have mounted only one arm to the micro-beam and the second one is connected to a separate electrical pad as shown in Fig. 3.4. It exploits the same nonlinear behavior like that presented in prototype I. More details about the gripping and applied force sensing mechanisms are presented in the following sections.

3.2.1 Gripping Mechanism

As the electrostatic field strength increases between the beam and the sidewall electrode, the beam reduces its curvature, resulting in a reduction of the gap between the moving and stationary arm tips. The mechanism is also used to grasp, hold, release micro-objects with ability of measuring the gripping force acting on the particle.

This is done by grounding the curved beam while the actuation signal is applied to the sidewall electrode. This electrical connection results in a potential difference that is used to excite the beam and allows the movable arm to move toward or away from the stationary arm.

This configuration has the ability to measure the gripping force acting on the object by applying another actuation signal to the stationary arm in addition to that applied to the micro-beam. It results in a potential difference between the two arms and, therefore, it can be used to measure the change in capacitance through a force-displacement relationship, as the applied voltage changes. The additional actuation signal will also provide another force to hold and secure the object during the manipulation.

3.2.2 Device Parameters

The curved beam and the moving arm dimensions are similar to the prototype I. The separation gap between the moving and the stationary arms is reduced to $g_o = 7 \mu\text{m}$. The stationary arm has a length ℓ_{sa} of $590 \mu\text{m}$ and a thickness h_{sa} of $60 \mu\text{m}$. These parameters are clearly shown in Fig. 3.5.

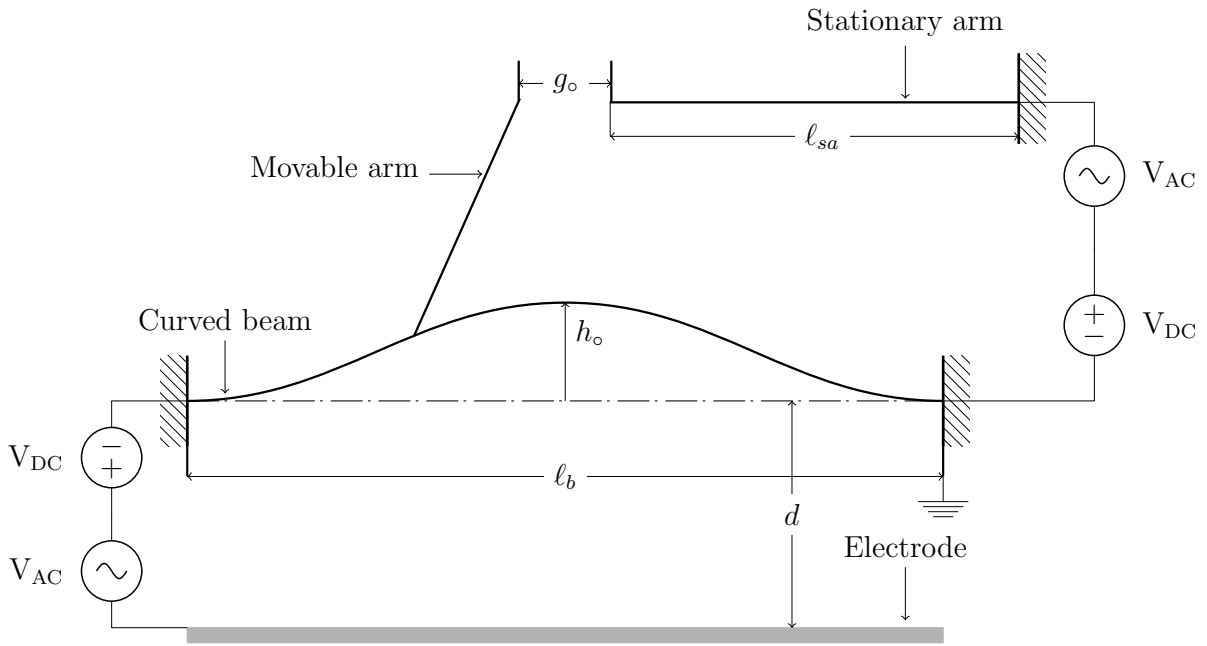


Figure 3.5: A schematic showing the tweezers' parameters of prototype II.

3.3 Fabrication Process

The two prototypes of electrostatically actuated micro-tweezers were fabricated out of a p-type $\langle 100 \rangle$ single crystal silicon on insulator (SOI) wafer. The device layer is $30 \pm 3 \mu\text{m}$ thick and it is Boron doped with a resistivity of $1 \Omega\cdot\text{cm}$. The buried oxide layer is

1 μm thick while the handle layer is 550 μm thick. The initial shape of the micro-beam curvature $w_o(x)$ was laid out to follow the expression

$$w_o(x) = \frac{h_o}{2} \left(1 - \cos\left(\frac{2\pi x}{\ell_b}\right) \right) \quad (3.1)$$

Table 3.1: Material properties of single crystal Silicon

Description	Value
Density (ρ)	2330 kg/m ³
Young's Modulus (E)	129 GPa
Yield strength (σ_y)	1.2 GPa
Poisson's ratio (ν)	0.22
Dielectric constant of the air (ε)	8.854×10^{-12} F/m

The fabrication process started with a SOI wafer with the material properties given in Table 3.1 and then it is cleaned using RCA to remove the contaminations on the device layer top surface. This step was performed before the high-temperature processing steps such as oxidation and diffusion. The fabrication process steps are described in details in the following content.

- **Step 1:** Metals Deposition

A seed layer of 30 nm Chrome (Cr) is deposited using an E-beam to ensure proper adhesion of the metallization layer, Fig. 3.6(a). Then, a 100 nm thick layer of Gold (Au) is sputtered on top of it as shown in Fig. 3.6(b).

- **Step 2:** Spin Coating Photoresist and Patterning

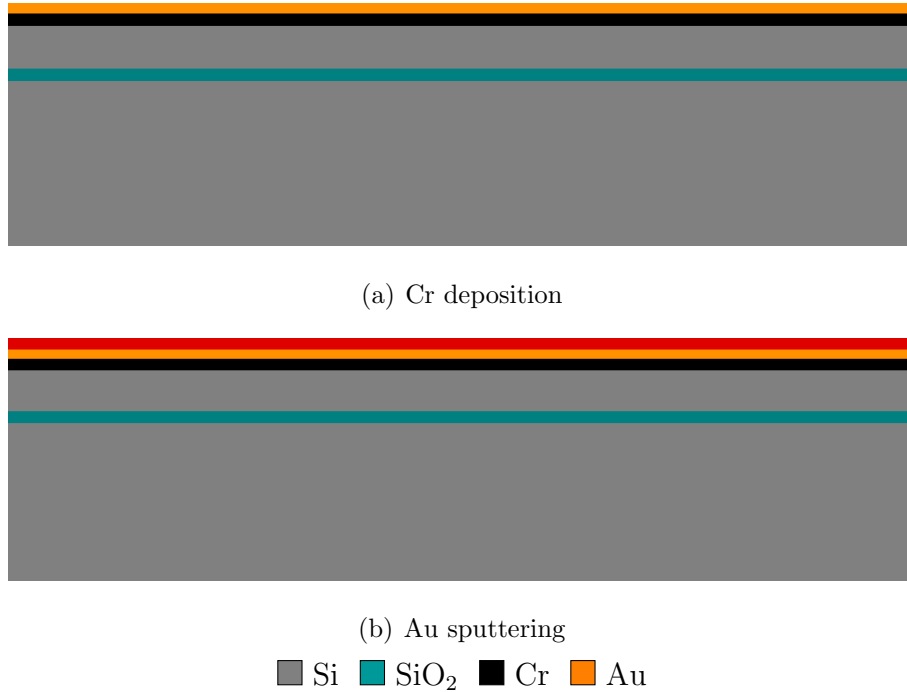


Figure 3.6: Metals deposition: (a) a 30 nm thick Cr deposited to serve as an adhesion layer for the metal and (b) A 100 nm thick Au layer sputtered on top of Cr layer.

A 1 μm layer of positive photoresist (Ph) is spun onto the wafer and then it is lithographically patterned by exposing it to UV light using Mask 1 as shown in Fig. 3.7(a). This results in a photoresist pattern on the contact pads only as shown in Fig. 3.7(b). The layout of Mask 1 is shown in Appendix A Fig. A.1.

- **Step 3:** Metallization Layers Etching

The contact pads are defined in the metal layers by wet etching the stacked metal layers using an ion milling machine. This is done by bombarding ions toward the metals. After that, the remaining photoresist is stripped off the pads using wet chemical stripping as shown in Fig. 3.8.

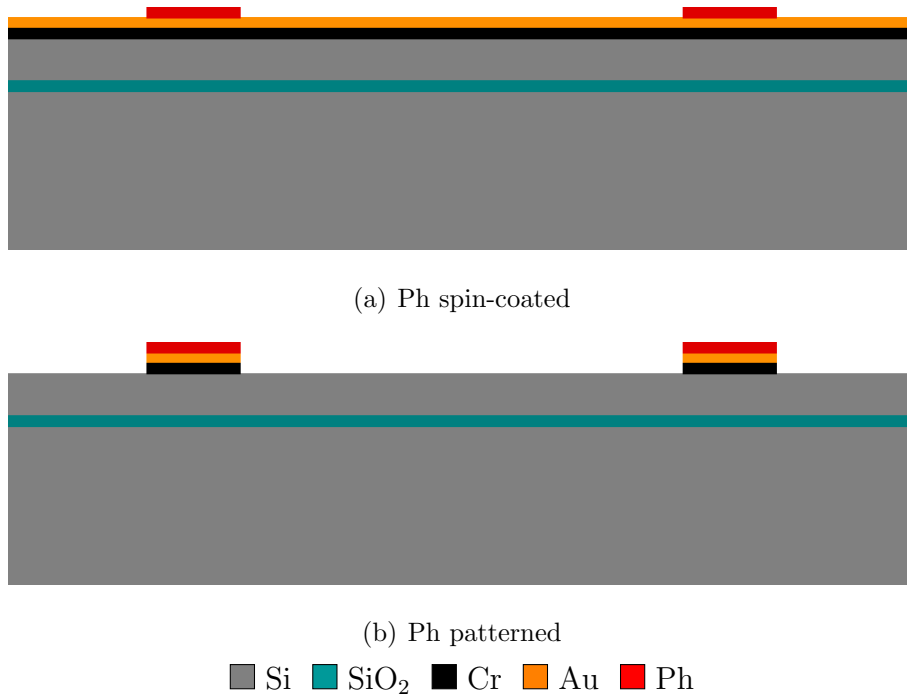


Figure 3.7: Photoresist layer: (a) spin-coated to cover the wafer and (b) expose to the UV-light and pattern using Mask 1.

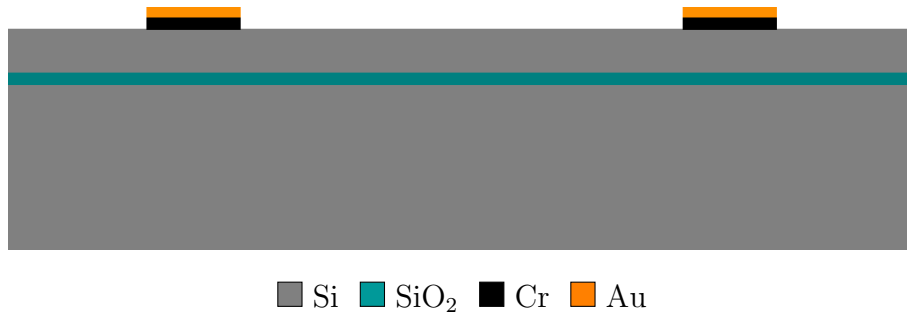


Figure 3.8: Etching the metallization layers and stripped off the remaining photoresist.

- **Step 4:** Silicon Etching

Another layer of positive photoresist is spun on to the wafer as shown in Fig. 3.9. It is

patterned using Mask 2 to define the device area, see Fig. 3.10. Then, a Deep Reactive Ion Etching (DRIE) is used to etch the silicon all the way through the exposed photoresist to the buried oxide, Fig. 3.11. Then, the unexposed photoresist is stripped away as shown in Fig. 3.12. The layout of Mask 2 is shown in Appendix A Fig. A.2.

Because the structural layer is large, this step is done with many short intervals of time to ensure a vertical edges along the structural layer and to protect the photoresist layer from burning.

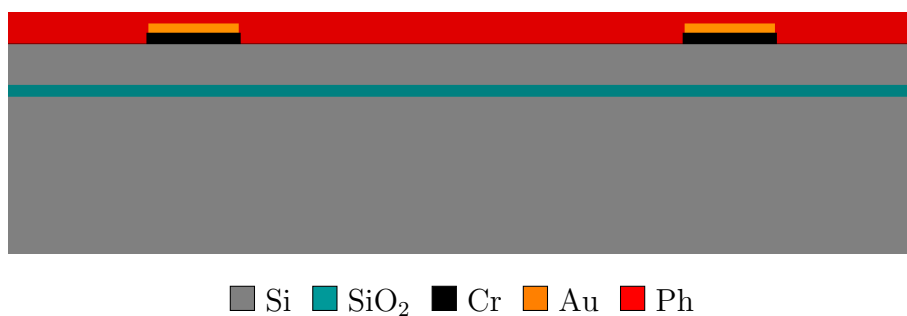


Figure 3.9: Ph layer spin-coated to cover the wafer.

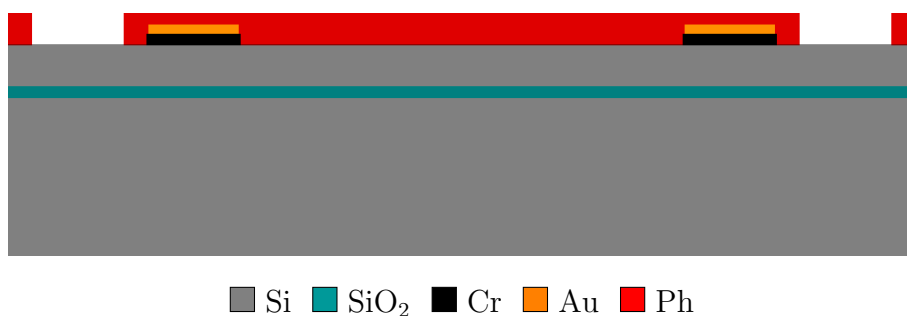


Figure 3.10: Ph layer exposed to the UV-light and pattern using Mask 2.

- **Step 5:** Device Release

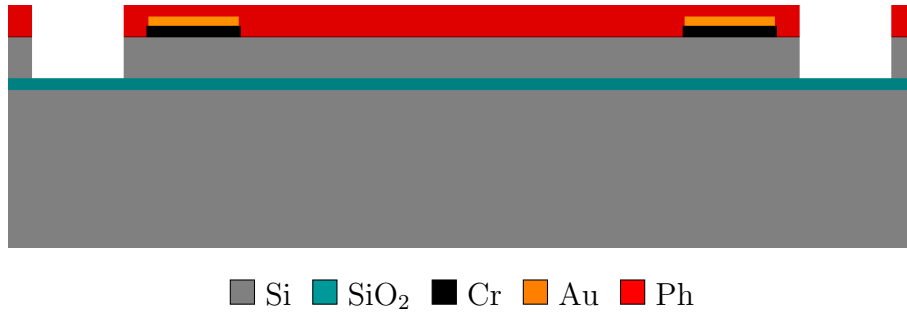


Figure 3.11: Device layer etching using DRIE.

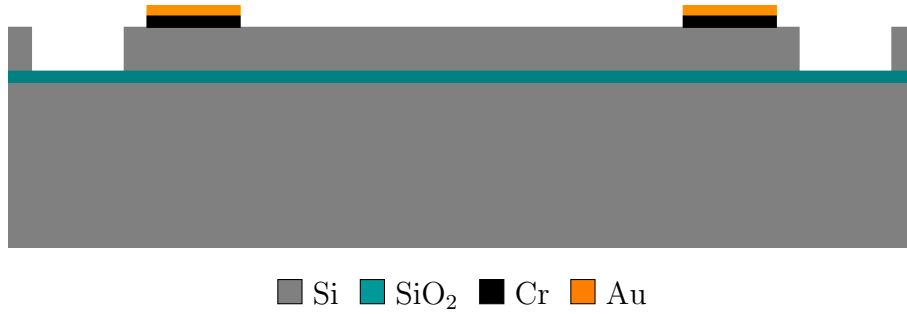


Figure 3.12: Unexposed Ph stripped away.

A back-side etching is also used to ensure that the thin structure layer is fully released by spinning a 1 μm layer of photoresist onto the backside surface of the wafer, Fig. 3.13. After that, Mask 3 is used to pattern photoresist and etch the handle silicon layer using DRIE all the way to the buried oxide layer, Fig. 3.14. The layout of Mask 3 is shown in Appendix A Fig. A.3.

The device movable layer is released by etching the buried oxide using wet chemical etcher (HF) with a specific concentration rate. It results in small etched areas underneath the contact pads and device supports which do not affect the structure fixation as shown in Fig. 3.15. Then, the wafer is diced into smaller chips using an interrogated dicing technique and wire bonding is performed on the desired areas of each chip as shown in Appendix A

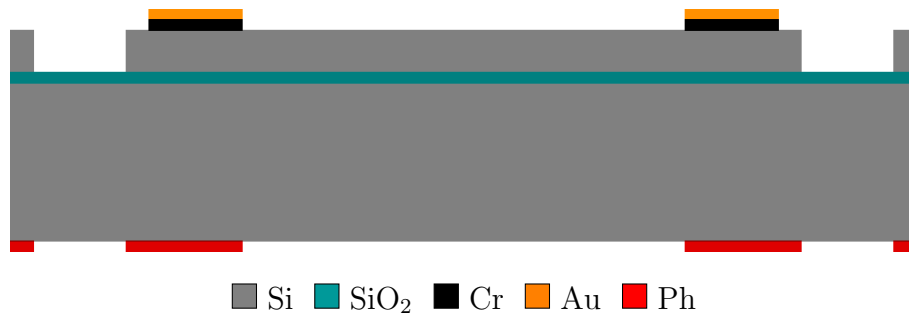


Figure 3.13: Backside Ph layer exposed to the UV-light and pattern using Mask 3.

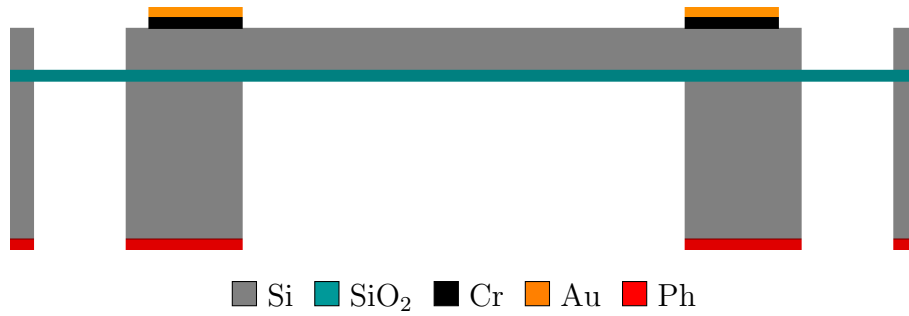


Figure 3.14: Handle layer etching using DRIE and unexposed photoresist stripped away.

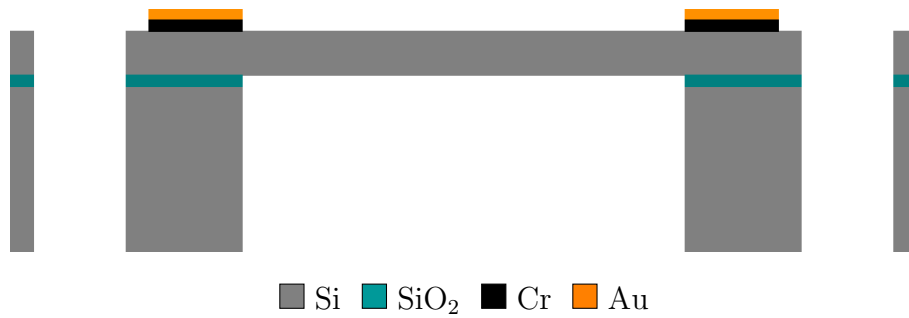
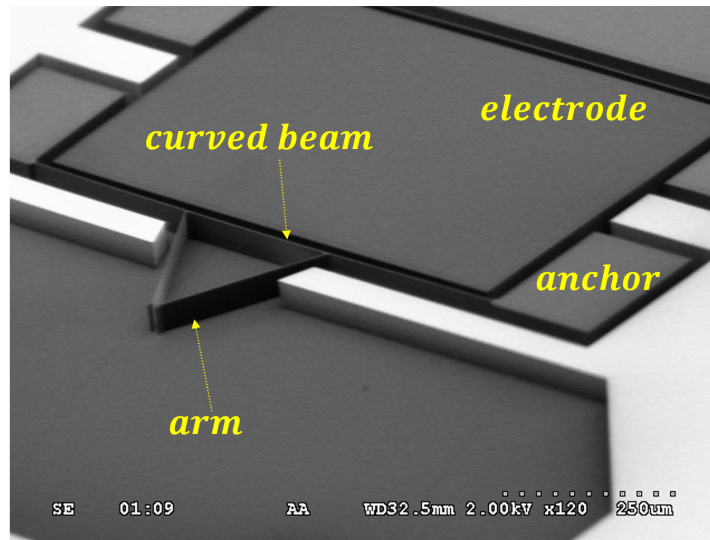
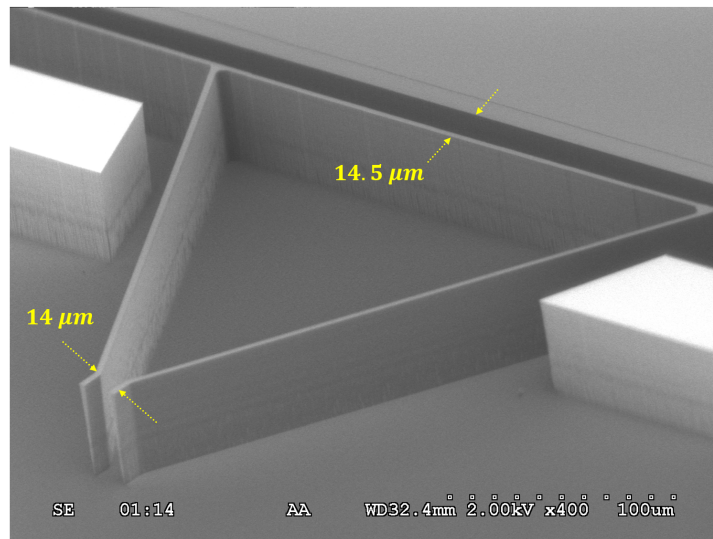


Figure 3.15: Releasing the device layer using wet chemical etcher (HF).

Fig. A.4. Scanning Electron Microscope [SEM](#) pictures of the fabricated prototype I before the backside etching are shown in Figs. [3.16\(a\)](#) and [\(b\)](#).



(a) Fabricated micro-tweezers



(b) Close-up on the grip arms

Figure 3.16: SEM pictures of: (a) the fabricated prototype I before the backside etching step and (b) a close-up on the grip arms.

3.4 Summary

In this chapter, we presented a novel and compact electrostatic micro-tweezers to manipulate particles. Two prototypes were introduced. The tweezers consist of two grip-arms mounted to an electrostatically actuated initially curved micro-beam in the first prototype and one arm only mounted to the curved micro-beam and the second arm was stationary in the second prototype. Both designs exploit bistable equilibria, resulting from a snap-through instability, to close the separation distance between the two arms allowing them to grasp a large range of objects. These include coarse and fine micro-objects depending on the applied voltage. The tweezers were fabricated using a p-type $< 100 >$ low resistivity Silicon on Insulator (SOI) wafer involving three masks.

Chapter 4

Tweezers Modeling

In this chapter, we present an analytical model for the electrostatic micro-tweezers. We derive the equation of motion of a curved micro-beam carrying two identical arms ‘representing prototype I’ using Euler-Bernoulli beam theory. The tweezers arms are modeled as rigid bodies and their elastic deformation are ignored. Then, a standard Reduced-Order Model (ROM) that uses a straight beam mode shapes being used as basis functions is developed to solve the equation of motion.

4.1 Equation of Motion

We derive the equations of motion and the associated boundary and initial conditions that govern the axial and transverse nonlinear responses of the electrostatic arch micro-tweezers that consists of a curved beam with a cross-sectional area A_b and an area moment of inertia I_b carrying two identical arms at points B_1 and B_2 located at distances ℓ_1 and ℓ_2 from the left end, Fig. 4.1. The arms are assumed rigid. Their mass and mass moments of inertia,

respectively m_a and J_a , are treated as concentrated point masses and rotary inertia.

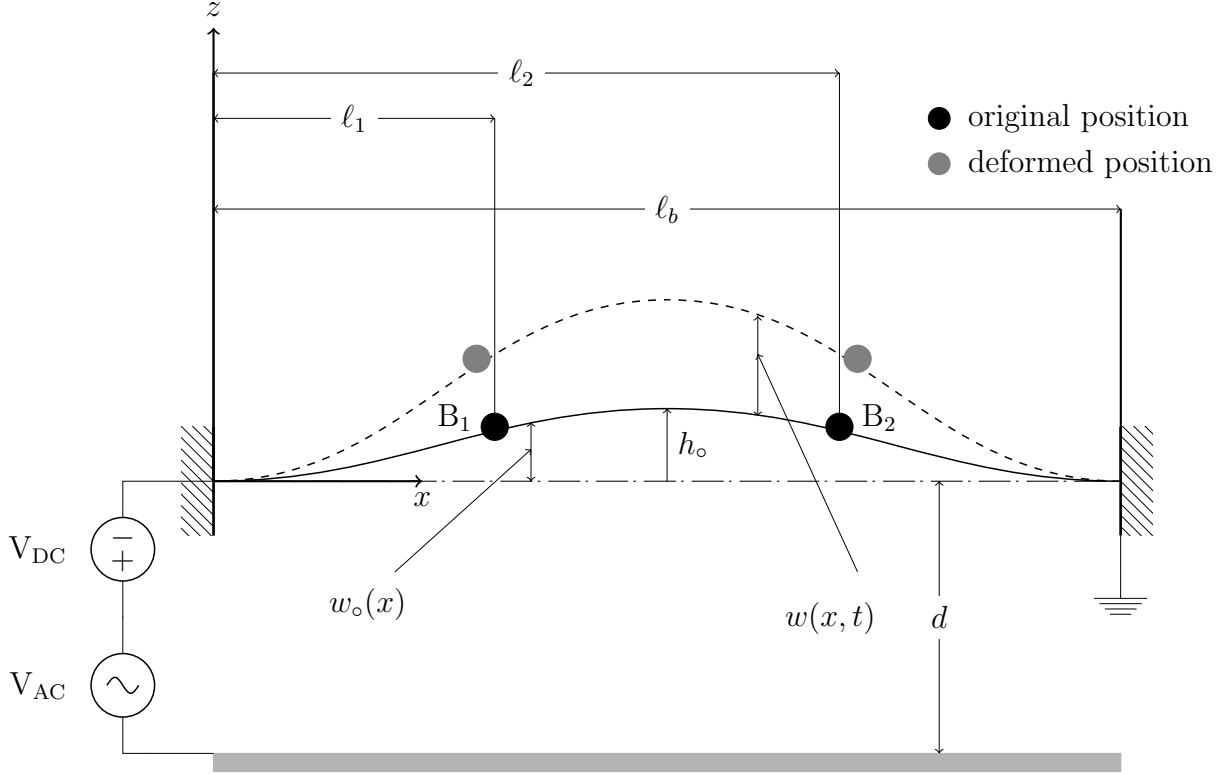


Figure 4.1: A schematic of the curved beam carrying two identical arms at points B_1 and B_2 .

Following [143,144] in the derivation of the equation of motion, we consider a differential beam element initially dx long. Its left edge \mathbf{P} is located at (x, w_o) as shown in Fig. 4.2. After the deformation, the left edge moves to \mathbf{P}^* at

$$x^* = x + u, \quad z^* = w + w_o \quad (4.1)$$

where u is the displacement along x -axis and w is the transverse displacement along z -axis measured from w_o .

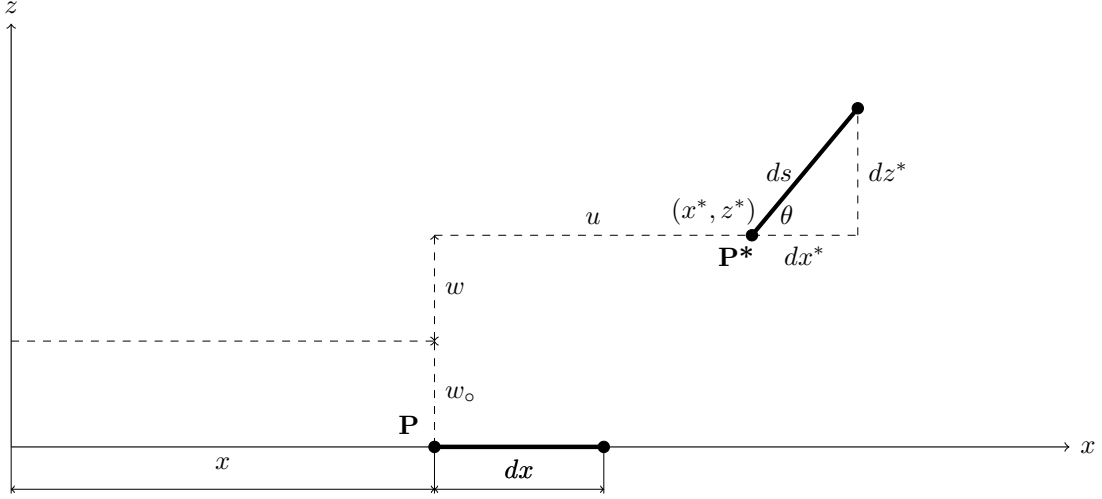


Figure 4.2: An element of the curved beam showing the location before, marked as \mathbf{P} , and after deformation, marked as \mathbf{P}^* .

Therefore, the deformed element length can be calculated as

$$ds = \sqrt{(dx^*)^2 + (dz^*)^2} \quad (4.2)$$

Then, differentiating x^* and z^* with respect to x yields

$$dx^* = (1 + u')dx, \quad dz^* = (w' + w'_0)dx \quad (4.3)$$

substituting Eq. (4.3) into Eq. (4.2) gives

$$ds = \sqrt{(1 + u')^2 + (w' + w'_0)^2} dx \quad (4.4)$$

Assuming a small initial rise $h_0 \ll \ell_b$, Eq. (4.4) can be simplified to

$$\lambda = \frac{ds}{dx} = \sqrt{1 + 2u' + u'^2 + w'^2 + 2w'_0w'} \quad (4.5)$$

Thus, the axial strain ε_{xx} of the beam element is given by

$$\varepsilon_{xx} = \frac{ds - dx}{dx} \quad (4.6)$$

Then, we scale the transverse displacement $w(x)$ and initial shape $w_0(x)$ to order $O(\epsilon^1)$, the axial displacement to order $O(\epsilon^2)$. The scaling orders of the other system parameters are listed in Table 4.1.

Table 4.1: Scaling orders of the tweezers' parameters

Parameter	Scaling Order $O(\epsilon^n)$
w	$O(\epsilon^1)$
u	$O(\epsilon^2)$
w' , w'' , w''' , w''''	$O(\epsilon^1)$
u' , u'' , u'''	$O(\epsilon^2)$
$\dot{w}' , \dot{w}'' , \ddot{w}' , \ddot{w}''$	$O(\epsilon^1)$
\dot{u}	$O(\epsilon^3)$
\ddot{u}	$O(\epsilon^4)$
ℓ_b , b_b , d	$O(\epsilon^0)$
h_b	$O(\epsilon^1)$
A_b	$O(\epsilon^1)$
I_b	$O(\epsilon^3)$

Expanding ε_{xx} in a Taylor series and retaining terms up to order $O(\epsilon^3)$, we can write

$$\varepsilon_{xx} = u' + w'_0 w' + \frac{1}{2} w'^2 \quad (4.7)$$

this formula describes the element elongation for the small strains and moderate rotations [144]. Recalling that for an Euler-Bernoulli beam model, the axial and transverse displacements can be written as

$$u = \bar{u} - \zeta \bar{w}', \quad w = \bar{w} \quad (4.8)$$

where the bar represents the displacement of the reference axis in both directions and ζ is a coordinate pointing into the curvature. Substituting this equation into Eq. (4.7), one can write the total strain of the initially curved beam up to order $O(\epsilon^3)$ as

$$\varepsilon_{xx} = \bar{u}' - \zeta \bar{w}'' + w'_o \bar{w}' + \frac{1}{2} \bar{w}'^2 \quad (4.9)$$

The beam element rotation angle θ can be expressed as

$$\sin \theta = \frac{dz^*}{ds} = \frac{w'_o + w'}{\lambda} \quad (4.10)$$

$$\cos \theta = \frac{dx^*}{ds} = \frac{1 + u'}{\lambda} \quad (4.11)$$

differentiating Eq. (4.10) and Eq. (4.11) with respect to the time (t) yields

$$\dot{\theta} \cos \theta = \frac{(1 + u')((1 + u')\dot{w}' - (w'_o + w')\dot{u}')}{(1 + 2u' + u'^2 + w'^2 + 2w'_o w')^{\frac{3}{2}}} \quad (4.12)$$

and using Eq. (4.11) in Eq. (4.12), we obtain

$$\dot{\theta} = \frac{(1 + u')\dot{w}' - (w'_o + w')\dot{u}'}{\lambda^2} \quad (4.13)$$

Expanding this form in a Taylor series, retaining terms up to order $O(\epsilon^4)$, recalling that u and w are evaluated here at the reference axis, where $\zeta = 0$, and using Eq. (4.8), one can rewrite $\dot{\theta}^2$ as

$$\dot{\theta}^2 = \dot{w}'^2 - 2\dot{w}'^2 \bar{u}' - 2\bar{w}'^2 \dot{w}'^2 - 4w'_o \bar{w}' \dot{w}'^2 \quad (4.14)$$

4.1.1 The Potential Energy

The potential energy U of the micro-tweezers can be expressed as¹

$$U = \frac{1}{2} \int_0^{\ell_b} \int_0^{A_b} (E \varepsilon_{xx}^2) dA_b dx \quad (4.15)$$

¹The arms are assumed rigid, thereby, its potential energy is zero.

where

$$\begin{aligned} \varepsilon_{xx}^2 = & \bar{u}'^2 + 2w'_o \bar{w}' \bar{u}' + w_o'^2 \bar{w}'^2 + \bar{w}'^2 \bar{u}' + w'_o \bar{w}'^3 + \frac{1}{4} \bar{w}'^4 \\ & - 2\zeta \bar{w}'' \bar{u}' - 2\zeta w'_o \bar{w}' \bar{w}'' - \zeta \bar{w}'^2 \bar{w}'' + \zeta^2 \bar{w}''^2 \end{aligned} \quad (4.16)$$

substituting this equation into Eq. (4.15) yields

$$U = \int_0^{\ell_b} \left(\underbrace{\frac{EA_b}{2} \left(\bar{u}' + w'_o \bar{w}' + \frac{\bar{w}'^2}{2} \right)^2}_{U_1} + \underbrace{\frac{EI_b}{2} \bar{w}''^2}_{U_2} \right) dx \quad (4.17)$$

4.1.2 The Kinetic energy

The kinetic energy T of the tweezers is the sum of the kinetic energies of the beam mass (T_{bm}) and rotary inertia (T_{br}) and the arm mass (T_{am}) and rotary inertia (T_{ar}). As a result, one can write the total kinetic energy as

$$T = T_{\text{bm}} + T_{\text{br}} + T_{\text{am}} + T_{\text{ar}} \quad (4.18)$$

where

$$\begin{aligned} T_{\text{bm}} + T_{\text{br}} &= \frac{1}{2} \int_0^V \rho ((\dot{\bar{u}} - \zeta \dot{\bar{w}}')^2 + \dot{\bar{w}}^2) dV \\ &= \frac{1}{2} \int_0^V \rho (\dot{\bar{u}}^2 - 2\zeta \dot{\bar{w}}' \dot{\bar{u}} + \zeta^2 \dot{\bar{w}}'^2 + \dot{\bar{w}}^2) dV \\ &= \frac{1}{2} \int_0^{\ell_b} (\rho A_b \dot{\bar{w}}^2 + \rho A_b \dot{\bar{u}}^2 + \rho I_b \dot{\bar{w}}'^2) dx \end{aligned} \quad (4.19)$$

The translational kinetic energy T_{am} of the tweezers' arm is

$$T_{\text{am}} = \frac{1}{2} \int_0^{\ell_b} m_a \delta_d \dot{\bar{w}}^2 dx \quad (4.20)$$

where δ_d is the sum of two Dirac-Delta functions expressed as

$$\delta_d = \delta_{d_1}(x - \ell_1) + \delta_{d_2}(x - \ell_2)$$

The rotary kinetic energy T_{ar} of the the tweezers' arm is

$$T_{\text{ar}} = \frac{1}{2} \int_0^{\ell_b} J_a \delta_d \dot{\theta}^2 dx \quad (4.21)$$

where J_a is

$$J_a = \frac{1}{3} m_a \ell_a^2 \quad (4.22)$$

using Eq. (4.14) in Eq. (4.21), one can write the arm kinetic energy as

$$T_{\text{ar}} = \frac{1}{2} \int_0^{\ell_b} J_a \delta_d (\dot{w}'^2 - 2\dot{w}'^2 \bar{u}' - 2\bar{w}'^2 \dot{w}'^2 - 4w'_o \bar{w}' \dot{w}'^2) dx \quad (4.23)$$

Thus, substitute Eqs. (4.19)–(4.21) into Eq. (4.18) to yield

$$\begin{aligned} T = \frac{1}{2} \int_0^{\ell_b} & \left(\underbrace{(\rho A_b + m_a \delta_d)}_{\mathbf{T}_1} \dot{w}^2 + \underbrace{\rho A_b}_{\mathbf{T}_2} \dot{u}^2 \right. \\ & \left. + \underbrace{(\rho I_b + J_a \delta_d (1 - 2\bar{u}' - 2\bar{w}'^2 - 4w'_o \bar{w}'))}_{\mathbf{T}_3} \dot{w}'^2 \right) dx \end{aligned} \quad (4.24)$$

This equation represents the total kinetic energy of the arch micro-tweezers.

4.1.3 Extended Hamilton Principle

The extended Hamilton's principle states that the variation of the summation of the Lagrangian $\mathcal{L} = T - U$ and the line integral of the virtual work done by nonconservative forces W_{nc} during a time interval from t_1 to t_2 must be equal to zero

$$\int_{t_1}^{t_2} \delta (T - U + W_{nc}) dt = 0 \quad (4.25)$$

where δ is a differential operator denoting the first variation.

The first variation of U_1 , which represents the mid-plane potential energy, in Eq. (4.17) is obtained as

$$\begin{aligned}
\int_{t_1}^{t_2} \delta U_1 dt &= \int_{t_1}^{t_2} EA_b \left(\bar{u}' + w'_o \bar{w}' + \frac{\bar{w}'^2}{2} \right) \delta \bar{u} dt \Big|_0^{\ell_b} \\
&\quad - \int_{t_1}^{t_2} \int_0^{\ell_b} EA_b \left(\bar{u}' + w'_o \bar{w}' + \frac{\bar{w}'^2}{2} \right)' \delta \bar{u} dx dt \\
&\quad + \int_{t_1}^{t_2} EA_b \left(\bar{u}' + w'_o \bar{w}' + \frac{\bar{w}'^2}{2} \right) \bar{w}' \delta \bar{w} dt \Big|_0^{\ell_b} \\
&\quad - \int_{t_1}^{t_2} \int_0^{\ell_b} EA_b \left(\left(\bar{u}' + w'_o \bar{w}' + \frac{\bar{w}'^2}{2} \right) \bar{w}' \right)' \delta \bar{w} dx dt \\
&\quad + \int_{t_1}^{t_2} EA_b \left(\bar{u}' + w'_o \bar{w}' + \frac{\bar{w}'^2}{2} \right) w'_o \delta \bar{w} dt \Big|_0^{\ell_b} \\
&\quad - \int_{t_1}^{t_2} \int_0^{\ell_b} EA_b \left(\left(\bar{u}' + w'_o \bar{w}' + \frac{\bar{w}'^2}{2} \right) w'_o \right)' \delta \bar{w} dx dt
\end{aligned} \tag{4.26}$$

similarly, the first variation of U_2 , which represents the section bending potential energy, can be written as

$$\begin{aligned}
\int_{t_1}^{t_2} \delta U_2 dt &= \int_{t_1}^{t_2} \int_0^{\ell_b} EI_b \bar{w}'' \delta \bar{w}'' dx dt \\
&\quad + \int_{t_1}^{t_2} \left(EI_b \bar{w}'' \delta \bar{w}' \Big|_0^{\ell_b} - EI_b \bar{w}''' \delta \bar{w} \Big|_0^{\ell_b} + \int_0^{\ell_b} EI_b \bar{w}^{iv} \delta \bar{w} dx \right) dt \\
&= \int_{t_1}^{t_2} EI_b \bar{w}'' \delta \bar{w}' dt \Big|_0^{\ell_b} - \int_{t_1}^{t_2} EI_b \bar{w}''' \delta \bar{w} dt \Big|_0^{\ell_b} + \int_{t_1}^{t_2} \int_0^{\ell_b} EI_b \bar{w}^{iv} \delta \bar{w} dx dt
\end{aligned} \tag{4.27}$$

The variation of the kinetic energy can be also evaluated via integration by parts of individual terms. The first variation of T_1 in Eq. (4.24) can be written as

$$\int_{t_1}^{t_2} \delta T_1 dt = \int_0^{\ell_b} (\rho A_b + m_a \delta_d) \dot{\bar{w}} \delta \bar{w} dx \Big|_{t_1}^{t_2} - \int_{t_1}^{t_2} \int_0^{\ell_b} (\rho A_b + m_a \delta_d) \ddot{\bar{w}} \delta \bar{w} dx dt \tag{4.28}$$

similarly the first variation of T_2 is

$$\int_{t_1}^{t_2} \delta T_2 dt = \int_0^{\ell_b} \rho A_b \dot{u} \delta \bar{u} dx \Big|_{t_1}^{t_2} - \int_{t_1}^{t_2} \int_0^{\ell_b} \rho A_b \ddot{u} \delta \bar{u} dx dt \quad (4.29)$$

and the first variation of T_3 can be written as [127]

$$\int_{t_1}^{t_2} \delta T_3 dt = \int_{t_1}^{t_2} \int_0^{\ell_b} \left(\frac{\partial T_3}{\partial \bar{w}'} \delta \bar{w}' + \frac{\partial T_3}{\partial \bar{u}'} \delta \bar{u}' + \frac{\partial T_3}{\partial \dot{\bar{w}}'} \delta \dot{\bar{w}}' \right) dx dt \quad (4.30)$$

Then, we divide the variation of Eq. (4.30) into three individual parts and then perform the integration by parts. Where the first variation of the first term can be obtained as

$$\int_{t_1}^{t_2} \int_0^{\ell_b} \left(\frac{\partial T_3}{\partial \bar{w}'} \right) \delta \bar{w}' dx dt = \int_{t_1}^{t_2} \gamma_1 \delta \bar{w} dt \Big|_0^{\ell_b} - \int_{t_1}^{t_2} \int_0^{\ell_b} \gamma_2 \delta \bar{w} dx dt \quad (4.31)$$

where γ_1 and γ_2 are defined to be

$$\begin{aligned} \gamma_1 &= -4J_a \delta_d \dot{w}'^2 (\bar{w}' + w'_o) \\ \gamma_2 &= -4J_a \delta'_d \dot{w}'^2 (\bar{w}' + w'_o) - 2J_a \delta_d (2\dot{w}'^2 (\bar{w}'' + w''_o) + 4\dot{w}' \dot{w}'' (\bar{w}' + w'_o)) \end{aligned} \quad (4.32)$$

where δ'_d is the Doublet functions and can be written as

$$\delta'_d = \delta'(x - \ell_1) + \delta'(x - \ell_2)$$

the first variation of the second term gives

$$\int_{t_1}^{t_2} \int_0^{\ell_b} \left(\frac{\partial T_3}{\partial \bar{u}'} \right) \delta \bar{u}' dx dt = \int_{t_1}^{t_2} \gamma_3 \delta \bar{u} dt \Big|_0^{\ell_b} - \int_{t_1}^{t_2} \int_0^{\ell_b} \gamma_4 \delta \bar{u} dx dt \quad (4.33)$$

where γ_3 and γ_4 are defined to be

$$\begin{aligned} \gamma_3 &= -2J_a \delta_d \dot{w}'^2 \\ \gamma_4 &= -2J_a \delta'_d \dot{w}'^2 - 4J_a \delta_d \dot{w}' \dot{w}'' \end{aligned} \quad (4.34)$$

while the first variation of the third term yields

$$\int_{t_1}^{t_2} \int_0^{\ell_b} \left(\frac{\partial T_3}{\partial \dot{w}'} \right) \delta \dot{w}' dx dt = \int_0^{\ell_b} \gamma_5 \delta \bar{w}' dx \Big|_{t_1}^{t_2} - \int_{t_1}^{t_2} \gamma_6 \delta \bar{w} dt \Big|_0^{\ell_b} + \int_{t_1}^{t_2} \int_0^{\ell_b} \gamma_7 \delta \bar{w} dx dt \quad (4.35)$$

where γ_5 , γ_6 and γ_7 are introduced as

$$\begin{aligned} \gamma_5 &= (\rho I_b + J_a \delta_d) \dot{w}' - 2J_a \delta_d \dot{w}' (2\bar{u}' + 2\bar{w}'^2 + 4w'_o \bar{w}' - 1) \\ \gamma_6 &= (\rho I_b + J_a \delta_d) \ddot{w}' - 2J_a \delta_d (4\dot{w}'^2 (\bar{w}' + w'_o) - \ddot{w}' (1 - 2\bar{u}' - 2\bar{w}'^2 - 4w'_o \bar{w}')) \\ \gamma_7 &= (\rho I_b + J_a \delta_d) \ddot{w}'' - 2J_a \delta'_d (4\dot{w}'^2 (\bar{w}' + w'_o) - \ddot{w}' (1 - 2\bar{u}' - 2\bar{w}'^2 - 4w'_o \bar{w}')) \\ &\quad - 2J_a \delta_d (\ddot{w}'' (2\bar{u}'' + 4(\bar{w}'' + \bar{w}''_o) (\bar{w}' + \bar{w}'_o)) + 8\dot{w}' \dot{w}'' (\bar{w}' + w'_o) + 4\dot{w}'^2 (\bar{w}'' + w''_o) \\ &\quad - \ddot{w}'' (1 - 2\bar{u}' - 2\bar{w}'^2 - 4w'_o \bar{w}')) \end{aligned} \quad (4.36)$$

The variation of the virtual work due to the electrostatic force, viscous linear damping and nonlinear squeeze-film damping can be written as

$$\int_{t_1}^{t_2} \delta W_{nc} dt = \int_{t_1}^{t_2} \left(\int_0^{\ell_b} F_{es} \delta \bar{w} dx - c_{va} \dot{u} \delta \bar{u} - (c_{vt} + c_{sf}) \dot{w} \delta \bar{w} \right) dt \quad (4.37)$$

where F_{es} is the electrostatic force and can be expressed as [1]

$$F_{es} = -\frac{1}{2} \frac{\epsilon b_b V(t)^2}{(d + w_o + \bar{w})^2} \quad (4.38)$$

the excitation voltage V is biased signal with the form of

$$V = V_{DC} + V_{AC} \cos(2\pi f_{ex} t) \quad (4.39)$$

where V_{DC} , V_{AC} and f_{ex} are the bias, amplitude and frequency of the waveform signal. Furthermore, the electrostatic force F_{es} can be modified to account for the electrostatic fringing field by replacing the width of the curved micro-beam b_b with an effective width b_e considering two models in the literature:

- Palmer's model [145]

$$F_{\text{PM}} = -\frac{1}{2} \frac{\epsilon b_b V(t)^2}{(d + w_o + \bar{w})^2} \left(1 + 0.65 \frac{(d + w_o + \bar{w})}{b_b} \right) \quad (4.40)$$

- Kimbali's model [146]

$$F_{\text{KM}} = -\frac{1}{2} \frac{\epsilon b_b V(t)^2}{(d + w_o + \bar{w})^2} \left(0.0612 + \frac{d^4}{b_b^4} ((d + w_o + \bar{w})^2)^2 \right. \\ \left. - 0.5 \frac{d^3}{b_b^3} (d + w_o + \bar{w})^2 + 1.5 \frac{d^2}{b_b^2} (d + w_o + \bar{w})^2 + 1.2 \right) \quad (4.41)$$

In addition, c_{va} and c_{vt} are the viscous damping coefficients in the axial and transverse directions, respectively. The squeeze-film damping accounts for energy losses due to the narrow channel between the beam and the sidewall electrode with a damping coefficient c_{sf} written as [147]

$$c_{sf} = \frac{\mu b_b^3}{(1 + 6Kn)(1 + w_o + \bar{w})^3} \quad (4.42)$$

where μ is air viscosity, $Kn = \lambda/d$ is Knudsen number and λ is the mean free path of air molecules at ambient pressure.

Substituting Eqs. (4.26)–(4.37) into Eq. (4.25) yields two nonlinear equations of motion describing the system response. The first equation governs the axial response and is

$$\rho A_b \ddot{u} + c_{va} \dot{u} + \gamma_4 - EA_b \left(\bar{u}' + w_o' \bar{w}' + \frac{\bar{w}'^2}{2} \right)' = 0 \quad (4.43)$$

Since the evaluation of the Dirac-Delta and the Doublet functions at the boundaries is zero, the boundary and initial conditions associated with Eq. (4.43) are

$$\bar{u}' + w_o' \bar{w}' + \frac{\bar{w}'^2}{2} = 0 \quad \text{or} \quad \bar{u} = 0 \quad \text{at} \quad x = 0 \quad \& \quad \ell_b \\ \dot{u} = 0 \quad \text{or} \quad \bar{u} = 0 \quad \text{at} \quad t_2 = 0 \quad (4.44)$$

The second equation of motion governs the transverse response and is

$$\begin{aligned}
& (\rho A_b + m_a \delta_d) \ddot{w} - (\rho I_b + J_a \delta_d) \ddot{w}'' - J_a \delta_d' \ddot{w}' + \gamma_8 + (c_{vt} + c_{sf}) \dot{w} + EI_b \bar{w}^{iv} \\
& - EA_b \left(\left(\bar{u}' + w'_o \bar{w}' + \frac{\bar{w}'^2}{2} \right) (w'_o + \bar{w}') \right)' = F_{es}
\end{aligned} \tag{4.45}$$

where

$$\begin{aligned}
\gamma_8 = & -2J_a \delta_d' (2\dot{w}'^2 (\bar{w}' + w'_o) - \ddot{w}' (1 - 2\bar{u}' - 2\bar{w}'^2 - 4w'_o \bar{w}')) \\
& - 2J_a \delta_d (\ddot{w}' (2\bar{u}'' + 4(\bar{w}'' + \bar{w}''_o) (\bar{w}' + \bar{w}'_o)) + 4\dot{w}' \dot{w}'' (\bar{w}' + w'_o) + 2\dot{w}'^2 (\bar{w}'' + w''_o)) \\
& - \ddot{w}'' (1 - 2\bar{u}' - 2\bar{w}'^2 - 4w'_o \bar{w}')
\end{aligned} \tag{4.46}$$

similar to the axial case, the evaluation of the Dirac-Delta and the Doublet functions at the boundaries is zero and, therefore, the boundary and initial conditions associated with Eq. (4.45) are

$$\begin{aligned}
\bar{w}''' - (\bar{u}' + w'_o \bar{w}' + \frac{\bar{w}'^2}{2}) (w'_o + \bar{w}') = 0 \quad \text{or} \quad \bar{w} = 0 \quad \text{at} \quad x = 0 \quad \& \quad \ell_b \\
\bar{w}'' = 0 \quad \text{or} \quad \bar{w}' = 0 \quad \text{at} \quad x = 0 \quad \& \quad \ell_b \\
\dot{w} = 0 \quad \text{or} \quad \bar{w} = 0 \quad \text{at} \quad t_2 = 0
\end{aligned} \tag{4.47}$$

Setting the time derivative terms equal to zero in Eq. (4.43), reduces it to a static equation which can be written as

$$\left(\bar{u}' + w'_o \bar{w}' + \frac{\bar{w}'^2}{2} \right)' = 0 \tag{4.48}$$

Equation (4.48) can be used to write \bar{u} in terms of \bar{w} by integrating once over x which results in

$$\bar{u}' = -w'_o \bar{w}' - \frac{\bar{w}'^2}{2} + c_1 \tag{4.49}$$

Integrating once more over x and recalling that the axial displacement at both ends is zero

$(\bar{u} = 0)$ results in

$$\bar{u}(0) = 0 \Rightarrow c_2 = 0 \quad (4.50a)$$

$$\bar{u}(\ell_b) = 0 \Rightarrow c_1 = \frac{1}{2\ell_b} \int_0^{\ell_b} (2w'_o \bar{w}' + \bar{w}'^2) dx \quad (4.50b)$$

Therefore, we can rewrite Eq. (4.49) as

$$\bar{u}' = -w'_o \bar{w}' - \frac{\bar{w}'^2}{2} + \frac{1}{2\ell_b} \int_0^{\ell_b} (2w'_o \bar{w}' + \bar{w}'^2) dx \quad (4.51)$$

differentiating this equation with respect to x yields

$$\bar{u}'' = -w''_o \bar{w}' - w'_o \bar{w}'' - \bar{w}' \bar{w}'' \quad (4.52)$$

substitute Eqs. (4.51) and (4.52) into γ_8 results in

$$\begin{aligned} \gamma_9 = & -2J_a \delta'_d (2\dot{\bar{w}}'^2 (\bar{w}' + w'_o) - \ddot{\bar{w}}' (1 - \frac{1}{\ell_b} \int_0^{\ell_b} (2w'_o \bar{w}' + \bar{w}'^2) dx - \bar{w}'^2 - 2w'_o \bar{w}')) \\ & - 2J_a \delta_d (\ddot{\bar{w}}' ((2\bar{w}'' + 4\bar{w}''_o) (\bar{w}' + \bar{w}'_o) - 2w''_o \bar{w}') + 4\dot{\bar{w}}' \dot{\bar{w}}'' (\bar{w}' + w'_o)) \\ & + 2\dot{\bar{w}}'^2 (\bar{w}'' + w''_o) - \ddot{\bar{w}}'' (1 - \frac{1}{\ell_b} \int_0^{\ell_b} (2w'_o \bar{w}' + \bar{w}'^2) dx - \bar{w}'^2 - 2w'_o \bar{w}') \end{aligned} \quad (4.53)$$

then, substituting Eqs. (4.51)–(4.53) into Eq. (4.45) yields

$$\begin{aligned} & (\rho A_b + m_a \delta_d) \ddot{\bar{w}} - (\rho I_b + J_a \delta_d) \ddot{\bar{w}}'' - J_a \delta'_d \dot{\bar{w}}' + \gamma_9 + (c_{vt} + c_{sf}) \dot{\bar{w}} + EI_b \bar{w}^{iv} \\ & - (w''_o + \bar{w}'') \frac{EA_b}{2\ell_b} \int_0^{\ell_b} (2w'_o \bar{w}' + \bar{w}'^2) dx = F_{es} \end{aligned} \quad (4.54)$$

which is subject to the following boundary conditions

$$\bar{w}(0) = 0, \quad \bar{w}'(0) = 0, \quad \bar{w}(\ell_b) = 0, \quad \bar{w}'(\ell_b) = 0$$

4.2 Nondimensional Equation of Motion

Here, we nondimensionalize the transverse equation of motion governing the tweezers' response, Eq. (4.54). For convenience, we introduce the following nondimensional variables [148]

$$\hat{w} = \frac{\bar{w}}{d}, \quad \hat{w}_o = \frac{w_o}{d}, \quad \hat{x} = \frac{\bar{x}}{l_b}, \quad t = \frac{\hat{t}}{T}, \quad \ell_1 = \frac{\hat{\ell}_1}{l_b}, \quad \ell_2 = \frac{\hat{\ell}_2}{l_b}$$

where $T = \sqrt{\rho A l_b^4 / EI}$ is a time scale. Substituting the nondimensional parameters into Eq. (4.54), considering the scaling proprieties in Table 4.1 and multiplying both sides by $(T^2/d \rho A_b)$ to yield

$$(1 + \alpha_1 \hat{\delta}_d) \ddot{\hat{w}} - (\alpha_2 + \alpha_4 \hat{\delta}_d) \ddot{\hat{w}}'' - \alpha_4 \hat{\delta}'_d \ddot{\hat{w}}' + \gamma_{10} + (\hat{c}_{vt} + \hat{c}_{sf}) \dot{\hat{w}} + \hat{w}^{iv} - \alpha_5 (\hat{w}_o'' + \hat{w}''') \int_0^1 (2\hat{w}'_o \hat{w}' + \hat{w}'^2) d\hat{x} = \alpha_6 F_{es} \quad (4.55)$$

The nondimensional coefficients α_i appearing in the equation are defined as

$$\alpha_1 = \frac{m_a}{m_b}, \quad \alpha_2 = \frac{I_b}{\ell_b^2 A_b}, \quad \alpha_3 = \frac{2 m_a \ell_a^2 d^2}{3 m_b \ell_b^4}, \quad \alpha_4 = \alpha_3 \frac{\ell_b^2}{d^2}, \quad \alpha_5 = 6 \left(\frac{d}{h_b} \right)^2$$

$$\alpha_6 = \frac{6 \epsilon \ell_b^4}{E h^3 d^3}, \quad \hat{c}_{vt} = \frac{c_{vt} \ell_b^4}{E I_b T}, \quad \hat{c}_{sf} = \left(\frac{b}{d} \right)^3 \frac{T}{m_b} \frac{\mu}{(1 + 6Kn)(1 + \hat{w}_o + \hat{w})^3}$$

and m_b is the beam mass. The concentrated mass and mass moment of inertia of the tweezers arm are represented by two Dirac-Delta functions

$$\hat{\delta}_d = \hat{\delta}\left(\hat{x} - \frac{\ell_1}{l_b}\right) + \hat{\delta}\left(\hat{x} - \frac{\ell_2}{l_b}\right)$$

and two Doublet functions

$$\hat{\delta}'_d = \hat{\delta}'\left(\hat{x} - \frac{\ell_1}{l_b}\right) + \hat{\delta}'\left(\hat{x} - \frac{\ell_2}{l_b}\right)$$

and γ_{10} is a combination of rotary terms of order $O(\epsilon^3)$

$$\begin{aligned}
\gamma_{10} = & \alpha_3 \hat{\delta}'_d (2\dot{w}'^2 (\hat{w}' + \hat{w}'_o) + \ddot{w}' (\int_0^1 (2\hat{w}'_o \hat{w}' + \hat{w}'^2) d\hat{x} + \hat{w}'^2 + 2\hat{w}'_o \hat{w}')) \\
& + \alpha_3 \hat{\delta}_d (\ddot{w}' ((2\hat{w}'' + 4\hat{w}''_o) (\hat{w}' + \hat{w}'_o) - 2\hat{w}''_o \hat{w}') + 4\dot{w}' \dot{w}'' (\hat{w}' + \hat{w}'_o)) \\
& + 2\dot{w}'^2 (\hat{w}'' + \hat{w}''_o) + \ddot{w}'' (\int_0^{\ell_b} (2\hat{w}'_o \hat{w}' + \hat{w}'^2) d\hat{x} + \hat{w}'^2 + 2\hat{w}'_o \hat{w}')
\end{aligned} \tag{4.56}$$

On the other hand, if we scale the electrostatic gap d at order $O(\epsilon^1)$ similar to the beam width h_b , the equation of motion, Eq. (4.55), would reduce to

$$\begin{aligned}
(1 + \alpha_1 \hat{\delta}_d) \ddot{w} - (\alpha_2 + \alpha_4 \hat{\delta}_d) \ddot{w}'' - \alpha_4 \hat{\delta}'_d \ddot{w}' + (\hat{c}_{vt} + \hat{c}_{sf}) \dot{w} + \hat{w}^{iv} \\
- \alpha_5 (\hat{w}''_o + \hat{w}'') \int_0^1 (2\hat{w}'_o \hat{w}' + \hat{w}'^2) d\hat{x} = \alpha_6 F_{es}
\end{aligned} \tag{4.57}$$

subject to the boundary conditions

$$\hat{w}(0) = 0, \quad \hat{w}'(0) = 0, \quad \hat{w}(1) = 0, \quad \hat{w}'(1) = 0 \tag{4.58}$$

and γ_{10} is scaled at order $O(\epsilon^5)$ with $O(\epsilon^2)$ hidden inside α_3 and, therefore, can be neglected.

4.3 Reduced-Order Model (ROM)

A reduced-Order model (ROM) based on a Galerkin approximation is utilized to solve the equations, Eq. (4.57) and Eq. (4.58). This technique discretizes the equation of motion in terms of a finite number of degrees-of-freedom describing the amplitude of mode shapes that satisfy the boundary conditions. In this case, we chose a standard ROM with straight beam mode shapes $\phi_i(x)$.

These modes can be found by dropping the nonlinear terms, arm inertia, damping coefficients and electrostatic force from Eq. (4.57) and then solving for the free vibration

problem of a straight-beam around an undeflected straight position. It results in [144]

$$\ddot{\hat{w}} + \hat{w}^{iv} = 0 \quad (4.59)$$

Equation (4.59) can be solved by assuming a general solution in the form of

$$\hat{w} = \phi_i(x)e^{i\omega_n t} \quad (4.60)$$

where ω_n are the n^{th} natural frequencies. Substituting Eq. (4.60) into Eq. (4.59), we get

$$\phi_i^{iv}(x) - \omega_n^2 \phi_i(x) = 0 \quad (4.61)$$

recall that the boundary conditions of the fixed-fixed beam at $x = 0$ and $x = 1$ are

$$\phi_i = 0 \quad \text{and} \quad \phi_i' = 0 \quad (4.62)$$

assuming a homogeneous solution for ϕ_i in the form

$$\phi_i(x) = Ce^{\beta x} \quad (4.63)$$

Then, substituting this form into Eq. (4.61), yields

$$\beta^4 - \omega_n^2 = 0 \quad (4.64)$$

Solving Eq. (4.64) gives four roots β_i as

$$\beta_{1,2} = \pm\sqrt{\omega_n} \quad \text{and} \quad \beta_{3,4} = \pm i\sqrt{\omega_n} \quad (4.65)$$

substituting these roots into Eq. (4.63) to get the free vibration mode shape

$$\phi_i(x) = A \cos(\beta_1 x) + B \sin(\beta_2 x) + C \cosh(\beta_3 x) + D \sinh(\beta_4 x) \quad (4.66)$$

where A, B, C and D are constants and can be found by applying the boundary conditions found in Eq. (4.62) into Eq. (4.66). It yields to four algebraic equations representing the eigenvalue problem for ω_n as follow

$$\begin{bmatrix} 1 & 0 & 1 & 0 \\ 0 & \beta & 0 & \beta \\ \cos \beta & \sin \beta & \cosh \beta & \sinh \beta \\ -\beta \sin \beta & \beta \cos \beta & \beta \sinh \beta & \beta \cosh \beta \end{bmatrix} \begin{Bmatrix} A \\ B \\ C \\ D \end{Bmatrix} = \begin{Bmatrix} 0 \\ 0 \\ 0 \\ 0 \end{Bmatrix} \quad (4.67)$$

Equating the determinant of the coefficients to zero, we solve the characteristic equation of the straight beam

$$1 - \cos \beta \cosh \beta = 0 \quad (4.68)$$

for the nontrivial roots β_n , Eq. (4.68) can be solved numerically to find up to the n^{th} natural frequencies of the straight beam ($\omega_n = \sqrt{\beta_n}$). The mode shapes associated with these eigenvalues are then determined by manipulating Eq. (4.67) and finding the three constants, A, B and C with respect to the fourth one, D , which can be an arbitrary number [127, 149].

This results in

$$B = -\frac{A(\cos(\beta) - \cosh(\beta))}{\sin(\beta) - \sinh(\beta)} \quad (4.69)$$

$$C = -A \quad (4.70)$$

$$D = \frac{A(\cos(\beta) - \cosh(\beta))}{\sin(\beta) - \sinh(\beta)} \quad (4.71)$$

The mode shapes of an un-deflected straight beam without the arm inertia are expressed as

$$\phi_i(x) = C_n((\cos(\beta_n x) - \cosh(\beta_n x)) + k_n(\sinh(\beta_n x) - \sin(\beta_n x))) \quad (4.72)$$

where

$$k_n = \frac{\cos(\beta_n x) - \cosh(\beta_n x)}{\sin(\beta_n x) - \sinh(\beta_n x)}$$

Figure 4.3 (a) shows the first three symmetric and (b) shows the first three anti-symmetric mode shapes of the straight beam.

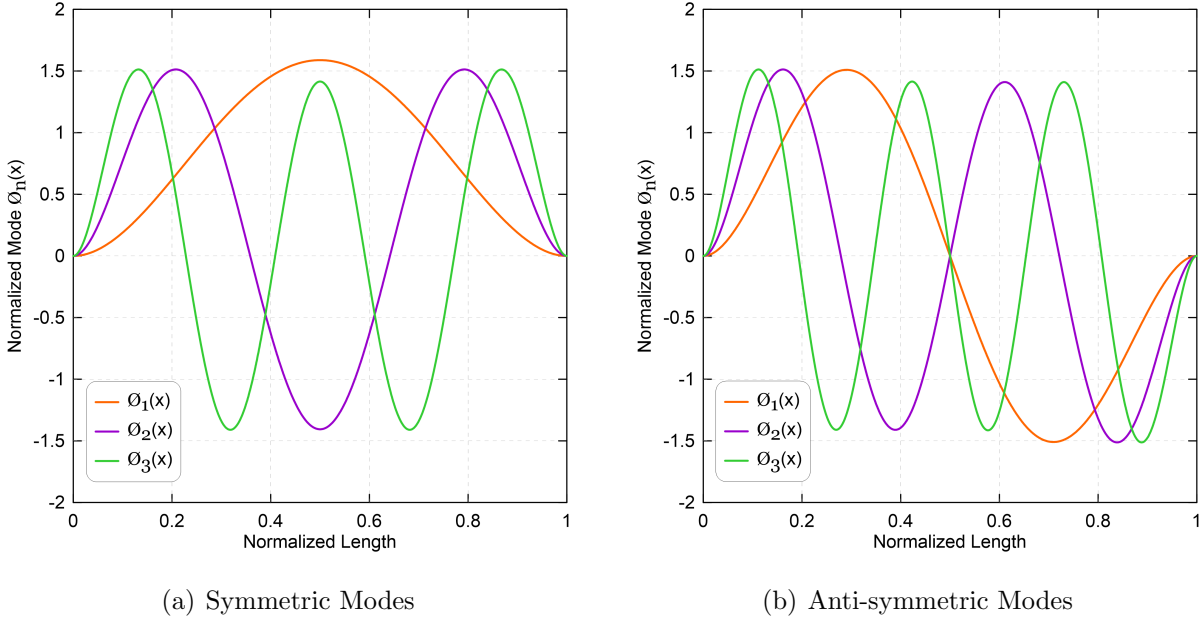


Figure 4.3: The nondimensional mode shapes of a straight beam: (a) the first three symmetric modes and (b) the first three anti-symmetric modes.

4.3.1 Static Analysis

Equations (4.57) and (4.58) were discretized using a straight beam mode shapes $\phi_i(x)$ as basis functions in a Galerkin expansion to obtain the ROM. We solve for the static deflection of the curved beam w_s as a function of the Root-Mean-Square voltage V_{RMS} by eliminating the time derivatives from the equation of motion to obtain a static equilibrium

equation as²:

$$w_s^{iv} = \alpha_5(w_o'' + w_s'') \int_0^1 (w_s'' + 2w_o'w_s')dx - \frac{\alpha_6 V_{\text{RMS}}^2}{(1 + w_o + w)^2} \quad (4.73)$$

and it is subjected to the boundary conditions

$$w_s(0) = 0, \quad w_s'(0) = 0, \quad w_s(1) = 0, \quad w_s'(1) = 0 \quad (4.74)$$

where

$$V_{\text{RMS}} = \sqrt{V_{\text{DC}}^2 + 0.5V_{\text{AC}}^2}$$

Then, we write the static deflection in terms of the Galerkin approximation as

$$w_s(x) = \sum_{i=1}^N \phi_i(x)u_i \quad ; \quad i = 1, \dots, N \quad (4.75)$$

where u_i are modal coordinates. Substituting this transformation form into Eqs. (4.73) and (4.74) and multiplying both sides by $(1 + w_o + w)^2$ to regularize the response near the singularity [16] yield

$$\begin{aligned} (1 + w_o + \sum_{i=1}^N \phi_i u_i)^2 \left(\sum_{i=1}^N \phi_i^{iv} u_i - \alpha_5(w_o'' + \sum_{i=1}^N \phi_i'' u_i) \int_0^1 \left(\sum_{i=1}^N \phi_i' u_i \right)^2 \right. \\ \left. + 2w_o' \sum_{i=1}^N \phi_i' u_i \right) dx + \alpha_6 V_{\text{RMS}}^2 = 0 \end{aligned} \quad (4.76)$$

multiplying the result by the mode shapes $\phi_j(x)$ and carrying out the integration over the beam length results in N algebraic equations describing the equilibrium position as

$$\begin{aligned} \int_0^1 \phi_j \left((1 + w_o + \sum_{i=1}^N \phi_i u_i)^2 \left(\sum_{i=1}^N \phi_i^{iv} u_i - \alpha_5(w_o'' + \sum_{i=1}^N \phi_i'' u_i) \int_0^1 \left(\sum_{i=1}^N \phi_i' u_i \right)^2 \right. \right. \\ \left. \left. + 2w_o' \sum_{i=1}^N \phi_i' u_i \right) dx + \alpha_6 V_{\text{RMS}}^2 \right) dx = 0 \end{aligned} \quad (4.77)$$

Those equations are then solved for u_i as functions of V_{RMS} to obtain the static deflection of the micro-tweezers.

²For sake of simplicity, we dropped over-hat ($\hat{\ }$) for now and so on.

4.3.2 Variation of the Natural Frequency under Electrostatic Forcing

We realize the tweezers' small vibrations problem by resolving the beam deflection into a static component $w_s(x)$ and a dynamic component $w_d(x, t)$

$$w(x, t) = w_s(x) + w_d(x, t) \quad (4.78)$$

substituting this form into Eqs. (4.57) and (4.58) and dropping the damping coefficients yields³

$$\begin{aligned} (1 + \alpha_1 \delta_d) \ddot{w}_d - (\alpha_2 + \alpha_4 \delta_d) \ddot{w}_d'' - \alpha_4 \delta_d' \ddot{w}_d' + w_s^{iv} + w_d^{iv} \\ - \alpha_5 (w_o'' + w_s'' + w_d'') \int_0^1 (2w_o'(w_s' + w_d') + (w_s' + w_d')^2) dx \\ = - \frac{\alpha_6 V_{\text{RMS}}^2}{(1 + w_o + w_s + w_d)^2} \end{aligned} \quad (4.79)$$

Thus, expand the right hand-side term around w_d using a Taylor series as

$$- \frac{\alpha_6 V_{\text{RMS}}^2}{(1 + w_o + w_s + w_d)^2} = - \frac{\alpha_6 V_{\text{RMS}}^2}{(1 + w_o + w_s)^2} - \frac{2\alpha_6 V_{\text{RMS}}^2}{(1 + w_o + w_s)^3} w_d \quad (4.80)$$

drop the high order terms and retain only up to the linear term in w_d , then substitute the resulting equation into Eq. (4.79) to obtain the results

$$\begin{aligned} (1 + \alpha_1 \delta_d) \ddot{w}_d - (\alpha_2 + \alpha_4 \delta_d) \ddot{w}_d'' - \alpha_4 \delta_d' \ddot{w}_d' + w_s^{iv} + w_d^{iv} \\ - \alpha_5 \left(w_d'' \int_0^1 (2w_s' w_o' + w_s'^2) dx + w_s'' \int_0^1 2(w_s' w_d' + w_o' w_d') dx \right. \\ \left. + w_o'' \int_0^1 2(w_o' w_d' + w_s' w_d') dx \right) = - \frac{2\alpha_6 V_{\text{RMS}}^2}{(1 + w_o + w_s)^3} w_d \end{aligned} \quad (4.81)$$

Once again, we write the dynamic component $w_d(x, t)$ in terms of the Galerkin approximation

$$w_d = \sum_{i=1}^N \phi_i(x) q_i(t) \quad ; \quad i = 1, \dots, N \quad (4.82)$$

³For sake of simplicity, we dropped (x) from the static competent and (x, t) from the dynamic competent.

where $q_i(t)$ are time-varying modal coordinates. Substituting this form in the small vibrations problem, replacing ϕ_i^{iv} with $\omega_n^2 \phi_i$ using Eq. (4.61), multiplying the result by the mode shapes $\phi_j(x)$ and carrying out the integration over the beam length results in N linear coupled ordinary differential equations describing the beam oscillations around the static equilibrium $w_s(x)$ at a given RMS voltage. Those equations can be written as

$$\begin{aligned}
(1 + \alpha_1 \delta_d) \ddot{q}_j - (\alpha_2 + \alpha_4 \delta_d) \sum_{i=1}^N \phi_i'' \ddot{q}_i \int_0^1 \phi_j dx - \alpha_4 \delta_d' \sum_{i=1}^N \phi_i' \ddot{q}_i \int_0^1 \phi_j dx \\
+ w_s^{iv} + q_j \omega_{i,j}^2 - \alpha_5 \left(\sum_{i=1}^N \phi_i'' q_i \int_0^1 \phi_j dx \int_0^1 (2w_s' w_s' + w_s'^2) dx \right. \\
+ w_s'' \int_0^1 \phi_j dx \int_0^1 2(w_s' \sum_{i=1}^N \phi_i' q_i + w_s' \sum_{i=1}^N \phi_i' q_i) dx \\
\left. + w_s'' \int_0^1 \phi_j dx \int_0^1 2(w_s' \sum_{i=1}^N \phi_i' q_i + w_s' \sum_{i=1}^N \phi_i' q_i) dx \right) \\
= - \frac{2\alpha_6 V_{\text{RMS}}^2}{(1 + w_s + w_s)^3} \sum_{i=1}^N \phi_i' q_i \int_0^1 \phi_j dx; \quad j = 1, \dots, N
\end{aligned} \tag{4.83}$$

The eigenvalue problem describing the beam oscillations around the static equilibrium $w_s(x)$ is obtained by substituting the harmonic form

$$\mathbf{q} = \begin{Bmatrix} q_1 \\ \vdots \\ q_N \end{Bmatrix} e^{i\omega t}$$

into Eq. (4.83). Substituting with $w_s(x)$ and V_{RMS} and solving the resulting un-damped eigenvalue problem, yields the first N^{th} natural frequencies and mode shapes of the arch micro-tweezers⁴.

⁴The eigenvalues analysis including the higher order rotary inertia term is discussed in Appendix B.

4.3.3 Dynamic Analysis

To evaluate the micro-tweezers motions around the static equilibrium w_s , we rewrite its total deflection as Eq. (4.78) and then substitute that transformation form into Eq. (4.57) to yield

$$(1 + \alpha_1 \delta_d) \ddot{w}_d - (\alpha_2 + \alpha_4 \delta_d) \ddot{w}_d'' - \alpha_4 \delta_d' \ddot{w}_d' + (c_{vt} + c_{sf}) \dot{w}_d + w_s^{iv} + w_d^{iv} = \alpha_5 (w_o'' + w_s'' + w_d'') \int_0^1 ((w_s' + w_d')^2 + 2w_o'(w_s' + w_d')) dx - \frac{\alpha_6 V(t)^2}{(1 + w_o + w_s + w_d)^2} \quad (4.84)$$

where $V(t)$ is expressed in Eq. (4.39). Substituting Eq. (4.82) into Eq. (4.84) and multiply both sides by $(1 + w_o + w_s + \sum_{i=1}^N \phi_i q_i)^2$ to yield

$$\begin{aligned} & (1 + w_o + w_s + \sum_{i=1}^N \phi_i q_i)^2 \left((1 + \alpha_1 \delta_d) \sum_{i=1}^N \phi_i \ddot{q}_i - (\alpha_2 + \alpha_4 \delta_d) \sum_{i=1}^N \phi_i'' \ddot{q}_i \right. \\ & \left. - \alpha_4 \delta_d' \sum_{i=1}^N \phi_i' \ddot{q}_i + (c_{vt} + c_{sf}) \sum_{i=1}^N \phi_i \dot{q}_i + w_s^{iv} + \sum_{i=1}^N \phi_i^{iv} q_i \right) = \\ & \alpha_5 (1 + w_o + w_s + \sum_{i=1}^N \phi_i q_i)^2 (w_o'' + w_s'' + \sum_{i=1}^N \phi_i'' q_i) \int_0^1 ((w_s' + \sum_{i=1}^N \phi_i' q_i)^2 \\ & + 2w_o'(w_s' + \sum_{i=1}^N \phi_i' q_i)) dx - \alpha_6 V(t)^2 \end{aligned} \quad (4.85)$$

Then, multiplying both sides by each mode shape ϕ_j and integrated over the beam length, we obtain a set of N discretized differential equations describing the tweezers'

motions in terms of modal coordinates q_i as⁵

$$\begin{aligned}
& \int_0^1 \phi_j \left((1 + w_o + w_s + \sum_{i=1}^N \phi_i q_i)^2 \left((1 + \alpha_1 \delta_d) \sum_{i=1}^N \phi_i \ddot{q}_i - (\alpha_2 + \alpha_4 \delta_d) \sum_{i=1}^N \phi_i'' \ddot{q}_i \right. \right. \\
& \left. \left. - \alpha_4 \delta_d' \sum_{i=1}^N \phi_i' \ddot{q}_i + (c_{vt} + c_{sf}) \sum_{i=1}^N \phi_i \dot{q}_i + w_s^{iv} + \sum_{i=1}^N \phi_i^{iv} q_i \right) \right) dx = \\
& \int_0^1 \phi_j \left(\alpha_5 (1 + w_o + w_s + \sum_{i=1}^N \phi_i q_i)^2 (w_o'' + w_s'' + \sum_{i=1}^N \phi_i'' q_i) \int_0^1 \left((w_s' + \sum_{i=1}^N \phi_i' q_i)^2 \right. \right. \\
& \left. \left. + 2w_o' (w_s' + \sum_{i=1}^N \phi_i' q_i) \right) dx - \alpha_6 V(t)^2 \right) dx; \quad j = 1, \dots, N
\end{aligned} \tag{4.86}$$

4.4 Summary

To sum-up, we utilized Euler-Bernoulli beam theory and the Extended Hamilton principle to derive the equation of motion describing the transverse response and the associated boundary and initial conditions of the electrostatic micro-tweezers. In this model, we assumed that the tweezers arms are rigid bodies and their elastic deformations is ignored. Then, a reduced order model based on a Galerkin approximation with the mode shapes of a straight beam was utilized to solve the equation of motion both statically and dynamically.

⁵The dynamic analysis including the higher order rotary inertia term is discussed in Appendix C.

Chapter 5

Characterizations of Initially Curved Micro-beams

In this chapter, we investigate analytically, numerically and experimentally the static and dynamic responses of the electrostatically actuated initially curved micro-beams. This step is required to better understanding the fundamental behaviors of the curved beam which serves as the platform for the tweezers' arms. The reduced-order model (ROM) that was developed above is solved analytically for static and dynamic responses. The results are then compared to those measured experimentally and numerically using a 2D Finite Element Model (FEM).

Part I: Simulation

5.1 Static Response

This section discusses the static deflection of the initially curved micro-beam mid-point $w_s(0.5)$ excited by a distributed electrostatic force. We consider a curved beam, Fig. 5.1, with a length of $\ell_b = 1000 \mu\text{m}$, the distance between the beam end supports, thickness and initial mid-point rise of $h_b = 3 \mu\text{m}$ and $h_o = 3.5 \mu\text{m}$, respectively.

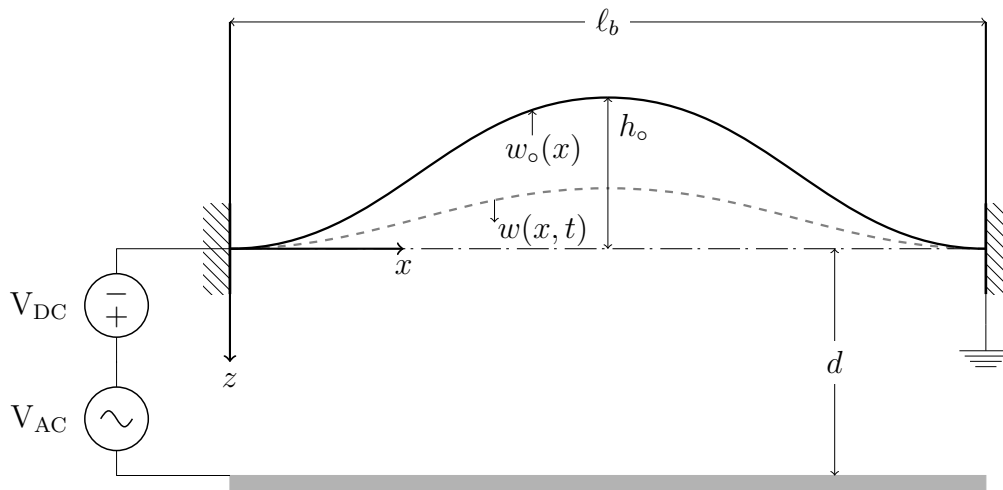


Figure 5.1: A schematic of the electrostatic curved beam actuator.

The initial capacitor gap between the sidewall electrode and the reference line is $d = 11.5 \text{ }\mu\text{m}$. The beam is made of Boron doped single crystal Silicon on Insulator (SOI) with a structural layer thickness of $b = 30 \text{ }\mu\text{m}$ and Young's Modulus $E = 129 \text{ GPa}$.

We obtained the variation of the micro-beam mid-point static equilibria as functions of the RMS voltage by solving Eq. (4.76). The solution fidelity depends on the type and number of mode shapes used in the Galerkin expansion [16]. Then, we carried out a convergence analysis to determine the minimum number of modes required in the Galerkin expansion by comparing the static deflection obtained from ROMs, Eq. (4.76), employing two-, three- and five symmetrical mode shapes and a parallel-plate electrostatic field model¹.

Figure 5.2 shows the variation in the mid-point static deflection $w_s(0.5)$ as a function the RMS voltage for the three ROMs. In all cases, two branches of stable equilibria marked as solid lines and two branches of unstable equilibria marked as dashed lines were observed. The results show that at least three symmetric modes are required for satisfactory model convergence. Using two modes in the model results in quantitative errors along the second branch of stable equilibria and qualitative errors along the second branch of unstable equilibria.

The figure also shows that the mid-point deflection decreases as the RMS voltage increases along the first branch of stable equilibria, corresponding to the beam initial curvature, until it jumps down at point S ($V_S = 112.7 \text{ V}$) along the line from S to ST towards the second branch of stable equilibria, corresponding to the initial counter-curvature. This jump is corresponding to the snap-through mechanism, see Fig. 2.1. At point S, the stable branch of equilibria meets the first branch of unstable equilibria in a saddle-node bifurcation.

¹For the convergence analysis, we ignore the effect of electrostatic fringing field.

Increasing the RMS voltage beyond the snap-through voltage V_S increases the counter deflection of the mid-point along the second stable branch until it reaches another saddle-node bifurcation demarcating the ‘pull-in instability’ at point P ($V_P = 153.2$ V) where it meets the second branch of unstable equilibria².

There are no physical stable equilibria beyond this point. On the other hand, decreasing the RMS voltage after snap-through decreases the counter-rise of the mid-point along the second stable branch until the beam snaps back and jumps up at point B ($V_B = 100.22$ V) along the line from B to R towards the first branch of stable equilibria, corresponding to the initial curvature³. At this point, the second stable branch of equilibria meets the first unstable branch in another saddle-node bifurcation.

Table 5.1 shows the relative errors among the three ROMs at a mid-point rise of -5.63 μm , along the beam initial counter-curvature, compare to those of a five-mode approximation⁴. We note that an odd number of mode shapes leads to faster and closer convergence than using an even number. Henceforth, we adopt the five-mode ROM approximation in the rest of the static analysis.

Table 5.1: The relative error of the converge analysis at $w_s = -5.63$ μm .

Number of mode shapes	Voltage (V)	Error %
Two	146.94	-3.05
Three	143.34	-0.53
Five	142.59	Not applicable

² V_S stands for snap-through voltage and V_P stands for pull-in voltage.

³ V_B stands for snap back voltage.

⁴The anti-symmetric modes do not have significant contributions to this analysis and, therefore, we ignore them.

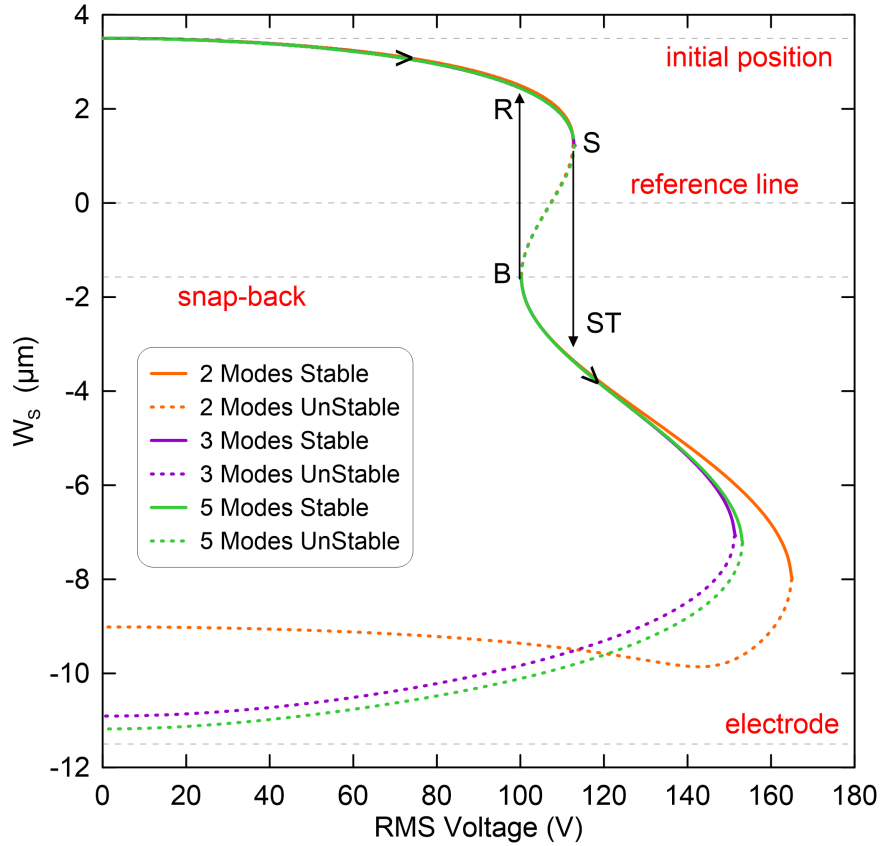


Figure 5.2: The beam mid-point deflection $w_s(0.5)$ as a function of the RMS voltage obtained from ROMs employing two- (marked with orange lines), three- (marked with magenta lines) and five-symmetric (marked with green lines) modes in the Galerkin expansion without accounting for the electrostatic fringing field. The branches of stable equilibria are marked in solid lines and branches of unstable equilibria are marked in dashed lines.

To validate the static results obtained analytically, the FEM package COMSOL Multiphysics (5.3a) [150] was also used to solve for the static response of the curved beam. A 3D model was created following the dimensions mentioned above and then a 2D model was obtained out of it. The stationary sidewall electrode ($1000 \times 30 \times 3$) μm^3 was placed

opposite to the curved beam and both of them were enclosed in air box of dimensions $(1000 \times 100 \times 270) \mu\text{m}^3$ to represent the electrostatic field. The beam was grounded while the electrode voltage was set to V_{RMS} as shown in Fig. 5.1. The boundary conditions fixed the beam at its supports.

Tetrahedral elements were used to mesh the beam, air box and stationary electrode. The total number of elements was 50,359 and their sizes varied in the range 10–80 μm . The Electromechanics module was used to perform the static analysis. An applied voltage was set initially to $V_{\text{RMS}} = 0 \text{ V}$ and gradually increased in step of 5 V over the range of 0–150 V to capture the locations of the snap-through and pull-in voltages.

Figure 5.3 shows the mid-point deflection values calculated by the FEM models marked by (\bullet) symbol and the ROMs employing three electrostatic field models: the traditional parallel-plate model (orange lines) [1] as well as Palmer's model (magenta lines) [145] and Kimbali's model (green lines) [146]. Comparing the results of the FEM and the parallel-plate ROM shows that ignoring the fringing field underestimates the electrostatic force and overestimates the saddle-node bifurcation points.

The ROMs accounting for the electrostatic fringing field compare well with the FEM. We found that the snap-through occurs at point S with voltage of ($V_{\text{S}} = 100.53 \text{ V}$), pull-in occurs at point P with voltage of ($V_{\text{P}} = 136.44 \text{ V}$) and snap back occurs at point B with voltage of ($V_{\text{B}} = 89.01 \text{ V}$), respectively. Henceforth, we adopt Kimbali's model because it better matches the FEM results.

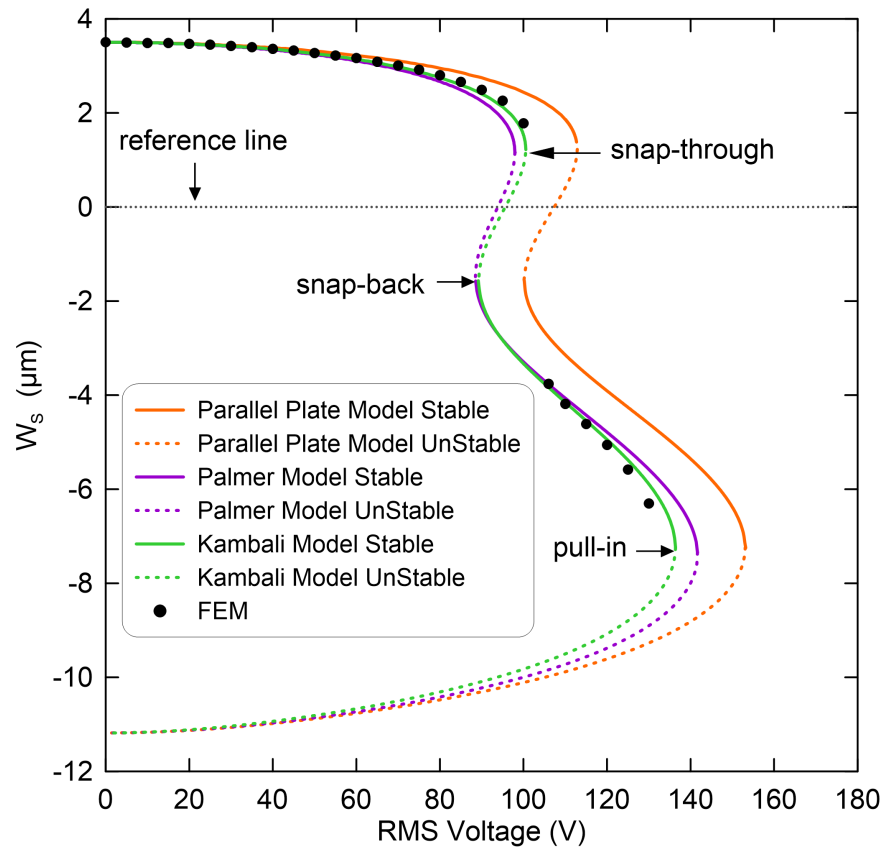


Figure 5.3: The beam mid-point deflection $w_s(0.5)$ as a function of the RMS voltage using the five-symmetric modes ROM with parallel-plate model marked with orange lines, Palmer's model marked with magenta lines, Kimbali's model marked with green lines and FEM marked with (\bullet) symbol. The branches of stable equilibria are marked in solid lines and branches of unstable equilibria are marked in dashed lines.

5.2 Variation of the Natural Frequency under Electrostatic Forcing

We investigate the impact of the electrostatic field strength represented by the RMS of the voltage waveform on the fundamental natural frequency of the curved micro-beam with dimensions listed above in section 5.1 as a function of the RMS voltage. Toward this, we substitute the static results obtained by employing a ROM with three symmetric, two anti-symmetric modes, and the electrostatic fringing field model using Kimbali expression into Eq. (4.83) and then solve for the corresponding eigenvalues⁵.

The first four natural frequencies (f_i) were calculated using the ROM and they correspond to the first in-plane symmetric mode, the first in-plane anti-symmetric mode, the second in-plane symmetric mode and the second in-plane anti-symmetric mode as shown in Figs. 4.3(a) and (b).

Zone I in Fig. 5.4 shows that the first natural frequency ($f_1 = 38.49$ kHz at $0 V_{\text{RMS}}$) marked with orange line (—) continuously drops along the first stable branch of equilibria, corresponding to the initial curvature, and it reaches zero at the snap-through voltage $V_S = 100.53$ V. Then, it increases as the RMS voltage increases along the second branch of equilibria marked as Zone III, corresponding to the initial counter-curvature, until it reaches $f_1 = 37.27$ kHz and then it suddenly drops and reaches zero at the pull-in voltage $V_P = 136.44$ V. The first drop indicates that the geometric nonlinearities dominate the electrostatic force nonlinearities. However, after the snap-through, the beam becomes closer to the electrode and, therefore, the electrostatic force nonlinearities dominate the geometric nonlinearities.

⁵The reason for considering the anti-symmetric modes is to investigate the changing in their frequencies as a function of the RMS voltage.

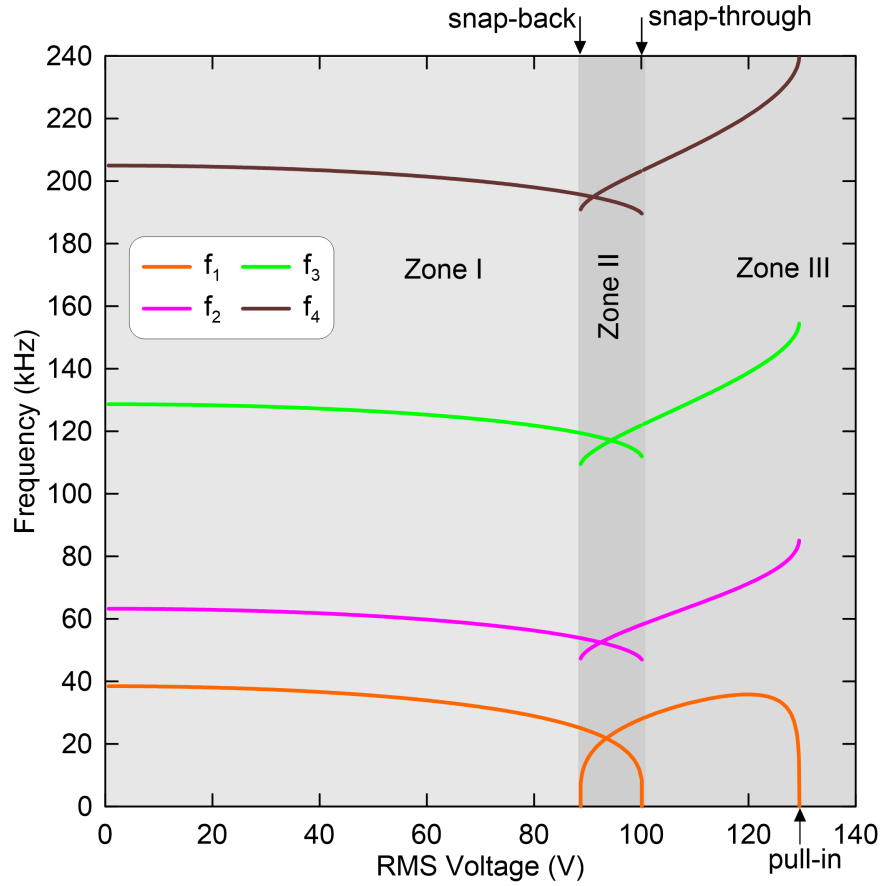


Figure 5.4: Variation in the first four natural frequencies of the curved beam as a function of the RMS voltage along: the first symmetric in-plane marked with orange line (---), first anti-symmetric in-plane marked with magenta line (---), second symmetric in-plane marked with green line (---) and second anti-symmetric in-plane brown line (---). Zone I represents the first stable equilibrium, corresponding to the beam initial curvature, Zone II represents two stable equilibria at the same RMS voltage and Zone III represents the second stable equilibrium, corresponding to the beam initial counter-curvature.

Decreasing the RMS voltage along the second branch and beyond the snap-through point reduces the natural frequency until it reaches zero at the snap back voltage of $V_B = 89.01$ V. The figure shows a region between the snap back and snap-through points marked as Zone II where the beam exhibits two natural frequencies at the same RMS voltage. The first value corresponds to the small oscillation around the initial curvature equilibrium position and the second value corresponds to another oscillation around the initial counter-curvature equilibrium position. We note that the two configurations have the same natural frequency of $f_1 = 90.5$ kHz at $V_{\text{RMS}} = 93.63$ V.

The second natural frequency ($f_2 = 63.3$ kHz at 0 V_{RMS}) marked with a solid magenta line (—) also varies continuously as the RMS voltage increases. It does not evince a discontinuity as the equilibrium position jumps from the first to the second stable branches of solution at the snap-through point. Similarly, the third natural frequency ($f_3 = 129.1$ kHz at 0 V_{RMS}) marked with a solid green line (—) and the fourth natural frequency ($f_4 = 205.2$ kHz at 0 V_{RMS}) marked with a solid brown line (—) vary within a small range of the RMS voltage. However, they show jumps to higher values after the snap-through. We note that these higher frequencies do not reach zero either at the snap-through nor at the pull-in points due to their strong geometric nonlinearities.

The FEM model was also used to validate these results and to evaluate the accuracy of ROM with a straight beam mode shapes to that of an initially curved beam. Figure 5.5 shows the variation in the natural frequencies of the first three modes obtained analytically using the ROM (solid lines) and numerically using the FEM marked as (●) symbols. In Fig. 5.5(a), the fundamental natural frequency f_1 drops twice to zero at the snap-through and pull-in voltages. However, the second frequency f_2 does not reach zero at either the snap-through voltage nor at the pull-in voltage as shown in Fig. 5.5(b). We observed an excellent agreement along the two branches of stable equilibria.

Additionally, we examine the model's validity by repeating the previous analysis for the third frequency f_3 . We found that a deviation between the models is slightly growing along the second branch of equilibria as shown in Fig. 5.5(c). This is due to the limited number of the straight beam modes begin used in the Galerkin expansions compared to the FEM of the curved beam.

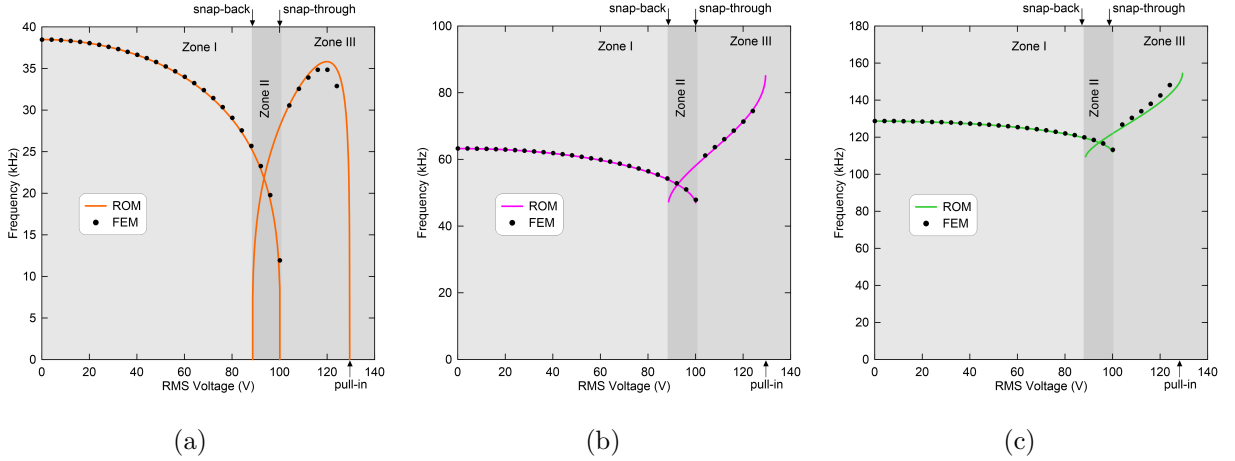


Figure 5.5: Variation of the first three natural frequencies as a function of the RMS voltages obtained using the ROM (solid line) and the FEM marked by (●) symbol of: (a) the fundamental natural frequency f_1 corresponding to the first in-plane symmetric mode, (b) the second frequency f_2 corresponding to the first in-plane anti-symmetric mode and (c) the third frequency f_3 corresponding to the second in-plane symmetric mode.

A comparison between the mode shapes of straight and curved beams at $0 V_{\text{RMS}}$ was carried out to visualize those deviations at the higher frequencies. Figure 5.6 shows the normalized mode shapes, where the y -axis is normalized with respect to the peak value of each mode and the x -axis is normalized with respect to the beam's length (ℓ_b).

The first symmetric mode $\phi_1(x)$ obtained for the curved beam is slightly wider than that of the straight beam. The second mode $\phi_2(x)$ is similar in both cases while the third

mode $\phi_3(x)$ exhibits some differences. On the other hand, no major changes are observed in the fourth mode $\phi_4(x)$ as shown in Fig. 5.6.

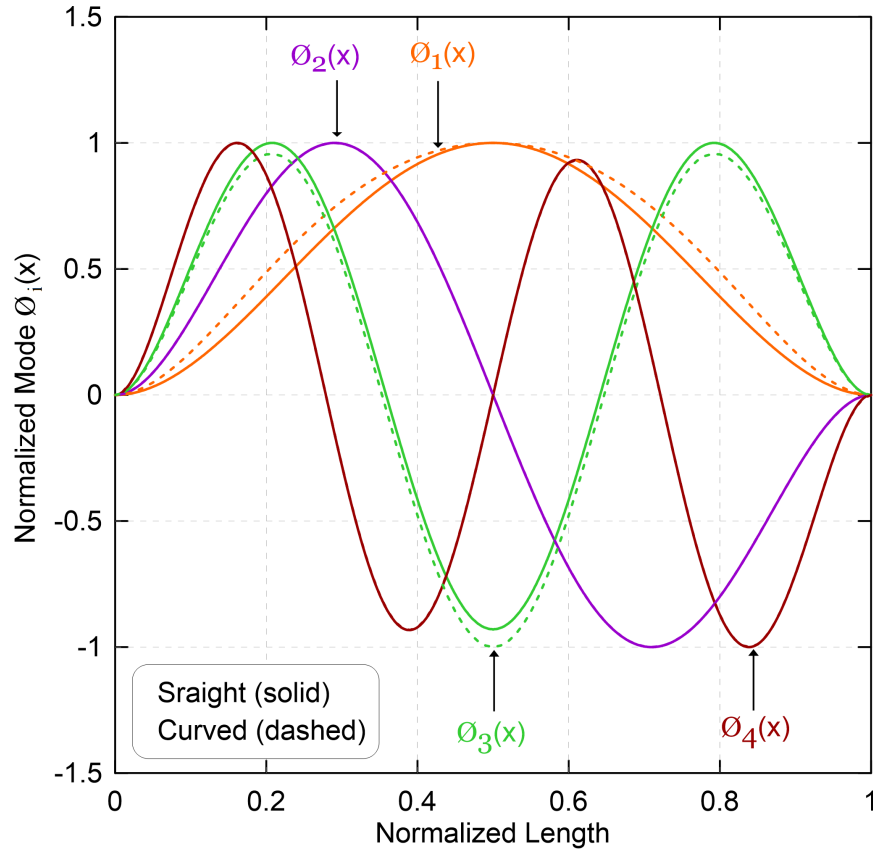


Figure 5.6: The first four mode shapes $\phi_i(x)$ at $V_{\text{RMS}} = 0$ V of: straight beam mode shapes marked as (solid lines) and actual mode shapes of curved beam obtained by the FEM and marked as (dashed lines).

These results confirm that using the straight beam mode shapes as a basis functions in the Galerkin expansion is sufficient to solve for the lowest eigenvalues of the initially curved beam at 0 V_{RMS} . However, these modes start changing their shapes as the RMS voltage increases and approaches the snap-through and the pull-in voltages specially for

the higher modes. To achieve excellent agreement between the two models, a higher order approximation or using the actual mode shapes of the curved beam is required.

5.3 Dynamic Response

The dynamic response has been investigated by subjecting the beam to a frequency sweep test in the vicinity of the fundamental frequency (f_1). In this analysis, the signal frequency f_{ex} was swept-up and down in a frequency range of 0–50 kHz, the quality factor Q was set to 15, the forcing signal was set to two levels: low V_{DC} and V_{AC} (linear case) and high V_{DC} and V_{AC} (nonlinear case).

Both levels correspond to an RMS voltage with only a single equilibrium point in the initial curvature. The frequency-response curve (FRC) was obtained using Long-Time Integration (LTI) with a time period T_s and the shooting method to generate periodic orbits and to determine their stability by evaluating their Floquet multipliers [148].

5.3.1 Linear Case

To dynamically evaluate the response of the beam mid-point displacement amplitude (w) and root-mean square (RMS) velocity (\dot{w}), Eq. (4.86) was integrated over a long-time period of $500 T_s$ using the ROM with a five-mode approximation. Then, the time-histories were evaluated over the last 200 signal periods to obtain the steady-state response.

The variation of the beam mid-point displacement amplitude and the RMS velocity obtained under a voltage waveform with $V_{DC} = V_{AC} = 2$ V and a frequency swept-up in the range of 5–50 kHz are shown in Fig. 5.7(a) and (b), respectively. This forcing level

corresponds to an RMS voltage of 2.44 V with an equilibrium point of $\approx 3.49 \mu\text{m}$ as shown in Fig. 5.3.

Figures 5.7 show that as the signal frequency increases, the response increases until it hits a superharmonic resonance of order-two at $f_{ex} = \frac{1}{2} f_1$, corresponding to a phase portrait with two orbits, and then increases until it approaches primary resonance at $f_{ex} = f_1$, corresponding to a phase-portrait with a single orbit (P-1). We note that the response is linear at this forcing level.

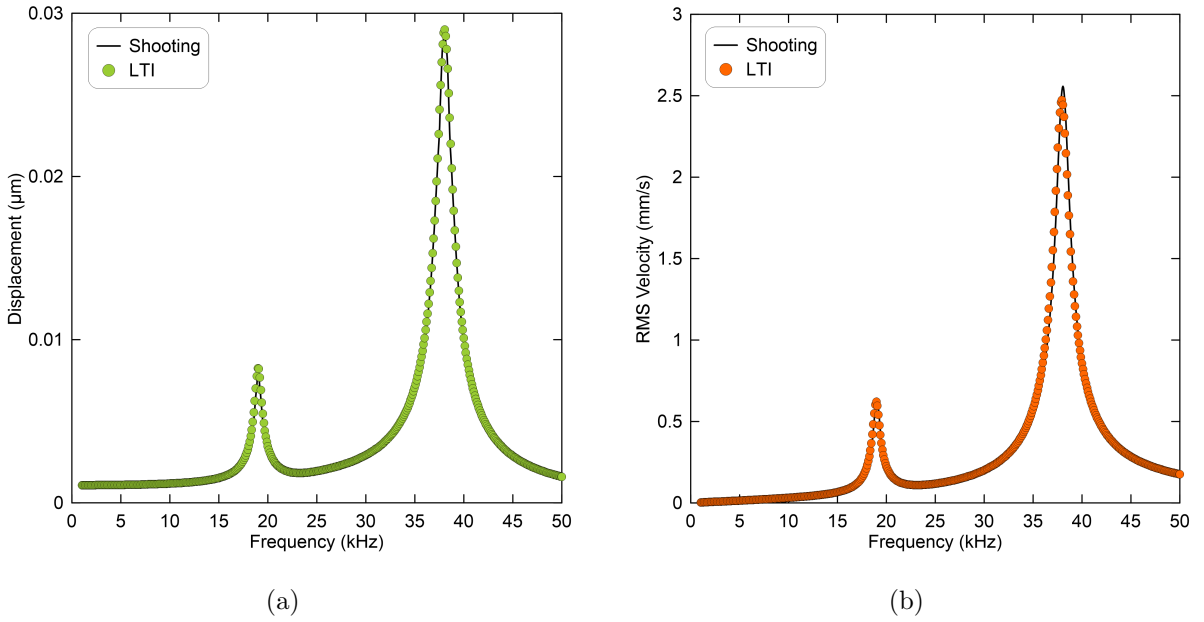


Figure 5.7: FRCs of the initially curved beam at $V_{DC} = V_{AC} = 2 \text{ V}$ of the beam mid-point: (a) displacement amplitude and (b) RMS velocity. The results obtained analytically using LTI are marked with symbols and shooting method are marked as solid black lines (—) for stable branches of solution.

The peaks appear in Figs. 5.7(a) and (b) came from the fact that the electrostatic force is a multi-frequency excitation. It can be seen by observing that the electrostatic force is

proportional to the square of the voltage waveform

$$\begin{aligned}
F_{ex} \propto V(t)^2 &= (V_{DC} + V_{AC} \cos(2\pi f_{ex}t))^2 \\
&= V_{DC}^2 + 2V_{DC}V_{AC} \cos(2\pi f_{ex}t) + \frac{1}{2}V_{AC}^2 - \frac{1}{2}V_{AC}^2 \sin(4\pi f_{ex}t) \\
&= (V_{DC}^2 + \frac{1}{2}V_{AC}^2) + 2V_{DC}V_{AC} \cos(2\pi f_{ex}t) - \frac{1}{2}V_{AC}^2 \sin(4\pi f_{ex}t)
\end{aligned} \tag{5.1}$$

Equation (5.1) shows that the electrostatic force consists of a static component proportional to $V_{DC}^2 + \frac{1}{2}V_{AC}^2$, a lower harmonic component at f_{ex} proportional to $2V_{DC}V_{AC}$, and a higher harmonic component at $2f_{ex}$ proportional to $\frac{1}{2}V_{AC}^2$. The higher harmonic excites primary resonance when the signal frequency is at $f_{ex} = \frac{1}{2} f_1$. While the lower harmonic excites primary resonance when the signal frequency is at $f_{ex} = f_1$.

Excellent agreement is observed between the LTI marked as (symbols) and the shooting method marked as (solid lines) where only stable branches of the solutions were observed⁶. We note that these small oscillations occur in an energy well called ‘narrow well’.

5.3.2 Nonlinear Case

As previously discussed in section 5.2, the electrostatic force has a significant softening effect on the beam's stiffness through its static component V_{DC} . This leads to a reduction in the natural frequencies. Adding a high V_{AC} results in large and complex motions characterized by two types of oscillations: a branch of small motions in a narrow well (linear case), a branch of medium-sized and large motions in a wider well [62]. These oscillations will be addressed in detail in the following.

As a case study, we increase the voltage waveform to $V_{DC} = V_{AC} = 40$ V corresponds to an RMS voltage of 48.98 V with only a one equilibrium point of 3.27 μm and a saddle-node bifurcation of -10.93 μm as shown in Fig. 5.3. The variation of the beam mid-point

⁶In this case, there was no Floquet multiplier exits the unit circle.

displacement amplitude and the RMS velocity obtained under this voltage waveform and a signal frequency f_{ex} swept-up in the range of 0–50 kHz are shown in Fig. 5.8(a) and (b), respectively.

The results obtained using LTI are marked with symbols. The shooting method stable branches of solution are marked with solid black lines (—) and the unstable branches of solution are marked with dashed red lines (- -). A complex dynamic response with multiple jumps up and down in addition to the co-existence of three stable branches of solution were observed.

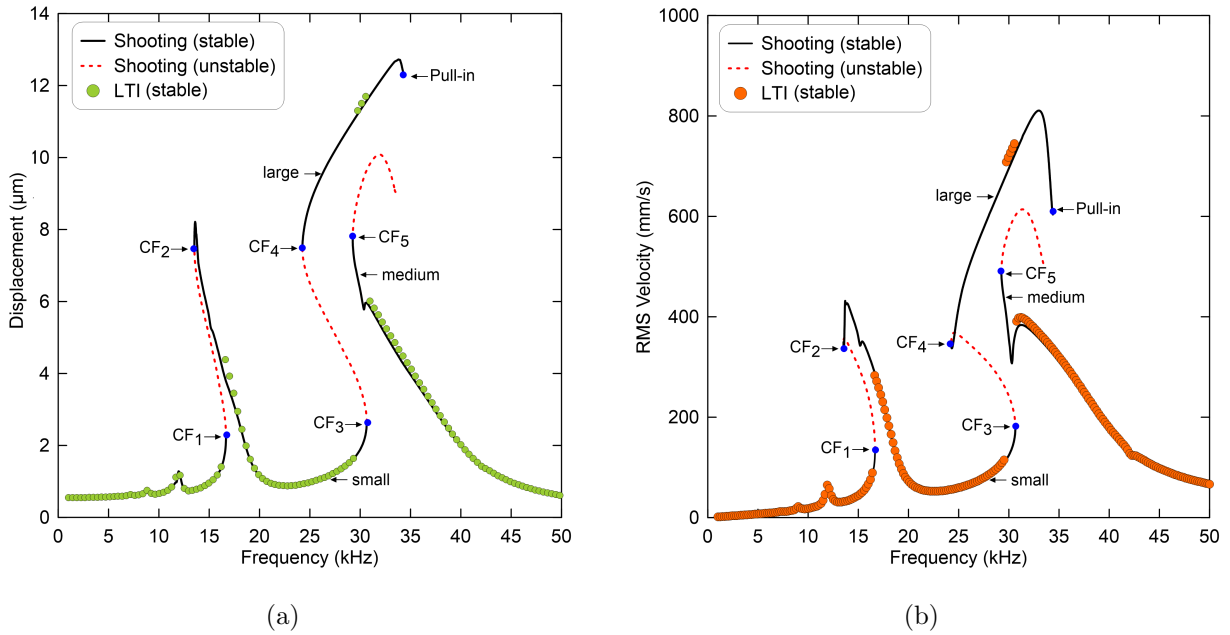


Figure 5.8: FRCs of the initially curved beam at $V_{DC} = V_{AC} = 40$ V of the beam mid-point: (a) displacement amplitude and (b) RMS velocity. The results obtained analytically using LTI are marked with symbols and shooting method are marked as solid black lines (—) for stable branches of solution and dashed red lines (- -) for unstable branches of solution.

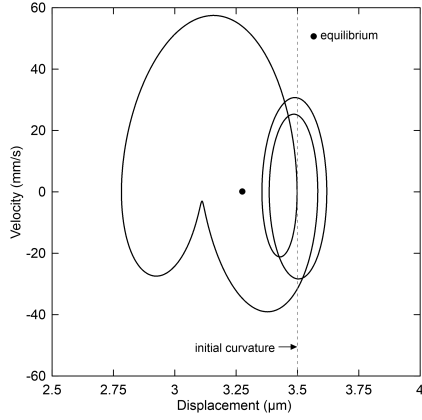
The results obtained using LTI, displacement amplitude marked with (●) symbols and

RMS velocity marked with (●) symbols, show that the responses gradually increase as the signal frequency increases until it hits a train of superharmonic resonances of: order-four at $f_{ex} = 9$ kHz, order-three at $f_{ex} = 12$ kHz and order-two at $f_{ex} = 16.5$ kHz. They crosspond to phase portraits shown in Figs. 5.9(a)–(c). Beyond that point, the response jumps up to an upper branch of solutions and then it increases as the signal frequency approaches the primary resonance.

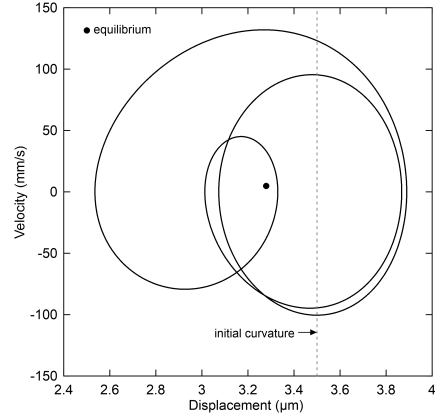
Then, it jumps up at $f_{ex} = 29.4$ kHz to an upper branch of stable solutions and its magnitude smoothly increases as the signal frequency further increases. This jump corresponds to a larger displacement around the equilibrium point in the wider well as shown in Fig. 5.8(a). To illustrate this motion, a phase-portrait at a signal frequency of $f_{ex} = 30.5$ kHz with a single orbit (P-1) is shown in Fig. 5.9(d). It indicates that the motion crosses the reference line and visiting far away area measured from the initial curvature.

After that, the mid-point magnitude jumps down to the lower branch of solutions as the signal frequency reaches $f_{ex} = 30.74$ kHz. The jump up and down in primary resonance vicinity has a discontinuity in the response resulting in a frequency band of 1.34 kHz as shown in Figs. 5.8(a) and (b), respectively. To investigate the stability and bifurcation types associated with those jumps which appear at the superharmonic and the primary resonances, we utilized the shooting method.

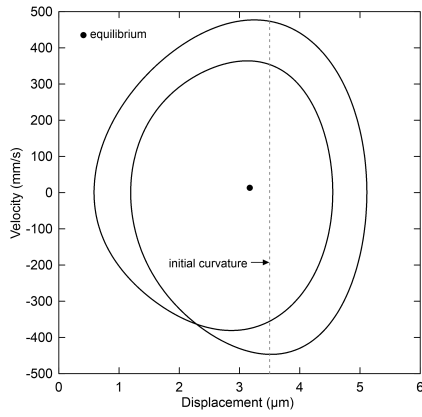
Figures. 5.8(a) and (b) show a train of superharmonic resonances of order-four, three and two along the branch of small stable solutions marked as solid black lines with phase-portraits similar to those presented in Figs. 5.9(a)–(c). A further increase in the signal frequency leads to increase in the magnitude until it jumps up at $f_{ex} = 16.67$ kHz to an upper stable branch of solutions through a cyclic-fold bifurcation demarcated by CF_1 (●). At point CF_1 , a Floquet multiplier exits the unit circle through +1 as the lower branch of stable solutions meets a branch of unstable solutions marked as a dashed red line.



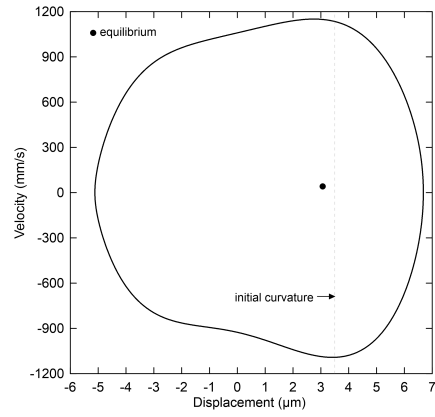
(a) $f_{ex} = 9$ kHz



(b) $f_{ex} = 12$ kHz



(c) $f_{ex} = 16.5$ kHz



(d) $f_{ex} = 30.5$ kHz

Figure 5.9: The phase-portraits around the stable equilibrium marked as (●) symbol at voltage waveform $V_{DC} = V_{AC} = 40$ V shows superharmonic resonance along the branch of small oscillations of: (a) order-four at $f_{ex} = 9$ kHz, (b) order-three at $f_{ex} = 12$ kHz and (c) order-two at $f_{ex} = 16.5$ kHz and (d) forced resonance with P-1 orbit at $f_{ex} = 30.5$ kHz.

Furthermore, the response increases as the signal frequency approaches the primary resonance and then it jumps up at $f_{ex} = 30.74$ kHz to a new branch of stable solutions through another cyclic-fold bifurcation marked CF_3 (●). This branch corresponds to a

first branch of a stable solution in the wider well, medium-sized oscillations, as shown in Figs. 5.8. At this bifurcation point, the stable branch meets another unstable branch of solutions and loses its stability where a Floquet multiplier exits the unit circle through +1.

Increasing the signal frequency after the jump up, results in deformations in the orbit shape indicated by variations in the beam mid-point displacement amplitude, Fig. 5.8(a), and its RMS velocity, Fig. 5.8(b), until it smoothly evolves into the branch of small oscillations beyond $f_{ex} = 30.74$ kHz and reduces the magnitude as it approaches P-1 orbits.

On the other hand, decreasing the signal frequency along the medium-sized branch, the response increases until it jumps up to a second branch of stable oscillation in the wider well, large oscillations, at $f_{ex} = 29.66$ kHz through a cyclic-fold bifurcation marked as CF₅ (●). At this point, the branch of stable solutions meets another unstable branch of solutions.

Keep increasing the frequency along the large branch of oscillations increases the mid-point displacement amplitude, Fig. 5.8(a) and its RMS velocity, Fig. 5.8(b), until it goes through a pull-in instability, marked as dynamic pull-in, and jumping down into contact with the sidewall electrode at a signal frequency of $f_{ex} = 34.47$ kHz where there are no stable equilibria beyond this point.

Decreasing the signal frequency along the same branch decreases the response which eventually jumps down at $f_{ex} = 24.25$ kHz to the small branch of oscillations through a cyclic-fold bifurcation marked CF₄ (●). At this point, the larger branch of oscillations meets the second unstable branch of oscillations. Further reduction in the signal frequency beyond CF₁ leads to increasing in the mid-point response until it meets the first unstable branch of solutions in a cyclic-fold bifurcation marked as CF₂ (●) at $f_{ex} = 13.45$ kHz.

A frequency band of 10.12 kHz was observed between CF₃ and the dynamic pull-in point. This band is wider than that obtained by LTI as clearly shown in Figs. 5.8(a)

and (b). We note that the primary resonance has hardening effect and superharmonic resonance has softening effect due to the interaction in the system's nonlinearities [51,62]. Finally, excellent agreement observed among the results obtained by LTI and the shooting method.

Part II: Experiment

We experimentally investigate the response of two classes of dubbed actuator I and actuator II. The actuators' as-designed dimensions are listed in Table 5.2. The actuation signal is supplied via a function generator and a voltage amplifier to the sidewall electrode while the curved micro-beam is grounded as shown in Fig. 5.10.

A negligible parasitic resistance R appears along the lines connecting the actuator to the voltage amplifier. A parasitic capacitance C appears across the substrate. A Laser Doppler Vibrometer (LDV) [151] is utilized to measure the in-plane motion of the beam mid-point while the actuator is tilted 70° [152] with respect to the horizon.

Table 5.2: Actuators as-designed dimensions in (μm).

	ℓ_b	h_b	h_o	b	d
Actuator I	1000	3	3.5	30	11.5
Actuator II	1000	3	3.6	30	11.5

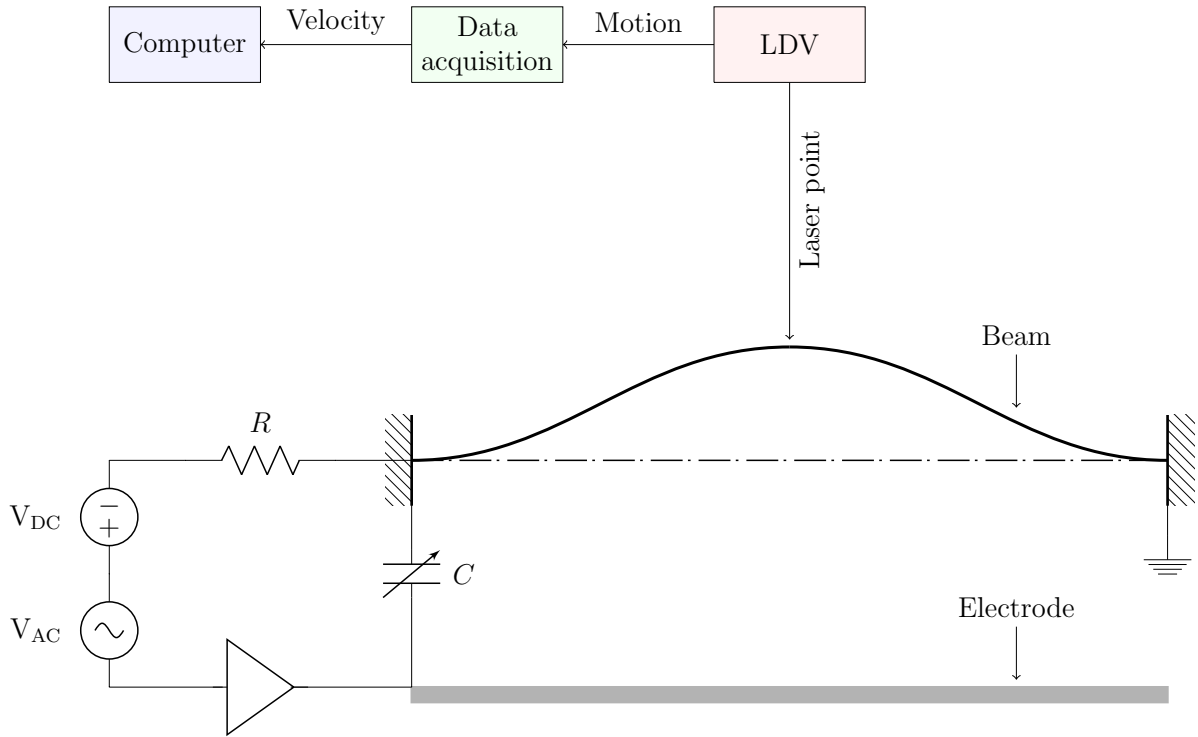


Figure 5.10: A schematic diagram of the experimental setup.

5.4 Actuator I

The natural frequencies of the actuator I were measured experimentally by applying a pulse train to the sidewall electrode with an amplitude of $V_{PI} = 18$ V, a signal frequency of $f_{ex} = 1$ kHz and a duty cycle of 0.8 %. The velocity of the mid-point \dot{w} was measured and the FFT of that signal was obtained to identify the dominant modes in the frequency domain, see Fig. 5.11(a). They were found to be the first in-plane bending mode, shown in Fig. 5.11(b), found at $f_{in} = 29$ kHz and the first out-of-plane bending mode, shown in Fig. 5.11(c), at $f_{out} = 226$ kHz. We also observed a second in-plane bending mode at 70 kHz.

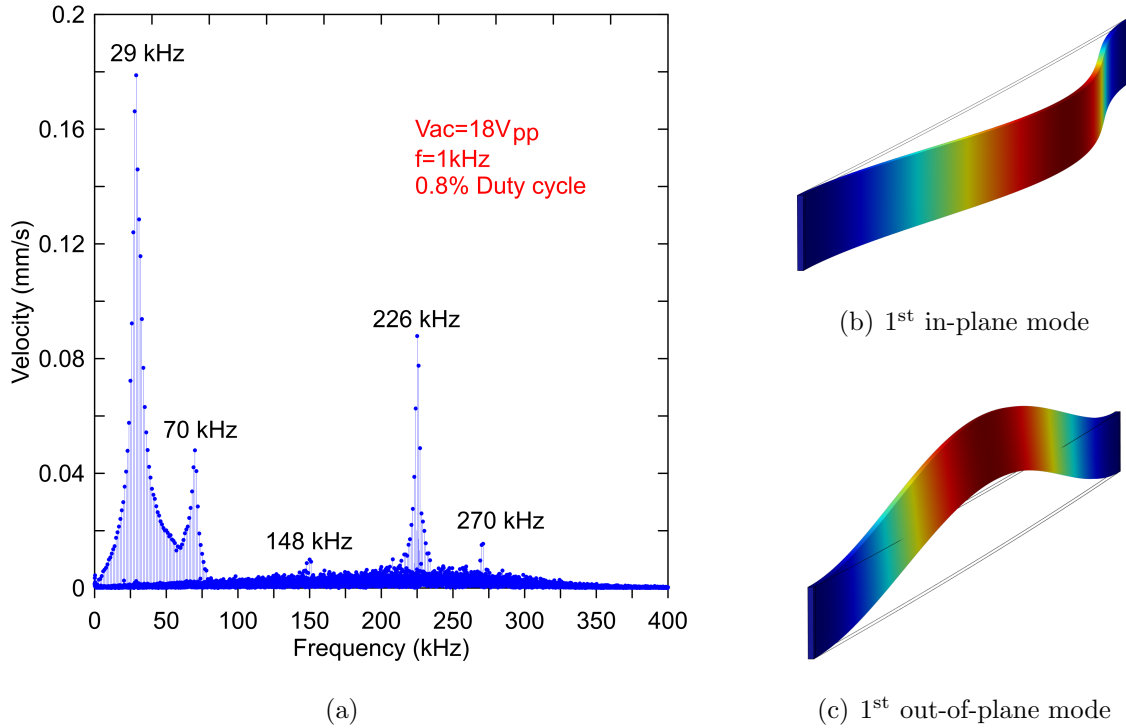


Figure 5.11: (a) FFT of the measured mid-point velocity \dot{w} for actuator I under the pulse train $V_{PI} = 18$ V, $f_{ex} = 1$ kHz and duty cycle 0.8 % showing its fundamental frequencies, (b) the first in-plane bending mode and (c) the first out-of-plane bending mode.

The fundamental natural frequency (f_{in}) was used to estimate the beam dimensions as-fabricated. This parameter identification technique [153] arrived at identical dimensions except for the structural layer thickness, the beam initial rise and electrostatic gap estimated as $h_b = 1.9$ μm , $h_o = 2.9$ μm and $d = 8$ μm , respectively. The differences between the designed and fabricated values are within the fabrication process uncertainty limits.

The identified dimensions were used to build a FEM of the actuator I using COMSOL software [150] and to obtain the mode shapes shown in Figs. 5.11 (b) and (c). A tetrahedral element was used to mesh the actuator with size varied in the range of 1080 μm . The sim-

ulated first in-plane and out-of-plane eigenvalues matched those measured experimentally.

5.4.1 Static Response

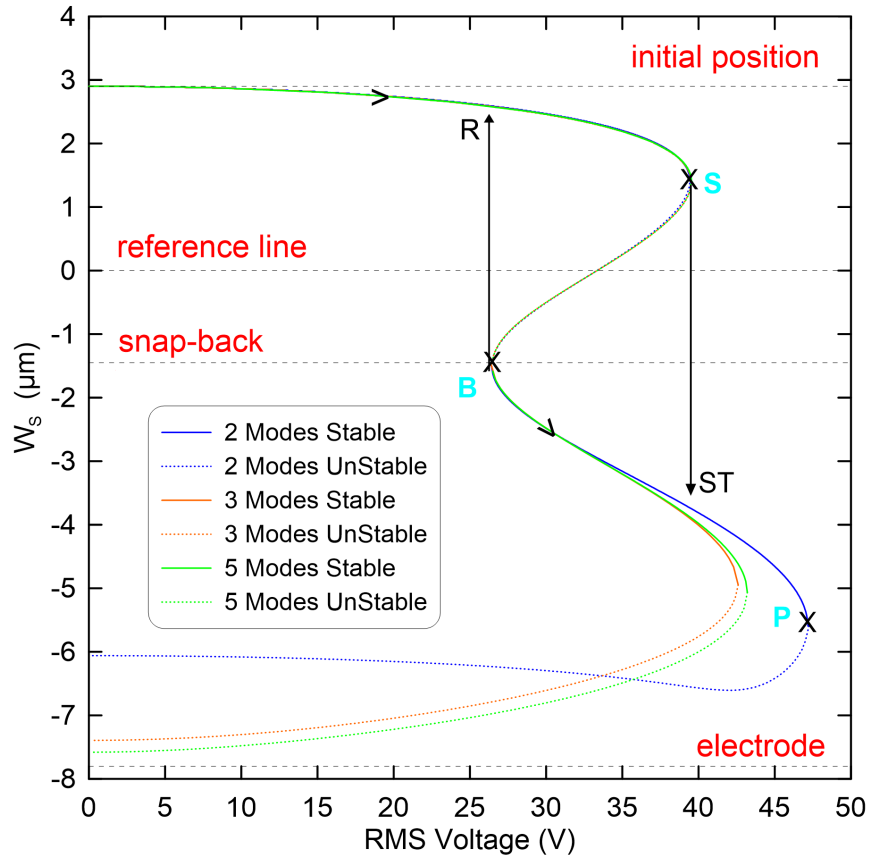


Figure 5.12: The beam mid-point deflection $w_s(0.5)$ of actuator I as a function of RMS voltage calculated from ROMs employing two, three and five symmetric modes. Stable equilibria are marked by solid lines and unstable equilibria are marked by dotted lines.

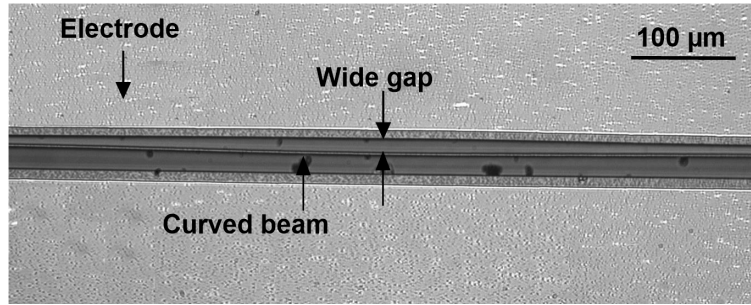
Using the identified dimensions and two-, three- and five-mode ROMs obtained from Eq. (4.77), we found the static equilibria of the micro-beam mid-point displacement $w_s(0.5)$

as a function of RMS voltage⁷. In all three cases, two branches of stable equilibria (marked by solid lines) and two branches of unstable equilibria (marked by dotted lines) are observed as shown in Fig. 5.12. The results show that at least three modes are required in the Galerkin expansion for model convergence. Therefore, we adopt a five-mode ROM in the rest of this work.

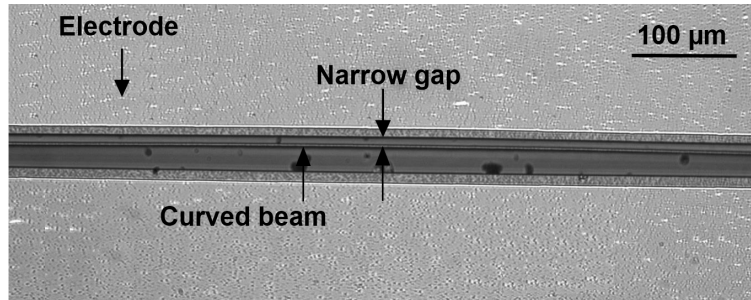
The results show that the beam approaches the straight position (marked as a reference line) with increasing RMS voltage and the mid-point rise decreasing along an upper branch of stable equilibria (corresponding to the initial curvature) until it meets a branch of unstable equilibria at a saddle-node bifurcation marked S ($V_S = 39.5$ V). This leads to a snap-through, where the beam jumps-down (along the line from S to ST) towards a lower branch of stable equilibria (corresponding to the initial counter-curvature). Increasing the voltage beyond that point, increases the mid-point counter rise along the lower stable branch until it reaches another saddle-node bifurcation marked P ($V_P = 43.2$ V) where it meets the another branch of unstable equilibria and goes through “pull-in” jumping-down into contact with sidewall electrode. Beyond this point, there are no stable equilibria.

On the other hand, decreasing the RMS voltage after snap-through reduces the mid-point counter-deflection along the lower stable branch until it meets the first unstable branch in a third saddle-node bifurcation marked B ($V_B = 26.45$ V). As a result, the beam snaps-back, jumping-up (along the line from B to R), towards the upper branch of stable equilibria (initial curvature). The two jumps demarcate a hysteresis region in the beam response. Figure 5.13 shows scanning electron microscopy (SEM) pictures for the curved beam configurations before (a) and after (b) the snap-through action.

⁷The electrostatic fringing field has been considered in this analysis using Eq. (4.41).



(a) Before snap-through



(b) After snap-through

Figure 5.13: SEM pictures showing the curved beam configurations: (a) before (initial curvature) and (b) after (counter initially curvature) the snap-through motion.

5.4.2 Dynamic Response

The dynamic response of the actuator I was measured experimentally under the voltage waveform $V_{DC} = V_{AC} = 18$ V. The RMS of this waveform is $V_{RMS} = 22.05$ V. It corresponds to a single stable equilibrium $w_s = 2.69$ μm near the initial beam curvature as shown in Fig. 5.12. To examine the resonant response of the first in-plane mode, the signal frequency was swept-up in a range of 5–45 kHz. Then, the time-histories of the mid-point velocity \dot{w} was measured using Laser-Doppler Vibrometer (LDV).

The frequency-response curve, Fig. 5.14, was constructed by evaluating the RMS veloc-

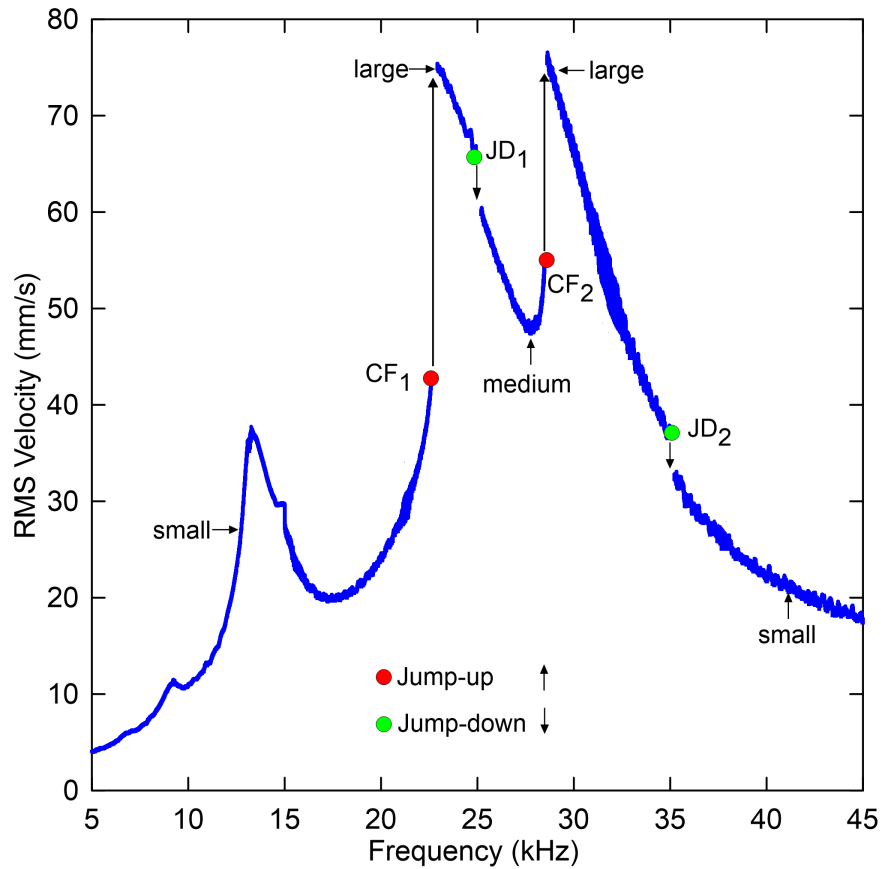


Figure 5.14: The measured frequency-response curve of the mid-point RMS velocity for $V_{DC} = V_{AC} = 18$ V shows three stable branches of oscillations: a branch of small orbits correspond to oscillations in a narrow-well and two branches of medium and large orbits corresponding to oscillations in a wider-well. The jump-up through cyclic-fold bifurcation is marked with (●) symbol and the jump-down is marked with (●) symbol.

ity over a window of 20,000 signal periods as a function of the signal frequency. It shows evidence of the superharmonic resonance of order two at $f_{ex} = 13.32$ kHz and the superharmonic resonance of order three at $f_{ex} = 9.17$ kHz. The response increases as the signal frequency approaches primary resonance until it jumps-up at $f_{ex} = 22.65$ kHz through a

cyclic-fold bifurcation, marked CF_1 (●), from a branch of small orbits, corresponding to oscillations in a narrow-well around the stable equilibrium, to a branch of large orbits, oscillations in a wider-well around the same equilibrium.

Beyond that point, the orbit size decreases as the signal frequency increases eventually jumping-down at $f_{ex} = 24.85$ kHz, through a bifurcation point marked JD_1 (●), from the large orbits branch to a branch of ‘medium’ orbits, also corresponding to oscillations in the wider-well. As the signal frequency further increases, the response undergoes a second jump-up through a cyclic-fold bifurcation at $f_{ex} = 28.42$ kHz, marked CF_2 (●), from the branch of medium orbits to the large orbits branch.

Beyond this point, the size of oscillations along the large orbits branch shrink as the signal frequency increases until it jumps-down at $f_{ex} = 34.9$ kHz through a bifurcation point, marked JD_2 (●), to the small orbits branch. The size of oscillations along the small orbits branch continues to decrease as the signal frequency further increases.

We note, therefore, that the double-peaks appearing in the vicinity of primary resonance are a result of the co-existence of three stable branches of orbits (solutions). The mechanisms underlying these branches are related to primary resonance oscillations of the beam around its stable equilibrium in a narrow-well, for the smaller branch, and a wider-well for the two larger branches, medium-sized and large. The response jumps-up from the narrow-well to the wider-well branches at CF_1 and jumps-down again to the narrow-well at JD_2 , Fig. 5.14.

To investigate those motions, we solved Eq. (4.86) by applying the shooting method [148] to generate the periodic orbits and to determine their stability by evaluating their Floquet multipliers. The simulated frequency-response curve of the beam mid-point RMS velocity, Fig. 5.15, is composed of three branches of stable solutions, marked by solid blue lines (—), and labeled as: small, medium and large and three unstable branches of

solution, marked by dashed red lines (- -). It is qualitatively similar to the experimental frequency-response curve although differences in peak magnitudes can be observed.

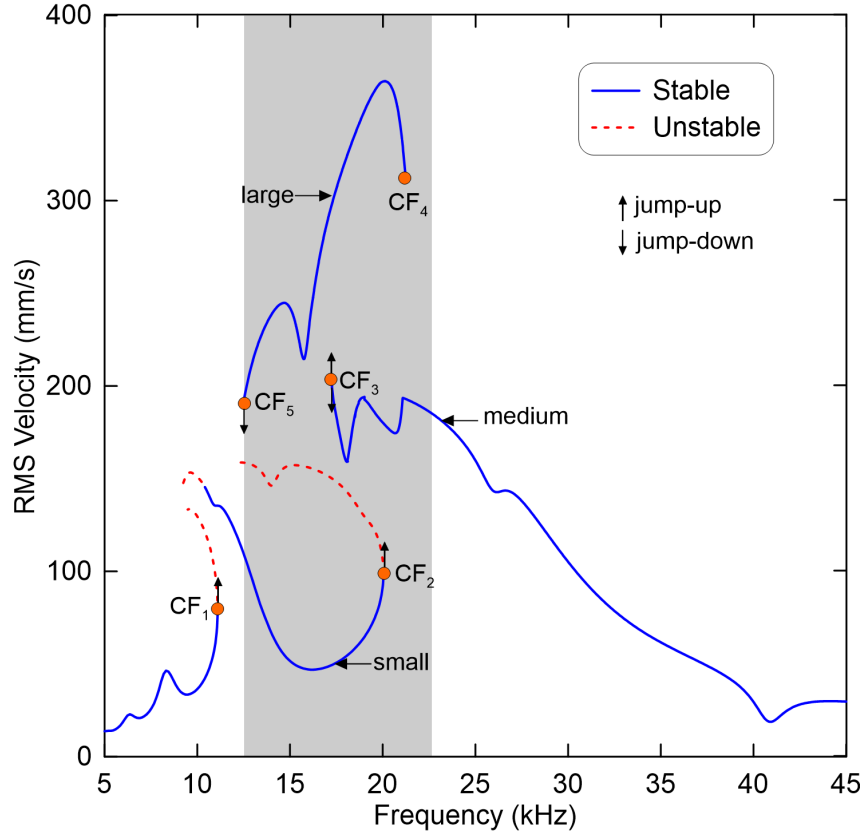


Figure 5.15: The simulated frequency-response curve of the mid-point RMS velocity of actuator I for $V_{DC} = V_{AC} = 18$ V shows three branches of stable oscillations marked solid blue lines (—). They are a branch of small orbits corresponding to oscillations in a narrow-well and two branches of medium-sized and large orbits corresponding to oscillations in a wider-well and three branches of unstable oscillations marked dashed red lines (- -).

Figure 5.15 also shows a train of superharmonic resonances with their peaks appearing at $f_{ex} = 6.25$ kHz for order four, $f_{ex} = 8.24$ kHz for order three and $f_{ex} = 10.9$ kHz for order

two. Increasing the signal frequency beyond the cyclic-fold bifurcation, marked by CF_1 (●), at $f_{ex} = 11.1$ kHz results in a sudden jump-up to an upper branch of stable solutions. At point CF_1 , a Floquet multiplier exits the unit circle through $+1$ as the smaller branch of stable solutions meets another branch of unstable solutions.

Decreasing the signal frequency along the upper branch of stable solutions, the orbits undergoes a series of period-doubling bifurcations and reverse period-doubling bifurcation before losing stability at $f_{ex} = 9.06$ kHz. The experimental frequency-response curve, Fig. 5.14, shows evidence of irregularity in the vicinity of the superharmonic resonance of order two at $f_{ex} = 13.09$ kHz and 15.01 kHz suggesting the presence of this complex behavior. However, this behavior is replicated in primary resonance at a larger scale and, therefore, will be studied in details there.

Figure 5.15 shows that the response magnitude increases as the signal frequency approaches primary resonance until it jumps-up at $f_{ex} = 20.07$ kHz through another cyclic-fold bifurcation, marked as CF_2 (●), from the branch of small to a branch of medium-sized, corresponds to the first branch of stable solutions in the wider-well.

The branch of small solutions disappears at CF_2 where it meets a branch of unstable solutions. Increasing the signal frequency after the jump-up, results in deformations in the orbit shape indicated by variations in the beam RMS velocity until it smoothly evolves into the branch of small orbits beyond $f_{ex} = 25.5$ kHz, Fig. 5.15.

On the other hand, decreasing the signal frequency after the jump-up results in a similar behavior until the response encounters a cyclic-fold bifurcation, marked CF_3 (●), at $f_{ex} = 17.26$ kHz. At that point, the response may jump-up to a branch of large oscillations, a second branch of stable solutions in the wider-well, or jumps-down to the branch of small oscillations in the narrow-well.

Increasing the signal frequency further along the large branch results in variation in

the RMS velocity as the orbit shape deforms until the beam goes into “pull-in” through a fourth cyclic-fold bifurcation, marked as CF₄ (●), at $f_{ex} = 21.25$ kHz. At that point, the beam jumps-down into contact with sidewall electrode and lost its stability. Decreasing the frequency along the same branch results in a similar behavior ending in jumps-down to the branch of small oscillations in the narrow well at $f_{ex} = 12.51$ kHz to the branch of small oscillations through a fifth cyclic fold bifurcation, marked as CF₅ (●).

Three branches of stable solutions co-exist in the shaded region of the frequency response curve shown in Fig. 5.15. They result in a complex dynamic behavior as discussed above. To elucidate this behavior, we constructed a bifurcation diagram in Fig. 5.16 for this frequency range of 12.56–23 kHz by stacking one-sided Poincaré section of the displacement w as the orbit crosses the velocity axis $\dot{w} = 0$ with a positive slope, on the side of the equilibrium point closer to sidewall electrode. It provides a detailed description of the dynamic response along each of the three stable branches of solution.

At the high-frequency end, a single period-one (P-1) orbit appears corresponding to the smooth transition region from the branch of small oscillations in the narrow-well to the branch of medium-sized oscillations in the wider-well marked as black line (—). The branch of medium-sized orbits encounters a bubble structure composed of a cascade of period-doubling bifurcations followed by a cascade of reverse period-doubling bifurcations as the signal frequency is swept-down. The first period-doubling bifurcation occurs at $f_{ex} = 21.1$ kHz where a Floquet multiplier exits the unit circle through -1. The second and third period-doubling bifurcations occur at $f_{ex} = 19.02$ kHz and $f_{ex} = 18.7$ kHz. Phase portraits of the resulting stable P-2, P-4 and P-8 orbits are shown Figs. 5.17(a)–(c).

The reverse period-doubling bifurcations occur at $f_{ex} = 18.46$ kHz, $f_{ex} = 18.32$ kHz and $f_{ex} = 18.08$ kHz, in the process reducing the P-8 orbits shown above to P-1 orbits for frequencies less than 18.08 kHz where the bubble structure is closed. Orbits along the

medium-sized branch shrink as frequency decreases further. The branch terminates in a cyclic-fold bifurcation, marked CF_3 (\bullet), resulting in a jump to the branch of large orbits, marked as a green line ($-$), or a jump to the branch of small orbits, Fig. 5.16.

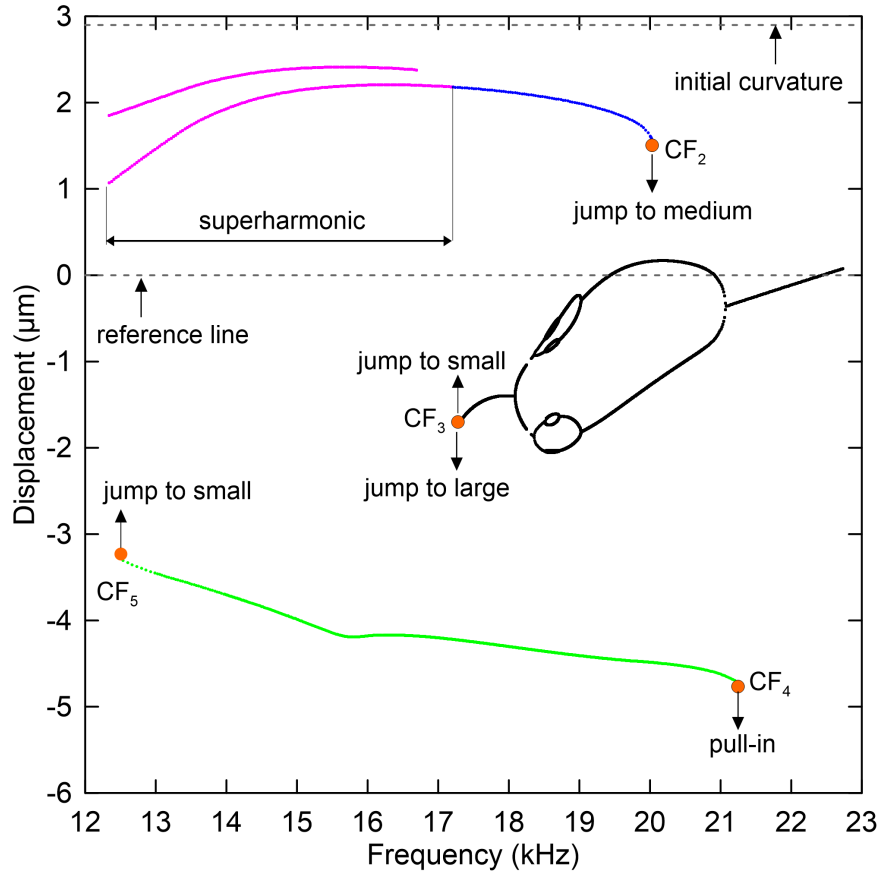


Figure 5.16: A bifurcation diagram of the shaded region in the frequency-response curve constructed by stacking one-sided Poincaré sections of the displacement w at positive slope crossings of the axis $\dot{w} = 0$ along: a small orbits branch, superharmonic orbits marked in magenta ($-$) and P-1 orbits marked in blue ($-$). A branch of medium-sized orbits is marked in black ($-$) and a branch of large orbits is marked in green ($-$).

The branch of small orbits is composed of a superharmonic resonant orbits marked as

a magenta line (—) and P-1 orbits marked in blue line (—). Comparing Figs. 5.15 and 5.16, we note that the bubble structure corresponds to the region between the two peaks in the frequency response curve while the peaks correspond to jumps from the branches of small and medium-sized orbits to the branch of large orbits.

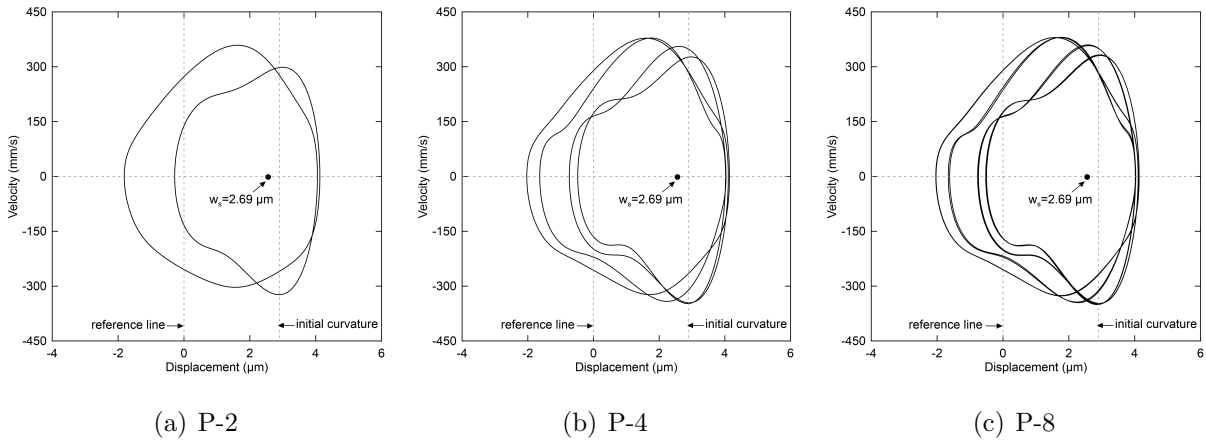


Figure 5.17: Phase portraits under the voltage waveform $V_{DC} = V_{AC} = 18$ V corresponding to a single stable equilibrium of $w_s = 2.69$ μm : (a) P-2 at $f_{ex} = 19.03$ kHz, (b) P-4 at $f_{ex} = 18.73$ kHz and (c) P-8 $f_{ex} = 18.53$ kHz.

To illustrate the relationships among the three branches of stable solutions and their potential wells, we show in Fig. 5.18 phase portraits of all three stable orbits at a signal frequency of $f_{ex} = 17.5$ kHz where the three branches co-exist. The large orbit (—) encompasses the small (—) and medium-sized (—) orbits. It can also be seen that the medium-sized and large orbits visit areas of phase-space far away from the equilibrium point w_s in contrast to the small orbit indicating that they oscillate in a much wider potential well than the small orbit.

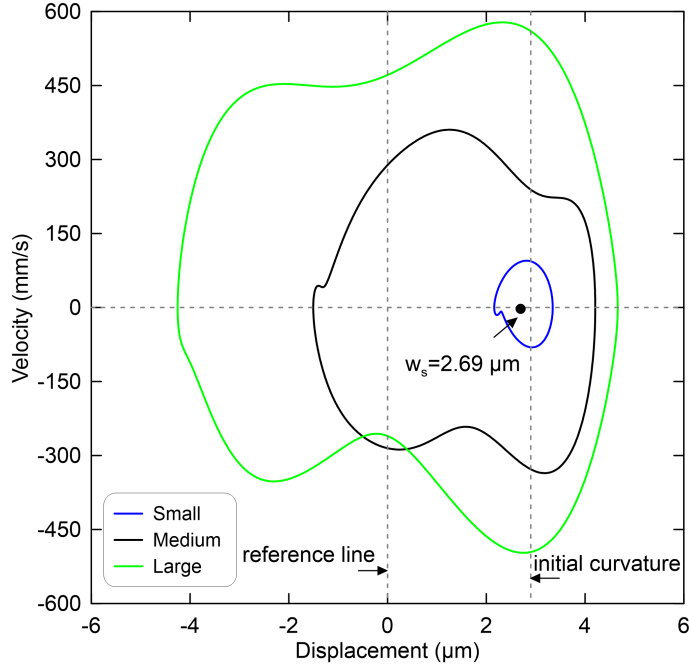


Figure 5.18: Phase portraits of three co-existing solution, small in blue (—), medium-sized in black (—) and large in green (—), under the voltage waveform $V_{DC} = V_{AC} = 18$ V, corresponding to a single stable equilibrium of $w_s = 2.69$ μm, and a signal frequency of $f_{ex} = 17.5$ kHz.

5.5 Actuator II

Actuators I and II are identical in dimensions except that the initial rise of II is $h_o = 3.6$ μm. Its natural frequencies were measured experimentally by applying a pulse train with an amplitude of $V_{PI} = 30$ V, a signal frequency of $f_{ex} = 1$ kHz and a duty cycle of 0.8 %. The mid-point velocity \dot{w} was measured and the FFT of that signal was obtained. The dominate peaks were found to be the first and second in-plane bending modes at $f_1 \approx 35$ kHz and $f_2 \approx 79$ kHz, respectively.

To investigate the motions of the first in-plane bending mode, the beam was excited with the signal waveform $V_{DC} = 30$ V and $V_{AC} = 7.5$ V resulting in a single stable equilibrium at $w_s = 3.29$ μm . The FFT of the measured mid-point velocity was reported in the linear scale (mm/s) at four discrete signal frequencies. The superharmonic resonance of order-two was observed at a signal frequency of $f_{ex} = 13$ kHz, Fig. 5.19(a), with the resonant (dominant) peak appearing at $2f$. Increasing the signal frequency to $f_{ex} = 18$ kHz showed a forced response with the dominant peak at f and smaller peaks at its integer multiples of $2f$ and $3f$ as shown in Fig. 5.19(b). These responses correspond to the branch of smaller oscillations in the narrow-well.

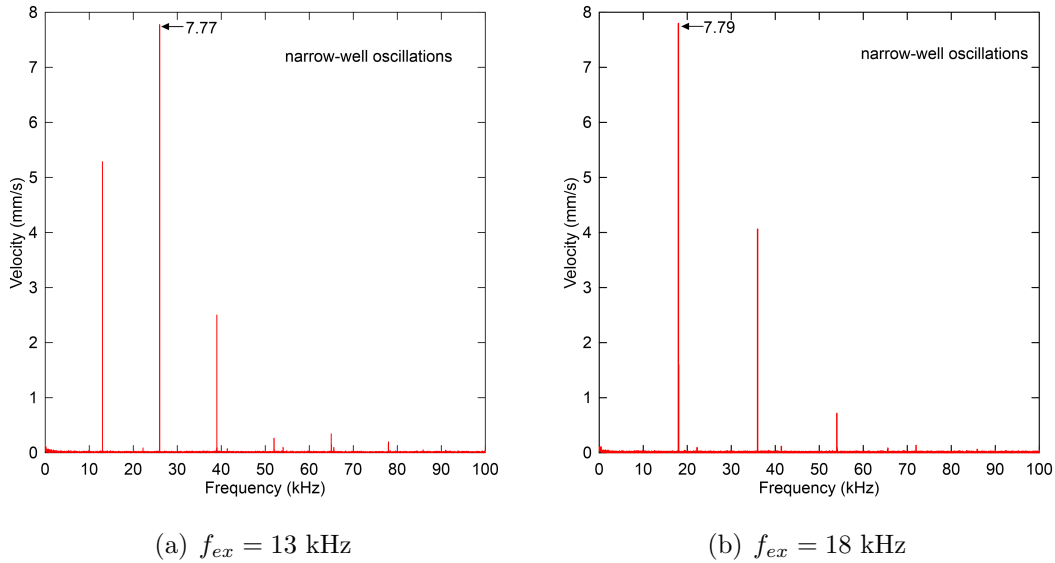


Figure 5.19: FFTs of the measured mid-point velocity (\dot{w}) for actuator II under the voltage waveform $V_{DC} = 30$ V and $V_{AC} = 7.5$ V at four discrete signal frequencies: (a) superharmonic response at $f_{ex} = 13$ kHz and (b) forced response at $f_{ex} = 18$ kHz.

Increasing the signal frequency to $f_{ex} = 26$ kHz sees a large increase in mid-point velocity, Fig. 5.20(a), corresponding to the branch of large oscillations in the wider well

underlying the first peak in Fig. 5.14. Beyond that frequency, the response jumps-down to the branch of medium-sized oscillations as detailed below. The response jumps-up again to the large branch as observed at the signal frequency of $f_{ex} = 28.5$ kHz as shown in Fig. 5.20(b). This corresponds to the second peak in Fig. 5.14.

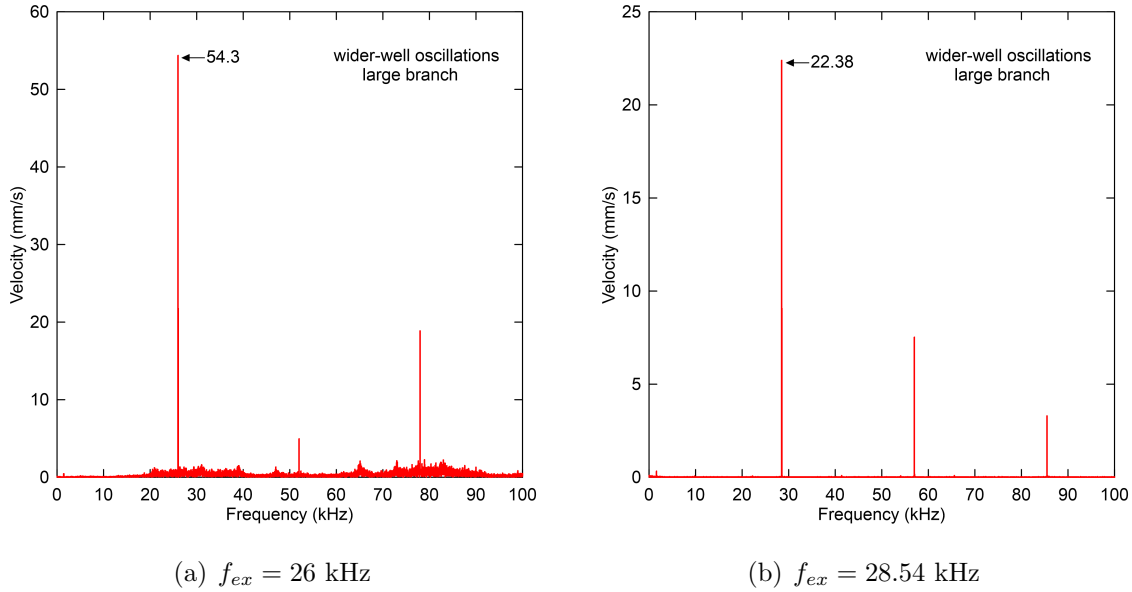


Figure 5.20: FFTs of the measured mid-point velocity (\dot{w}) for actuator II under the voltage waveform $V_{DC} = 30$ V and $V_{AC} = 7.5$ V at four discrete signal frequencies: (a) resonant response at $f_{ex} = 26$ kHz and (b) resonant response at $f_{ex} = 28.5$ kHz.

A detailed examination of oscillations along the medium-sized branch is presented in Figs. 5.21 and 5.22. FFTs of the mid-point velocity at six discrete signal frequencies are reported in linear (mm/s) and dB scale ($0\text{dB} = 1$ m/s) to better capture smaller features. Under the larger forcing level applied to actuator II, a chaotic attractor develops within the bubble structure. FFTs of the actuator response within the attractor are shown in Figs. 5.21(a) linear and (b) dB scales at a signal frequency of $f_{ex} = 26.75$ kHz. The figures demonstrate evidence of chaos with a wide-based spectrum and an elevated noise-floor.

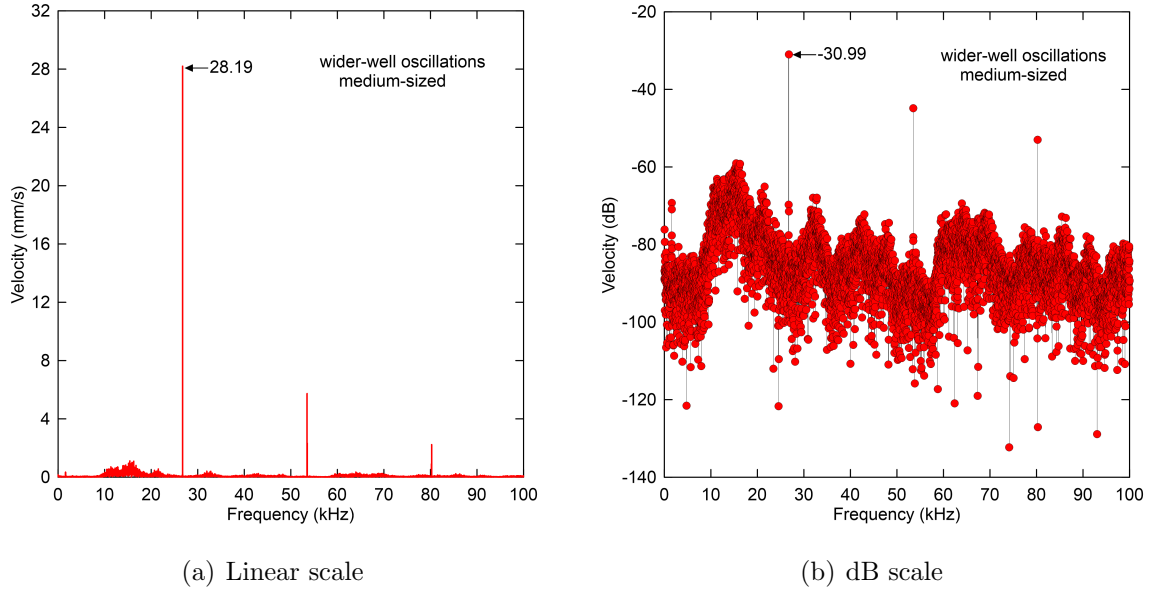


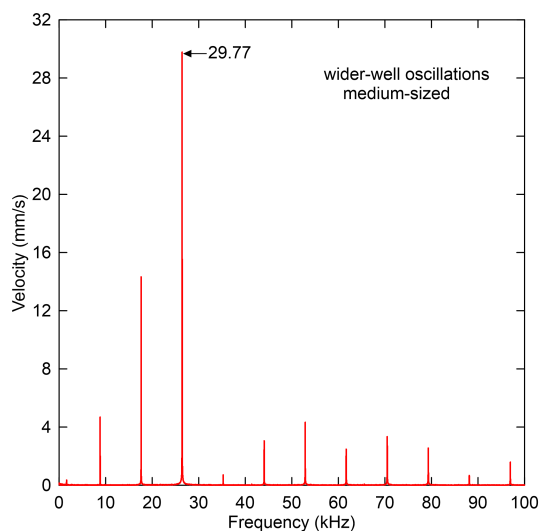
Figure 5.21: FFTs of the measured mid-point velocity (\dot{w}) for actuator II under the signal waveform $V_{DC} = 30$ V and $V_{AC} = 7.5$ V and signal frequency of $f_{ex} = 26.75$ kHz show evidence of a chaotic attractor in: (a) linear scale and (b) dB scale.

Odd-periodic windows appear also within the attractor including period-three (P-3), period-five (P-5) and period-six (P-6) windows observed at the signal frequencies $f_{ex} = 26.44$ kHz, $f_{ex} = 26.83$ kHz and $f_{ex} = 27.19$ kHz and shown in Figs. 5.22(a)–(f), respectively. We note that the response amplitude along this branch is significantly lower than that observed on the larger branch at $f_{ex} = 26$ kHz, Fig. 5.20(a).

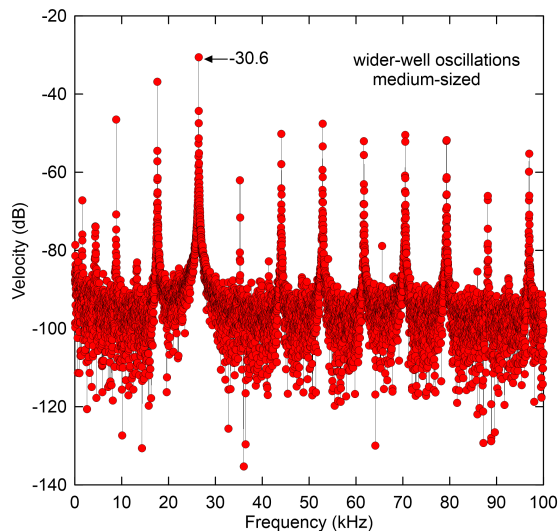
Increasing the signal frequency along the medium-sized branch, the chaotic attractor terminates in a cascade of reverse period-doubling bifurcations as the orbit size shrinks. A period-four (P-4) orbit appears at $f_{ex} = 27.27$ kHz, Fig. 5.22(g) linear and (h) dB scales, and period-two (P-2) appears at $f_{ex} = 27.38$ kHz, Fig. 5.22(i) linear and (j) dB scales.

At the upper end of this branch, the response undergoes a second jump-up through a

cyclic-fold bifurcation to the large branch of oscillations with a period-one (P-1) orbit as shown in Fig. 5.20(b).

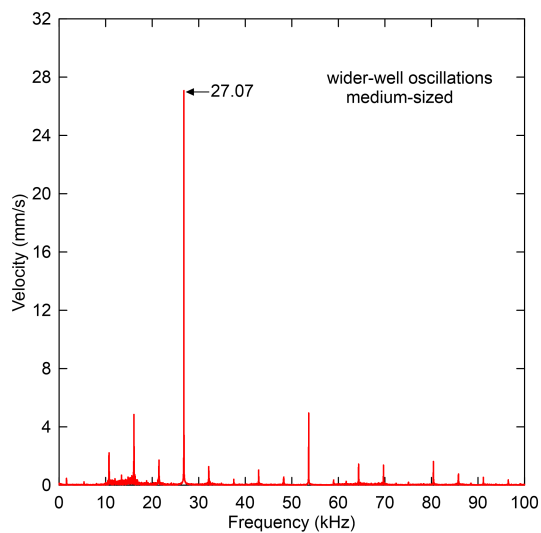


(a) Linear scale

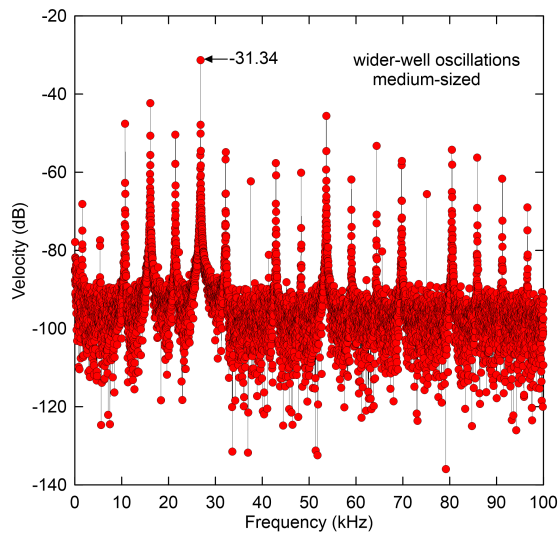


(b) dB scale

P-3 at $f_{ex} = 26.44$ kHz

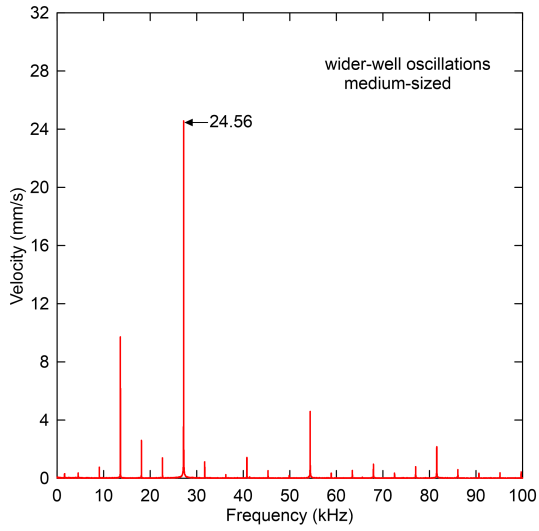


(c) Linear scale

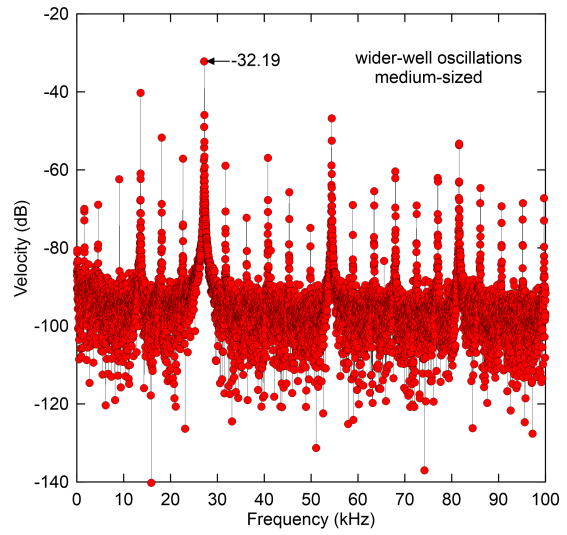


(d) dB scale

P-5 at $f_{ex} = 26.83$ kHz

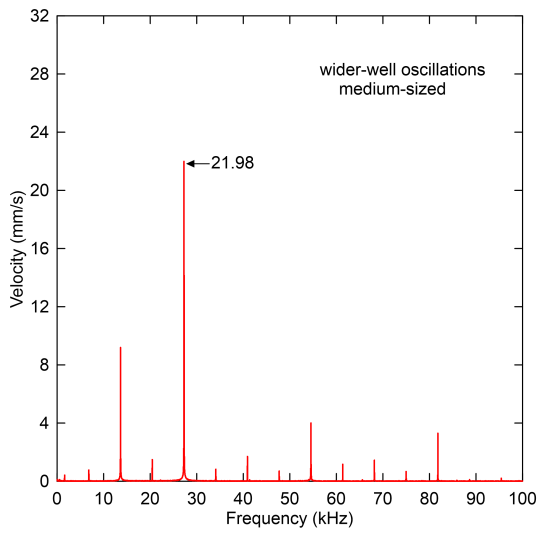


(e) Linear scale

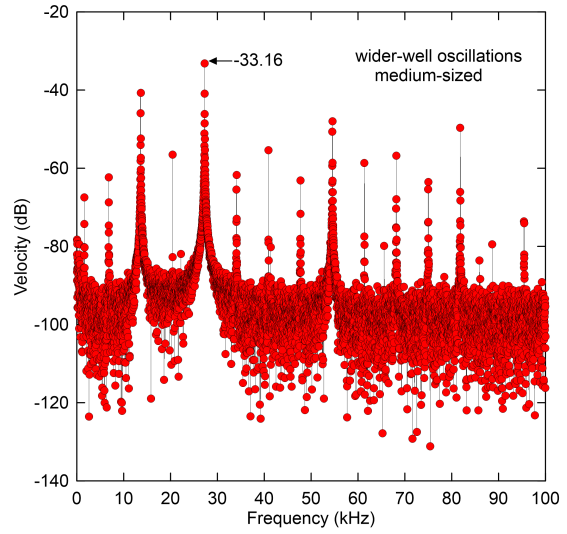


(f) dB scale

P-6 at $f_{ex} = 27.19$ kHz

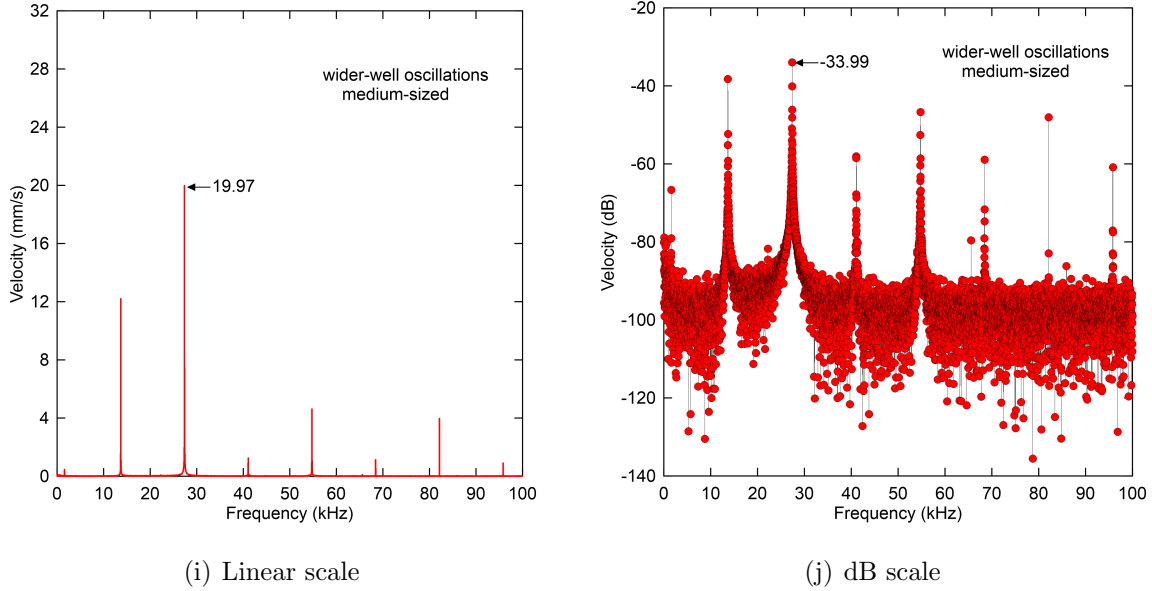


(g) Linear scale



(h) dB scale

P-4 at $f_{ex} = 27.27$ kHz



P-2 at $f_{ex} = 27.38$ kHz

Figure 5.22: FFTs of the measured mid-point velocity (\dot{w}) in dB scale for actuator II under the signal waveform $V_{DC} = 30$ V and $V_{AC} = 7.5$ V shows evidence of a chaotic attractor with odd windows: a period-three (P-3) orbit at $f_{ex} = 26.44$ kHz (a) linear and (b) dB scales, a period-five (P-5) orbit at $f_{ex} = 26.83$ kHz (c) linear and (d) dB scales and a period-six (P-6) orbit at $f_{ex} = 27.19$ kHz (e) linear and (f) dB scales. Evidence of a cascade of reverse period-doubling bifurcations is also shown with (g) linear and (h) dB scales a period-four (P-4) orbit at $f_{ex} = 27.27$ kHz and a period-two (P-2) orbit at $f_{ex} = 27.38$ kHz (i) linear and (j) dB scales.

5.6 Summary

This chapter investigated the static and dynamic responses of the electrostatically excited initially curved micro-beam which it serves as a platform for the micro-tweezers' arms. We carried out a convergence analysis to determine the required number of mode in the

Galerkin expansion. We found that at least three symmetric modes are required for the model convergence. Evidence of multiple stable solutions around only one stable equilibrium was observed analytically and experimentally. The transition between these branches leads to a complex behavior. A cascade of period-doubling bifurcations and a cascade of reverse period-doubling bifurcations along the medium-sized branch were observed in addition to chaotic attractor developed within that structure.

Chapter 6

Characterizations of Micro-Tweezers

This chapter provides criteria for the design of electrostatic arch micro-tweezers. It can be operated in two modes: a traditional quasi-static mode and a dynamic mode. To satisfy this criteria, we carry out a detailed static analysis and modal response of the micro-tweezers to establish their operational modes using a finite-element model (FEM) and a Reduced-Order model (ROM). Finally, we study the adequacy of standard ROM based on straight beam mode shapes as basis functions in representing the tweezers response.

6.1 Static Operational Mode

6.1.1 Platform Deflection

We consider the prototype I, Fig. 3.1, with the dimensions listed in section 3.1.2. The change in its mid-point deflection as a function of the RMS voltage was evaluated using Eq. (4.76). In this analysis, the arms are modeled as rigid bodies in the ROM.

Figure 6.1 shows two branches of stable equilibria marked as solid lines (—) and two branches of unstable equilibria marked as dashed lines (- -) obtained by solving a five-mode ROM approximation and taking into account the effect of the electrostatic fringing field modeled by Kimbali [146]. The results are then compared to those obtained by the FEM with flexible arms marked as (◆) symbol and without flexible arms marked as (●) symbol. Note that only stable branches of the solutions are reported from the FEM models.

The figure also shows that the mid-point deflection $w_s(0.5)$ decreases as the RMS voltage increases along the first branch of stable equilibria and corresponding to the beam initial curvature until it jumps down, along the line from S to ST, towards the second branch of stable equilibria and corresponding to the initial counter-curvature. This jump down corresponds to the snap-through. We note that at the jumping point, the stable branch of solutions meets the first branch of unstable solutions in a saddle-node bifurcation marked as point S ($V_S = 100.53$ V).

Increasing the voltage beyond the snap-through V_S increases the counter deflection of the mid-point along the second stable branch of solutions until it loses its stability at point P ($V_P = 136.35$ V) by going down into contact with the sidewall electrode through another bifurcation point demarcating the pull-in instability. At that point, the second stable branch of solutions meets the second unstable branch of solutions. We note that there are no physical stable equilibria beyond that point.

Decreasing the RMS voltage after point S decreases the counter deflection of the mid-point along the second stable branch of solutions until it jumps along the line from B to R towards the first stable branch of solutions, corresponds to the initial curvature. We note that the second stable branch of solutions meets the first unstable branch of solutions in a third saddle-node bifurcation marked as point B ($V_B = 89.01$ V).

The FEM model was then used to examine the arms contribution on the static response

of the tweezers' platform (curved beam). Toward this, a 3D FEM model similar to that described in section 5.1 was built and then converted to a 2D model. A total of 50,359 tetrahedral elements were used to mesh the micro-tweezers. Their sizes varied in the range of 10–80 μm .

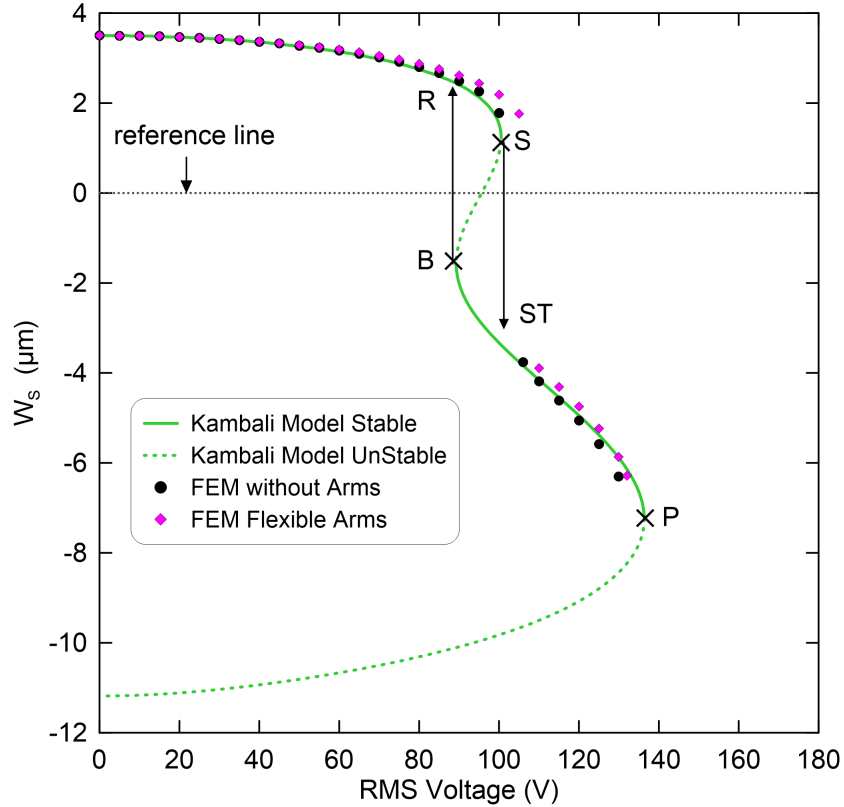


Figure 6.1: Variation in the beam mid-point deflection $w_s(0.5)$ as a function of the RMS voltage obtained using: a five-mode ROM accounting for the electrostatic fringing field. The branches of stable solutions are marked as solid green lines (—) and the branches of unstable solutions are marked as dashed green lines (- -). The FEM without arms are marked as (●) symbol and with flexible arms are marked as (◆) symbol.

The tweezers were grounded, Fig. 3.3, while the sidewall electrode voltage was set

initially to $V_{\text{RMS}} = 0$ V and increased gradually over the range of 0–150 V. It is a required step to capture the locations of the snap-through and the pull-in voltages and to compare their values to those without arms obtained using the five-mode ROM and the FEM.

Figure 6.1 shows that the ROM compares well with the FEM along the two stable branches, marked as (●) symbol, in the absence arms. However, introducing the flexible arms, marked as (◆) symbol, increases the voltage requirement for the snap-through from 100.53 V to 105.18 V and reduces the voltage requirement for the pull-in from 136.35 V to 132.24 V. Indeed, the results are qualitatively similar with the arms although differences along the second branch of stable equilibria can be observed.

Table 6.1 compares the snap-through and the pull-in voltages obtained using the five-mode ROM and the FEM with and without the arms. It shows that the results are within an acceptable range of agreement. We also found that the static response of the curved micro-beam did not change significantly with the arms. Therefore, an Euler-Bernoulli beam model of the curved beam alone is adequate to predict and analyze the tweezers' static operating mode.

Table 6.1: Comparison of snap-through and pull-in voltages obtained using the ROM and the 2D FEM.

Model	V_S (V)	V_B (V)	V_P (V)
ROM	100.53	88.8	136.35
FEM without arms	99.84	–	130.5
FEM with arms	105.18	–	132.24

6.1.2 Grip Range

For pick-and-place tasks, the micro-tweezers is operated in a static mode by applying a quasi-static voltage waveform to the sidewall electrode in order to change the arm tips separation following a desired trajectory to approach, hold, and release micro-objects as desired. Provided that the changes in voltage magnitude occur over much longer times than the fundamental period, the response will remain close to that predicted by the static analysis.

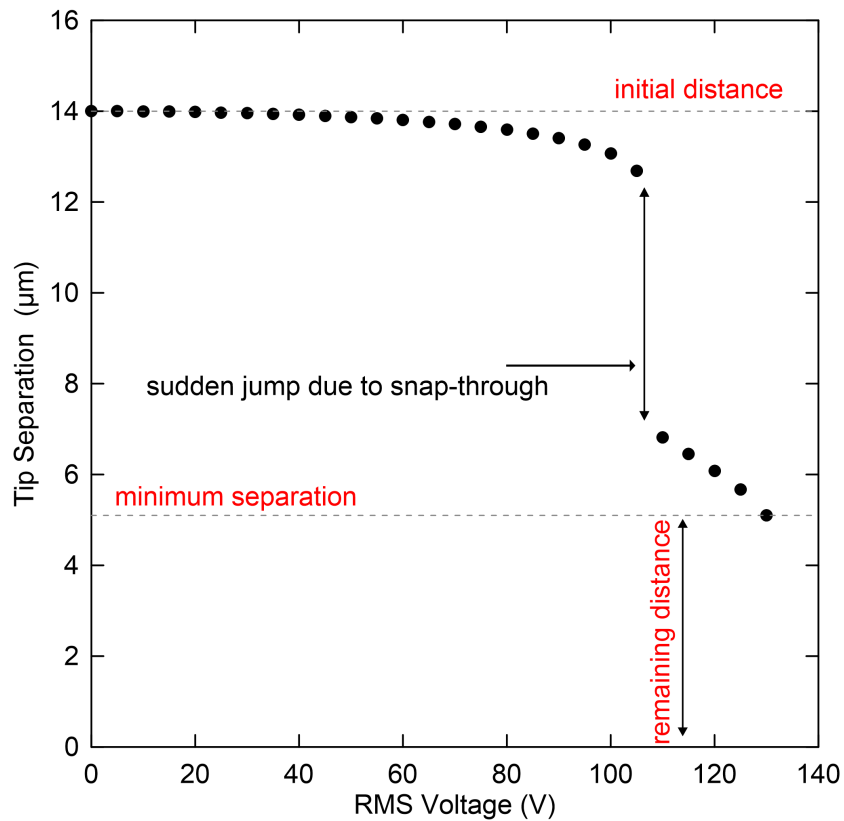


Figure 6.2: The tips separation as a function of RMS voltage calculated using the 2D FEM.

We found that for an applied voltage $V(t)$ less than the snap-through voltage V_S , the

gap between the beam mid-point and the sidewall electrode decreases along a first branch of stable equilibria, close to the initial curvature shown in Fig. 3.2(a). This allows the tweezers arms to slowly approach each other and, therefore, hold and manipulate coarse micro-objects with diameters in a range of 12.5–14 μm as shown in Fig. 6.2.

Increasing the voltage beyond V_S leads to a jump down to a second branch of stable equilibria in the vicinity of the initial counter-curvature shown in Fig. 3.2(b). This results in a further reduction in the separation gap between the arm tips allowing the tweezers to smoothly grasp, manipulate and release fine micro-objects with diameters in the range of 5–7.5 μm .

On the other hand, the pull-in instability occurs at a higher voltage not captured by the large voltage step in this FEM simulation. The arms configuration along the first stable branch and the second stable branch of solutions are clearly shown in Figs. 6.3(a) at $V_{\text{RMS}} = 95 \text{ V}$ and (b) at $V_{\text{RMS}} = 130 \text{ V}$, respectively.

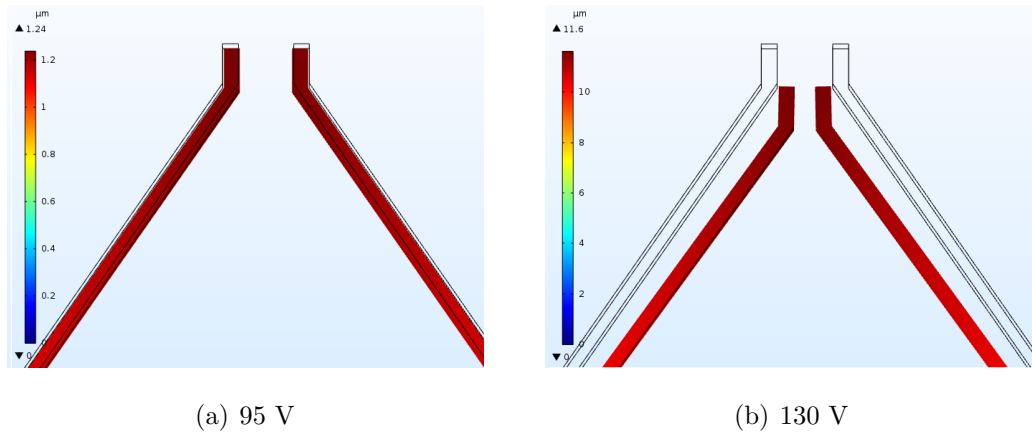


Figure 6.3: A snapshot of the arms configuration (a) before at $V_{\text{RMS}} = 95 \text{ V}$ and (b) after at $V_{\text{RMS}} = 130 \text{ V}$ the snap-through.

6.1.3 Dynamic Mode of Operation

In this section, we investigate the adequacy of this modeling paradigm, five-mode ROM, in the study of the proposed dynamic operating mode. First, we investigate the impact of dynamic operation on the tweezers functionality. In this case, the tweezers is operated by applying a harmonic excitation with a frequency in the vicinity of one of the tweezers' resonances.

This may have an impact on maintaining the arms rigidity, a necessary condition for the tweezers functionality, since some modes may involve arms flexibility. The operating space 'operational map' of the tweezers should, therefore, include only those resonances that do not excite modes involving arms flexibility. Furthermore, the actuated modes should command arms motions that are in-phase allowing the arms to close on and to release the object in tandem.

Towards that end, we carried out a modal analysis of the micro-tweezers using a 2D FEM while varying the arms length ℓ_a over the range of 0–250 μm . We obtained the first five symmetric (SY) and asymmetric (ASY) mode shapes $\phi_i(x)$ and eigenvalues 'natural frequencies' f_i throughout that range. Figure 6.4 shows that the natural frequencies of the tweezers first symmetric, dotted black line (...), and asymmetric, dotted magenta line (...), modes decrease smoothly as the arms length increases dropping from $f_1 = 38.48$ kHz to 23.68 kHz and from $f_2 = 63.25$ kHz to 46.76 kHz, respectively.

At the limit of arms length $\ell_a = 250$ μm , the arms maintains their rigidity as they move in-phase towards each other and while the mounting platform deforms for both the first symmetric, Fig. 6.5(a), and the first asymmetric, Fig. 6.5(b), modes. This shows that tweezers with arms length throughout this examined range can use either of these modes for the dynamic operation to tap and characterize micro-objects or to lyse cells.

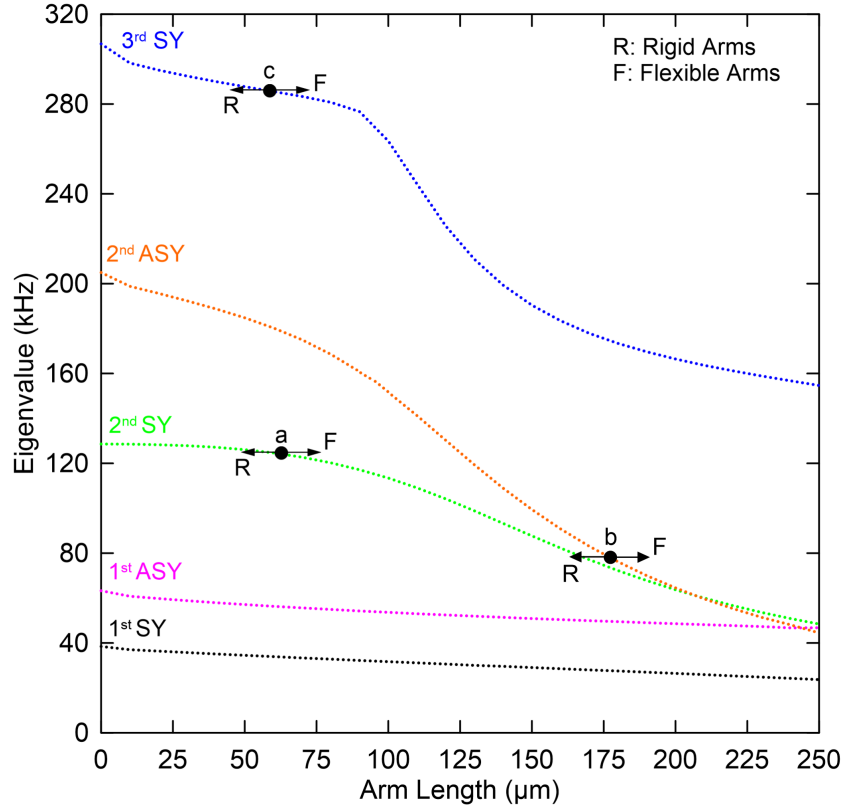


Figure 6.4: Variation of the first five natural frequencies, 1st SY mode (black), 1st ASY mode (magenta), 2nd SY mode (green), 2nd ASY mode (orange) and 3rd SY mode (blue), of the arch micro-tweezers as the arms length varies from 0 to 250 μm obtained using a 2D FEM.

The natural frequencies of the second and third symmetric modes remain almost constant up to an arms length of $\ell_a \approx 70 \mu\text{m}$ and $\ell_a \approx 65 \mu\text{m}$ at the points marked a and c along the dotted green (...) and blue (...) lines in Fig. 6.4, respectively. We found that the arms behave as rigid bodies throughout this initial range. However, their flexibility becomes significant and the natural frequencies drop faster beyond that range.

Furthermore, the compliance of the beam sub-span between the two arms ‘middle sub-

span' is reduced as their length increase culminating in two interior nodes merging and resulting in each mode resembling the symmetric mode below it at $\ell_a = 250 \mu\text{m}$ as shown in Figs. 6.5(c) and (e). We note that those modes are not suitable for dynamic operation in this range because of the arms' flexibility.

We also found that the natural frequency of the second asymmetric mode, dotted orange line (...) in Fig. 6.4, drops continuously as the arms length increases. Along this line, the arms are rigid up to an arm lengths of $\ell_a \approx 180 \mu\text{m}$, marked as point b. Beyond that length, they become flexible. The arms motions associated with this mode, Fig. 6.5(d), are out-of-phase precluding its use in the dynamic operation.

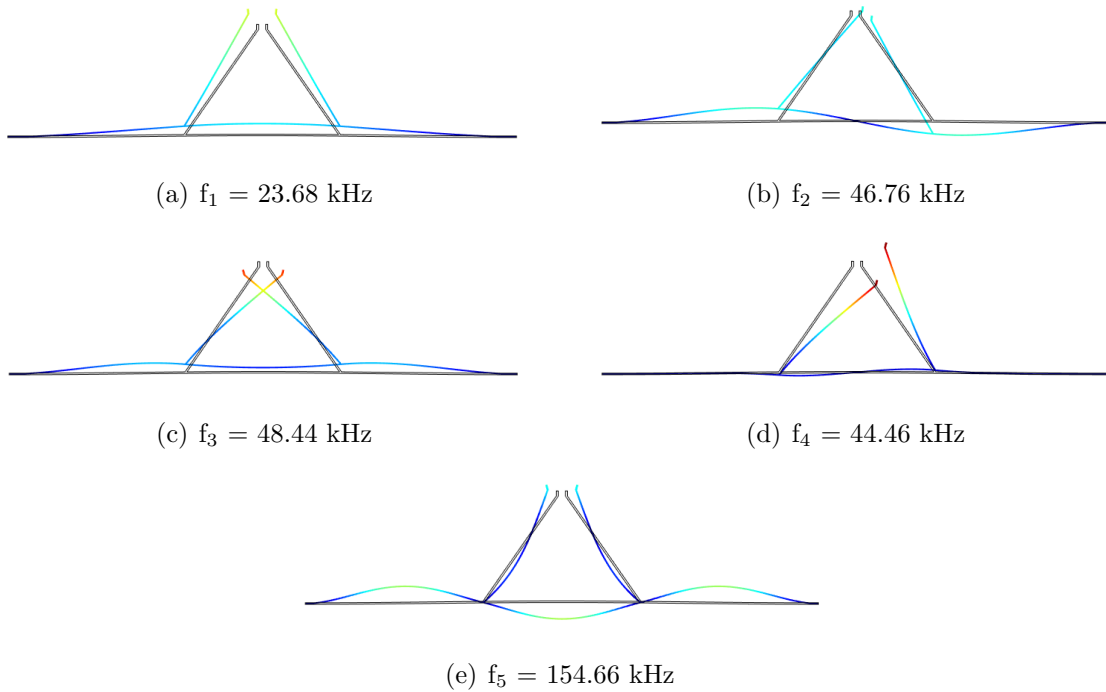


Figure 6.5: (a) The first SY, (b) the first ASY, (c) the second SY, (d) the second ASY and (e) the third SY mode shapes of the arch micro-tweezers with arms length of $\ell_a = 250 \mu\text{m}$.

Finally, we found that the arms divide the beam span into a middle sub-span brackets

by them and two outer sub-spans on either side of them. It results in crossover phenomena among the mode shapes adding another limitation to the operating range due to the possibility of complex one-to-one modal interactions among those modes [142].

Two crossovers were observed in the arms length range under study as shown in Fig. 6.6. The first occurs between the second symmetric and asymmetric modes at $l_a \approx 200 \mu\text{m}$. The second crossover occurs between the first and second asymmetric modes at $l_a \approx 240 \mu\text{m}$.

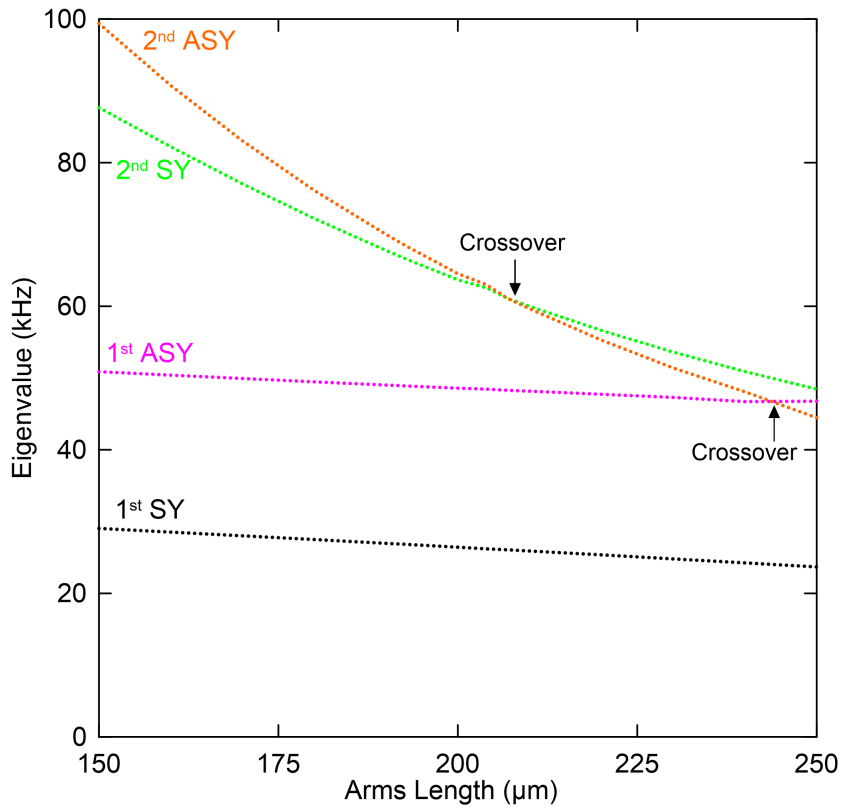


Figure 6.6: A close-up view showing the crossover points between the 1st ASY, 2nd SY and 2nd ASY modes.

6.1.4 ROM Validation

Second, we examine the adequacy of ROMs to represent the tweezers response by comparing the results of modal analysis carried out using the FEM described above to that obtained using a ROM based on the first five mode shapes of a straight beam. The tweezers arms are assumed rigid in the ROM and represented by concentrated masses and mass moments of inertia as described in chapter 4.

Table 6.2 compares the natural frequencies of the first five modes obtained from the two models for the mounting platform only ‘curved micro-beam’ and a micro-tweezers with arms length of $\ell_a = 250 \mu\text{m}$. The models are in excellent agreement in the first case but the ROM fails to capture any of the micro-tweezers' natural frequencies beyond the fundamental frequency (f_1). While these results indicate that the five-mode ROM is adequate for micro-beams, they put its adequacy to represent micro-tweezers' response in question.

Table 6.2: Comparison of the first five natural frequencies (in kHz) of the micro-tweezers at two arms lengths obtained from a ROM with rigid arms and an FEM with flexible arms.

		$\ell_a = 0 \mu\text{m}$				
Model	f_1	f_2	f_3	f_4	f_5	
ROM	38.48	63.25	128.65	204.96	306.72	
FEM	38.48	63.25	128.61	204.95	306.76	
		$\ell_a = 250 \mu\text{m}$				
ROM	23.21	30.44	96.38	109.49	129.55	
FEM	23.68	46.76	48.44	44.47	154.66	

To investigate the origins of the ROM shortcomings, we obtained the natural frequencies

of the tweezers' first five modes as the arms length varied from 0 to 250 μm using the five-mode ROM and compared them to those obtained from the FEM in subsection 6.1.3. The ROM results are shown as solid lines while the FEM results are shown as dotted lines in Fig. 6.7.

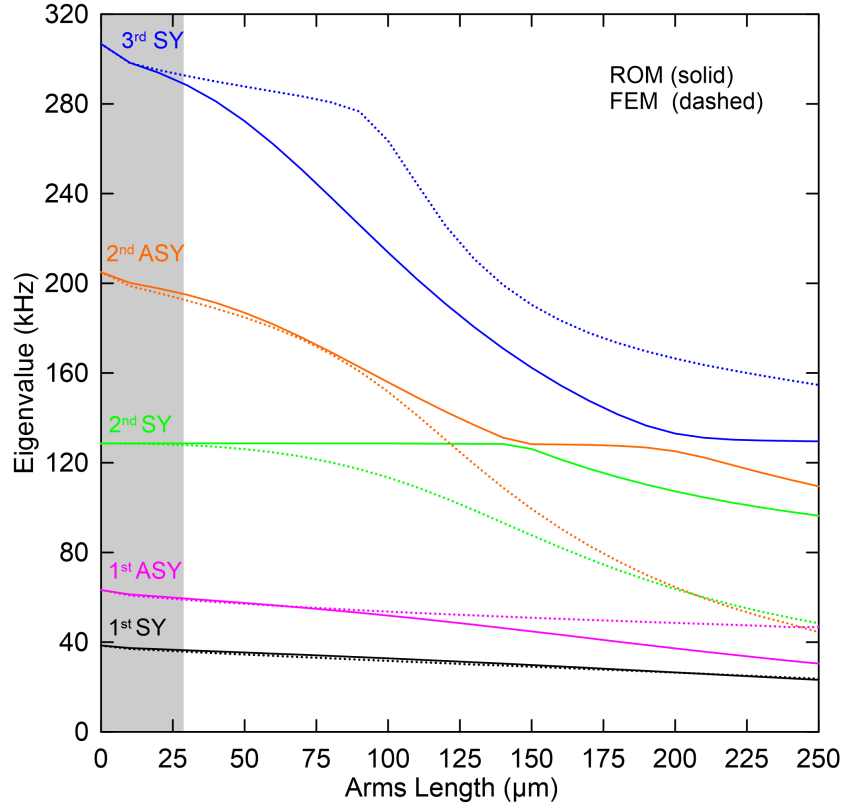


Figure 6.7: Variation of the first five natural frequencies, 1st SY mode (black), 1st ASY mode (magenta), 2nd SY mode (green), 2nd ASY mode (orange) and 3rd SY mode (blue), of the arch micro-tweezers as the arms length varies from 0 to 250 μm obtained using a five-mode ROM (solid lines) and a 2D FEM (dotted lines).

Excellent agreement is observed between the two models for shorter arms length $\ell_a \leq 27 \mu\text{m}$, the gray shaded region in the figure, as well as for the first symmetric mode

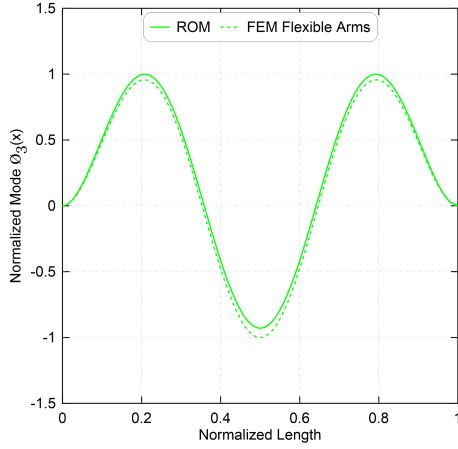
throughout the arms length range under study. As a result, the five-mode ROM is an adequate representation of micro-tweezers in these cases. While the agreement between natural frequencies obtained from the two models is excellent for the first and second asymmetric modes for arms length up to $\ell_a \approx 100 \mu\text{m}$, it is limited only to arms length up to $\ell_a = 27 \mu\text{m}$ for the second and third symmetric modes, Fig. 6.7.

Further increase in arms length results in higher kinetic and potential ‘flexibility’ energies along them where the ROMs fail to predict the natural frequencies beyond the first symmetric mode. Therefore, the five-mode ROM is inadequate to represent the response of tweezers with $\ell_a > 27 \mu\text{m}$ for operating frequencies above the fundamental natural frequency where it is likely to contain significant contributions from higher modes.

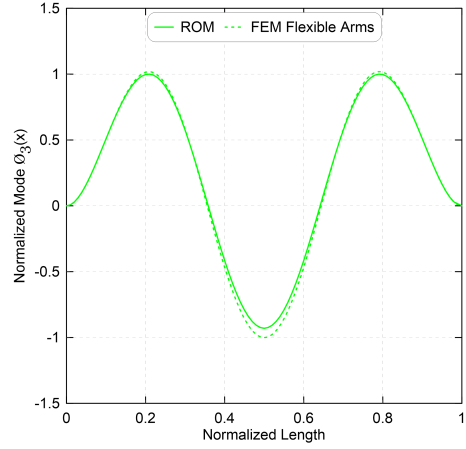
In addition, the results show that the ROM mis-identifies modal interactions that occur among higher modes as the arms length changes. While the FEM predicts the two crossovers listed in subsection 6.1.3, the ROM predicts veering between the second symmetric and the second asymmetric modes at $\ell_a \approx 130 \mu\text{m}$ and between the second asymmetric and third symmetric modes at $\ell_a \approx 200 \mu\text{m}$ as shown in Fig. 6.7.

We provide additional insight into the mechanisms underlying the inadequacy of the five-mode ROM to model micro-tweezers by comparing its constituent straight beam mode shapes to those of the tweezers' platform obtained from the FEM in the absence ($\ell_a = 0 \mu\text{m}$) and presence of three lengths flexible arms: $\ell_a = 50, 150$ and $250 \mu\text{m}$. We also investigate the effects of the arms lengths on the nodal locations of those modes.

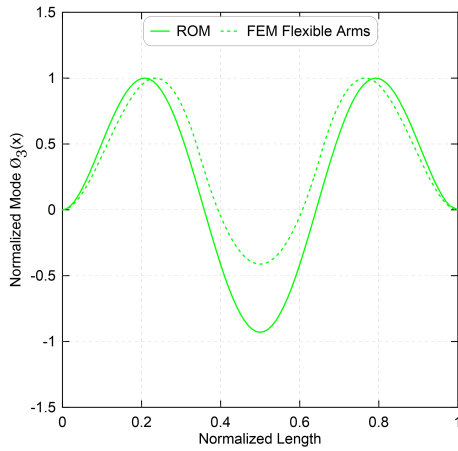
Differences between the first symmetric $\phi_1(x)$ and first asymmetric $\phi_2(x)$ modes of the platform and a straight beam are negligible over the entire arms length range under study. A comparison of the second symmetric $\phi_3(x)$ mode of a straight beam (solid lines) and the tweezers' platform (dashed lines) is shown in Fig. 6.8. The modes are normalized with respect to the peak value and the beam length ℓ_b along the x -axis.



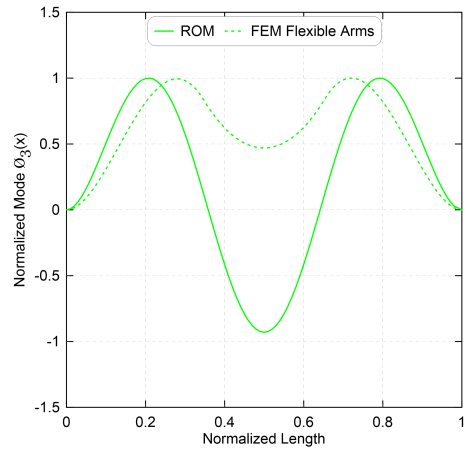
(a) $\ell_a = 0 \mu\text{m}$



(b) $\ell_a = 50 \mu\text{m}$



(c) $\ell_a = 150 \mu\text{m}$



(d) $\ell_a = 250 \mu\text{m}$

Figure 6.8: The second symmetric mode $\phi_3(x)$ of the tweezers platform (dashed lines) for flexible arms lengths: (a) $\ell_a = 0 \mu\text{m}$, (b) $\ell_a = 50 \mu\text{m}$, (c) $\ell_a = 150 \mu\text{m}$ and (d) $\ell_a = 250 \mu\text{m}$ compared to that of a straight beam (solid lines).

The differences between the straight beam and the platform modes are negligible for arms length up to $\ell_a = 50 \mu\text{m}$, Figs. 6.8(a) and (b), indicating that the arms are not interrupting the platform motions. However, this agreement deteriorates as the arms length,

their kinetic and potential energies, further increases. The change in the energy balance along the span leads to significant changes in the nodal locations as they approach each other, Fig. 6.8(c) at arms length of $\ell_a = 150 \mu\text{m}$, merge and disappear at arms length of $\ell_a = 250 \mu\text{m}$, Fig. 6.8(d).

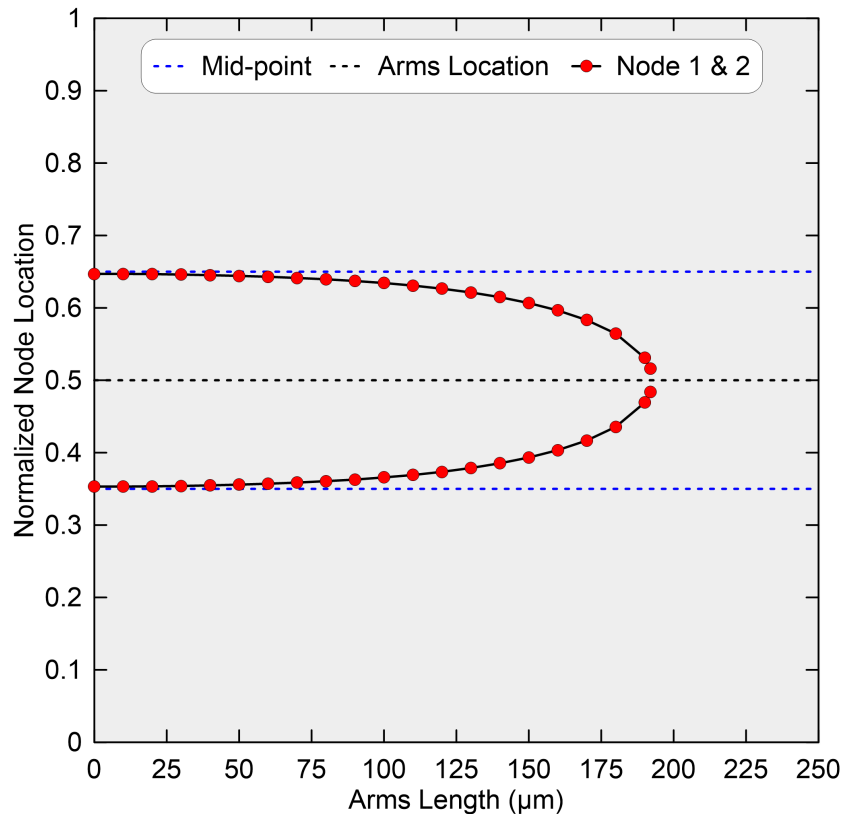


Figure 6.9: Variation in the locations of the interior nodes marked by (\bullet) of the second symmetric mode $\phi_3(x)$ of the tweezers platform with flexible arms as functions of the arms length. The platform mid-point is marked as a dashed black line (- -). The arms attachment points are marked as dashed blue lines (- -).

We track the nodal locations along the platform span using the FEM of the tweezers as functions of the arms length in the range of 0–250 μm . Figure 6.9 shows that the interior

nodes marked by (●) symbols are stationary up to an arms length of 50 μm . However, for longer arms length the energy balance along the beam span changes resulting in a reduction in the potential energy (relative deformation or ‘compliance’) of the beam middle sub-span, between the two arms, as the nodes smoothly approach each other, merge and disappear at $\ell_a \approx 180 \mu\text{m}$. It results in a shape resembling that of a straight beam first symmetric mode. Throughout this process, the arms act as energy sinks effectively isolating the middle sub-span from the platform vibrations.

The platform and the straight beam second asymmetric modes $\phi_4(x)$ are in agreement in the absence of arms. Once arms are introduced, the platform mode diverges progressively from the straight beam mode as can be seen in Fig. 6.10(a) for $\ell_a = 50 \mu\text{m}$ with the outer nodes moving toward the center node. This process continues as the arms length increases to $\ell_a = 150 \mu\text{m}$, Fig. 6.10(b), but reverses at some point with outer nodes ending up further away from the center node, at $\ell_a = 250 \mu\text{m}$ Fig. 6.10(c), than they are for a straight beam. For this mode, longer arms ($\ell_a = 250 \mu\text{m}$) result in energy localization in middle sub-span between the two arms compared to the outer sub-spans, which corresponds to increase in the relative compliance of the middle sub-span.

The nodal locations of the second asymmetric mode $\phi_4(x)$ as functions of arms length are shown in Fig. 6.11. The outer nodes, 1 and 3, are marked with (●) symbols while the center node 2 is marked with (●) symbols. The outer nodes move toward the center node, merge into it at $\ell_a = 240 \mu\text{m}$ and reemerge to move away from the center node beyond that length.

On the other hand, the location of the center node is insensitive to variation in arms length because of the underlying anti-symmetry of the the platform mode. Crossover occurs between the first and second asymmetric modes at $\ell_a \approx 240 \mu\text{m}$, Fig. 6.6, with $\phi_4(x)$ resembling $\phi_2(x)$. As the arms length increase to approach the crossover point, the middle

sub-span experiences vibration isolation. Beyond the crossover point, energy distribution along the span is reversed with middle sub-span experiencing energy localization compared to the outer sub-spans.

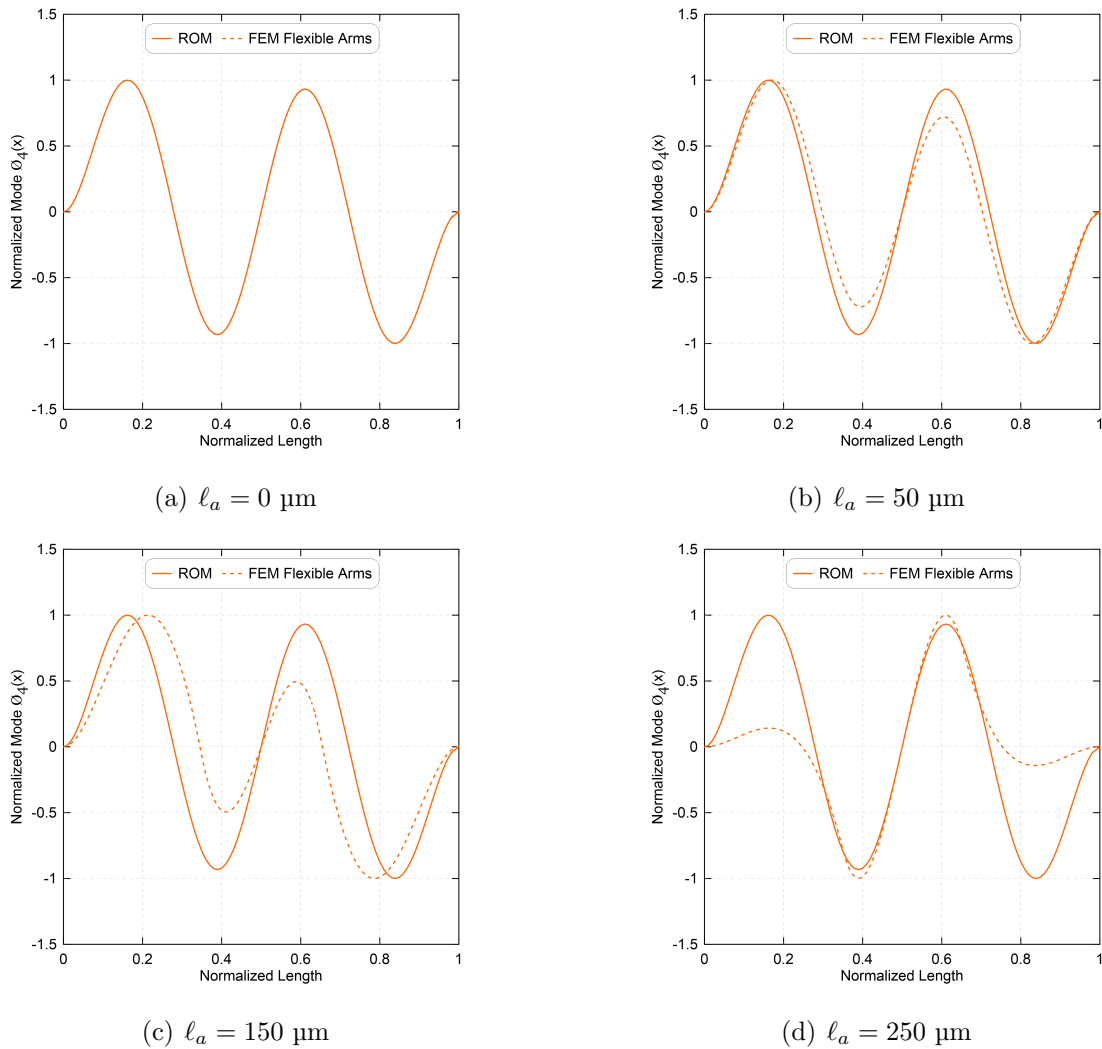


Figure 6.10: The second asymmetric mode $\phi_4(x)$ of the tweezers platform (dashed lines) for flexible arms lengths: (a) $\ell_a = 0 \mu\text{m}$, (b) $\ell_a = 50 \mu\text{m}$, (c) $\ell_a = 150 \mu\text{m}$ and (d) $\ell_a = 250 \mu\text{m}$ compared to that of a straight beam (solid lines).

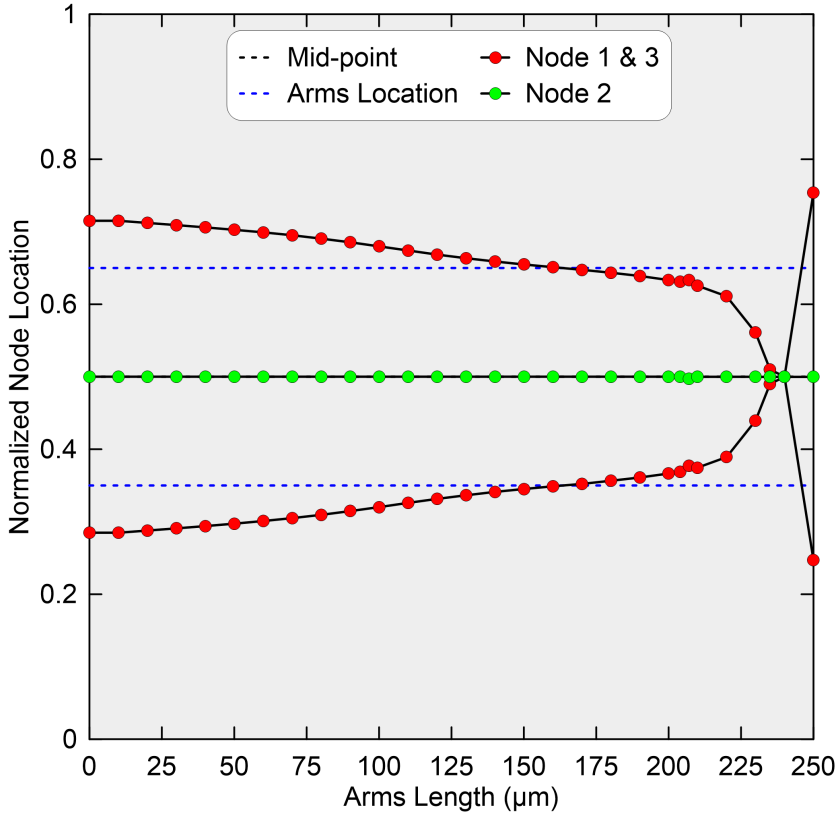
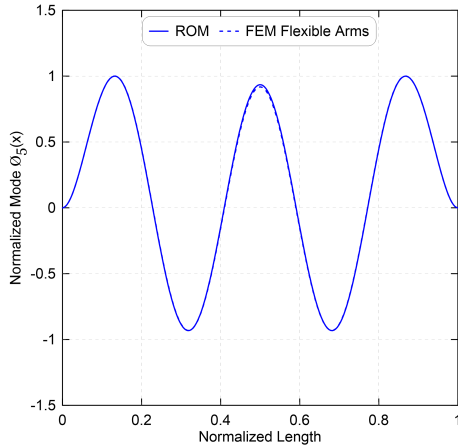


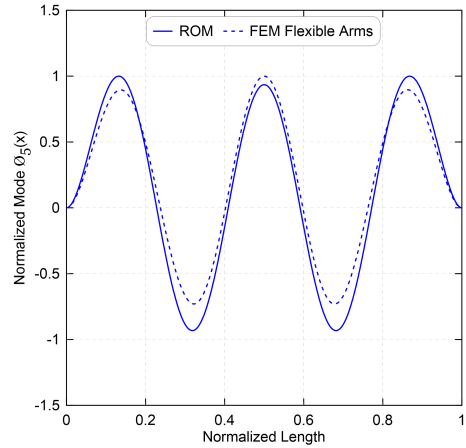
Figure 6.11: Variation in the locations of the outer nodes marked with (\bullet) and center node marked with (\bullet) of the second asymmetric mode $\phi_4(x)$ of the tweezers platform with flexible arms as functions of the arms length. The platform mid-point is marked as a dashed black line (- -). The arms attachment points are marked as dashed blue lines (- -).

We also found that differences between the third symmetric $\phi_5(x)$ modes of the platform and a straight beam were negligible up to $\ell_a = 50 \mu\text{m}$ as shown in Fig. 6.12(a). This indicates that the arms do not significantly affect the platform motions. The agreement between the modes deteriorates as the arms length increase to the point where the two interior nodes disappear for arms length of $\ell_a = 150 \mu\text{m}$, Fig. 6.12(b), and $\ell_a = 250 \mu\text{m}$, Fig. 6.12(c), respectively. The two outer nodes also approach the center with the mode shape resembling

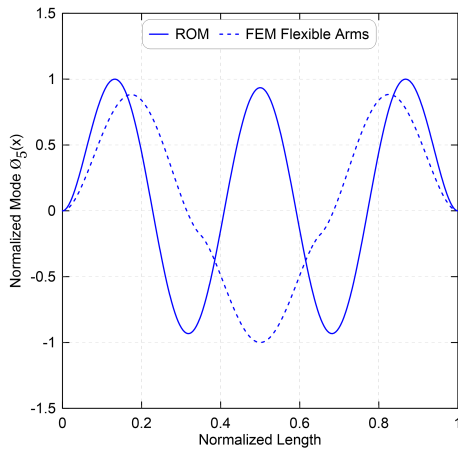
the second symmetric mode of a straight beam.



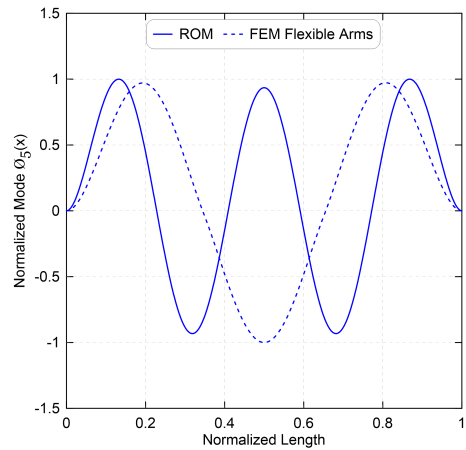
(a) $\ell_a = 0 \mu\text{m}$



(b) $\ell_a = 50 \mu\text{m}$



(c) $\ell_a = 150 \mu\text{m}$



(d) $\ell_a = 250 \mu\text{m}$

Figure 6.12: The third asymmetric mode $\phi_5(x)$ of the tweezers platform (dashed lines) for flexible arms lengths: (a) $\ell_a = 0 \mu\text{m}$, (b) $\ell_a = 50 \mu\text{m}$, (c) $\ell_a = 150 \mu\text{m}$ and (d) $\ell_a = 250 \mu\text{m}$ compared to that of a straight beam (solid lines).

We track the locations of those nodes as functions of arms length as shown in Fig. 6.13. The interior nodes, 2 and 3, marked by (●) symbols remain stationary up to an arms length

of 90 μm where they abruptly merge and disappear. Similarly, the outer nodes, 1 and 4, marked by (●) symbols are almost stationary until the same length range where they start approaching the arms attachment points. Therefore, the energy distribution along the platform span can be classified into two zones. In zone I, it resembles that of a straight beam third symmetric mode $\phi_5(x)$. In zone II, the middle sub-span experiences a reduction in potential energy and vibration isolation with $\phi_5(x)$ resembling $\phi_3(x)$.

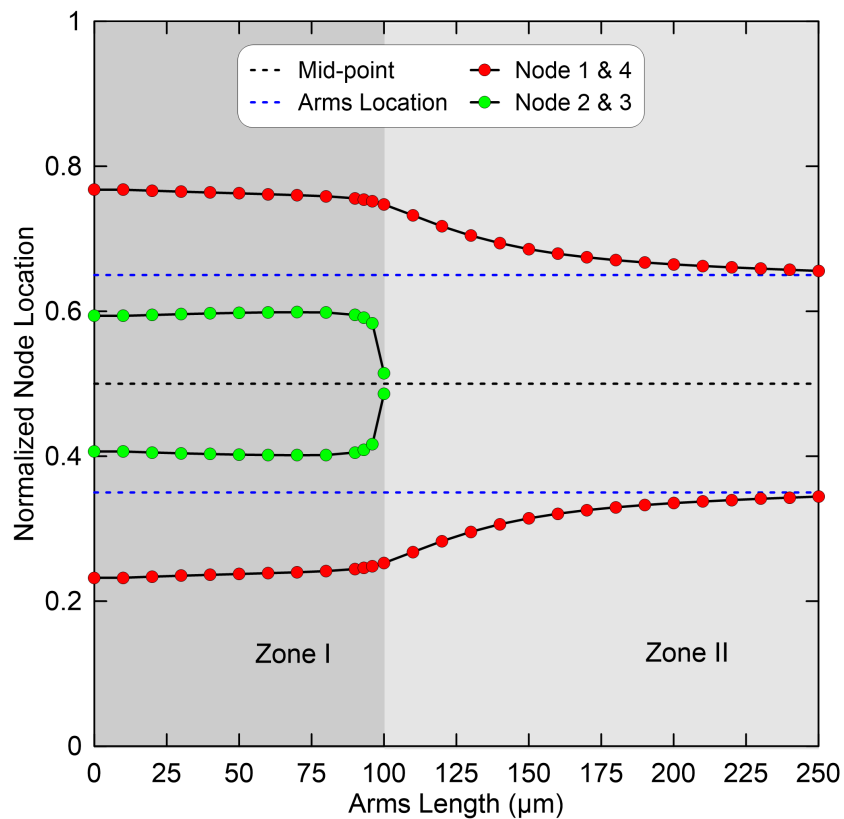


Figure 6.13: Variation in the locations of the outer nodes marked with (●) and interior nodes marked with (●) of the third symmetric mode $\phi_5(x)$ of the tweezers platform with flexible arms as functions of the arms length. The platform mid-point is marked as a dashed black line (- -). The arms attachment points are marked as dashed blue lines (- -).

Similar changes in the platform higher mode shapes were also found as the arms length increase. The locations of their nodes as functions of arms length are shown in Fig. 6.14 for the third asymmetric mode $\phi_6(x)$, Fig. 6.15 for the fourth symmetric mode $\phi_7(x)$, Fig. 6.16 for the fourth asymmetric mode $\phi_8(x)$ and Fig. 6.17 for the fifth symmetric mode $\phi_9(x)$, respectively.

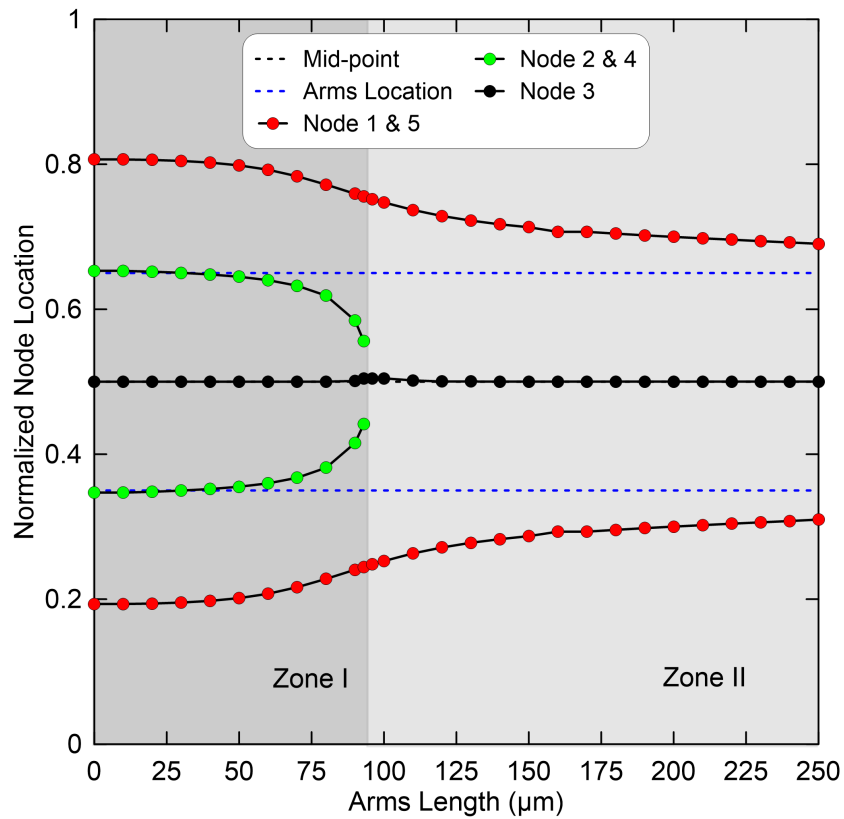


Figure 6.14: Variation in the locations of the outer nodes marked by (●), interior nodes marked by (●) and the center node marked by (●) of the third asymmetric mode $\phi_6(x)$ of the tweezers platform with flexible arms as functions of the arms length. The platform mid-point is marked as a dashed black line (- -). The arms attachment points are marked as dashed blue lines (- -).

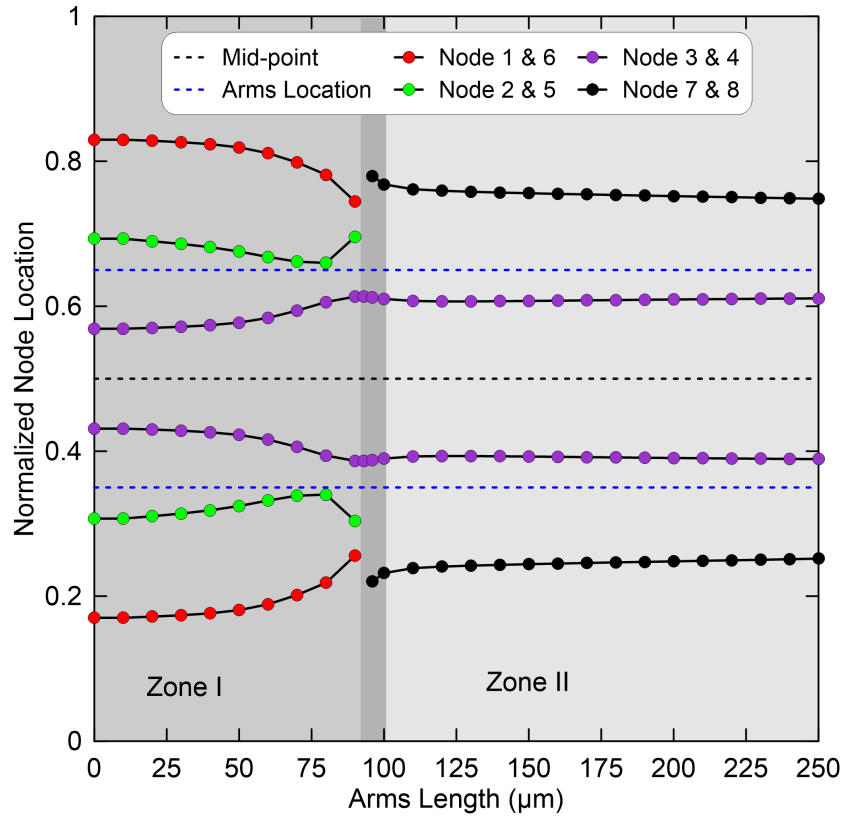


Figure 6.15: Variation in the locations of the outer nodes marked by (\bullet , \bullet and \bullet) and interior nodes marked by (\bullet) of the fourth symmetric mode $\phi_7(x)$ of the tweezers platform with flexible arms as functions of the arms length. The platform mid-point is marked as a dashed black line (- -). The arms attachment points are marked as dashed blue lines (- -).

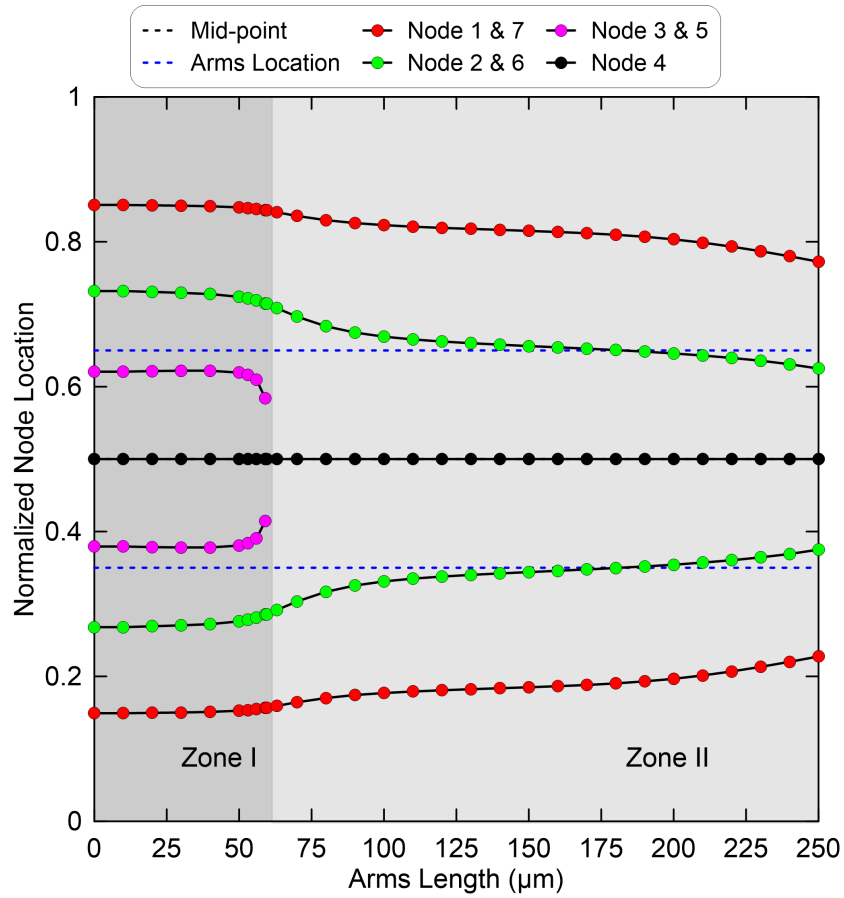


Figure 6.16: Variation in the locations of the outer nodes marked by (● and ●), interior nodes marked by (●) and the center node marked by (●) of the fourth asymmetric mode $\phi_8(x)$ of the tweezers platform with flexible arms as functions of the arms length. The platform mid-point is marked as a dashed black line (- -). The arms attachment points are marked as dashed blue lines (- -).

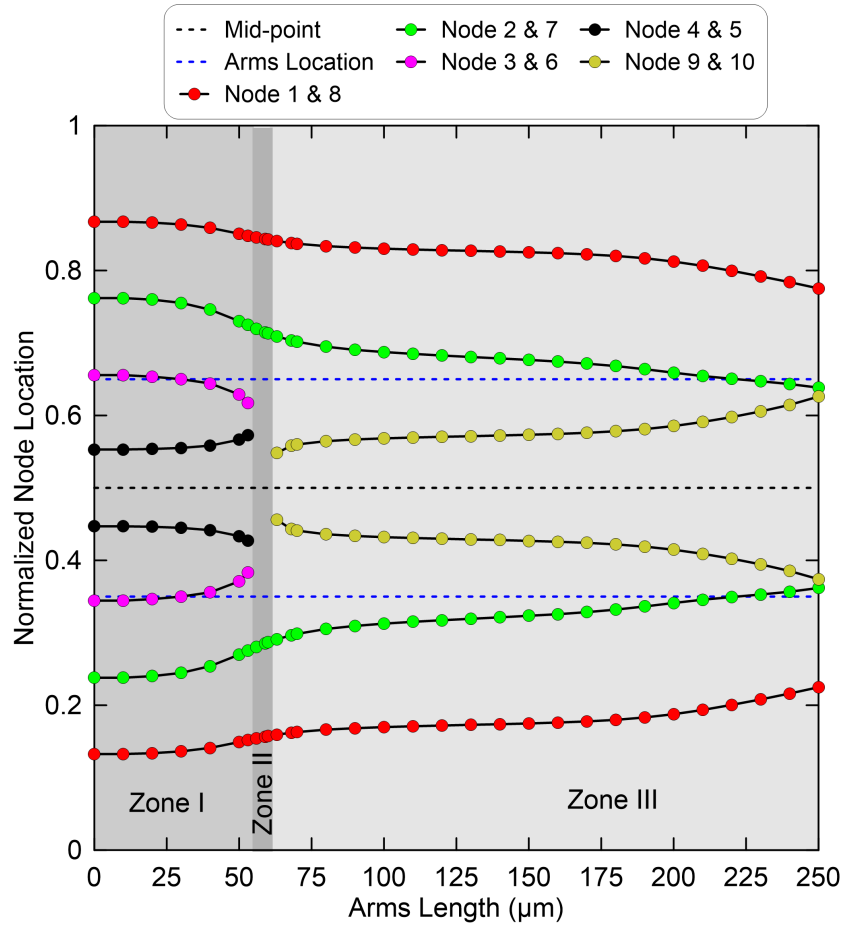


Figure 6.17: Variation in the locations of the outer nodes marked by (● and ●), interior nodes marked by (●, ● and ●) of the fifth symmetric mode $\phi_9(x)$ of the tweezers platform with flexible arms as functions of the arms length. The platform mid-point is marked as a dashed black line (- -). The arms attachment points are marked as dashed blue lines (- -).

6.1.5 Variation of the Natural Frequency under Electrostatic Forcing

We investigate the impact of the electrostatic field strength represented by the RMS of the voltage waveform on the fundamental natural frequency of the platform. Figure 6.18 compares the results of the five-mode ROM to those of the FEM in the presence and absence of arms ($\ell_a = 250 \mu\text{m}$) as functions of V_{RMS} . In the absence of arms, the fundamental natural frequency f_1 predicted by the ROM solid orange lines (—) is in agreement with that predicted by the FEM (\star) symbols. It drops as V_{RMS} increases and the platform mid-point deflects below the initial curvature, Fig. 3.2(a), and reaches zero at the snap-through voltage $V_S = 112 \text{ V}$.

The fundamental natural frequency of the second equilibrium in the vicinity of the counter-curvature, Fig. 3.2(b), increases from $f_1 = 0$ at the snap-back voltage $V_B = 100.2 \text{ V}$ as V_{RMS} increases and the platform mid-point deflects further, until it reaches a maximum of $f_1 = 37.27 \text{ kHz}$ before it suddenly drops and reaches zero at the pull-in voltage $V_P = 151 \text{ V}$. In the region between the snap-back and snap-through voltages, the platform is bistable with a natural frequency corresponding to each equilibrium.

In the presence of arms, the ROM predictions of the fundamental natural frequency f_1 solid magenta lines (—) are in agreement with those of the FEM (\bullet) symbols for equilibria in the vicinity of the initial curvature. However, it fails to predict the natural frequencies corresponding to equilibria in the vicinity of the counter-curvature.

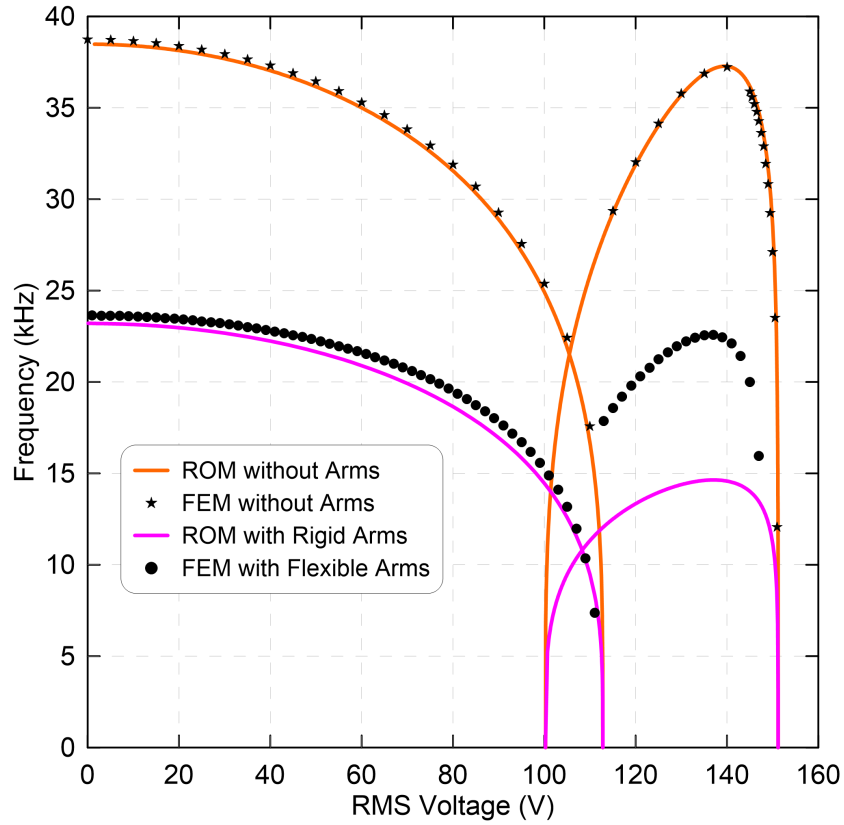


Figure 6.18: Variation of the fundamental natural frequency of the tweezers platform as functions of RMS voltage in the absence of arms, ROM results as shown as orange lines (—) and FEM results are shown as (\star) symbols, and in the presence of arms ($\ell_a = 250 \mu\text{m}$), ROM results are shown as magenta lines (—) and FEM results are shown as (\bullet) symbols.

6.2 Summary

This chapter investigates the design criteria required for electrostatic arch micro-tweezers that can grasp and manipulate micro-objects in a static mode and characterize them in a dynamic mode. In particular, it provides a map for the minimum operational requirements of the static and dynamic modes of operation.

The results showed the capability of the micro-tweezers to grasp particle with diameters in the range of 5–14 μm and an operating voltage range extending from snap-back voltage ($V_B = 89.01 \text{ V}$) to pull-in voltage ($V_P = 136.44 \text{ V}$). Beyond the snap-through point, the tweezers has the ability to smoothly compress and hold objects.

We found that at a minimum, the dynamic mode mandates that the micro-tweezers is operated at a resonance to reduce the actuation voltage requirements and maximize the grip range. The mode shape corresponding to the working resonance must maintain arms rigidity to minimize control requirements and the complexity of the forces applied by the arms on the micro-object under test. In addition, the arms motions should be in-phase to guarantee that they can apply well regulated normal ‘tension and compression’ forces to the micro-object rather than the complex combination of normal and shear forces that arise when the arms motions are not in tandem.

Chapter 7

Concluding Remarks

In this chapter, we summarize and discuss the most important findings in this dissertation. These findings focus on the fundamental behavior of the initially curved micro-beam which serves as a platform for the tweezers' arms as well as the use of the snap-through motion to build simple, compact and efficient electrostatic micro-tweezers. The limitations of this research and suggestions for the future work are also summarized.

7.1 Summary of Contributions

7.1.1 Arch Micro-tweezers

We investigated the feasibility of using parallel-plate actuators to build MEMS micro-tweezers to manipulate and characterize micro-particles. Two operational modes were designed. The first mode uses a bias voltage V_{DC} to approach, hold and release an object while the second mode uses a biased AC signal $V(t)$ to release, probe and interact with the

object. The tweezers' operational range and its potential for manipulating micro-particles have been examined. Two models are used in this study: a 2D finite element model (FEM) and a Reduced-Order model (ROM). The later model is developed by discretizing the equation of motion using straight beam mode shapes without accounting for the arms inertia as basis functions in a Galerkin expansion.

The results show that for an applied voltage $V(t)$ less than the snap-through voltage V_S , the gap between the beam mid-point and the sidewall electrode decreases allowing the tweezers arms to slowly approach each other and, therefore, hold and manipulate coarse micro-objects with diameters in a range of 12.5–14 μm . Increasing the voltage beyond V_S leads to a jump down to a second branch of stable equilibria resulting in a further reduction in the separation gap and allowing the tweezers to smoothly grasp fine micro-objects with diameters in the range of 5–7.5 μm .

We also found that at a minimum, the dynamic mode mandates that the micro-tweezers is operated at a resonance to reduce the actuation voltage requirements and maximize the grip range. This, however, must be operated with a mode shape that maintains the arms rigidity, a necessary condition for the tweezers functionality, since some modes may involve arms flexibility. In addition, the actuated modes should command arms motions that are in-phase allowing the arms to close on and to release the object in tandem. As a result, the operating space of the tweezers should, therefore, include only those resonances that do not excite modes involving arms flexibility.

The FEM results show that the arms kinetic and potential energies divide the beam span into a middle sub-span, bracketed by the arms, and two outer sub-spans, on either side of them, and result in significant changes in the relative compliance of the three sub-spans. These changes lead to vibration isolation or energy localization in the middle sub-span depending on the arms length and the operational mode shape.

Vibration isolation undermines the mode usability for actuation since it reduces the grip range. Variation in arms length also lead to crossover phenomena among the tweezers' modes. For the arms length range under investigation, we found that only mode shapes that satisfied the design criteria was the first symmetrical mode shape of the platform. Higher modes were found to involve arms flexibility, vibration isolation of the middle sub-span or mode crossover.

The adequacy of the ROM in representing the tweezers response was investigated by comparing its static response and modal analysis to that of the FEM. The ROM was found adequate to model micro-tweezers operated statically or dynamically by exciting the first symmetric mode provided that the motions remain small. It was found inadequate for motions that venture outside the initial curvature potential well or involve higher modes via direct excitation or modal interaction. These shortcomings can be remedied by adding higher order modes of a straight beam to the basis functions or using the 'native' mode shapes of the tweezers.

7.1.2 Initially Curved Beam

We also examined the static and dynamic responses of the electrostatically actuated curved micro-beams that serve as a platforms for the tweezers. Evidence of primary resonance and superharmonic resonances of orders two and three were observed. Experimental results showed the co-existence of three stable orbits under excitation waveforms with RMS voltage less than the snap-back voltage, and thus possessing only one stable equilibrium. Those orbits belong to three branches of stable solutions around the equilibrium, namely a branch of small orbits within a narrow potential well and two branches of medium-size and large orbits within a wider potential well. The transition between these branches resulted in a characteristic double-peak frequency-response curve.

We also found evidence of a bubble structure, a cascade of period-doubling bifurcations and a cascade of reverse period-doubling bifurcations, along the medium-sized branch. Chaos developed within that structure at larger excitation levels. Even though orbits along the large oscillations branch appear in phase-space to have characteristics similar to those of dynamic snap-through, this is not the case here since these orbits encircle a single stable equilibrium only.

7.2 Research Limitations

While the results in this dissertation are promising, it is important to recognize the limitations summarized below:

- As mentioned in previous chapters, parallel-plate actuated arch micro-tweezers overcome the drawbacks of existing interdigitated comb-finger tweezers, namely a large footprint and complex fabrication processes. However, their grip range is limited by the nonlinear pull-in instability to approximately one-third the capacitive gap compared to interdigitated comb-finger drives that have been more effective increasing the grip range and reducing the actuation voltage.
- The proposed micro-tweezers do not have a sensing capability. This shortcoming limits its usability in applications where the grip force can damage sensitive targets, such as biological cells.
- We also found that only the first symmetric mode shape of the platform can be used to operate the tweezers in the dynamic mode. This places a limit in the operational frequency of tweezers up to its fundamental natural frequency. Frequencies beyond this range, may trigger contributions from higher modes involving arms flexibility,

vibration isolation of the middle sub-span or mode crossover. All of which will undermine the tweezers usability.

7.3 Directions for Future Study

Some pathways that can be pursued as a continuation of this dissertation are summarized as follows:

- Experimental validation for the proposed operating modes of the micro-tweezers are a mandatory step that will provide insights towards a better understanding of the tweezers performance.
- Deploy the dynamic operating mode of the micro-tweezers as a test platforms to measure the stiffness of the micro objects placed between the arms tips.
- The existing analytical model can be further extended to account for the arms flexibility and to study its adequacy in representing the tweezers response. It can also be used to investigate modal interactions between the platform and the grip arms.
- Design and fabricate the second generation of micro-tweezers to obtain a larger grip range and the capability to measure the grip force.

7.4 List of Publications

The following is a list of the publications related to this dissertation and collaboration with colleagues:

• **Peer-reviewed Journal Papers**

- **Alneamy, A.**, Khater, M., Al-Ghamdi, M., Abdel-Aziz, A., Heppler, G., & Abdel-Rahman, E. (2020). “Large Oscillation of Electrostatically Actuated Curved Beams.” *Journal of Micromechanics and Microengineering*. (In press: JMM-104691.R1)
- **Alneamy, A.**, Heppler, G., Abdel-Rahman, E., & Khater, M. (2020). “On Design and Analysis of Electrostatic Arch Micro-tweezers.” *Journal of Vibration and Acoustics*. (Under Review: VIB-20-1230).
- **Alneamy, A.**, Khater, M. E., Abdel-Aziz, A. K., Heppler, G. R., & Abdel-Rahman, E. M. (2020). “Electrostatic arch micro-tweezers.” *International Journal of Non-Linear Mechanics*, 118, 103298.
- **Alneamy, A.**, M. Al-Ghamdi, S. Park, M. Khater, E. Abdel-Rahman, and G. Heppler. “Dimpled electrostatic MEMS actuators.” *Journal of Applied Physics* 125, no. 2 (2019): 024304.
- **Alneamy, A.** M., M. E. Khater, M. S. Al-Ghamdi, S. Park, G. R. Heppler, and E. M. Abdel-Rahman. “Dual actuation micro-mirrors.” *Journal of Micromechanics and Microengineering* 28, no. 7 (2018): 075014.
- Al-Ghamdi, Majed S., **Ayman M Alneamy**, Sangtak Park, Beichen Li, Mahmoud E. Khater, Eihab M. Abdel-Rahman, Glenn R. Heppler, and Mustafa Yavuz. “Nonlinear Parameter Identification of a Resonant Electrostatic MEMS Actuator.” *Sensors* 17, no. 5 (2017): 1121.
- Al-Ghamdi, M. S., M. E. Khater, K. M. E. Stewart, **Alneamy, A.**, E. M. Abdel-Rahman, and A. Penlidis. “Dynamic bifurcation MEMS gas sensors.” *Journal of Micromechanics and Microengineering* 29, no. 1 (2018): 015005.

• **International conference Papers**

- **Ayman Alneamy**, Eihab Abdel-Rahman, Glenn Heppler, Ahmed Abdel Aziz, and Mahmoud Khater. Chaos in Electrostatically Actuated Arch Beams. *International Nonlinear Dynamics Conference*, Rome, Italy, February 2019, p.312.
- **Ayman Alneamy**, Mahmoud Khater, Ahmed Abdel Aziz, Glenn Heppler, Eihab Abdel-Rahman. Electrostatic Arch Micro-Tweezers. *Euromech 603: Dynamics of Micro and Nano Electromechanical Systems*, Porto, Portugal, September 2018, pp. 88-91.
- **Ayman Alneamy**, Mahmoud Khater, Sangtak Park, Eihab Abdel-Rahman, & Glenn Heppler. Electrostatic versus Electromagnetic Micromirrors Actuation. *International Congress of Theoretical and Applied Mechanics*, Montreal, August (21-26) 2016, paper # 130082.
- **AM Alneamy**, MS Al-Ghamdi, M Khater, B Li, RS Almikhlaifi, S Park, EM Abdel-Rahman, GR Heppler. On the Dynamics of Dimpled Electrostatic MEMS Actuators. *European Nonlinear Dynamics Conference*, Budapest, Hungary, June 25-30, 2017, paper # 399.
- H. Nafissi, **A. M. Alneamy**, E. M. Abdel-Rahman, and R. Mansour. Toward Electrostatic Atomic Force Microscopy. *Euromech 603: Dynamics of Micro and Nano Electromechanical Systems*, Porto, Portugal, September 2018, pp. 124–128.
- MS Alghamdi, **AM Alneamy**, M. Khater, and E. M. Abdel-Rahman. Low-

Frequency Tapping in Electrostatic MEMS Actuators, invited, *Conference on Theory and Modern Applications of Non-linear Dynamics: In Memory of Professor Ali H. Nayfeh*, Abu Dhabi, January 28-29, 2018.

- MS Alghamdi, M. Khater, **AM Alneamy**, and E. M. Abdel-Rahman. Sensitivity Analysis of Cantilever-Based Bifurcation MEMS Sensors. *Conference on Structural Nonlinear Dynamics and Diagnosis: In memoriam: Ali H. Nayfeh, University Distinguished Professor Emeritus of nonlinear dynamics (1933-2017)*, Tangier, June 25-27, 2018.
- MS Al-Ghamdi, M Khater, KME Stewart, **A Alneamy**, R Almikhlaifi, S Park, EM Abdel-Rahman, A Penlidis. Demonstration of Electrostatic MEMS Bifurcation Sensors. *European Nonlinear Dynamics Conference*, Budapest, Hungary, June 25-30, 2017, paper # 378.

References

- [1] S D Senturia. *Microsystem design*. Springer Science & Business Media, 2007.
- [2] D Koester, A Cowen, R Mahadevan, M Stonefield, and B Hardy. PolyMUMPs design handbook. *MEMSCAP Inc*, 2003.
- [3] K Miller, A Cowen, G Hames, and B Hardy. SOIMUMPs design handbook. *MEM-ScAP Inc., Durham*, 2004.
- [4] *University of Waterloo, UW-MEMS Design Handbook (ver. 5)*. 2010.
- [5] C Liu. *Foundations of MEMS*. Pearson Education India, 2012.
- [6] T Hsu. *MEMS & microsystems: design and manufacture*. McGraw-Hill Boston, 2002.
- [7] G Rebeiz and J Muldavin. RF MEMS switches and switch circuits. *IEEE Microwave magazine*, 2(4):59–71, 2001.
- [8] J Pal, Y Zhu, Ji Lu, D Dao, and F Khan. RF MEMS switches for smart antennas. *Microsystem Technologies*, 21(2):487–495, 2015.

- [9] R Bauer, A Paterson, C Clark, D Uttamchandani, and W Lubeigt. Output characteristics of Q-switched solid-state lasers using intracavity MEMS micromirrors. *IEEE Journal of Selected Topics in Quantum Electronics*, 21(1):356–363, 2014.
- [10] S Muntwyler, B Kratochvil, F Beyeler, and B Nelson. Two-axis micro-tensile tester chip for measuring plant cell mechanics. In *SENSORS, 2010 IEEE*, pages 2451–2454. IEEE, 2010.
- [11] A Persano, F Quaranta, A Cola, A Taurino, G De Angelis, R Marcelli, and P Siciliano. Ta₂O₅ thin films for capacitive RF MEMS switches. *Journal of Sensors*, 2010, 2010.
- [12] H Chen, WJ Sun, ZD Sun, and JTW Yeow. Second-order sliding mode control of a 2D torsional MEMS micromirror with sidewall electrodes. *Journal of Micromechanics and Microengineering*, 23(1):015006, 2012.
- [13] TEAM NANOTEC - MICRO- AND NANOFABRICATION TECHNOLOGY. Conical probe for tapping mode 300 khz resonant frequency, 2017. <https://www.team-nanotec.de/index.cfm?contentid=10&shopAction=listProducts&shopCatID=76¤tPage=1>,.
- [14] K Kim, X Liu, Y Zhang, and Y Sun. Nanonewton force-controlled manipulation of biological cells using a monolithic MEMS microgripper with two-axis force feedback. *Journal of micromechanics and microengineering*, 18(5):055013, 2008.
- [15] Y Jia and Q Xu. MEMS microgripper actuators and sensors: The state-of-the-art survey. *Recent Patents on Mechanical Engineering*, 6(2):132–142, 2013.

- [16] M Younis, E Abdel-Rahman, and A Nayfeh. A reduced-order model for electrically actuated microbeam-based MEMS. *Journal of Microelectromechanical systems*, 12(5):672–680, 2003.
- [17] S Yang and Q Xu. A review on actuation and sensing techniques for MEMS-based microgrippers. *Journal of Micro-Bio Robotics*, 13(1-4):1–14, 2017.
- [18] A Nayfeh, M Younis, and E Abdel-Rahman. Dynamic pull-in phenomenon in MEMS resonators. *Nonlinear dynamics*, 48(1-2):153–163, 2007.
- [19] H Yang, D Choi, J Lee, and J Yoon. Modeling, fabrication and demonstration of an electrostatic actuator with a coplanar pre-charged electrode. *Journal of Micromechanics and Microengineering*, 21(8):085012, 2011.
- [20] A Alneamy, M Al-Ghamdi, S Park, M Khater, E Abdel-Rahman, and G Heppler. Dimpled electrostatic MEMS actuators. *Journal of Applied Physics*, 125(2):024304, 2019.
- [21] H Ren, F Tao, W Wang, and J Yao. An out-of-plane electrostatic actuator based on the lever principle. *Journal of Micromechanics and Microengineering*, 21(4):045019, 2011.
- [22] S He, R Mrad, and J Chong. Repulsive-force out-of-plane large stroke translation micro electrostatic actuator. *Journal of Micromechanics and Microengineering*, 21(7):075002, 2011.
- [23] E Chan and R Dutton. Electrostatic micromechanical actuator with extended range of travel. *Journal of microelectromechanical Systems*, 9(3):321–328, 2000.

- [24] D Piyabongkarn, Y Sun, R Rajamani, A Sezen, and B Nelson. Travel range extension of a MEMS electrostatic microactuator. *IEEE Transactions on Control Systems Technology*, 13(1):138–145, 2004.
- [25] S Towfighian, S He, and R Ben Mrad. A low voltage electrostatic micro actuator for large out-of-plane displacement. In *ASME 2014 International Design Engineering Technical Conferences and Computers and Information in Engineering Conference*. American Society of Mechanical Engineers Digital Collection, 2014.
- [26] D Kim, M Lee, B Kim, and Y Sun. A superelastic alloy microgripper with embedded electromagnetic actuators and piezoelectric force sensors: a numerical and experimental study. *Smart materials and structures*, 14(6):1265, 2005.
- [27] S Jericho, M Jericho, T Hubbard, and M Kujath. Micro-electro-mechanical systems microweavers for the manipulation of bacteria and small particles. *Review of Scientific Instruments*, 75(5):1280–1282, 2004.
- [28] P Krulevitch, A Lee, P Ramsey, J Trevino, and M Hamilton, Jand Northrup. Thin film shape memory alloy microactuators. *Journal of microelectromechanical systems*, 5(4):270–282, 1996.
- [29] W Johnson and L Warne. Electrophysics of micromechanical comb actuators. *Journal of Microelectromechanical Systems*, 4(1):49–59, 1995.
- [30] F Alsaleem, M Younis, and H Ouakad. On the nonlinear resonances and dynamic pull-in of electrostatically actuated resonators. *Journal of Micromechanics and Microengineering*, 19(4):045013, 2009.

- [31] M Sulfridge, T Saif, N Miller, and M Meinhart. Nonlinear dynamic study of a bistable mems: Model and experiment. *Journal of Microelectromechanical Systems*, 13(5):725–731, 2004.
- [32] S Krylov and r Dick. Pull-in dynamics of electrostatically actuated bistable micro beam. In *Advanced Materials and Technologies for Micro/Nano-Devices, Sensors and Actuators*, pages 117–128. Springer, 2010.
- [33] C Goll, W Bacher, B Büstgens, D Maas, W Menz, and WK Schomburg. Microvalves with bistable buckled polymer diaphragms. *Journal of Micromechanics and Micro-engineering*, 6(1):77, 1996.
- [34] H Matoba, T Ishikawa, C-J Kim, and R Muller. A bistable snapping microactuator. In *Proceedings IEEE Micro Electro Mechanical Systems An Investigation of Micro Structures, Sensors, Actuators, Machines and Robotic Systems*, pages 45–50. IEEE, 1994.
- [35] R Receveur, R Marxer, Cand Woering, V Larik, and N de Rooij. Laterally moving bistable MEMS DC switch for biomedical applications. *Journal of microelectromechanical systems*, 14(5):1089–1098, 2005.
- [36] J Rossiter, B Stoimenov, and T Mukai. A self-switching bistable artificial muscle actuator. In *2006 SICE-ICASE International Joint Conference*, pages 5847–5852. IEEE, 2006.
- [37] Y Zhang, Y Wang, Z Li, Y Huang, and D Li. Snap-through and pull-in instabilities of an arch-shaped beam under an electrostatic loading. *Journal of Microelectromechanical Systems*, 16(3):684–693, 2007.

- [38] B Charlot, W Sun, K Yamashita, H Fujita, and H Toshiyoshi. Bistable nanowire for micromechanical memory. *Journal of Micromechanics and Microengineering*, 18(4):045005, 2008.
- [39] L Buchailot, O Millet, El Quévy, and D Collard. Post-buckling dynamic behavior of self-assembled 3D microstructures. *Microsystem technologies*, 14(1):69–78, 2008.
- [40] I Pane and T Asano. Investigation on bistability and fabrication of bistable pre-stressed curved beam. *Japanese Journal of Applied Physics*, 47(6S):5291, 2008.
- [41] S Krylov, B Ilic, D Schreiber, S Seretensky, and H Craighead. The pull-in behavior of electrostatically actuated bistable microstructures. *Journal of Micromechanics and Microengineering*, 18(5):055026, 2008.
- [42] S Tella, A Hajjaj, and M Younis. The effects of initial rise and axial loads on MEMS arches. *Journal of Vibration and Acoustics*, 139(4), 2017.
- [43] P Fanning and T Boothby. Three-dimensional modelling and full-scale testing of stone arch bridges. *Computers & Structures*, 79(29-30):2645–2662, 2001.
- [44] W Ren, T Zhao, and I Harik. Experimental and analytical modal analysis of steel arch bridge. *Journal of Structural Engineering*, 130(7):1022–1031, 2004.
- [45] F Magalhães, Álvaro Cunha, and E Caetano. Dynamic monitoring of a long span arch bridge. *Engineering Structures*, 30(11):3034–3044, 2008.
- [46] D Joe, Y Linzon, V Adiga, R Barton, M Kim, B Ilic, S Krylov, J Parpia, and H Craighead. Stress-based resonant volatile gas microsensor operated near the critically buckled state. *Journal of Applied Physics*, 111(10):104517, 2012.

- [47] H Ouakad and M Younis. On using the dynamic snap-through motion of MEMS initially curved microbeams for filtering applications. *Journal of Sound and Vibration*, 333(2):555–568, 2014.
- [48] M Hafiz, L Kosuru, A Ramini, K Chappanda, and M Younis. In-plane MEMS shallow arch beam for mechanical memory. *Micromachines*, 7(10):191, 2016.
- [49] A Alneamy, M Khater, A Abdel-Aziz, G Heppler, and E Abdel-Rahman. Electrostatic arch micro-tweezers. *International Journal of Non-Linear Mechanics*, 118:103298, 2020.
- [50] A Alneamy, M Khater, M Alghamdi, A Abdel-Aziz, G Heppler, and E Abdel-Rahman. Large oscillation of electrostatically actuated curved beams. *Journal of Micromechanics and Microengineering*, 2020.
- [51] S Alkharabsheh and M Younis. Statics and dynamics of MEMS arches under axial forces. *Journal of Vibration and Acoustics*, 135(2), 2013.
- [52] A Nayfeh and S Emam. Exact solution and stability of postbuckling configurations of beams. *Nonlinear Dynamics*, 54(4):395–408, 2008.
- [53] J Qiu, J Lang, and A Slocum. A curved-beam bistable mechanism. *Journal of microelectromechanical systems*, 13(2):137–146, 2004.
- [54] S Krylov, B Ilic, and S Lulinsky. Bistability of curved microbeams actuated by fringing electrostatic fields. *Nonlinear Dynamics*, 66(3):403, 2011.
- [55] J Han, J Ko, Y Kim, and B Kwak. Parametric study and optimization of a micro-optical switch with a laterally driven electromagnetic microactuator. *Journal of Micromechanics and Microengineering*, 12(6):939, 2002.

- [56] S Park and D Hah. Pre-shaped buckled-beam actuators: theory and experiments. *Sensors and Actuators A: Physical*, 148(1):186–192, 2008.
- [57] A Michael and C Kwok. Design criteria for bi-stable behavior in a buckled multi-layered MEMS bridge. *Journal of Micromechanics and microengineering*, 16(10):2034, 2006.
- [58] H Ouakad, M Younis, F Alsaleem, R Miles, and W Cui. The static and dynamic behavior of MEMS arches under electrostatic actuation. In *ASME 2009 International Design Engineering Technical Conferences and Computers and Information in Engineering Conference*, pages 607–616. American Society of Mechanical Engineers Digital Collection, 2009.
- [59] L Medina, R Gilat, and S Krylov. Symmetry breaking in an initially curved prestressed micro beam loaded by a distributed electrostatic force. *International Journal of Solids and Structures*, 51(11-12):2047–2061, 2014.
- [60] H Ouakad and M Younis. The dynamic behavior of MEMS arch resonators actuated electrically. *International Journal of Non-Linear Mechanics*, 45(7):704–713, 2010.
- [61] L Ruzziconi, A Bataineh, M Younis, W Cui, and S Lenci. Nonlinear dynamics of an electrically actuated imperfect microbeam resonator: experimental investigation and reduced-order modeling. *Journal of micromechanics and microengineering*, 23(7):075012, 2013.
- [62] A Ramini, M Bellaredj, M Al Hafiz, and M Younis. Experimental investigation of snap-through motion of in-plane MEMS shallow arches under electrostatic excitation. *Journal of Micromechanics and Microengineering*, 26(1):015012, 2015.

- [63] A Hajjaj, F Alfosail, N Jaber, S Ilyas, and M Younis. Theoretical and experimental investigations of the crossover phenomenon in micromachined arch resonator: part I simultaneous 1: 1 and 2: 1 internal resonances. *Nonlinear Dynamics*, 99(1):407–432, 2020.
- [64] A Hajjaj, F Alfosail, N Jaber, S Ilyas, and M Younis. Theoretical and experimental investigations of the crossover phenomenon in micromachined arch resonator: part II linear problem. *Nonlinear Dynamics*, 99(1):393–405, 2020.
- [65] K Das and R Batra. Symmetry breaking, snap-through and pull-in instabilities under dynamic loading of microelectromechanical shallow arches. *Smart Materials and Structures*, 18(11):115008, 2009.
- [66] L Medina, R Gilat, and S Krylov. Latching in bistable electrostatically actuated curved micro beams. *International Journal of Engineering Science*, 110:15–34, 2017.
- [67] A Hajjaj, N Alcheikh, and M Younis. The static and dynamic behavior of MEMS arch resonators near veering and the impact of initial shapes. *International Journal of Non-Linear Mechanics*, 95:277–286, 2017.
- [68] A Hajjaj, M Hafiz, and M Younis. Mode coupling and nonlinear resonances of MEMS arch resonators for bandpass filters. *Scientific reports*, 7:41820, 2017.
- [69] N Krakover, B Ilic, and S Krylov. Displacement sensing based on resonant frequency monitoring of electrostatically actuated curved micro beams. *Journal of Micromechanics and Microengineering*, 26(11):115006, 2016.
- [70] A Alneamy, M Khater, A Abdel Aziz, G Heppler, and E Abdel-Rahman. Electrostatic arch micro-tweezers. In *Euromech 603: Dynamics of Micro and Nano Electromechanical Systems, Porto, Portugal*, pages 88–91. Universidade do Porto. Reitoria, 2018.

- [71] A Tocchio, A Caspani, and G Langfelder. Mechanical and electronic amplitude-limiting techniques in a MEMS resonant accelerometer. *IEEE Sensors Journal*, 12(6):1719–1725, 2011.
- [72] A Hajjam and S Pourkamali. Fabrication and characterization of MEMS-based resonant organic gas sensors. *IEEE Sensors Journal*, 12(6):1958–1964, 2011.
- [73] R Mestrom, R Fey, J Van Beek, K Phan, and H Nijmeijer. Modelling the dynamics of a MEMS resonator: simulations and experiments. *Sensors and Actuators A: Physical*, 142(1):306–315, 2008.
- [74] M Ghayesh and M Farokhi, Hand Amabili. Nonlinear behaviour of electrically actuated MEMS resonators. *International Journal of Engineering Science*, 71:137–155, 2013.
- [75] L Chua and T Lin. Chaos in digital filters. *IEEE Transactions on Circuits and Systems*, 35(6):648–658, 1988.
- [76] A Luo and F Wang. Chaotic motion in a micro-electro-mechanical system with non-linearity from capacitors. *Communications in Nonlinear Science and Numerical Simulation*, 7(1-2):31–49, 2002.
- [77] K Cuomo, A Oppenheim, and S Strogatz. Synchronization of Lorenz-based chaotic circuits with applications to communications. *IEEE Transactions on circuits and systems II: Analog and digital signal processing*, 40(10):626–633, 1993.
- [78] M Younis and A Nayfeh. A study of the nonlinear response of a resonant microbeam to an electric actuation. *Nonlinear Dynamics*, 31(1):91–117, 2003.

- [79] S Liu, A Davidson, and Q Lin. Simulation studies on nonlinear dynamics and chaos in a MEMS cantilever control system. *Journal of Micromechanics and Microengineering*, 14(7):1064, 2004.
- [80] J Bienstman, J Vandewalle, and R Puers. The autonomous impact resonator: a new operating principle for a silicon resonant strain gauge. *Sensors and Actuators A: Physical*, 66(1-3):40–49, 1998.
- [81] J Stulemeijer, R Herfst, and J Bielen. Chaos in electrostatically actuated RF-MEMS measured and modeled. In *2009 IEEE 22nd International Conference on Micro Electro Mechanical Systems*, pages 920–922. IEEE, 2009.
- [82] M Al-Ghamdi, M Khater, and E Abdel-Rahman. Switching intermittency. *Applied Physics Letters*, 113(15):153501, 2018.
- [83] X Zhao, C Reddy, and A Nayfeh. Nonlinear dynamics of an electrically driven impact microactuator. *Nonlinear Dynamics*, 40(3):227–239, 2005.
- [84] M Mita, M Arai, S Tensaka, D Kobayashi, Philippe Basset, A Kaiser, P Masquelier, L Buchaillet, D Collard, and H Fujita. Electrostatic impact-drive microactuator. In *Technical Digest. MEMS 2001. 14th IEEE International Conference on Micro Electro Mechanical Systems (Cat. No. 01CH37090)*, pages 590–593. IEEE, 2001.
- [85] B DeMartini, H Butterfield, J Moehlis, and K Turner. Chaos for a microelectromechanical oscillator governed by the nonlinear Mathieu equation. *Journal of Microelectromechanical Systems*, 16(6):1314–1323, 2007.
- [86] H Haghghi and A Markazi. Chaos prediction and control in MEMS resonators. *Communications in Nonlinear Science and Numerical Simulation*, 15(10):3091–3099, 2010.

- [87] E Miandoab, H Pishkenari, A Yousefi-Koma, and F Tajaddodianfar. Chaos prediction in MEMS-NEMS resonators. *International Journal of Engineering Science*, 82:74–83, 2014.
- [88] A Nayfeh, H Ouakad, F Najar, S Choura, and E Abdel-Rahman. Nonlinear dynamics of a resonant gas sensor. *Nonlinear Dynamics*, 59(4):607–618, 2010.
- [89] W Zhang, O Tabata, T Tsuchiya, and G Meng. Noise-induced chaos in the electrostatically actuated MEMS resonators. *Physics Letters A*, 375(32):2903–2910, 2011.
- [90] H Li, X Liao, S Ullah, and Li Xiao. Analytical proof on the existence of chaos in a generalized Duffing-type oscillator with fractional-order deflection. *Nonlinear Analysis: Real World Applications*, 13(6):2724–2733, 2012.
- [91] F Tajaddodianfar, H Pishkenari, and M Yazdi. Prediction of chaos in electrostatically actuated arch micro-nano resonators: Analytical approach. *Communications in Nonlinear Science and Numerical Simulation*, 30(1-3):182–195, 2016.
- [92] S Luo, S Li, T Phung, and J Hu. Chaotic behavior and adaptive control of the arch MEMS resonator with state constraint and sector input. *IEEE Sensors Journal*, 18(17):6986–6995, 2018.
- [93] S Yin and B Epureanu. Experimental enhanced nonlinear dynamics and identification of attractor morphing modes for damage detection. 2007.
- [94] A Seleim, S Towfighian, E Delande, E Abdel-Rahman, and G Heppler. Dynamics of a close-loop controlled MEMS resonator. *Nonlinear Dynamics*, 69(1-2):615–633, 2012.
- [95] N Nguyen and C Ho, Sand Low. A polymeric microgripper with integrated thermal actuators. *Journal of Micromechanics and Microengineering*, 14(7):969, 2004.

- [96] K Ivanova, T Ivanov, A Badar, B Volland, I Rangelow, D Andrijasevic, F Sümeecz, S Fischer, M Spitzbart, W Brenner, and I Kostic. Thermally driven microgripper as a tool for micro assembly. *Microelectronic Engineering*, 83(4-9):1393–1395, 2006.
- [97] B Solano and D Wood. Design and testing of a polymeric microgripper for cell manipulation. *Microelectronic Engineering*, 84(5-8):1219–1222, 2007.
- [98] K Andersen, K Carlson, D Petersen, K Mølhave, V Eichhorn, S Fatikow, and P Bøggild. Electrothermal microgrippers for pick-and-place operations. *Microelectronic engineering*, 85(5-6):1128–1130, 2008.
- [99] N Chronis and L Lee. Electrothermally activated SU-8 microgripper for single cell manipulation in solution. *Journal of Microelectromechanical systems*, 14(4):857–863, 2005.
- [100] B Volland, K Ivanova, T Ivanov, Y Sarov, E Guliyev, A Persaud, J-P Zöllner, S Klett, I Kostic, and IW Rangelow. Duo-action electro thermal micro gripper. *Microelectronic engineering*, 84(5-8):1329–1332, 2007.
- [101] A Dow, B Jazizadeh, N Kherani, and I Rangelow. Development and modeling of an electrothermally MEMS microactuator with an integrated microgripper. *Journal of Micromechanics and Microengineering*, 21(12):125026, 2011.
- [102] R Mackay, H Le, S Clark, and J Williams. Polymer micro-grippers with an integrated force sensor for biological manipulation. *Journal of micromechanics and microengineering*, 23(1):015005, 2012.
- [103] Z Wang, X Shen, and X Chen. Design, modeling, and characterization of a MEMS electrothermal microgripper. *Microsystem Technologies*, 21(11):2307–2314, 2015.

- [104] P Shivhare, G Uma, and M Umopathy. Design enhancement of a chevron electrothermally actuated microgripper for improved gripping performance. *Microsystem Technologies*, 22(11):2623–2631, 2016.
- [105] R Voicu, C Tibeica, R Müller, A Dinescu, M Pustan, and C Birleanu. Design, simulation and testing of polymeric microgrippers with V-shaped electrothermal actuators and encapsulated heaters. In *2016 International Semiconductor Conference (CAS)*, pages 89–92. IEEE, 2016.
- [106] A Somà, S Iamoni, R Voicu, R Müller, M Al-Zandi, and C Wang. Design and experimental testing of an electro-thermal microgripper for cell manipulation. *Microsystem Technologies*, 24(2):1053–1060, 2018.
- [107] F Beyeler, D Bell, B Nelson, Y Sun, A Neild, S Oberti, and Jürg Dual. Design of a micro-gripper and an ultrasonic manipulator for handling micron sized objects. In *2006 IEEE/RSJ International Conference on Intelligent Robots and Systems*, pages 772–777. IEEE, 2006.
- [108] E Abdel-Rahman, M Younis, and A Nayfeh. Characterization of the mechanical behavior of an electrically actuated microbeam. *Journal of Micromechanics and Microengineering*, 12(6):759, 2002.
- [109] J Varona, E Saenz, S Fiscal-Woodhouse, and A Hamoui. Design and fabrication of a novel microgripper based on electrostatic actuation. In *2009 52nd IEEE International Midwest Symposium on Circuits and Systems*, pages 827–832. IEEE, 2009.
- [110] J Chang, B Min, J Kim, S Lee, and L Lin. Electrostatically actuated carbon nanowire nanotweezers. *Smart materials and structures*, 18(6):065017, 2009.

- [111] B Chen, Y Zhang, and Y Sun. Active release of microobjects using a MEMS microgripper to overcome adhesion forces. *Journal of microelectromechanical systems*, 18(3):652–659, 2009.
- [112] H Chang, H Zhao, F Ye, G Yuan, J Xie, M Kraft, and W Yuan. A rotary comb-actuated microgripper with a large displacement range. *Microsystem technologies*, 20(1):119–126, 2014.
- [113] B Volland, H Heerlein, and I Rangelow. Electrostatically driven microgripper. *Microelectronic engineering*, 61:1015–1023, 2002.
- [114] F Beyeler, A Neild, S Oberti, D Bell, Y Sun, J Dual, and B Nelson. Monolithically fabricated microgripper with integrated force sensor for manipulating microobjects and biological cells aligned in an ultrasonic field. *Journal of microelectromechanical systems*, 16(1):7–15, 2007.
- [115] T Chen, L Sun, L Chen, W Rong, and X Li. A hybrid-type electrostatically driven microgripper with an integrated vacuum tool. *Sensors and Actuators A: Physical*, 158(2):320–327, 2010.
- [116] S Bazaz, F Khan, and R Shakoor. Design, simulation and testing of electrostatic SOI MUMPs based microgripper integrated with capacitive contact sensor. *Sensors and Actuators A: Physical*, 167(1):44–53, 2011.
- [117] M Hamed, P Salimi, and M Vismeh. Simulation and experimental investigation of a novel electrostatic microgripper system. *Microelectronic Engineering*, 98:467–471, 2012.
- [118] Q Xu. Design, fabrication, and testing of an MEMS microgripper with dual-axis force sensor. *IEEE Sensors Journal*, 15(10):6017–6026, 2015.

- [119] H Demaghsi, H Mirzajani, and H Ghavifekr. A novel electrostatic based microgripper (cellgripper) integrated with contact sensor and equipped with vibrating system to release particles actively. *Microsystem technologies*, 20(12):2191–2202, 2014.
- [120] B Piriyanont, A Fowler, and S Moheimani. Force-controlled MEMS rotary microgripper. *Journal of Microelectromechanical Systems*, 24(4):1164–1172, 2015.
- [121] K Amjad, S Bazaz, and Y Lai. Design of an electrostatic MEMS microgripper system integrated with force sensor. In *2008 International Conference on Microelectronics*, pages 236–239. IEEE, 2008.
- [122] F Khan, S Bazaz, and M Sohail. Design, implementation and testing of electrostatic SOI MUMPs based microgripper. *Microsystem technologies*, 16(11):1957–1965, 2010.
- [123] A Kalaiarasi and S Thilagar. Design and modeling of electrostatically actuated microgripper. In *Proceedings of 2012 IEEE/ASME 8th IEEE/ASME International Conference on Mechatronic and Embedded Systems and Applications*, pages 7–11. IEEE, 2012.
- [124] G Perret, T Lacornerie, F Manca, S Giordano, M Kumemura, N Lafitte, L Jalabert, M Tarhan, E Lartigau, F Cleri, H Fujita, and D Collard. Real-time mechanical characterization of dna degradation under therapeutic x-rays and its theoretical modeling. *Microsystems & nanoengineering*, 2(1):1–9, 2016.
- [125] Zhang, L and Reutzell, E and Michaleris, P. Finite element modeling discretization requirements for the laser forming process. *International Journal of Mechanical Sciences*, 46(4):623–637, 2004.

- [126] F Najar, S Choura, S El-Borgi, EM Abdel-Rahman, and AH Nayfeh. Modeling and design of variable-geometry electrostatic microactuators. *Journal of micromechanics and microengineering*, 15(3):419, 2004.
- [127] L Meirovitch. *Fundamentals of vibrations*. Waveland Press, 2010.
- [128] X Zhao, E Abdel-Rahman, and A Nayfeh. A reduced-order model for electrically actuated microplates. *Journal of Micromechanics and Microengineering*, 14(7):900, 2004.
- [129] G W Vogl and A H Nayfeh. A reduced-order model for electrically actuated clamped circular plates. *Journal of Micromechanics and Microengineering*, 15(4):684, 2005.
- [130] S Saghir, M Bellaredj, A Ramini, and M Younis. Initially curved microplates under electrostatic actuation: theory and experiment. *Journal of Micromechanics and Microengineering*, 26(9):095004, 2016.
- [131] A Jallouli, N Kacem, G Bourbon, P Le Moal, V Walter, and J Lardies. Pull-in instability tuning in imperfect nonlinear circular microplates under electrostatic actuation. *Physics Letters A*, 380(46):3886–3890, 2016.
- [132] L Medina, R Gilat, and S Krylov. Bistability criterion for electrostatically actuated initially curved micro plates. *International Journal of Engineering Science*, 130:75–92, 2018.
- [133] Y Chen. On the vibration of beams or rods carrying a concentrated mass. 1963.
- [134] P Laura, J Pombo, and E Susemihl. A note on the vibrations of a clamped-free beam with a mass at the free end. *Journal of Sound and Vibration*, 37(2):161–168, 1974.

- [135] J Wu and S Luo. Free vibration analysis of a rectangular plate carrying any number of point masses and translational springs by using the modified and quasi-analytical and numerical combined methods. *International journal for numerical methods in engineering*, 40(12):2171–2193, 1997.
- [136] S Maiz, D Bambill, C Rossit, and P Laura. Transverse vibration of Bernoulli–Euler beams carrying point masses and taking into account their rotatory inertia: Exact solution. *Journal of Sound and Vibration*, 303(3-5):895–908, 2007.
- [137] P Laura, C Filipich, and V Cortinez. Vibrations of beams and plates carrying concentrated masses. *Journal of Sound Vibration*, 117:459–465, 1987.
- [138] M Amabili, M Pellegrini, F Righi, and F Vinci. Effect of concentrated masses with rotary inertia on vibrations of rectangular plates. *Journal of sound and vibration*, 295(1-2):1–12, 2006.
- [139] S Alkharabsheh and M Younis. Dynamics of MEMS arches of flexible supports. *Journal of Microelectromechanical Systems*, 22(1):216–224, 2012.
- [140] F Alfossail, A Hajjaj, and M Younis. Theoretical and experimental investigation of two-to-one internal resonance in MEMS arch resonators. *Journal of Computational and Nonlinear Dynamics*, 14(1), 2019.
- [141] F Najar, M Ghommem, and A Abdelkefi. A double-side electrically-actuated arch microbeam for pressure sensing applications. *International Journal of Mechanical Sciences*, 178:105624, 2020.
- [142] W Lacarbonara, H Arafat, and A Nayfeh. Non-linear interactions in imperfect beams at veering. *International Journal of Non-Linear Mechanics*, 40(7):987–1003, 2005.

- [143] W Lacarbonara. *A theoretical and experimental investigation of nonlinear vibrations of buckled beams*. PhD thesis, Virginia Tech, 1997.
- [144] S Emam. *A theoretical and experimental study of nonlinear dynamics of buckled beams*. PhD thesis, Virginia Tech, 2002.
- [145] P Osterberg and S Senturia. M-TEST: a test chip for MEMS material property measurement using electrostatically actuated test structures. *Journal of Microelectromechanical systems*, 6(2):107–118, 1997.
- [146] P Kambali and A Pandey. Capacitance and force computation due to direct and fringing effects in MEMS/NEMS arrays. *IEEE Sensors Journal*, 16(2):375–382, 2015.
- [147] S Krylov. Lyapunov exponents as a criterion for the dynamic pull-in instability of electrostatically actuated microstructures. *International Journal of Non-Linear Mechanics*, 42(4):626–642, 2007.
- [148] A Nayfeh and B Balachandran. *Applied nonlinear dynamics: analytical, computational, and experimental methods*. John Wiley & Sons, 2008.
- [149] J Humar. *Dynamics of structures*. CRC press, 2012.
- [150] COMSOL Multiphysics V. 5.3a . www.comsol.com. COMSOL AB, Stockholm, Sweden. 2018.
- [151] Ploytec-Inc. *OFV-5000 Vibrometer Controller User Manual*. Available online: <http://www.polytec.com>.
- [152] M Gopanchuk, M Arabi, N Nelson-Fitzpatrick, M S Al-Ghamdi, E Abdel-Rahman, and M Yavuz. Characterization of a non-interdigitated comb drive. In *ASME 2018*

International Design Engineering Technical Conferences and Computers and Information in Engineering Conference. American Society of Mechanical Engineers Digital Collection, 2018.

- [153] M Al-Ghamdi, A Alneamy, S Park, L, M Khater, E Abdel-Rahman, G Heppler, and M Yavuz. Nonlinear parameter identification of a resonant electrostatic MEMS actuator. *Sensors*, 17(5):1121, 2017.
- [154] S Liu, M Fukuoka, and N Sakai. A finite element model for simulating temperature distributions in rotating food during microwave heating. *Journal of Food Engineering*, 115(1):49–62, 2013.
- [155] J Nicholson and L Bergman. Vibration of thick plates carrying concentrated masses. *Journal of Sound and Vibration*, 103(3):357–369, 1985.
- [156] M Gürgöze. On the eigenfrequencies of a cantilever beam with attached tip mass and a spring-mass system. *Journal of Sound and Vibration*, 190(2):149–162, 1996.
- [157] J Wu, D Chen, and H Chou. On the eigenvalues of a uniform cantilever beam carrying any number of spring–damper–mass systems. *International journal for numerical methods in engineering*, 45(9):1277–1295, 1999.

APPENDICES

Appendix A

Masks Design with Integrated Dicing

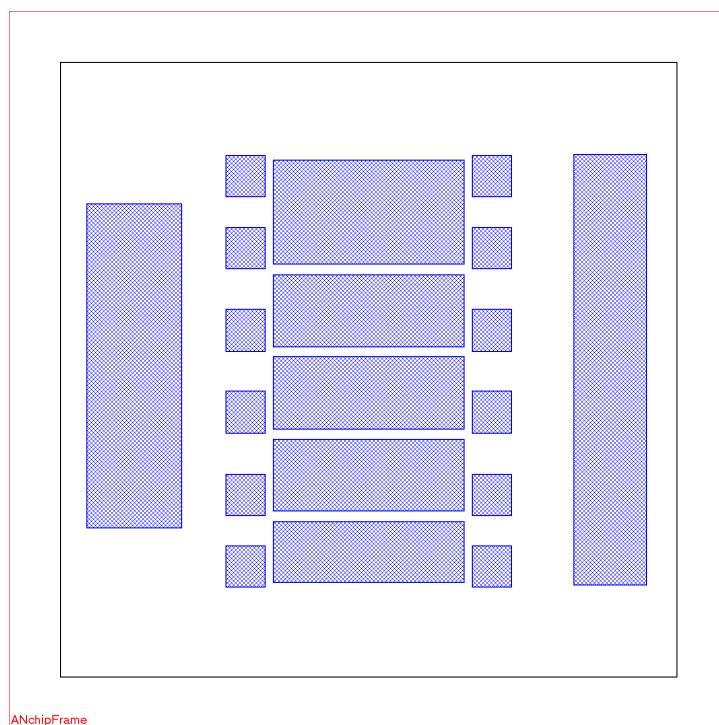


Figure A.1: Mask1 for the metalization layers.

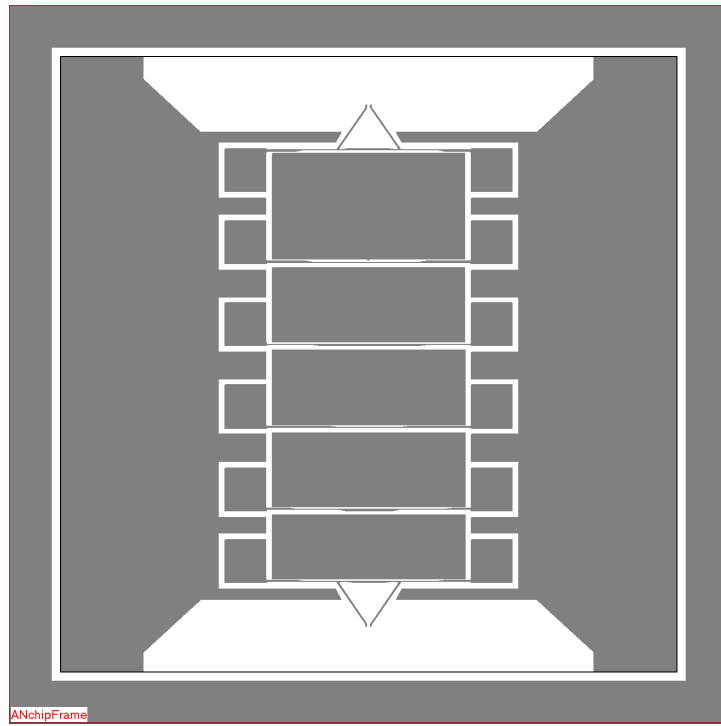


Figure A.2: Mask 2 used to define the device area on the top photoresist layer.

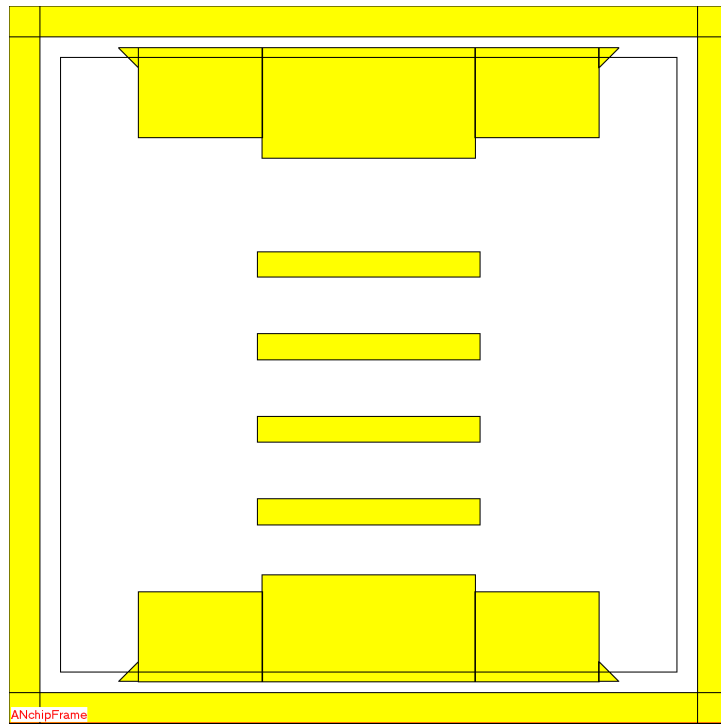


Figure A.3: Mask 3 used to define the backside etched area on the bottom photoresist layer.

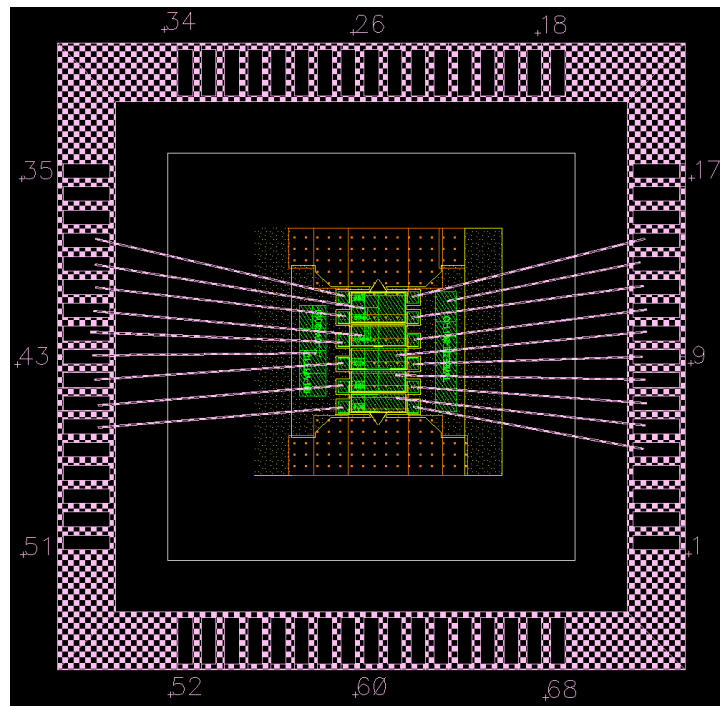


Figure A.4: Wire bonding performed on 68 PGA chip carries for the electrical connection.

Appendix B

Eigenvalues Analysis Including Higher Order Rotary Inertia Terms

In this analysis, we are considering the system equation of motion, Eq. (4.55). Then, the beam deflection $w(x, t)$ is split into two components, a static deflection $w_s(x)$ due to a static load V_{RMS} and a dynamic deflection $w_d(x, t)$ as shown in Eq. (4.78). Then, substituting Eq. (4.78) into Eq. (4.55) and dropping the damping terms results in¹

$$\begin{aligned} (1 + \alpha_1 \delta_d) \ddot{w}_d - (\alpha_2 + \alpha_4 \delta_d) \ddot{w}_d'' - \alpha_4 \delta_d' \ddot{w}_d' + \gamma_{10} + w_s^{iv} + w_d^{iv} \\ - \alpha_5 (w_o'' + w_s'' + w_d'') \int_0^1 (2w_o' (w_s' + w_d') + (w_s' + w_d')^2) dx \\ = \frac{\alpha_6 V_{\text{RMS}}^2}{(1 + w_o - w_s - w_d)^2} \end{aligned} \quad (\text{B.1})$$

¹For sake of simplicity, we dropped over-hat ($\hat{\ }$) for now and so on.

where γ_{10} is a combination of rotary terms of order $O(\epsilon^3)$

$$\begin{aligned}
\gamma_{10} = & \alpha_3 \delta'_d \left(2\dot{w}'_d{}^2 (w'_s + w'_d + w'_o) + \ddot{w}'_d \left(\int_0^1 (2w'_o (w'_s + w'_d) + w_s'^2 + 2w'_s w'_d + w_d'^2) dx \right. \right. \\
& \left. \left. + w_s'^2 + 2w'_s w'_d + w_d'^2 + 2w'_o (w'_s + w'_d) \right) \right) \\
& + \alpha_3 \delta_d \left(\ddot{w}'_d \left((2w_s'' + 2w_d'' + 4w_o'')(w'_s + w'_d + w'_o) - 2w_o''(w'_s + w'_d) \right) \right. \\
& \left. + 4\dot{w}'_d \dot{w}_d'' (w'_s + w'_d + w'_o) + 2\dot{w}'_d{}^2 (w_s'' + w_d'' + w_o'') \right. \\
& \left. + \ddot{w}_d'' \left(\int_0^{\ell_b} (2w'_o (w'_s + w'_d) + w_s'^2 + 2w'_s w'_d + w_d'^2) dx + w_s'^2 + 2w'_s w'_d + w_d'^2 \right. \right. \\
& \left. \left. + 2w'_o (w'_s + w'_d) \right) \right)
\end{aligned} \tag{B.2}$$

Note that the electrostatic force linearized around w_s is shown in Eq. (4.80). Drop the high order terms and retain only up to the linear term in w_d , then substitute the resulting equation into Eq. (B.1) yields

$$\begin{aligned}
(1 + \alpha_1 \delta_d) \ddot{w}_d - (\alpha_2 + \alpha_4 \delta_d) \ddot{w}_d'' - \alpha_4 \delta'_d \ddot{w}'_d + \gamma_{11} + w_s^{iv} + w_d^{iv} \\
- \alpha_5 \left(w_d'' \int_0^1 (2w'_s w'_o + w_s'^2) dx + w_s'' \int_0^1 2(w'_s w'_d + w'_o w'_d) dx \right. \\
\left. + w_o'' \int_0^1 2(w'_o w'_d + w'_s w'_d) dx \right) = \frac{2\alpha_6 V_{\text{RMS}}^2}{(1 + w_o - w_s)^3} w_d
\end{aligned} \tag{B.3}$$

where γ_{11} is a combination of rotary terms of order $O(\epsilon^3)$ linearized around w_d

$$\begin{aligned}
\gamma_{11} = & \alpha_3 \delta'_d \left(2\dot{w}'_d{}^2 (w'_s + w'_d + w'_o) + \ddot{w}'_d \left(\int_0^1 (2w'_o (w'_s + w'_d) + w_s'^2 + 2w'_s w'_d + w_d'^2) dx \right. \right. \\
& \left. \left. + w_s'^2 + 2w'_s w'_d + w_d'^2 + 2w'_o (w'_s + w'_d) \right) \right) \\
& + \alpha_3 \delta_d \left(\ddot{w}'_d \left((2w_s'' + 2w_d'' + 4w_o'')(w'_s + w'_d + w'_o) - 2w_o''(w'_s + w'_d) \right) \right. \\
& \left. + 4\dot{w}'_d \dot{w}_d'' (w'_s + w'_d + w'_o) + 2\dot{w}'_d{}^2 (w_s'' + w_d'' + w_o'') \right. \\
& \left. + \ddot{w}_d'' \left(\frac{1}{\ell_b} \int_0^{\ell_b} (2w'_o (w'_s + w'_d) + w_s'^2 + 2w'_s w'_d + w_d'^2) dx + w_s'^2 + 2w'_s w'_d + w_d'^2 \right. \right. \\
& \left. \left. + 2w'_o (w'_s + w'_d) \right) \right)
\end{aligned} \tag{B.4}$$

This equation, (B.4), can be simplified as

$$\begin{aligned}
\gamma_{11} = & \alpha_3 \delta'_d \left(\ddot{w}'_d \left(\int_0^1 (2w'_o w'_s + w_s'^2) dx + w_s'^2 + 2w'_o w'_s \right) \right) \\
& + \alpha_3 \delta_d \left(\ddot{w}'_d ((2w_s'' + 4w_o'')(w'_s + w'_o) - 2w_o'' w'_s) \right) \\
& + \ddot{w}''_d \left(\int_0^{\ell_b} (2w'_o w'_s + w_s'^2) dx + w_s'^2 + 2w'_o w'_s \right)
\end{aligned} \tag{B.5}$$

Next, we apply the Galerkin expansion on Eq. (4.81) to solve the eigenvalue problem by assuming that

$$w_d(x, t) = \sum_{i=1}^N \phi_i(x) q_i(t) \tag{B.6}$$

Similarly to the previous analysis outlined above, substituting Eq. (B.6) into Eq. (B.3) and replace ϕ_i^{iv} with $\omega_n^2 \phi_i$ using Eq. (4.61), the outcome equation is then multiplied by the mode shape ϕ_j on both sides and integrating along the beam length from $x = 0$ to $x = 1$ to yield

$$\begin{aligned}
(1 + \alpha_1 \delta_d) \ddot{q}_j - (\alpha_2 + \alpha_4 \delta_d) \sum_{i=1}^N \phi_i'' \ddot{q}_i \int_0^1 \phi_j dx - \alpha_4 \delta'_d \sum_{i=1}^N \phi_i' \ddot{q}_i \int_0^1 \phi_j dx \\
+ \gamma_{12} \int_0^1 \phi_j dx + w_s^{iv} + q_j \omega_{i,j}^2 - \alpha_5 \left(\sum_{i=1}^N \phi_i'' q_i \int_0^1 \phi_j dx \int_0^1 (2w'_s w'_o + w_s'^2) dx \right. \\
+ w_s'' \int_0^1 \phi_j dx \int_0^1 2(w'_s \sum_{i=1}^N \phi_i' q_i + w'_o \sum_{i=1}^N \phi_i' q_i) dx \\
\left. + w_o'' \int_0^1 \phi_j dx \int_0^1 2(w'_o \sum_{i=1}^N \phi_i' q_i + w'_s \sum_{i=1}^N \phi_i' q_i) dx \right) \\
= \frac{2\alpha_6 V_{\text{RMS}}^2}{(1 + w_o - w_s)^3} \sum_{i=1}^N \phi_i' q_i \int_0^1 \phi_j dx
\end{aligned} \tag{B.7}$$

where

$$\begin{aligned}
\gamma_{12} = & \alpha_3 \delta'_d \left(\sum_{i=1}^N \phi'_i \ddot{q}_i \left(\int_0^1 (2w'_o w'_s + w_s'^2) dx + w_s'^2 + 2w'_o w'_s \right) \right) \\
& + \alpha_3 \delta_d \left(\sum_{i=1}^N \phi'_i \ddot{q}_i \left((2w_s'' + 4w_o'')(w'_s + w'_o) - 2w_o'' w'_s \right) \right) \\
& + \sum_{i=1}^N \phi_i'' \ddot{q}_i \left(\int_0^{\ell_b} (2w'_o w'_s + w_s'^2) dx + w_s'^2 + 2w'_o w'_s \right)
\end{aligned} \tag{B.8}$$

This equation represents a system of linearly coupled differential equations in terms of the modal coordinates q_j . Solving the eigenvalue problem associated with this system results in the first n^{th} natural frequencies of the arch micro-beam with attachments under electrostatic force.

Appendix C

Dynamic Analysis Including Higher Order Rotary Inertia Terms

The dynamic response under static voltage V_{DC} and time-varying voltage V_{AC} of the arch beam with attachments can be investigated. This is done by assuming that the mid-point rise deflection $w(x, t)$ is consisting of static component $w_s(x)$, and dynamic component $w_d(x, t)$ as shown in Eq. (4.78).

Similarly to the previous analysis, we substitute Eq. (4.78) into Eq. (4.57) and keep the nonlinearities terms result in an equation representing the dynamic response of the micro-tweezers as follows

$$\begin{aligned}
& (1 + \alpha_1 \delta_d) \ddot{q}_j - (\alpha_2 + \alpha_4 \delta_d) \sum_{i=1}^N \phi_i'' \ddot{q}_i \int_0^1 \phi_j dx - \alpha_4 \delta_d' \sum_{i=1}^N \phi_i' \ddot{q}_i \int_0^1 \phi_j dx \\
& + \gamma_{13} \int_0^1 \phi_j dx - \alpha_5 (w_o'' + w_s'' + \sum_{i=1}^N \phi_i'' q_i) \int_0^1 \phi_j dx \int_0^1 (2w_o'(w_s' + \sum_{i=1}^N \phi_i' q_i) \\
& + (w_s' + \sum_{i=1}^N \phi_i' q_i)^2) dx + c_{vt} + c_{sf}) \sum_{i=1}^N \phi_i \dot{q}_i + w_s^{iv} + \sum_{i=1}^N \phi_i^{iv} q_i \\
& = \frac{\alpha_6 V(t)^2}{(1 + w_o - w_s - \sum_{i=1}^N \phi_i q_i)^2} \int_0^1 \phi_j dx
\end{aligned} \tag{C.1}$$

where γ_{13} is

$$\begin{aligned}
\gamma_{10} = & \alpha_3 \delta_d' \left(2 \sum_{i=1}^N \phi_i'^2 \dot{q}_i^2 (w_s' + \sum_{i=1}^N \phi_i' q_i + w_o') + \sum_{i=1}^N \phi_i' \ddot{q}_i \left(\int_0^1 (2w_o'(w_s' + \sum_{i=1}^N \phi_i' q_i) + w_s'^2 \right. \right. \\
& + 2w_s' \sum_{i=1}^N \phi_i' q_i + \sum_{i=1}^N \phi_i'^2 q_i^2) dx + w_s'^2 + 2w_s' \sum_{i=1}^N \phi_i' q_i + \sum_{i=1}^N \phi_i'^2 q_i^2 \\
& \left. \left. + 2w_o'(w_s' + \sum_{i=1}^N \phi_i' q_i) \right) \right) \\
& + \alpha_3 \delta_d \left(\sum_{i=1}^N \phi_i' \ddot{q}_i ((2w_s'' + 2 \sum_{i=1}^N \phi_i'' q_i + 4w_o'') (w_s' + \sum_{i=1}^N \phi_i' q_i + w_o') \right. \\
& \left. - 2w_o'' (w_s' + \sum_{i=1}^N \phi_i' q_i) \right) \\
& + 4 \sum_{i=1}^N \phi_i' \dot{q}_i \sum_{i=1}^N \phi_i'' \dot{q}_i (w_s' + \sum_{i=1}^N \phi_i' q_i + w_o') + 2 \sum_{i=1}^N \phi_i'^2 \dot{q}_i^2 (w_s'' + \sum_{i=1}^N \phi_i'' q_i + w_o'') \\
& + \sum_{i=1}^N \phi_i''^2 \ddot{q}_i \left(\int_0^1 (2w_o'(w_s' + \sum_{i=1}^N \phi_i' q_i) + w_s'^2 + 2w_s' \sum_{i=1}^N \phi_i' q_i + \sum_{i=1}^N \phi_i'^2 q_i^2) dx \right. \\
& \left. + w_s'^2 + 2w_s' \sum_{i=1}^N \phi_i' q_i + \sum_{i=1}^N \phi_i'^2 q_i^2 + 2w_o'(w_s' + \sum_{i=1}^N \phi_i' q_i) \right)
\end{aligned} \tag{C.2}$$

Appendix D

Supplementary Data

This appendix contains supplementary results related to the modal analysis and the ROM validation of the micro-tweezers presented in Chapter 6. We investigate the adequacy of the five-mode ROM with rigid arms in the study of the proposed dynamic operating mode and then compared them to those of flexible arms. This will provide more insights about the importance and effects of the arms flexibility and how they are affecting the tweezers operation.

D.1 Modal Analysis

We compare the eigenvalues obtained using the ROM to those of the 2D FEM with rigid as well as flexible arms. In this study, we vary the arms length ℓ_a over the range of 0–250 μm . Then, we obtained the first five symmetric (SY) and asymmetric (ASY) mode shapes $\phi_i(x)$ and eigenvalues ‘natural frequencies’ f_i throughout that range.

Figure D.1 shows that the natural frequencies of the tweezers first symmetric, dotted

black line (...), and asymmetric, dotted magenta line (...), modes decrease smoothly as the arms length increases dropping from $f_1 = 38.48$ kHz to 25.36 kHz and from $f_2 = 63.25$ kHz to 38.27 kHz, respectively. On the other hand, the higher modes are experiencing dramatic decrease in their values as the arms length exceeds $\ell_a \geq 50$ μm .

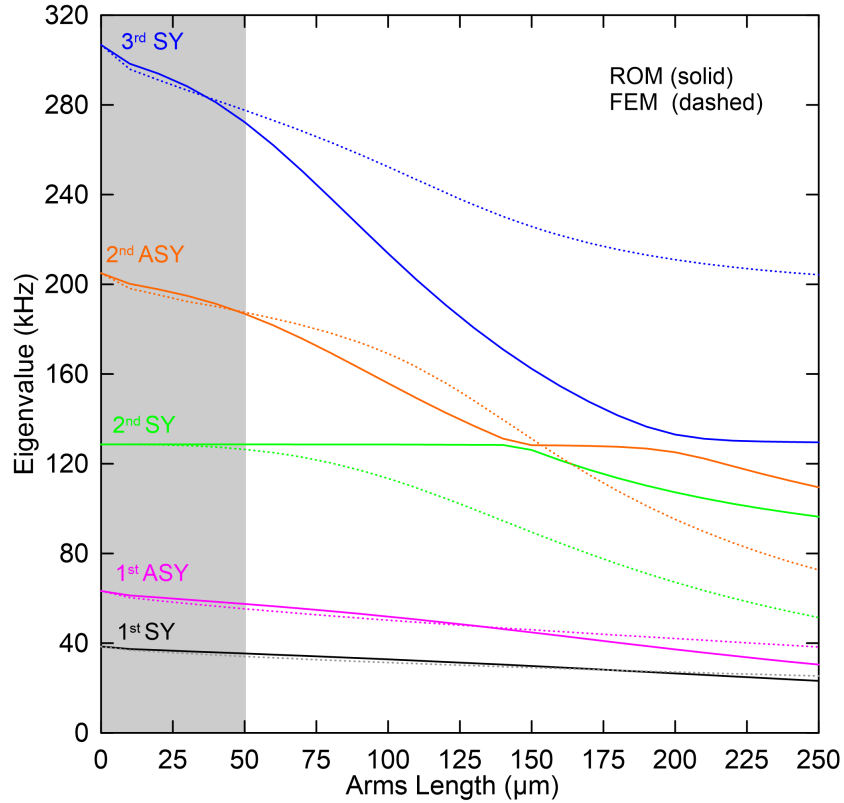


Figure D.1: Variation of the first five natural frequencies, 1st SY mode (black), 1st ASY mode (magenta), 2nd SY mode (green), 2nd ASY mode (orange) and 3rd SY mode (blue), of the arch micro-tweezers with rigid arms as the length varies from 0 to 250 μm obtained using a 2D FEM.

Then, we examine the adequacy of ROMs to represent the tweezers' response by comparing the results of the modal analysis carried out using the FEM described in Chapter 6

to that obtained using a ROM based on the first five mode shapes of a straight beam. The tweezers arms are assumed rigid and represented by concentrated masses and mass moments of inertia in the ROM and FEM.

Table D.1 compares the natural frequencies of the first five modes obtained from the two models for the mounting platform only ‘curved micro-beam’ and micro-tweezers with rigid arms length with $\ell_a = 250 \mu\text{m}$. The models are in excellent agreement in the first case but the ROM fails to capture any of the tweezers' natural frequencies beyond the fundamental frequency (f_1).

Table D.1: Comparison of the first five natural frequencies (in kHz) of the micro-tweezers with rigid arms at two arms lengths obtained from a ROM and an FEM.

	$\ell_a = 0 \mu\text{m}$				
Model	f_1	f_2	f_3	f_4	f_5
ROM	38.48	63.25	128.65	204.96	306.72
FEM	38.48	63.25	128.61	204.95	306.76
	$\ell_a = 250 \mu\text{m}$				
ROM	23.21	30.44	96.38	109.49	129.55
FEM	25.36	38.27	51.42	72.63	204.24

D.2 ROM Validation

To investigate the origins of the ROM shortcomings, we obtained the natural frequencies of the tweezers' first five modes as the arms length varied from 0 to 250 μm using the

five-mode ROM and compared them to those obtained from the FEM. The ROM results are shown as solid lines while the FEM results are shown as dotted lines in Fig. D.1.

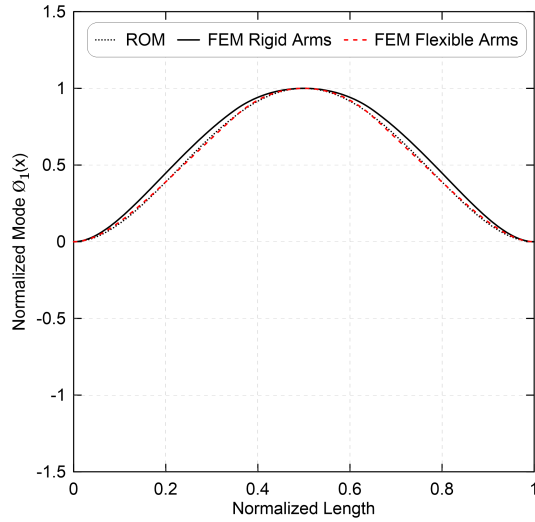
Excellent agreement is observed between the two models for shorter arms length $\ell_a \leq 50 \mu\text{m}$, the gray shaded region in the figure, as well as for the first symmetric mode throughout the arms length range under study. As a result, the five-mode ROM is an adequate representation of the micro-tweezers along that mode. While the agreement between natural frequencies obtained from the two models is excellent for the first and second asymmetric modes for arms length up to $\ell_a \approx 150 \mu\text{m}$ and $\ell_a \approx 50 \mu\text{m}$, it is limited only to arms length up to $\ell_a \approx 50 \mu\text{m}$ for the second and $\ell_a \approx 45 \mu\text{m}$ for the third symmetric modes, Fig. D.1.

Further increase in arms length results in higher kinetic energy along them where the ROMs fail to predict the natural frequencies beyond the first symmetric mode. Therefore, the five-mode ROM is inadequate to represent the tweezers response up to $\ell_a > 50 \mu\text{m}$ for operating frequencies above the first and second natural frequencies.

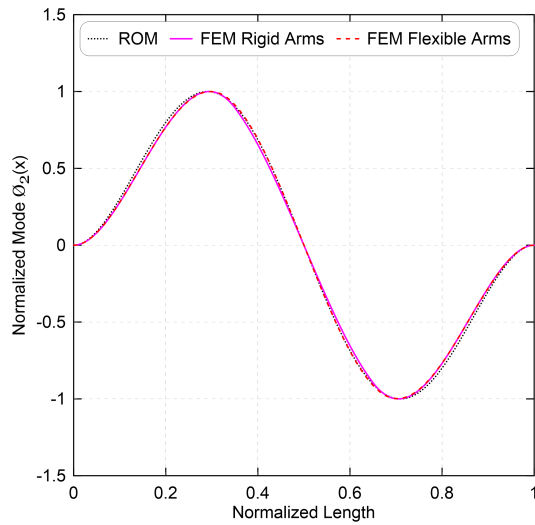
The ROM also predicts two veering between the second symmetric and the second asymmetric modes at $\ell_a \approx 130 \mu\text{m}$ and between the second asymmetric and third symmetric modes at $\ell_a \approx 200 \mu\text{m}$ as shown in Fig. D.1. This, however, is not the case for the FEM where there is no veering or even interaction between the modes. We also found that the ROM mis-identifies modal interactions ‘crossover’ that occurs among higher modes for the platform with flexible arms as shown in Fig. 6.6.

We provide additional insight into the mechanisms underlying the inadequacy of the five-mode ROM to model micro-tweezers by comparing its constituent straight beam mode shapes to those of the tweezers' platform obtained from the FEM in the absence ($\ell_a = 0 \mu\text{m}$) and presence of three lengths arms: $\ell_a = 50, 150$ and $250 \mu\text{m}$. We also investigate the effects of the arms lengths on the nodal locations of those modes. Note that we are comparing

the straight beam mode shapes to that of the FEM with rigid and flexible arms.



(a) 1st SY



(b) 1st ASY

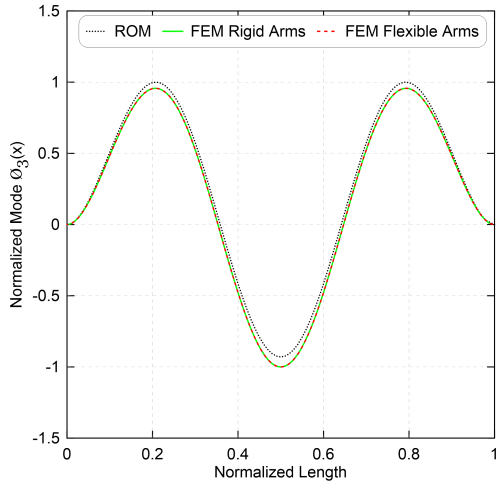
Figure D.2: The mode shapes obtained using ROM for a straight beam (dotted lines) and FEM for a curved beam with 250 μm rigid arms (solid lines) and flexible arms (dashed lines): (a) 1st symmetric (SY) and (b) 1st anti-symmetric (ASY) modes.

Differences between the first symmetric $\phi_1(x)$ and first asymmetric $\phi_2(x)$ modes of the platform and a straight beam are negligible over the entire arms length range under study for ROM with rigid arms (dotted lines) and FEM with rigid (solid lines). The results are then compared to those with flexible arms (dashed lines) as shown in Figs. D.2(a) and (b), respectively. The modes are normalized with respect to the peak value and the beam length ℓ_b along the x -axis.

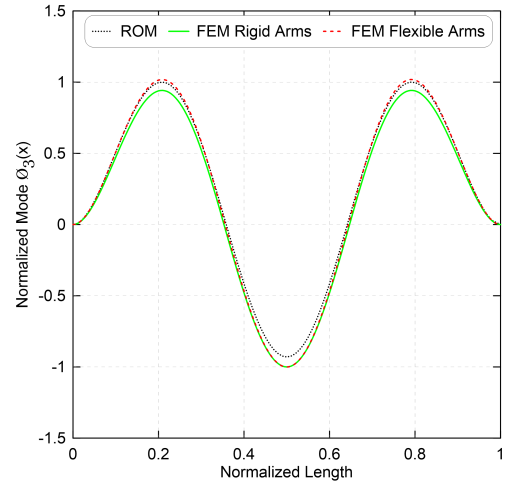
A comparison of the second symmetric $\phi_3(x)$ mode of a straight beam (solid black lines) and the tweezers' platform with rigid arms (solid green lines) and with flexible arms (dashed red lines) is shown in Fig. D.3. The differences between the straight beam and the platform modes are negligible for arms length up to $\ell_a = 50 \mu\text{m}$ along the three models, Figs. D.3(a) and (b), indicating that the rigid and flexible arms are not interrupting the platform motions along that operating range. However, this agreement slightly deteriorates as the arms length, their kinetic energy in the case of the platform rigid arms and their kinetic and potential energies in the case of the platform flexible arms, further increases.

The change in the energy balance along the span leads to a significant small changes in the nodal locations as they approach each other as shown in Fig. D.3(c) at arms length of $\ell_a = 150 \mu\text{m}$ and Fig. D.3(d) at $\ell_a = 250 \mu\text{m}$, respectively. Comparing this movement to that of the flexible arms shows that the arms potential energy is significant at the higher length resulting in nodal locations that approach each other merge and disappear at $\ell_a = 250 \mu\text{m}$. Indeed, the five-mode ROM is an adequate representation for the tweezers response with rigid arms.

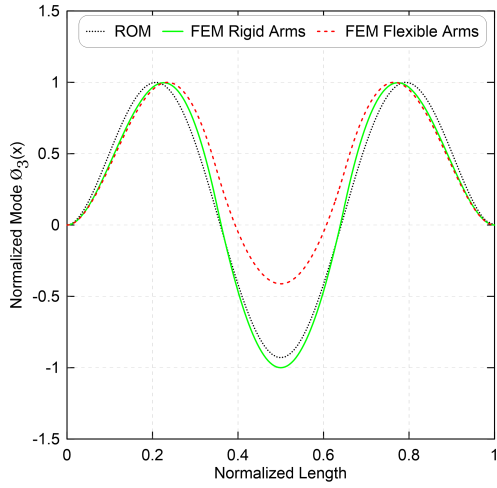
We track the nodal locations along the platform span using the FEM of the tweezers as functions of the arms length in the range of 0–250 μm . Figure D.4(a) shows that the interior nodes marked by (●) symbols are stationary up to arms length of $\approx 125 \mu\text{m}$. These nodes do not disappear for longer arms length.



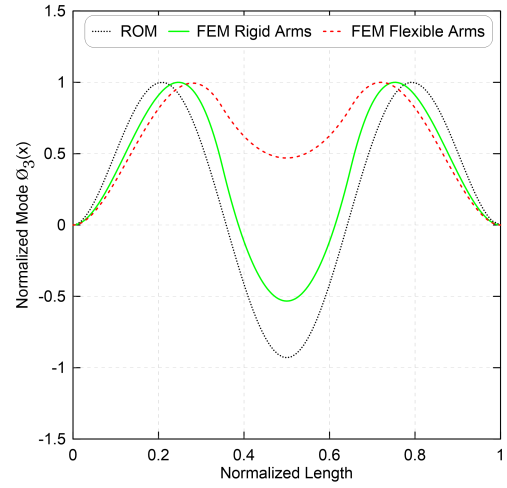
(a) $\ell_a = 0 \mu\text{m}$



(b) $\ell_a = 50 \mu\text{m}$



(c) $\ell_a = 150 \mu\text{m}$



(d) $\ell_a = 250 \mu\text{m}$

Figure D.3: The second symmetric mode $\phi_3(x)$ of the tweezers platform with rigid arms (solid green lines) and with flexible arms (dashed red lines) for arms lengths: (a) $\ell_a = 0 \mu\text{m}$, (b) $\ell_a = 50 \mu\text{m}$, (c) $\ell_a = 150 \mu\text{m}$ and (d) $\ell_a = 250 \mu\text{m}$ compared to that of a straight beam (black dotted lines).

This, however, is not that case for the platform with flexible arms where a change in the energy balance along the beam span occurs resulting in a reduction in the potential energy of the beam middle sub-span, between the two arms, as the nodes smoothly approach each other, merge and disappear at $\ell_a \approx 180 \mu\text{m}$. Comparing the mode shapes of the platform with rigid and flexible arms shows that in the first case, the shape is representing the second symmetric mode of a straight beam, however, in the second case the shape is resembling that of a straight beam first symmetric mode.

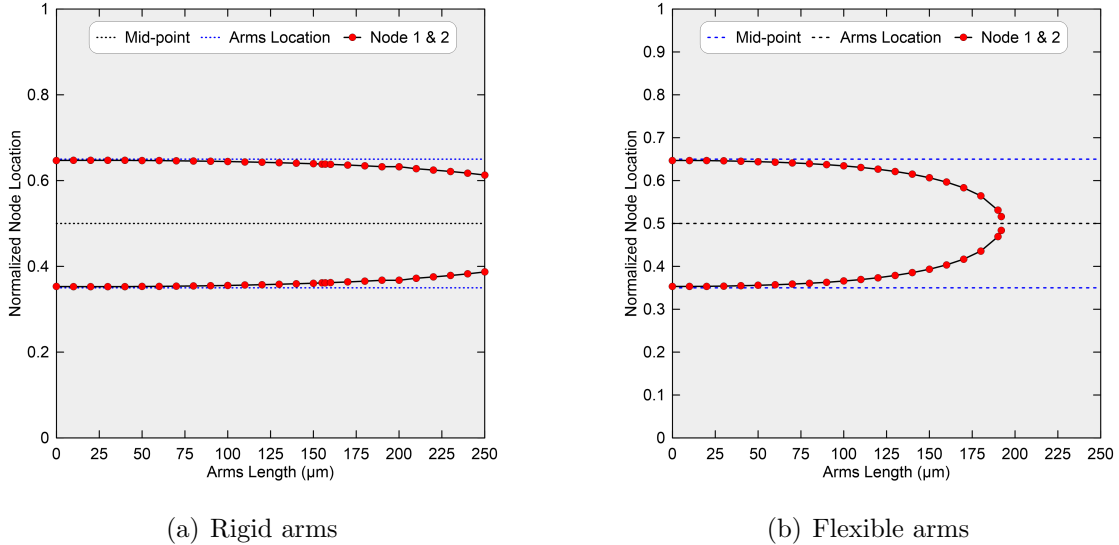


Figure D.4: Variation in the locations of the interior nodes marked by (•) of the second symmetric mode $\phi_3(x)$ of the tweezers platform as functions of the arms length: (a) rigid and (b) flexible arms. The platform mid-point is marked as a dashed black line (- -). The arms attachment points are marked as dashed blue lines (- -).

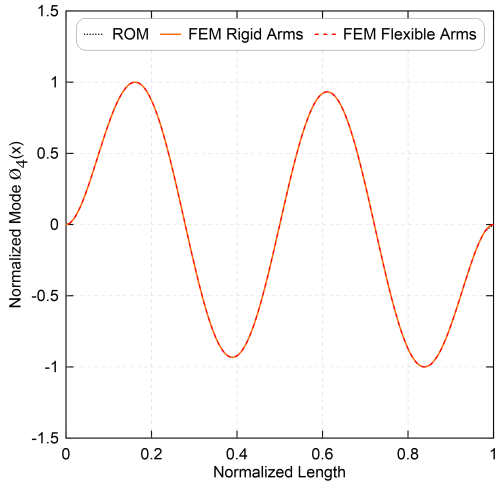
The platform and the straight beam second asymmetric modes $\phi_4(x)$ are in agreement in the absence of arms as shown in Fig. D.5(a). However, the platform mode diverges progressively from the straight beam mode in the presence of the arms, Fig. D.5(b) for

$\ell_a = 50 \text{ }\mu\text{m}$, with the outer nodes moving toward the center node. This process continues as the arms length increases to $\ell_a = 150 \text{ }\mu\text{m}$, Fig. D.5(c), and $\ell_a = 250 \text{ }\mu\text{m}$, Fig. D.5(d).

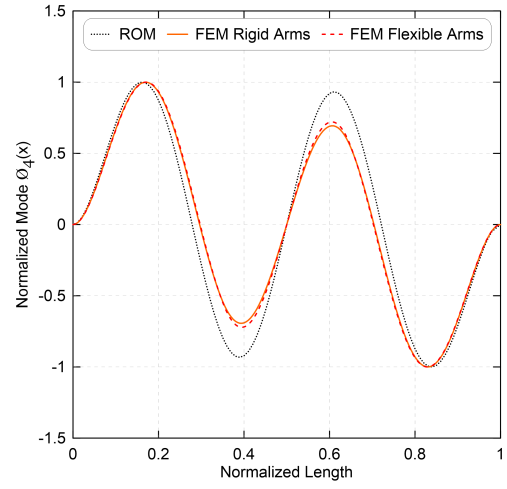
For this mode, longer arms ($\ell_a = 250 \text{ }\mu\text{m}$) result in energy localization in middle sub-span between the two arms compared to the outer sub-spans, which corresponds to increase in the relative compliance of the middle sub-span. On the other hand, similar mode shape for the platform with rigid and flexible arms observed at higher arms length. We also note that the outer nodes of the platform with flexible arms are moving toward the center node faster than that with rigid arms. This is due to the additional potential energy added to the platform total energy. We also found that the location of the center node is insensitive to variation in arms length because of the underlying anti-symmetry of the the platform mode.

The nodal locations of the second asymmetric mode $\phi_4(x)$ as functions of arms length are shown in Fig. D.6 for both cases. The outer nodes 1 and 3 are marked with (●) symbols while the center node 2 is marked with (●) symbols. For the platform with rigid arms, the outer nodes move toward the center node and then they move away from it at $\ell_a \approx 130 \text{ }\mu\text{m}$ as shown in Fig. D.6(a). However, they move toward the center node, merge into it at $\ell_a = 240 \text{ }\mu\text{m}$ and reemerge to move away from the center node beyond that length for the platform with flexible arms as shown in Fig. D.6(b).

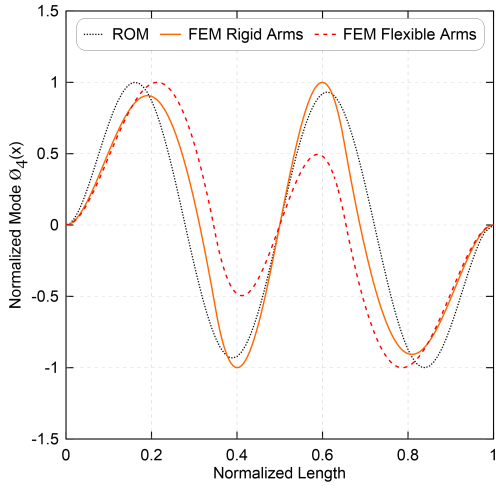
We also found that differences between the third symmetric $\phi_5(x)$ modes of the platform with rigid and flexible and a straight beam were negligible up to $\ell_a = 50 \text{ }\mu\text{m}$ a shown in Fig. D.7(a) and (b). This indicates that the arms do not significantly affect the platform motions. The agreement between the modes deteriorates as the arms length increase to the point where the two interior nodes approach each other for arms length of $\ell_a = 150 \text{ }\mu\text{m}$, Fig. D.7(c), and disappear for $\ell_a = 250 \text{ }\mu\text{m}$, Fig. D.7(d), respectively. We found that as the two outer nodes approach the center resulting in a shape resembles that of the second



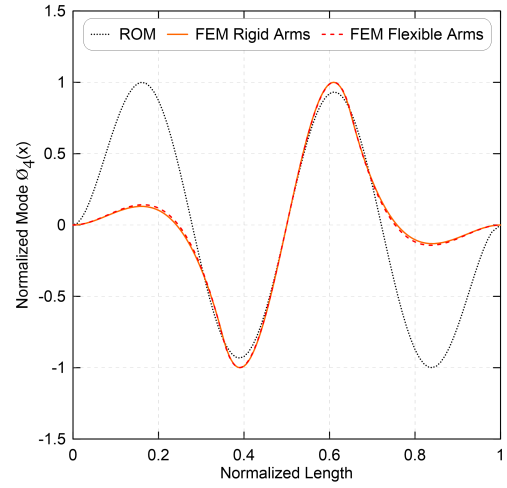
(a) $\ell_a = 0 \mu\text{m}$



(b) $\ell_a = 50 \mu\text{m}$

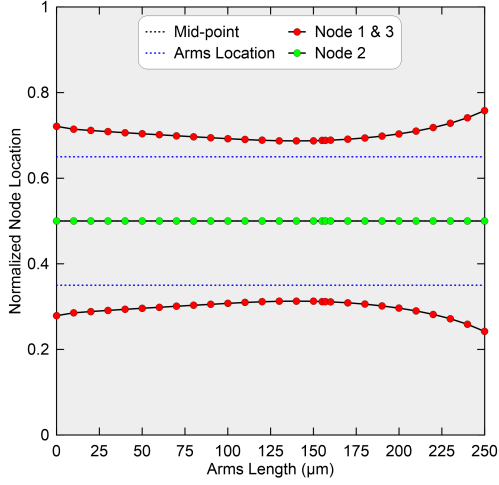


(c) $\ell_a = 150 \mu\text{m}$

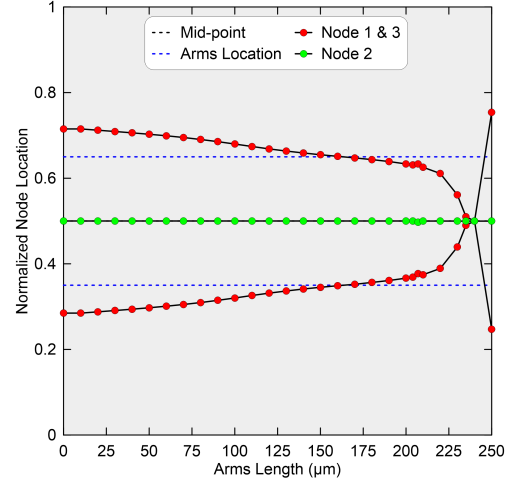


(d) $\ell_a = 250 \mu\text{m}$

Figure D.5: The second asymmetric mode $\phi_4(x)$ of the tweezers platform with rigid arms (solid orange lines) and with flexible arms (dashed red lines) for arms lengths: (a) $\ell_a = 0 \mu\text{m}$, (b) $\ell_a = 50 \mu\text{m}$, (c) $\ell_a = 150 \mu\text{m}$ and (d) $\ell_a = 250 \mu\text{m}$ compared to that of a straight beam (black dotted lines).



(a) Rigid arms



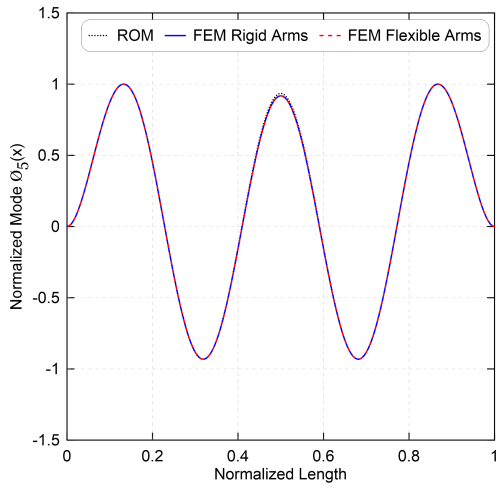
(b) Flexible arms

Figure D.6: Variation in the locations of the outer nodes marked with (●) and center node marked with (●) of the second asymmetric mode $\phi_4(x)$ of the tweezers platform as functions of the arms length: (a) rigid and (b) flexible arms. The platform mid-point is marked as a dashed black line (- -). The arms attachment points are marked as dashed blue lines (- -).

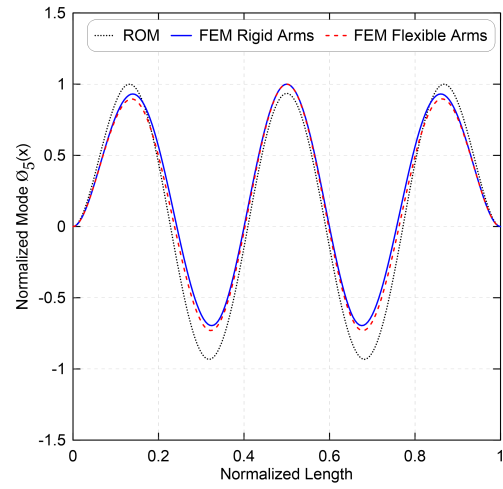
symmetric mode of a straight beam for the platform with rigid and flexible arms.

We also track the locations of those nodes as functions of arms length as shown in Fig. D.8. The interior nodes 2 and 3 marked by (●) symbols remain stationary up to an arms length of $\approx 145 \mu\text{m}$ for the platform with rigid arms and $\approx 90 \mu\text{m}$ for the platform with flexible arms where they abruptly merge and disappear. Similarly, the outer nodes 1 and 4 marked by (●) symbols are almost stationary until the same length range where they start approaching the arms attachment points. This occurs in both cases.

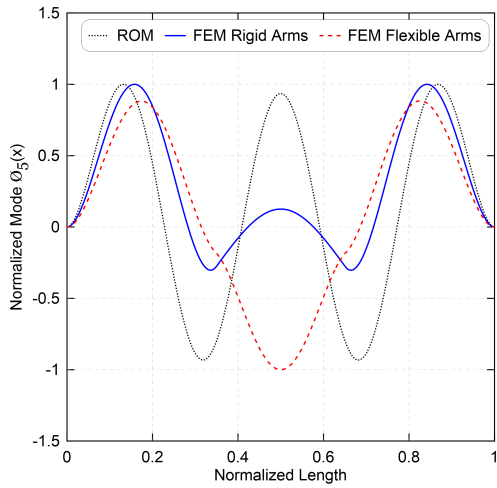
Therefore, the energy distribution along the platform span can be classified into two zones: it resembles that of a straight beam third symmetric mode $\phi_5(x)$ marked as zone I and $\phi_5(x)$ resembling $\phi_3(x)$ marked as zone II. This shows that the arms potential energy



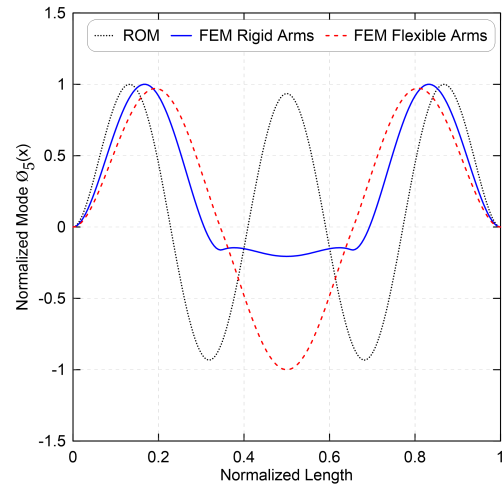
(a) $\ell_a = 0 \mu\text{m}$



(b) $\ell_a = 50 \mu\text{m}$



(c) $\ell_a = 150 \mu\text{m}$



(d) $\ell_a = 250 \mu\text{m}$

Figure D.7: The third symmetric mode $\phi_5(x)$ of the tweezers platform with rigid arms (solid blue lines) and with flexible arms (dashed red lines) for arms lengths: (a) $\ell_a = 0 \mu\text{m}$, (b) $\ell_a = 50 \mu\text{m}$, (c) $\ell_a = 150 \mu\text{m}$ and (d) $\ell_a = 250 \mu\text{m}$ compared to that of a straight beam (black dotted lines).

has a significant effect of the platform motion and, therefore, it requires careful design to maintain the tweezers functionality.

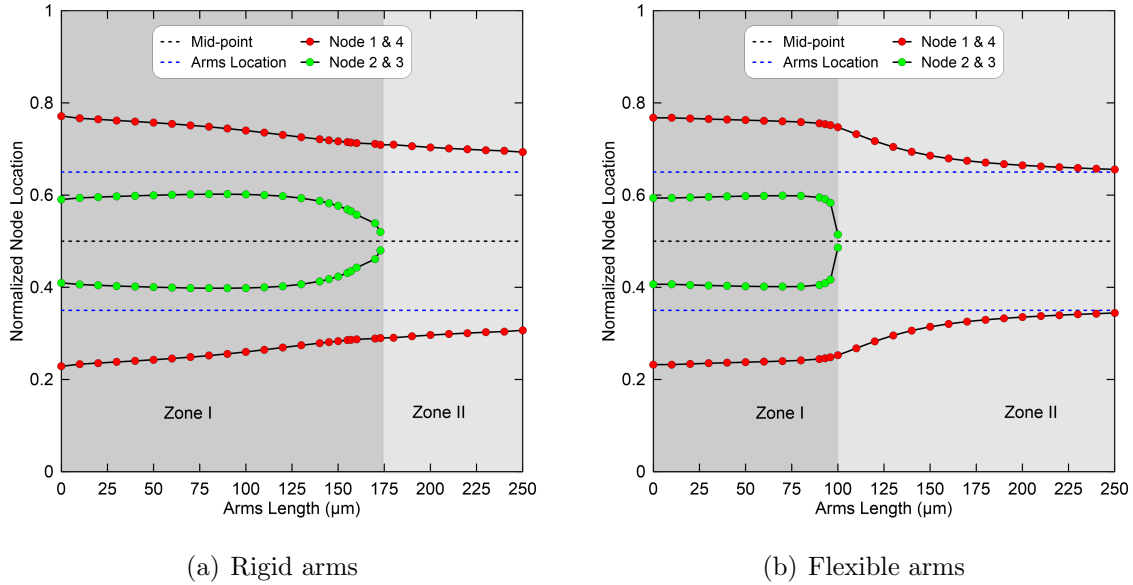
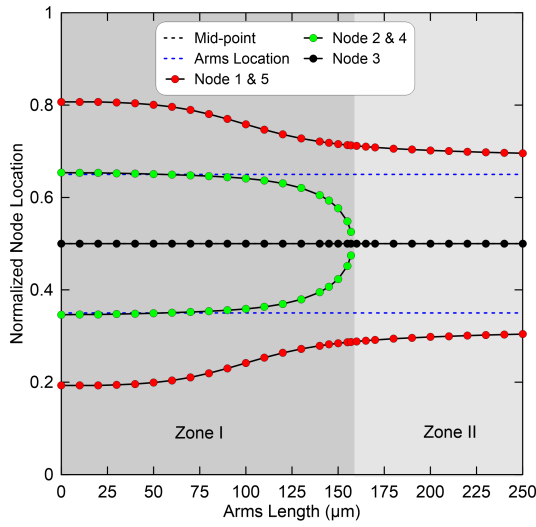
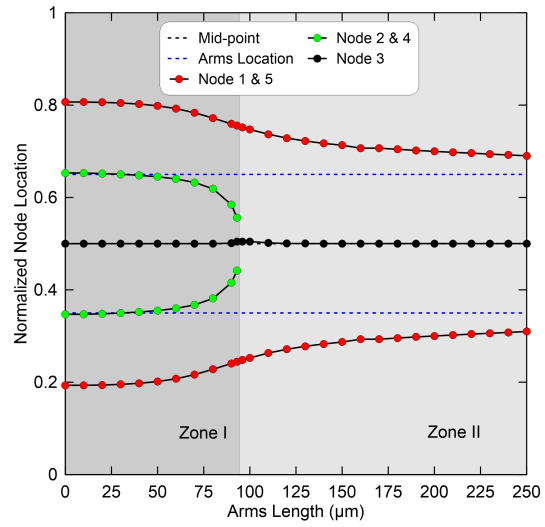


Figure D.8: Variation in the locations of the outer nodes marked with (●) and interior nodes marked with (●) of the third symmetric mode $\phi_5(x)$ of the tweezers platform as functions of the arms length: (a) rigid and (b) flexible arms. The platform mid-point is marked as a dashed black line (- -). The arms attachment points are marked as dashed blue lines (- -).

Similar changes in the platform higher mode shapes were also found as the arms length increase. The locations of their nodes as functions of arms length are shown in Fig. D.9 considering rigid and flexible arms for the third asymmetric mode $\phi_6(x)$, Fig. D.10 for the fourth symmetric mode $\phi_7(x)$, Fig. D.11 for the fourth asymmetric mode $\phi_8(x)$ and Fig. D.12 for the fifth symmetric mode $\phi_9(x)$, respectively.

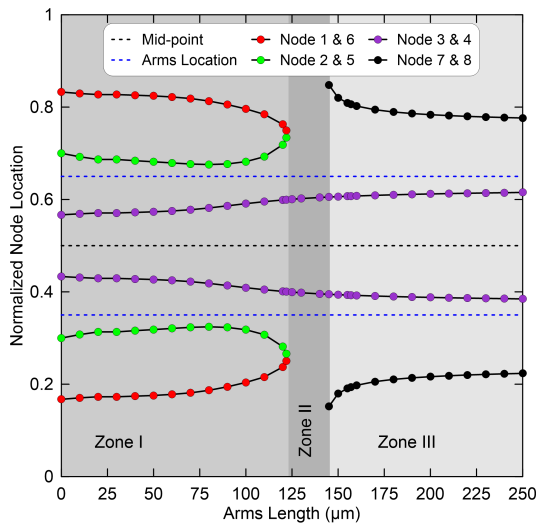


(a) Rigid arms

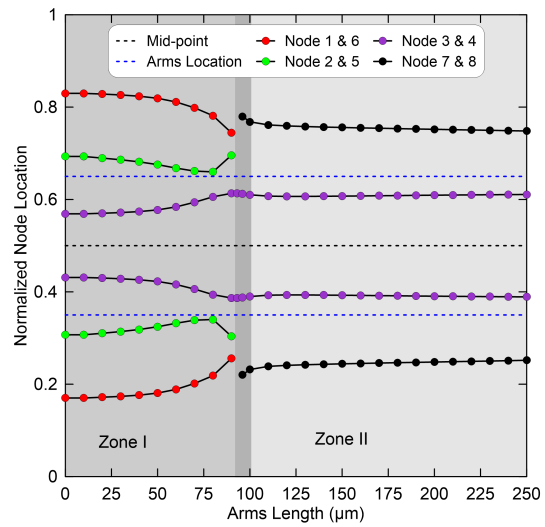


(b) Flexible arms

Figure D.9: Variation in the locations of the outer nodes marked by (●), interior nodes marked by (●) and the center node marked by (●) of the third asymmetric mode $\phi_6(x)$ of the tweezers platform as functions of the arms length: (a) rigid and (b) flexible arms. The platform mid-point is marked as a dashed black line (- -). The arms attachment points are marked as dashed blue lines (- -).

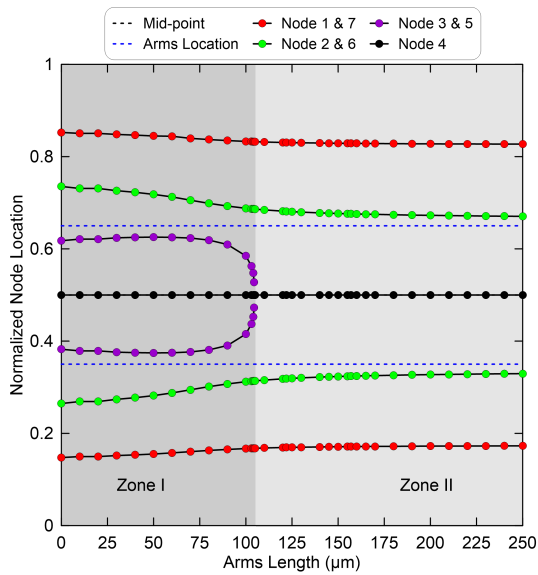


(a) Rigid arms

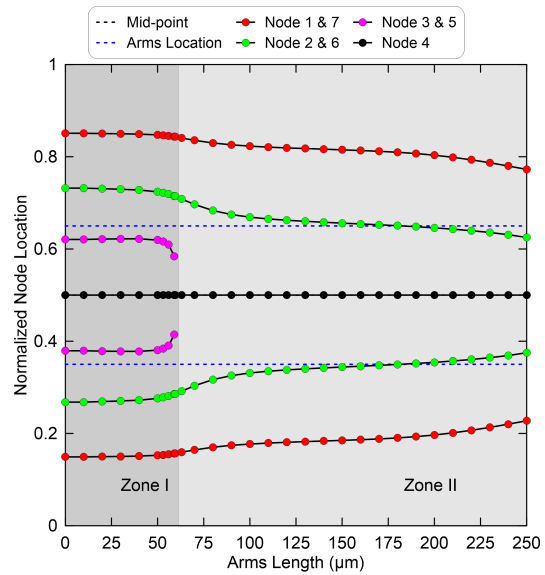


(b) Flexible arms

Figure D.10: Variation in the locations of the outer nodes marked by (●, ● and ●) and interior nodes marked by (●) of the fourth symmetric mode $\phi_7(x)$ of the tweezers platform as functions of the arms length: (a) rigid and (b) flexible arms. The platform mid-point is marked as a dashed black line (- -). The arms attachment points are marked as dashed blue lines (- -).

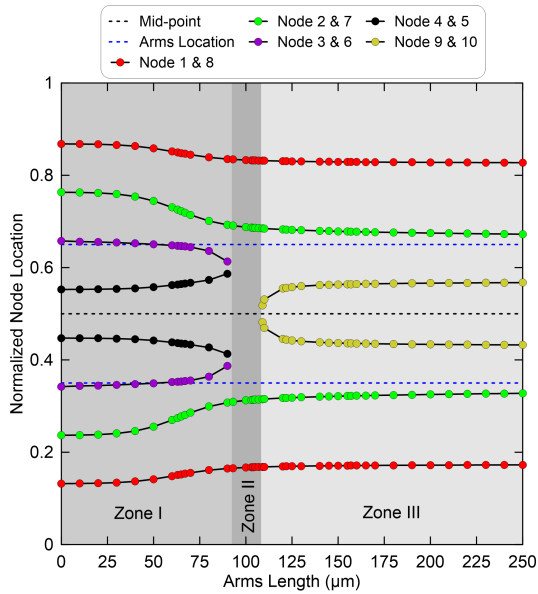


(a) Rigid arms

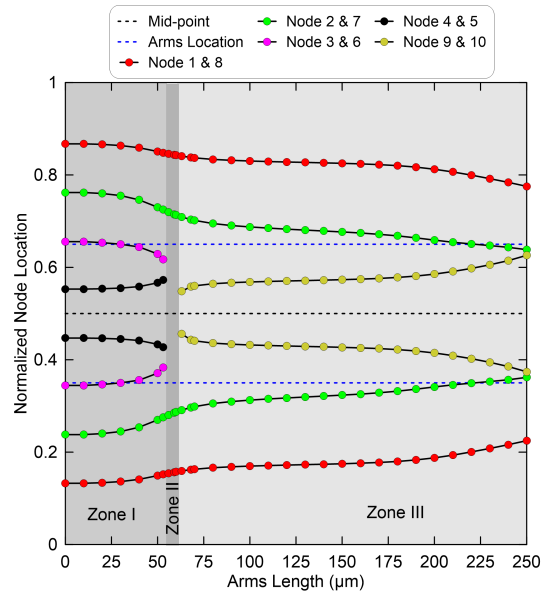


(b) Flexible arms

Figure D.11: Variation in the locations of the outer nodes marked by (● and ●), interior nodes marked by (●) and the center node marked by (●) of the fourth asymmetric mode $\phi_8(x)$ of the tweezers platform as functions of the arms length: (a) rigid and (b) flexible arms. The platform mid-point is marked as a dashed black line (- -). The arms attachment points are marked as dashed blue lines (- -).



(a) Rigid arms



(b) Flexible arms

Figure D.12: Variation in the locations of the outer nodes marked by (● and ●), interior nodes marked by (●, ● and ●) of the fifth symmetric mode $\phi_9(x)$ of the tweezers platform as functions of the arms length: (a) rigid and (b) flexible arms. The platform mid-point is marked as a dashed black line (- -). The arms attachment points are marked as dashed blue lines (- -).

D.3 Tweezers Mode Shapes with Flexible Arms

Table D.2: The mode shapes of the micro-tweezers without and with 50 μm flexible arms obtained using 2D FEM.



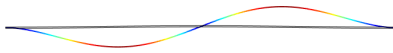

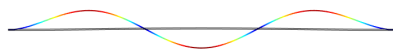
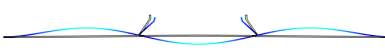
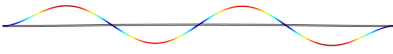
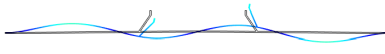
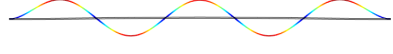
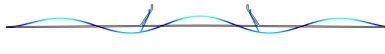
Mode shape #	Arm length ℓ_a	
	No arms	50 μm
Mode 1		
Mode 2		
Mode 3		
Mode 4		
Mode 5		

Table D.3: The mode shapes of the micro-tweezers with 150 μm and 250 μm flexible arms obtained using 2D FEM.

Mode shape #	Arm length ℓ_a	
	150 μm	250 μm
Mode 1		
Mode 2		
Mode 3		
Mode 4		
Mode 5		